RADIATION DAMAGE ACCUMULATION AND ASSOCIATED MECHANICAL HARDENING IN THIN FILMS AND BULK MATERIALS

A Thesis
Presented to
The Academic Faculty

by

Aaron Yehudah Dunn

In Partial Fulfillment
of the Requirements for the Degree
Doctor of Philosophy in the
Woodruff School of Mechanical Engineering

Georgia Institute of Technology
May 2016

RADIATION DAMAGE ACCUMULATION AND ASSOCIATED MECHANICAL HARDENING IN THIN FILMS AND BULK MATERIALS

Approved by:

Professor Laurent Capolungo, Advisor
Woodruff School of Mechanical Engineering
Georgia Institute of Technology

Professor Chaitanya Deo
Nuclear and Radiological Engineering, Woodruff School of Mechanical Engineering
Georgia Institute of Technology

Professor David McDowell
Woodruff School of Mechanical Engineering, School of Materials Science and Engineering
Georgia Institute of Technology

Rémi Dingreville, Ph.D.
Structural and Thermal Analysis
Sandia National Laboratories

Professor Naresh Thadhani
School of Material Science and Engineering
Georgia Institute of Technology

Enrique Martínez-Saez, Ph.D.
Material Science and Technology Division
Los Alamos National Laboratory

Date Approved: February 25, 2016

To my grandfather, Yehudah Ashkenazi, whose scientific curiosity was unparalleled.

To my parents, Revill and Sara, for their ever-constant support of my scientific endeavors.

To Ed Davis and Don Haynes, two of the greatest teachers around, who have influenced myself and countless others to fearlessly pursue our passions.

ACKNOWLEDGEMENTS

I would like to thank my advisor Laurent Capolungo for his excellent and thorough support of my work; Rémi Dingreville and Enrique Martínez-Saez for their support during my time spent at Sandia National Laboratories and Los Alamos National Laboratories as well as their scientific contributions and advice throughout this process; all of the people that have collaborated with me over the course of my studies including Mathieu McPhie, Laura Agudo-Merida, Ignacio Martin-Bragado, Brittany Muntifering, Khalid Hattar, and Blas Uberuaga; my outstanding labmates at Georgia Tech: Manas Upahyay, Pierre-Alexandre Juan, Nicolas Bertin, Cameron Sobie, and Laura Leclercq; and my friends, fellow students, and bandmates Chris Bishop, Peter McKeon, and Matthew Jordan.

TABLE OF CONTENTS

LIST OF TABLES

LIST OF FIGURES

LIST OF ABBREVIATIONS

1D	One dimensional
3D	Three dimensional
BCA	Binary collision approximation
BKS	Bacon, Kocks, and Scattergood model for irradiation-induced hardening
CD	Cluster dynamics
DB	Dispersed barrier hardening model for irradiation-induced hardening
DPA	Displacements per atom
FEM	Finite element method
FKH	Friedel, Kroupa, and Hirsh model for irradiation-induced hardening
iMPALE	Material Point Arbitrary Lagrangian Eulerian Code
MFRT	Mean field rate theory
OKMC	Object-oriented kinetic Monte Carlo
PAS	Positron annihilation spectroscopy
PKA	Primary knock-on atom
PPM	Parts per million
SCD	Stochastic cluster dynamics
SIA	Self-interstitial atom
SRSCD	Spatially resolved stochastic cluster dynamics
TEM	Transmission electron microscopy

SUMMARY

The overall purpose of this dissertation is to develop a multi-scale framework that can simulate radiation defect accumulation across a broad range of time and length scales in metals.

In order to accurately describe defect accumulation in heterogeneous microstructures and under complex irradiation conditions, simulation methods are needed that can explicitly account for the effect of non-homogeneous microstructures on damage accumulation. In this dissertation, an advanced simulation tool called spatially resolved stochastic cluster dynamics (SRSCD) is developed for this purpose. The proposed approach relies on solving spatially resolved coupled rate equations of standard cluster dynamics methods in a kinetic Monte Carlo scheme. Large-scale simulations of radiation damage in polycrystalline materials are enabled through several improvements made to this method, including a pseudo-adaptive meshing scheme for cascade implantation and implementation of this method in a synchronous parallel kinetic Monte Carlo framework.

The performance of the SRSCD framework developed in this dissertation is assessed by comparison to other simulation methods such as cluster dynamics and object kinetic Monte Carlo and experimental results including helium desorption from thin films and defect accumulation in neutron-irradiated bulk iron. The computational scaling of the parallel framework is also investigated for several test cases of irradiation conditions.

SRSCD is next used to investigate radiation damage in three main types of microstructures, using α-iron as a test material: iron thin films, coarse-grained bulk iron, and nanocrystalline iron. SRSCD is used to investigate the mechanisms involved with defect accumulation in irradiated materials, such as effective diffusivity of helium in thin films and the effect of grain boundary sink strength on defect accumulation in nano-grained metals, and to predict defect populations in irradiated materials for comparison with experiments. Particular emphasis is placed on the role of microstructural features such as free surfaces and grain

boundaries in influencing damage accumulation.

Finally, the methodology developed in this dissertation is applied in the context of multiscale modeling and experimental design. To complete the multi-scale transition between defect-level behavior and macroscopic material property changes caused by irradiation, the relationship between mechanical loading and radiation damage is investigated. The impact of radiation damage on hardening of irradiated materials is investigated by using the results of SRSCD as inputs into polycrystalline crystal plasticity simulations. This is carried out in bulk iron by fitting hardening models to experimental data from neutron irradiation of iron and then used to predict hardening under irradiation conditions beyond what has already been accomplished in experimental studies. In addition, SRSCD is used to demonstrate the temperature shift required to achieve equivalent damage accumulation in irradiation conditions with significantly differing dose rates, such as in the case of using ion irradiation to simulate damage from neutron irradiation.

In this dissertation, the development of SRSCD and its application in a multi-scale framework to predict macroscopic material property changes in metals represents a significant improvement over the state of the art due to improved simulations of defect accumulation and direct upscaling of results into polycrystalline plasticity models. The tools and understanding of defect behavior developed here will allow predictive modeling of metal degradation in reactor-relevant damage environments, including the defected microstructure and macroscopic material property changes due to irradiation.

CHAPTER I

INTRODUCTION

1.1 Motivation

1.1.1 Perspective: current and future nuclear industry

The development of advanced structural materials has advanced in parallel with the continued development of nuclear reactors throughout the history of the industry. Today, the majority of the world's nuclear power installations are Generation II reactors, which were built between the 1960s and 1990s and many of which are rapidly approaching the end of their design lifetimes [182, 3]. In view of reactor lifetime extension programs currently being implemented, predictive capabilities of the extent to which their structural materials will continue to degrade over the ensuing decades is needed. Reactors under planning and construction today include Generation III and III+ fission reactors such as EPR, or the Evolutionary Power Reactor (shown in Figure 1a) [3]. These reactors generate electricity using the same basic design philosophy as Generation II reactors but have enhanced levels of safety made possible by the many years of research, development, and experience with Generation II reactors [3]. By contrast, future Generation IV fission reactors will operate using new designs and are expected to achieve greater safety, environmental performance, proliferation safeguards, and efficiency in generating electricity [133]. As such, these reactors will operate at higher temperatures and in more intense radiation environments than previous generations, requiring the development of new structural materials. Finally, the future application of fusion power requires materials are needed which can withstand much higher radiation doses and temperatures than commercial fission reactors [219, 146]. As test reactors such as the International Thermonuclear Experimental Reactor (ITER, Figure 1b) and the DEMOnstration Power Plant (DEMO) are designed, the field of materials development for application in such extreme environments is rapidly advancing.

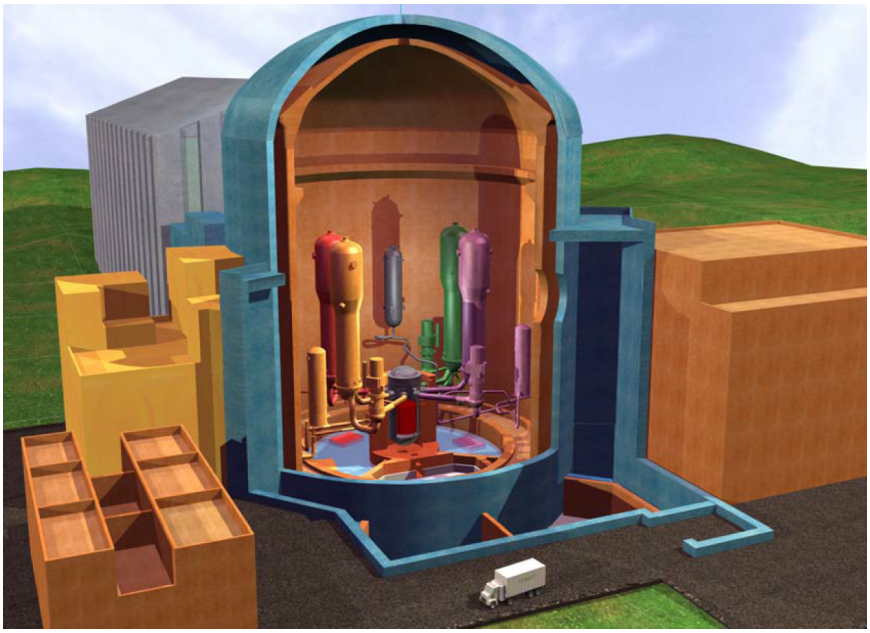

(a) EPR generation III+ reactor

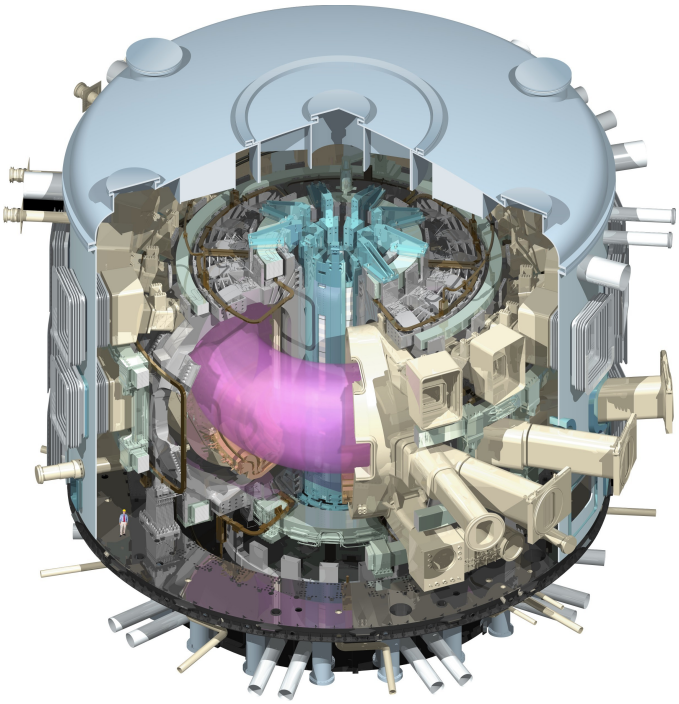

(b) ITER fusion reactor

Figure 1: (1a) Diagram of the European Pressurized Reactor (EPR), a generation III+ pressurized water reactor [228]. (1b) Diagram of ITER, an experimental fusion reactor under construction in France [100].

1.1.2 Extreme environments for nuclear materials: radiation and temperature

Radiation environment: Structural materials in nuclear reactors are subjected to extreme conditions including neutron and gamma irradiation and high temperatures and are expected to maintain mechanical strength throughout the lifetime of the reactor. As discussed in Section 2.1.1, radiation damage in metals is caused by incident particles such as neutrons colliding with lattice atoms and displacing them from their lattice sites. The total quantity of damage, or dose, in an irradiated metal is frequently measured in the total number of atomic displacements per lattice atom, or dpa. In commercial fission reactors, structural materials are subjected to neutron bombardment which causes displacement damage in the material at rates ranging from $10^{-12} - 10^{-6}$ dpa per second, depending on the proximity to the core and the reactor type [139, 2]. Fast fission reactors such as the High Flux Isotope Reactor (HFIR) at Oak Ridge National Laboratory and the BOR-60 reactor in Dimitrovgrad, Russia, typically used for nuclear research, have generally higher dose rates on the order of 10^{-7} dpa$\cdot$s^{-1} [234]. The radiation environment in future fusion reactors is expected include dose rates also on the order of 10^{-7} dpa$\cdot$s^{-1}, in addition to experiencing an increased energy spectrum of neutrons created in the fusion reaction [116]. In all of these reactors, transmutation reactions due to neutron absorption and subsequent decay by the structural material also leads to the production of gases such as hydrogen and helium inside the material [234].

Temperature environment: The temperatures that structural materials (such as the interior wall of the pressure vessel) in nuclear reactors are subjected to vary depending on the reactor type as well. Operating temperatures in typical thermal fission reactors as well as fast fission reactors are subjected to temperatures of approximately 400° C [133]. By contrast, proposed Generation 4 reactor designs will operate at temperatures ranging from 400° C to 800° C [133]. Figure 2 shows the radiation dose and temperature ranges for Generation 2-3 reactors as well as several proposed Generation 4 designs. Future fusion reactors plasma-facing materials are expected to operate under temperatures that are even higher, from 500° C to 900° C [27]. The confluence of all of these factors, including radiation

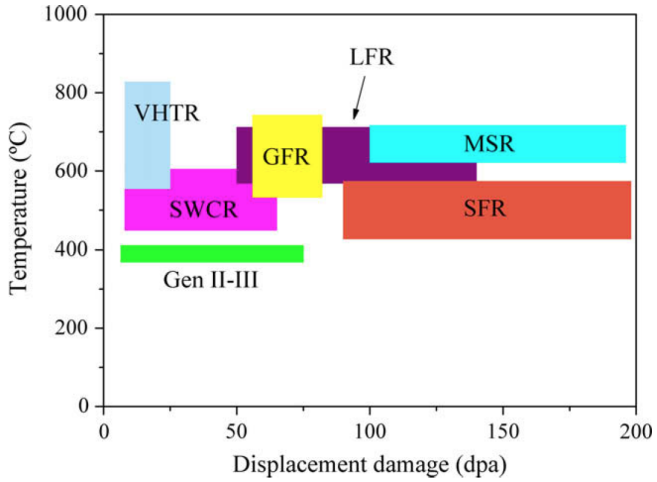

Figure 2: Temperature and dpa ranges in Generation 2-3 reactors as well as several proposed Generation 4 reactor designs. Proposed Generation 4 reactors include the Very High Temperature Reactor (VHTR), the Gas-Cooled Fast Reactor (GFR), the Lead-Cooled Gas Reactor (LFR), the Molten Salt Reactor (MSR), the Supercritical Water Cooled Reactor (SWCR), and the Sodium-Cooled Fast Reactor (SFR) (reproduced with permission from from Marques et al. [133]).

dose, temperature, and the production of gases, can lead to the formation of defects which degrade the mechanical properties of structural materials, as discussed in later sections.

Challenges in reproducing reactor irradiation conditions: Although reactor structural materials are subjected to a wide variety of temperatures, doses, dose rates, and gas production rates, the range of input parameters that can be studied in experiments of radiation damage is much more limited. Due to the cost, radioactive safety concerns, and timescales associated with neutron irradiation experiments in experimental reactors such as HFIR, irradiation experiments are instead frequently carried out in laboratories using various ion beams in place of neutron damage [73, 2, 117, 122]. Under such irradiation conditions, dose rate and temperature can be adjusted to best suit the experiment, by adjusting the focus of the ion beam and placing the irradiated material on a heated stage. Dose rates in ion beam irradiation experiments are typically much higher than neutron irradiation, frequently reaching $10^{-3} - 10^{-2}$ dpa·s^{-1} [170, 2]. These high dose rates allow experimentalists to react the same radiation doses that reactors would encounter in years

over a matter of minutes to hours. However, as damage conditions in ion beam irradiation experiments are not equivalent to the conditions that materials will be expected to withstand in true reactors, experimental results cannot be compared directly with material behavior in realistic reactor conditions. Therefore, models are needed which can reproduce experimentally observed behaviors such defect populations and material property changes and link those observations to predicted behaviors in realistic reactor environments.

1.1.3 Materials in use and under development for nuclear applications and their microstructural changes under irradiation

Several different material types are currently in use or under development for nuclear applications. Typical requirements for such materials include resistance to damage accumulation, low cross-sections for transmutation, high strength, and high melting temperatures (significantly above temperatures that might occur during an accident). Examples of some of the material types either in use or under development are given below:

1. **Reactor pressure vessel (RPV) steels:** These are steels with several alloying elements, including Cu, Mn, Ni, C, P, Si, Mo, Al, Cr, and Co [143]. As the integrity of the reactor pressure vessel is essential for the safety of a nuclear reactor, these steels are chosen for their strength and ability to withstand radiation damage. For experimental purposes, these steels are frequently replaced by simpler model alloys, although the more complex steels have been shown to exhibit significantly lower damage accumulation after irradiation [143].

2. **Zirconium alloys:** This is a group of several zirconium-based alloys with alloying elements such as Sn, Fe, Cr, Ni, Nb, and O. These alloys are typically used for the fuel cladding in nuclear reactors due to their neutron transparency and high melting temperature [9]. Nevertheless, due to their proximity to the nuclear fuel, cladding materials must withstand radiation doses of tens to hundreds of dpa in Generation IV nuclear reactors [9].

3. **Oxide dispersion strengthened (ODS) steels:** ODS steels are a new class of material that has been proposed for both cladding and fusion reactor uses [9, 229, 154].

These are steels with nanometer-scale oxide inclusions that act as recombination sites for radiation damage, allowing the material to be used at elevated temperatures and in severe neutron damage environments [229].

4. **Nano-laminate materials:** These materials are composed typically of nanoscale layers of two different immiscible metals, such as Cu-Nb or Cu-W [144, 50, 49, 77, 98]. Like ODS steels, the high volume density of interfaces between metallic layers act as recombination sites for radiation damage, reducing degradation under severe displacement damage conditions.

5. **Nanocrystalline metals:** Instead of creating a high density of interfaces using oxides or inter-metallic interfaces as in the cases of ODS steels and nano-laminates, nanocrystalline metals take advantage of a high density of grain boundaries to act as recombination sites for radiation damage [249, 210, 118].

Under irradiation, a variety of microstructural changes can occur in metals due to radiation damage accumulation. Such changes include the formation of voids and bubbles [40, 19], dislocation loops [198, 82], stacking fault tetrahedra [110, 241], precipitates [78, 177], and the segregation of solutes at grain boundaries [106, 70]. These microstructural changes in turn lead to macrostructural degradation of material properties such as hardening [67, 38], embrittlement [67, 156, 153], and swelling [130, 43, 36]. These processes are described in more detail in Chapter 2.

1.1.4 Multi-scale modeling: link between atomic-level material behavior and macroscopic mechanical properties

Radiation damage formation, defect accumulation, and subsequent mechanical property changes are inherently multi-scale temporal phenomena, ranging from timescales associated with neutron damage events to the lifetime of reactors. In addition, these same processes are also multi-scale spatial phenomena, ranging from atomistic scale defects to nuclear reactor components in size. Therefore, a wide variety of computational tools exist to study radiation damage and radiation effects ranging from atomistic and ab-initio models at the atomic scale [101, 198, 217, 215, 168, 242, 75, 74, 197, 204] to kinetic Monte Carlo models

at the scale of individual defects [197, 222, 240, 22, 200, 101, 102, 74] to continuum-scale models of defect concentrations [161, 162, 105, 124, 207, 124, 64, 245, 142] and hardening [185, 155, 125, 72, 115, 13, 24] to polycrystalline models of material response to radiation damage [158, 7, 53, 21, 171, 172, 244].

To bridge the gaps between the time and length scales of each method, a multi-scale approach for simulating radiation damage and associated material changes is often taken. In this dissertation, a multi-scale modeling approach is achieved by using the results of ab-initio and atomistic models as inputs into higher-scale models which simulate defect accumulation inside various irradiated metals. At the highest scale, macroscopic models then use the defect accumulation results from the intermediate scale models as inputs to investigate the resulting macroscopic material changes such as hardening caused by the presence of radiation-induced defects. Therefore, the overall purpose of this dissertation is to **(1) develop multi-scale models that can bridge the gaps between individual defect-level behaviors, damage accumulation at experimentally relevant timescales and doses, and macroscopic material property changes in irradiated materials; and (2) use these models to study radiation damage accumulation and associated macroscopic material property changes in a variety of metals and radiation conditions.** The scientific questions that these models will address, as well as the innovations necessary to achieve these goals, are listed in the following sections.

1.2 Scientific questions and innovation

Although extensive experimental, theoretical, and modeling work has been performed to study radiation damage and radiation effects in irradiated metals, several gaps remain in the literature with regards to creating an explicit link between the defects produced in irradiation, their accumulation in various temperature and damage conditions, and their ultimate impact on the macroscopic material properties of an irradiated metal. In order to address these gaps, this dissertation will address the following scientific questions:

In metals, the defected microstructure of an irradiated material has been shown to depend strongly on radiation damage conditions. Temperature, total dose, dose rate, and type

of irriadiation (neutrons, helium ions, self-ions, etc) have been shown to have a strong effect on the formation and accumulation of radiation-induced defects [254, 253, 67, 209, 255]. The presence of helium has also been shown to cause an increase in void density and decrease in average void size in irradiated metals [32] and both dislocation loops and voids have been shown to evolve in density and average size after post-irradiation annealing at different temperatures [209]. Figure 6 shows examples of these effects on damage accumulation in neutron- and ion-irradiated iron and steels. Therefore, the first question to be investigated in this dissertation is:

How do radiation conditions such as temperature, dose rate, and damage type influence radiation defect accumulation in irradiated metals? (Q1)

Radiation damage accumulation is also strongly dependent on the pre-irradiated microstructure of metals, including crystallography [39, 38], the presence of grain boundaries [210, 118], impurities and alloying elements [118, 143, 97], bi-material interfaces [144, 50], and other micro-structural features that may interact with radiation damage. Of particular interest in this work are grain boundaries, bi-material interfaces, and free surfaces. These micro-structural features introduce non-homogeneity in the defect populations within an irradiated metal by acting as sinks for radiation defects, leading to effects such as void-denuded zones near grain boundaries and bubble formation on interfaces [255, 49]. Examples of such spatially heterogeneous effects can be seen in Figure 3. To capture the effects of such inhomogeneous phenomena, spatially resolved models are needed that can explicitly model the material microstructure and its impact on radiation damage accumulation. Therefore, the second question to be investigated in this dissertation is:

How does the presence of interfaces, grain boundaries, free surfaces, and other micro-structural elements influence radiation defect accumulation in irradiated metals? (Q2)

The scientific impact of this dissertation is the development of the capability to simulate

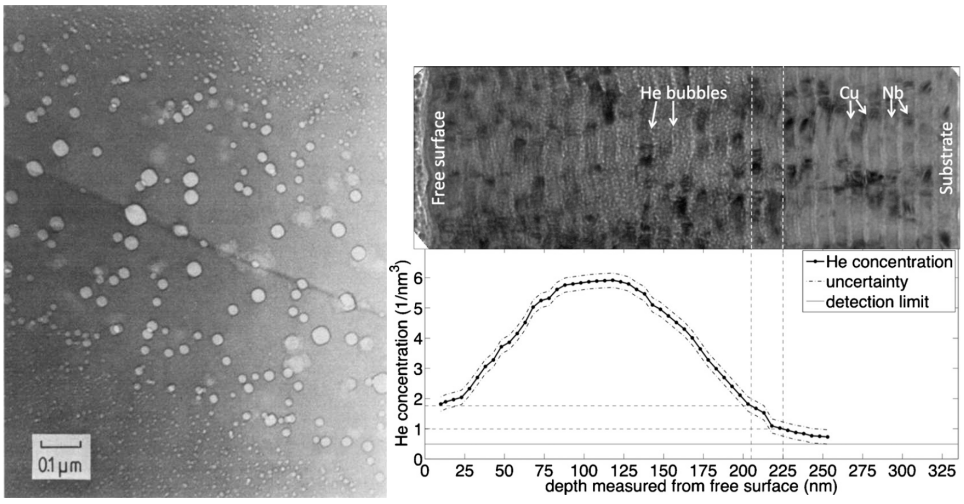

(a) (b)

Figure 3: 3a Helium bubble size and density near a grain boundary in nickel, showing a decrease in number and increase in average void diameter near the boundary (reproduced with permission from [108]). 3b Helium bubble formation in a ion-irradiated Cu-Nb nano-laminate, with most helium bubble formation occurring on bi-material interfaces (reproduced with permission from [49]).

of radiation damage and hardening in realistic radiation conditions and complex, spatially inhomogeneous microstructures. The suite of tools developed in this work are intended to help understand the aging process of current nuclear plants as well as inform the design and optimization of materials for use in future generations of nuclear installations, such as nano-laminates and oxidative dispersion strengthened (ODS) steels [144, 50, 49, 77, 98, 229, 154].

1.3 Scope of the thesis

This dissertation aims to create a multi-scale modeling framework for relating atomic-scale radiation damage to macroscopic changes in material properties in metals under realistic irradiation conditions. Therefore, this dissertation is organized in the following manner:

Chapter 2 describes the mutli-scale processes associated with radiation damage and radiation effects in metals, and discusses the state of the art in modeling techniques used for simulating these processes. Strengths and weaknesses of these various models are presented, and the modeling technique stochastic cluster dynamics is presented as a method with the capability of mitigating some of the weaknesses of traditional models.

Chapter 3 discusses the development of the main model of radiation damage accumulation used in this dissertation, spatially resolved stochastic cluster dynamics (SRSCD). The theoretical development of the method is presented, followed by all of the subsequent computational improvements made to the model to allow for larger-scale and more realistic simulations, including a synchronous parallel kinetic Monte Carlo implementation.

In Chapter 4, SRSCD is applied to several material systems and irradiation conditions. These material systems include thin films, bulk materials, and nano-grained polycrystals. Irradiation conditions simulated include Frenkel pair irradiation, displacement cascade damage, and helium implantation. An emphasis is made on comparing simulated results to experiments as well as predicting defect accumulation outside of the input space that has already been explored experimentally. Physical mechanisms that govern radiation defect accumulation are also explored.

In Chapter 5, the prospects of using SRSCD in the context of multiscale modeling and experimental design are investigated through two examples. First, the coupling between radiation damage and mechanical fields is discussed. This study includes a multi-scale framework, using defect accumulation results from lower-scale simulations as inputs into polycrystalline radiation hardening simulations. Next, SRSCD is used to investigate the temperature shift required in experiments using one source of damage (such as ions) as a proxy for another source (such as neutrons) due to the difference in dose rates between the two sources.

Finally, conclusions of this dissertation are presented in Chapter 6.

CHAPTER II

RADIATION DAMAGE, RADIATION EFFECTS, AND ASSOCIATED MODELING TOOLS

In this chapter, the scientific background for many of the processes and models that are investigated throughout this dissertation are discussed. In Section 2.1, the multi-scale phenomenon of displacement damage, defect accumulation, and radiation effects is presented. Experimental techniques used to investigate these phenomena at each time and length scale are also discussed. In Section 2.2, the computational tools that are used to study radiation damage are also discussed in a multi-scale framework, starting with atomic scale simulation methods and building towards efficient models of damage accumulation such as stochastic cluster dynamics. These models form the basis for the modeling techniques developed in Chapter 3.

2.1 Radiation damage and radiation effects in metals

Radiation damage in metals has been studied for decades in order to understand radiation-induced aging of metals, a central topic in the development of safer nuclear installations and next-generation reactors [34, 41, 40, 73]. In this section, the main sources of radiation damage, the defects caused by this damage, and the macroscopic changes observed due to radiation damage will be discussed.

2.1.1 Primary radiation damage

When a single atom is displaced from its lattice site in a metal, it forms a pair of defects: a vacant lattice site and an atom in an interstitial position between lattice sites. This vacancy and self-interstitial atom (SIA) pair is called a Frenkel pair. In irradiated metals, primary damage is caused when an incident high-energy particle strikes an atom inside a metallic lattice and displaces it from its lattice site, creating a Frenkel pair. The first atom struck by the incident particle is called the primary knock-on atom or PKA. If a PKA is imparted

kinetic energy above a threshold value for displacement E_d (25 eV in FCC copper, 35-45 eV in BCC iron) [109, 151], it will be energetic enough to displace from its lattice site and form a Frenkel pair. However, if the PKA is very energetic, it can also cause collide with other lattice atoms and displace them from their atomic lattice sites. The number of atoms that are displaced due to a single PKA can be estimated using the binary collision approximation (BCA) model of Norgett, Robinson, and Torrens (NRT) [152]. In the NRT model, the number of displaced atoms N_d is given as a function of the PKA energy available for damage production T_d:

$$N_d(T_d) = \begin{cases} 0 & T_d < E_d \\ 1 & E_d < T_d < \frac{2E_d}{0.8} \\ \frac{0.8T_d}{2E_d} & \frac{2E_d}{0.8} < T_d < \infty \end{cases}$$

where the value of T_d is given by the energy deposited in the PKA by the incident particle minus the energy lost to electronic stopping power.

When the PKA energy is very high and a large number of atoms are displaced from their lattice site, a displacement cascade is formed. In this case, a small region of the crystal lattice is displaced at once, creating a short-lived thermal spike that locally melts a small region of the material. The size of this locally melted region is on the order of 1000 nm^3 for displacement cascades with PKA energy of 20 keV in typical metals [204]. Examples of thermal spike phases of displacement cascades with PKA energies of 10 keV and 50 keV in iron are shown in Figure 4a. After a few picoseconds, most of the atoms region affected by the thermal spike phase collapse back into their lattice positions, but a few stable defects, including vacancies, SIAs, and clusters of these defects, are left behind. Atomistic simulations of cascade damage have indicated that for large cascades, the numbers of surviving displaced atoms after the thermal spike phase of the cascade fall below the NRT estimate due to in-cascade recombination of vacancies and interstitials [204, 206]. The structure of these cascades vary from material to material and depending on the PKA energy, but in general cascade formation is very important to radiation damage accumulation because stable clusters of vacancies or self-interstitial atoms can form during the cascade event itself [206, 165, 46, 235, 10, 203]. An example of the dependence of the size of interstitial clusters

formed in cascades on the PKA energy of the cascade is shown in Figure 4b.

Several different types of incident particles can cause primary radiation damage. Examples of such particles include gamma rays, electrons, neutrons, light ions, and heavy ions [109, 239]. Depending on the incident particle type and energy, either Frenkel pairs or displacement cascades can be formed. Gamma rays, electrons, and light ions primarily form Frenkel pairs while neutrons and heavy ions frequently form displacement cascades. The dose rate in dpa·s^{-1} due to these incident particles depends on the energy and fluence of these particles, and can vary from $10^{-12} - 10^{-6}$ dpa·s^{-1} [139, 234] for neutron damage to 10^{-2} dpa·s^{-1} [170, 2] during heavy ion irradiation.

In addition to displacement damage, gases such as hydrogen and helium can also occur in the metallic lattice either through direct implantation or transmutation from neutron irradiation [234]. These can either take interstitial sites in the crystal lattice, or they frequently interact with displacement damage, for example by taking substitutional sites in vacancies created by atomic displacements [75, 145]. As will be discussed in later sections, the presence of these gases can strongly influence the subsequent evolution of radiation damage in metals.

2.1.2 Defect types and behaviors

As discussed in Section 2.1.1, defects generated by radiation damage include vacancies, SIAs, gas atoms, and clusters of these defects. As these defects accumulate and interact within a metal, they can agglomerate into larger defect clusters [40, 254, 110, 253, 67, 259]. Depending on the constituents of a given cluster and the type of metal lattice, clusters can take a variety of geometric forms. In addition, defects of various types including clusters can have varying diffusivities. In this section, the most common radiation-induced defects and clusters are described, along with their structure and most common behaviors. The following is a list of the most common defects and defect clusters found in simulations and experimental observations of irradiated materials:

1. **Vacancies** are empty sites in the atomic lattice. They diffuse by exchanging position with nearest-neighbor lattice atoms [74] and are frequently mobile in metals at room

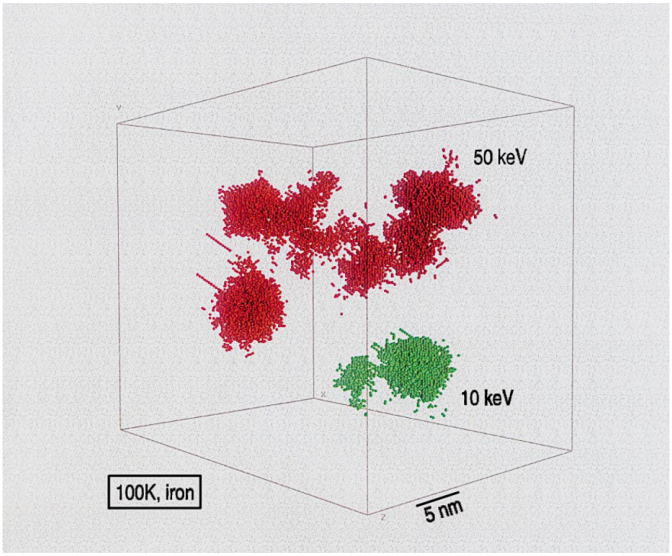

(a)

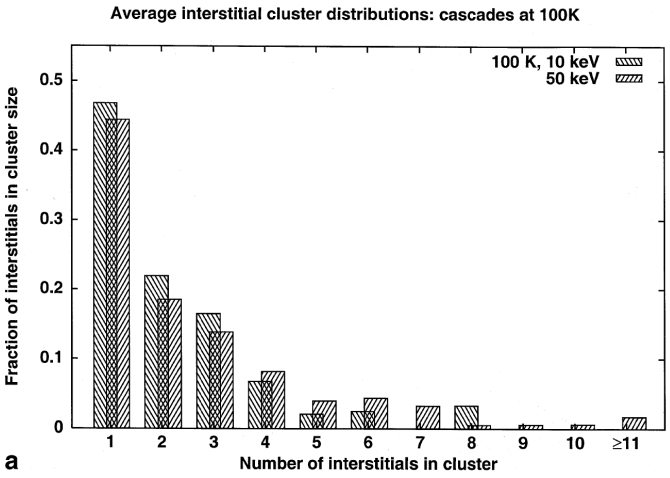

(b)

Figure 4: 4a Example of cascades formed by PKAs of 10 keV and 50 keV in α-Fe. 4b Interstitial defect cluster distributions produced in 10 keV and 50 keV cascades. Depending on the PKA energy, the number and size of defect clusters formed in-cascade can vary significantly (reproduced with permission from from Stoller et al. [206]).

temperature.

2. **Self-interstitial atoms (SIAs)** are atoms taking interstitial sites in between lattice sites. They frequently share a lattice site with lattice atoms in a dumbbell orientation [243]. SIAs diffuse by moving between dumbbell positions on nearest-neighbor atoms, and are highly mobile at room temperature [74].

3. **Interstitial gas atoms** such as He or H also take interstitial dumbbell positions, similarly to SIAs. The energy barrier to diffusion between atomic sites for these atoms is frequently very low (< 0.1 eV) [216] and they typically diffuse very quickly until they reach a trapping site such as a vacancy or a grain boundary.

4. **Small vacancy clusters** take a variety of geometric forms such as tetrahedral or planar [64], depending on the material type and the size of the cluster. These defects can also be highly mobile in metals, with diffusion mechanisms governed by exchange of lattice atoms with vacancies [74, 75].

5. **Small SIA clusters** (2-4 SIAs) can take crowdion or planar form. They are typically quite mobile, and are characterized by one-dimensional diffusion followed by periodic changes in diffusion direction [197, 198].

6. **Small gas-vacancy clusters** such as HeV are formed when interstitial helium or hydrogen interact with vacancies and vacancy clusters. In this case, they take a substitutional position inside the vacancy cluster. These clusters can be highly mobile or quite immobile, depending on the number of helium and vacancies in the cluster and the metal type [216].

7. **Voids** are large spherical cluster of vacancies [40]. These can grow to sizes on the order of nanometers and can be detected using experimental techniques such as TEM, as shown in Figure 5a. Voids are typically only mobile in high-temperature materials [43].

8. **Dislocation loops** are circular arrangements of either vacancies or SIAs [198, 82]. In the case of interstitial dislocation loops, circular clusters of atoms are inserted in

between two atomic planes in a given slip system. By contrast, vacancy loops are sections of an atomic plane that are missing from a slip system. The preferred orientation of these loops varies depending on the material type and irradiation conditions. Dislocation loops can be extremely mobile, and frequently diffuse in one dimension in the direction of their Burgers vector, perpendicular to their atomic plane [198]. An example of dislocation loops in irradiated iron is shown in Figure 5c.

9. **Bubbles** are similar to voids in that they are spherical and contain vacancies, but bubbles also contain some gas atoms such as helium or hydrogen. An example of helium bubbles in copper is shown in Figure 5b. Bubbles are typically more stable than voids, as the presence of gas atoms increases the binding energy of vacancies to the bubble [145]. Similarly to voids, bubbles are typically considered to be immobile except under high temperatures [19].

10. **Stacking fault tetrahedra (SFTs)** are an alternative arrangement of vacancies that is found only in FCC metals. These defects are tetrahedral rearrangements of the lattice atoms such that free volume is concentrated on the edges of the SFT [110, 241]. Figure 5d shows stacking fault tetrahedra in gold formed by annealing rather than radiation damage.

As these defects diffuse throughout a metal, they can annihilate (when a vacancy and SIA recombine to re-form an undamaged lattice site), become trapped at impurities, or get absorbed by sinks such as linear dislocations, grain boundaries, or free surfaces [101, 215, 95, 80, 225, 162]. Large groups of dislocation loops can also form larger structures such as dislocation loop rafts or dislocation loops decorating linear dislocations present in the metal before irradiation [240]. The complex behaviors and interactions between defects and defect clusters depend on many factors, including metal type, damage type, and irradiation conditions. Since the final mechanical property changes experienced by irradiated metals are dependent on the quantity and type of defects formed during irradiation, understanding the link between the metal microstructure, defect types, and radiation conditions is critical in modeling macroscopic material changes in irradiated metals.

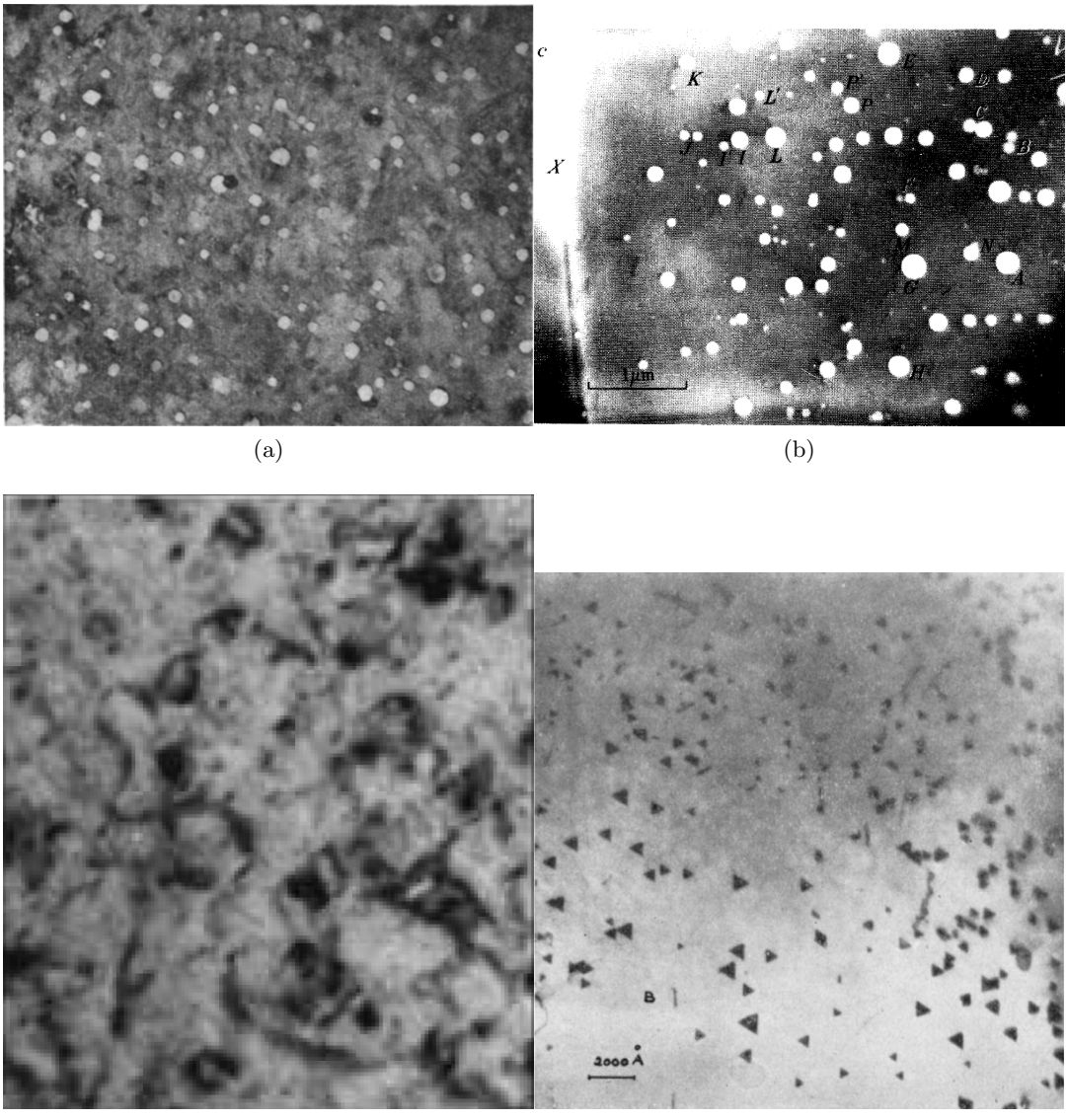

(a) (b)

(c) (d)

Figure 5: Example TEM images of common radiation-induced defects in metals: 5a voids (reproduced with permission from [40], $\times 60,000$ magnification), 5b helium bubbles (reproduced with permission from from [19]), 5c dislocation loops (reproduced with permission from from [209], 200 nm image width), and 5d stacking fault tetrahedra (reproduced with permission from from [241])

2.1.3 Influence of irradiation conditions on damage accumulation

Radiation damage accumulation is the process of small, individual defects such as vacancies and SIAs produced in primary damage diffusing and accumulating into large, stable defects. The type, size, and quantity of defects that accumulate during irradiation of a metal are strongly dependent on the the irradiation conditions including temperature, dose rate, and the presence of displacement cascades, and the presence of gases such as helium [209, 170, 79, 22, 32, 31]. Figure 6 shows several examples of the dependence of the irradiated microstructure on the irradiation conditions. The following general trends for dependence on irradiation conditions can be observed in irradiated metals:

1. As the **total dose** (in dpa) increases in an irradiated metal, the concentration of radiation defects present in a material typically increases until a saturation limit is reached, after which point the number of defects remains the same while the average defect size typically grows [253]. This leads to a larger concentration and larger average size of defects as the dose increases, as shown in Figure 6a. Defect concentrations typically saturate between 10^{23} and 10^{25} m^{-3} [67], while cluster sizes can range from < 1 nm to > 100 nm [40, 19, 67, 32, 209].

2. **Dose rate** (in dpa$\cdot s^{-1}$) can also influence damage formation if defects are added faster than the rate at which defects interact with each other. This can lead to effects such as increased swelling temperatures and larger cluster sizes in materials implanted at higher dose rates [170].

3. **Increasing temperature** is typically linked to a decrease in defect concentration and a corresponding increase in average defect size, as smaller defects are unstable at higher temperatures, leaving large, stable defects behind [253, 209]. This effect can be seen in Figures 6b and 6d.

4. **The presence of gases** such as helium can have the opposite effect as temperature because helium-vacancy clusters are more stable than vacancy clusters of the same size [32, 31, 4], allowing small stable bubbles to form when the content of helium is

high. This effect is seen in Figure 6c.

5. **Damage type** (Frenkel pair or cascade) is also an important factor for radiation defect accumulation, as defect clusters that are formed in cascades are frequently more stable than point defects. The spatial arrangement of defects in a cascade causes correlated between defects, increasing cluster sizes and densities relative to Frenkel pair implantation, which is more evenly distributed throughout the material [22, 202].

The complex interplay between all of these factors makes predicting the precise defect content in an irradiated material difficult, and emphasizes the need for modeling tools which can predictively simulate defect accumulation under a variety of implantation conditions.

2.1.4 Influence of pre-irradiated microstructure on damage accumulation

The microstructure of an irradiated material is also a primary factor in the accumulation of radiation damage. Several factors influenced by material microstructure strongly influence radiation defect behaviors, such as defect migration and binding energies, the presence of sinks and traps for defects, and internal stresses. These factors are all dependent on the material microstructure. Some of the microstructural variations that influence defect accumulation are:

1. **Metal choice and alloying composition:** Depending on the metal or alloy being irradiated, different defect types may be more energetically favorable, leading to the formation of such different structures as vacancy loops, voids, or stacking fault tetrahedra [82, 68]. Changes in the composition of alloying elements can alter defect migration energies, as in the case of helium clusters Fe and Fe-Cr alloys [216], which in turn alters long-term defect accumulation. The presence of alloying elements can also lead to precipitation of solute phases during irradiation [143]. In general, formation, diffusion, and accumulation of defects in a given metal or alloy are material-dependent processes.

2. **Initial dislocation content from work hardening:** Work-hardened metals have a higher dislocation content within the grain interior than pristine metals, leading to

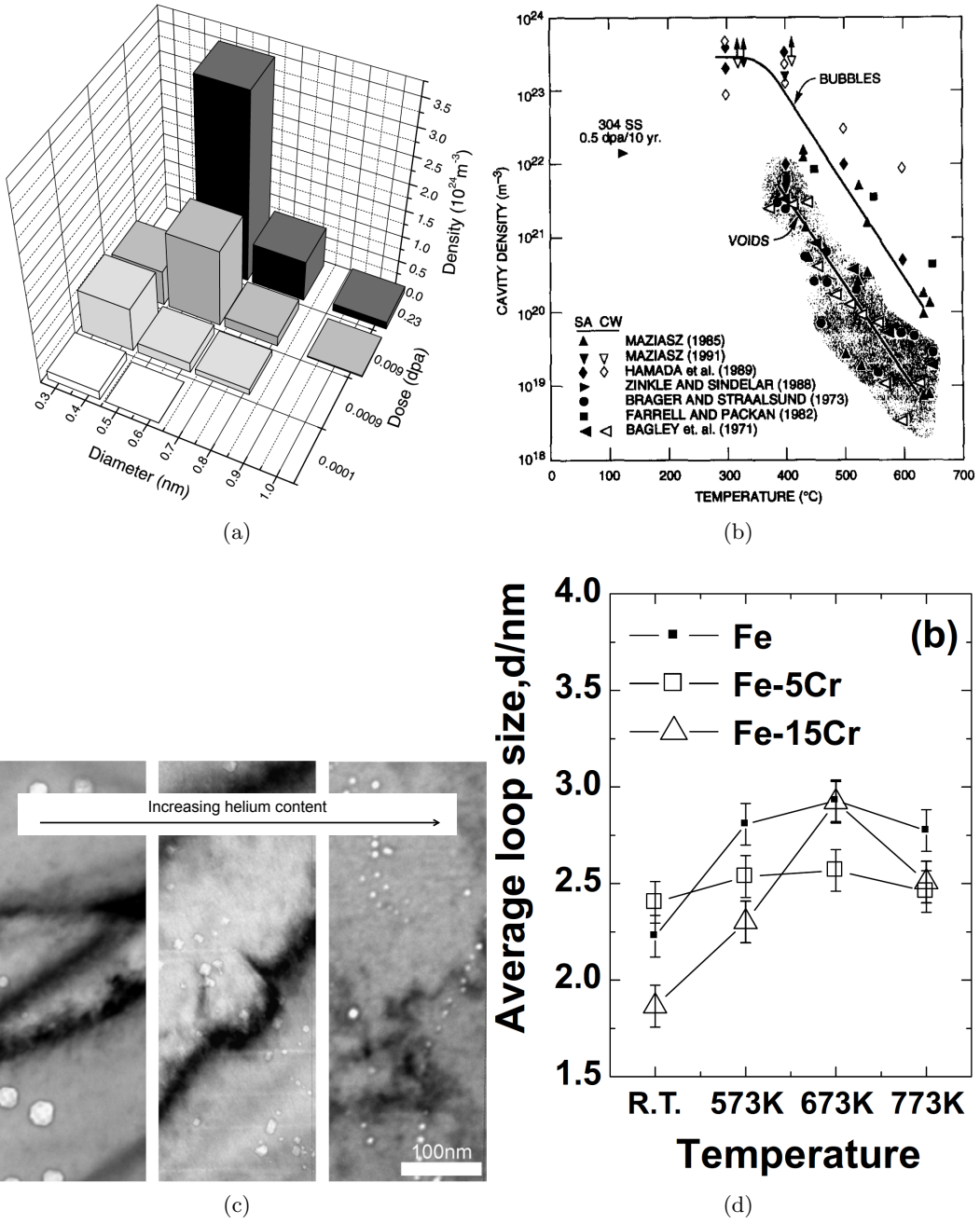

(a) (b) (c) (d)

Figure 6: 6a Dependence of cavity size distribution on total dose in neutron-irradiated α-Fe (reproduced with permission from [67]). 6b Temperature dependence of cavity density in neutron-irradiated austenitic stainless steels (reproduced with permission from [253]). 6c TEM image showing dependence of cavity size and density on helium content in ion-irradiated iron (reproduced with permission from [32]). 6d Dependence of average dislocation loop size on post-irradiation annealing temperature in He^+-irradiated iron and Fe-Cr alloys (reproduced with permission from [209]).

changes in damage evolution. Dislocations can act as sinks and fast-diffusion pathways for radiation defects [96, 94, 95], and have been shown to alter the long-term damage accumulation in irradiated metals by influencing helium desorption [208], decreasing hardening [5], and acting as pinning sites for dislocation loops [222, 223].

3. **Grain size:** Metals with nanocrystalline microstructures frequently exhibit greater radiation tolerance than coarse-grained metals [210, 118]. This property is due to the fact that grain boundaries can act as sinks for defects, enhancing recombination and decreasing defect accumulation in their proximity [90, 227].

4. **Presence of precipitates:** Some metals such as oxide dispersion strengthened (ODS) steels have been created with a high concentration of nanoscale precipitates [257, 229], which act as recombination sites in much the same way as grain boundaries mentioned above. These materials also show increased resistance to radiation damage accumulation.

5. **Presence of inter-metallic interfaces:** Nano-laminate materials are created by creating nanoscale layers of immiscible metals, such as Cu and Nb. The inter-metallic interfaces between layers act both as recombination sites for point defects and storage sites for helium [144, 50], allowing increased radiation tolerance with decreasing layer thickness.

The final three examples listed above include materials in which the ability of interfaces to act as recombination sites for point defects is utilized in order to decrease radiation damage accumulation. These materials are all referred to as nano-structured materials. Figure 7 shows examples of nano-structured materials with defect accumulation that is strongly dependent on the material's microstructure. In Figure 7a, helium-implanted 5 nm Cu-Nb laminate materials are shown to limit the size of helium bubbles that form. In Figure 7b, increased helium bubble formation on grain boundaries and decreased bubble size is seen in helium-irradiated nanocrystalline iron. As materials are designed for use with microstructures tailored for a specific response to radiation damage, modeling tools will

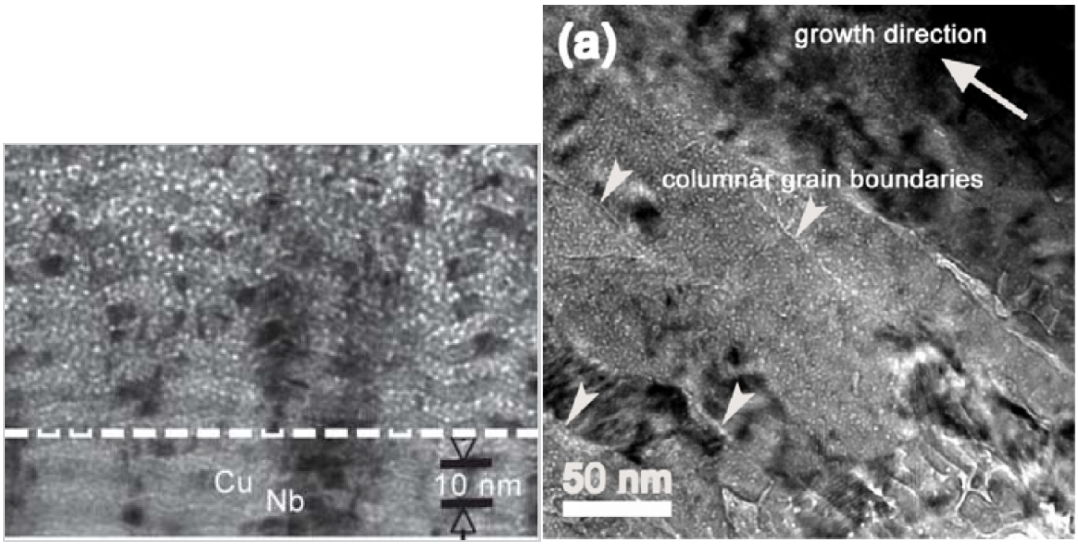

(a) (b)

Figure 7: Radiation damage in nanostructured materials: 7a Helium bubbles in 5 nm Cu-Nb multilayered material with average size of 1-2 nm (reproduced with permission from [144]). 7b Helium bubbles nanocrystalline Fe, showing increased bubble growth on grain boundaries (reproduced with permission from [249]).

need to take these microstructures into account and predict their performance in realistic reactor conditions.

2.1.5 Radiation effects: hardening, swelling, and embrittlement

The presence of large amounts of radiation damage in irradiated materials can cause macroscopic changes in material properties, called radiation effects. Radiation effects differ from radiation damage in that they can be measured macroscopically and occur over timescales ranging from seconds to years, depending on the material and irradiation conditions. Figure 8 shows several examples of radiation effects. Common radiation effects in irradiated metals include hardening, embrittlement, and swelling, as described below.

Hardening in irradiated metals is characterized by an increase in the initial yield point during elasto-plastic deformation of an irradiated metal [67, 38]. This effect is caused by radiation defects acting as obstacles to dislocation motion, as will be discussed in Section 5.1. Increases in initial tensile yield strength of several hundred MPa can be observed in irradiated metals, depending on the material and irradiation conditions [38]. The links

between the concentration and size of radiation defects and the amount of hardening have been studied using modeling at several scales including atomistic [11, 14, 169, 164] and dislocation dynamics [196, 89] models, which operate on length scales on the order of tens to hundreds of nm. By contrast, continuum models of radiation hardening [185, 155, 125, 72, 115, 13, 24] operate on the continuum scale and are discussed further in Section 5.1.

Embrittlement and loss of ductility also typically accompanies hardening in irradiated metals. This is caused by the buildup of stress at defects such as voids that act as pinning points for dislocations, leading to crack formation. Embrittlement is manifested as an upward shift in the ductile-brittle transition temperature and is strongly correlated to the change in yield stress due to hardening [153]. Stress-strain curves of neutron-irradiated iron also show decreased ductility before ultimate failure of tensile specimens with increasing dose [67]. Embrittlement is a major concern for nuclear safety as structural materials such as pressure vessels may become brittle over their lifetimes [156, 153].

Swelling can also occur in irradiated metals If an excess of vacancies and vacancy clusters such as voids or bubbles accumulates, adding volume to a metallic lattice [130, 43, 36]. Alloys not designed to be radiation resistant can experience swelling of several tens of percents under high irradiation [130]. This effect is seen typically at doses greater than 1 dpa and is therefore a concern for reactors designed to withstand large doses, such as fusion reactors. The presence of helium also strongly influences swelling, as helium acts as stable nuclei for cavities which then increase the volume of the material [130, 40]. An example of swelling in an irradiated stainless steel sample is shown in Figure 8c.

Other radiation effects are also observed in irradiated metals such as radiation-induced creep, decrease in fracture toughness, and irradiation induced stress corrosion cracking. These are long-term concerns for irradiated metals as cavities that form on grain boundaries can grow under stress [154]. Overall, the presence of radiation damage in metals is associated with radiation effects that degrade the mechanical properties and safety of nuclear materials. Therefore, design of new materials for extreme reactor environments such as fusion is focused on creating materials that can enhance the recombination of defects as well as limit the size of any defects that do form.

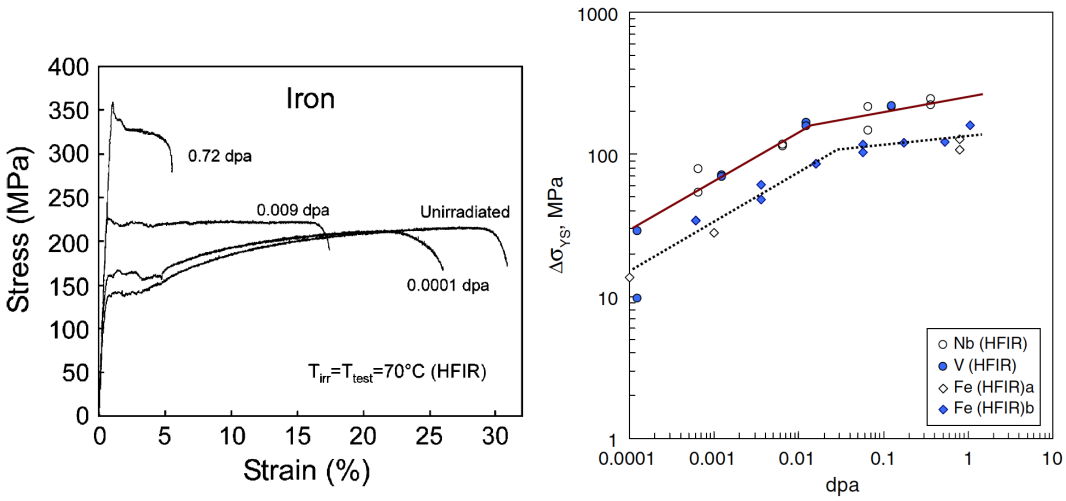

(a) (b)

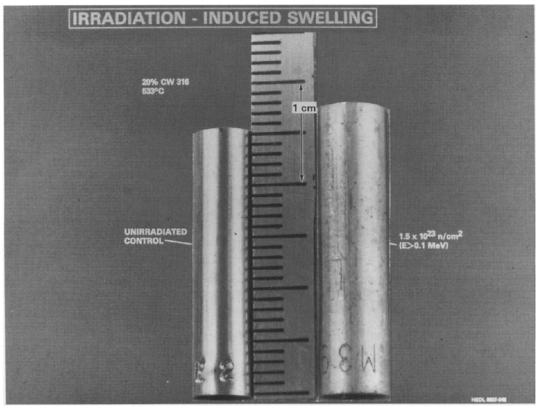

(c)

Figure 8: 8a Stress-strain curves of neutron-irradiated pure Fe at various doses, showing hardening and decrease in ductility with increasing dose (reproduced with permission from [67]). 8b Change in 0.2% yield strength of neutron-irradiated pure metals as a function of radiation dose (reproduced with permission from [38]). 8c Example of irradiation-induced swelling in fast neutron-irradiated 316 stainless steel (reproduced with permission from [130]).

2.2 Models of radiation defects and damage accumulation

Understanding the links between material, radiation conditions, radiation damage accumulation, and changes in material properties such as hardening and embrittlement is necessary for the development of new materials for use in the next generations of nuclear reactors. Modeling tools must connect information at several scales scales ranging from atomistic to macroscopic in order to investigate how material and radiation conditions are linked to mesoscopic damage accumulation and macroscopic changes in material properties. In this section, the main models used to study radiation damage are presented and the scales at which they operate are discussed.

2.2.1 Ab-initio and atomistic models

Description: At the smallest scale, radiation damage and radiation defects are studied using ab-initio and atomistic models. These models resolve every atom in a given volume of crystal lattice. In ab-initio techniques such as density functional theory [176], the energies of various lattice configurations are computed using quantum mechanical descriptions of the atoms in the lattice. Atomistic models, by contrast, use empirical functions to describe the potential of the atoms being modeled [45]. Atomistic models can be used both for molecular statics simulations, in which the system is minimized in energy at zero Kelvin and energies of various lattice configurations are compared, and molecular dynamics simulations in which defects can diffuse and interact throughout the lattice [197, 198].

Application: defect structures, behaviors, and energies: Atomic-scale techniques are most often used to study the energetics and kinetics of individual defect behaviors, as well as the formation of radiation damage. Such models have been used to investigate point defect properties such as the lattice position that an SIA takes in iron [149] and the mechanism by which vacancies exchange lattice sites [74]. Atomistic simulations can also be used to investigate the lowest energy configuration of defect clusters in a given crystal lattice, helping to determine whether vacancy clusters form spherical voids or dislocation loops in different crystal lattices [82]. The structure and defects that are created during displacement

cascades of various PKA energies has also been investigated using such methods [206, 165, 46, 235, 10, 203], as shown in Figure 4a.

Ab-initio and atomistic modeling also provides crucial inputs into higher-scale models discussed in later sections. The main inputs into higher-scale models for defect accumulation are the allowed defects in a given material system, their diffusivity (the diffusion prefactor D_0 and activation energy E_m for migration between lattice positions as well as the dimensionality of their diffusion), and the binding energy E_b of various defects to each other. These parameters are different for each material type and have a significant impact on the overall accumulation of damage in the material. Diffusion parameters can be quantified using molecular dynamics methods, for example by allowing fast-diffusing defects to move through a crystal lattice at different temperatures and fitting the resulting diffusivity to an Arrhenius law, given by [6]:

$$D = D_0 e^{-\frac{E_m}{k_b T}} \tag{1}$$

An example of such a fit for several sizes of SIA clusters, adapted from Soneda et al. [198], is shown in Figure 9a. Ab-initio and atomistic models can also quantify the energy barrier E_m for defects to exchange lattice sites by finding the lowest energy paths for defects to move between lattice sites [74]. An example of ab-initio study of the energy barrier for diffusion of small interstitial clusters in α-Fe is shown in Figure 9b. Using the approaches described above, the migration energy E_m and diffusion prefactor D_0 for diffusion have been investigated for a wide variety of radiation defect types in several metallic systems. Examples of mobile defects for which migration parameters have been computed using these methods are vacancies and vacancy clusters, SIAs and small SIA clusters, dislocation loops, and helium-vacancy clusters [74, 198, 216, 140, 75].

The binding energy $E_b(ij)$ of a defect i to an object j is the difference in the formation energy of the bound defect-object cluster $E_f(ij)$ and the formation energy of the defect and the object, separately $E_f(i) + E_f(j)$:

$$E_b(ij) = E_f(i) + E_f(j) - E_f(ij) \tag{2}$$

Atomic-scale models can estimate these binding energies by comparing the energy of a

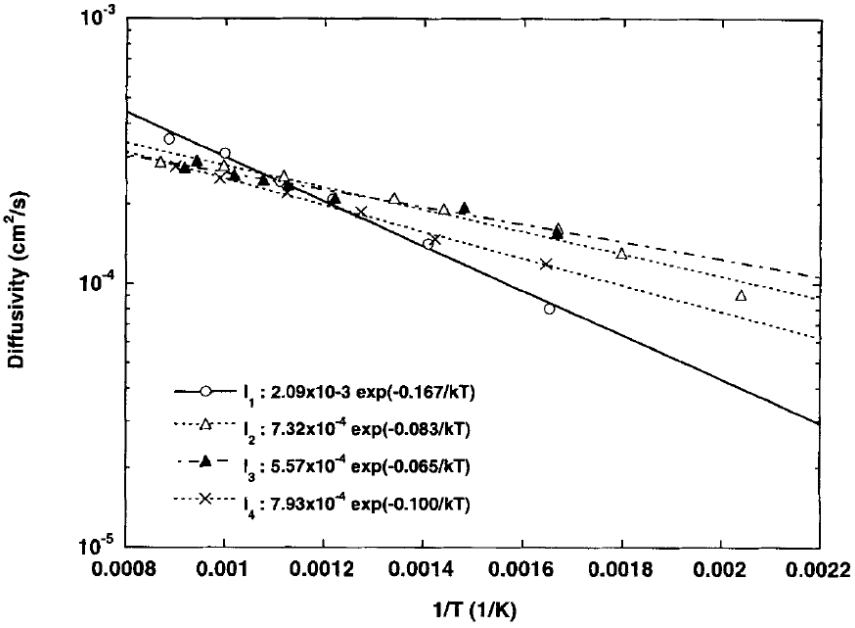

(a)

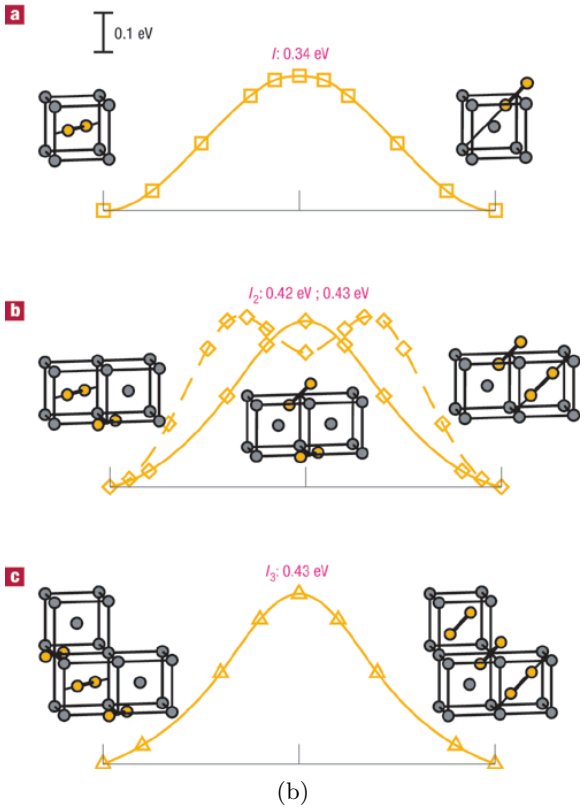

(b)

Figure 9: 9a Arrhenius plot of diffusivities of several small defects in α-Fe, used to find diffusion prefactor D_0 and migration energy E_m (reproduced with permission from [198]). 9b plots of the lowest energy paths and atomic configurations for diffusion of small interstitial clusters in α-Fe from ab-initio simulations (reproduced with permission from [74]).

simulated system with the bound and unbound defects inside. Binding energies of defects to other defects as well as defects to structures such as grain boundaries, bi-material interfaces, and linear dislocations have been quantified using these methods [96, 140, 95, 225].

Atomic-scale computational techniques have several advantages and drawbacks. Atomic-scale models operate with fewer simplifying assumptions then mesoscale and continuum models, allowing direct simulation and observation of defect behaviors and energies. However, the timescale associated with most atomistic simulations is on the order of picoseconds and length scales are typically on the order of tens of nanometers [206, 198]. Some accelerated atomistic techniques such as temperature accelerated dynamics (TAD) [195] and parallel replica dynamics (PRD) [236] exist to simulate larger timescales, but are limited in the physical size of the system and the number of defects that can be simulated. Therefore, atomistic and ab-initio models are not ideal tools for simulating long-term defect accumulation in irradiated materials. In addition, the various energies and defect structures predicted can be strongly dependent on the empirical potential used in atomistic simulations [128, 86, 87]. Overall, atomistic models provide information on defect structure, behaviors, and energetics but cannot capture collective defect behaviors over long timescales. Instead, these data can be input into higher order models such as those discussed in Sections 2.2.2 and 2.2.3. Therefore atomistic and ab-initio modeling is a critical first step in developing multi-scale models that can predict macroscopic material changes due to the presence of radiation damage.

2.2.2 Rate theory and cluster dynamics models

In order to reach time and length scales representative of irradiation in experimental and reactor environments, defect accumulation must be simulated using higher-scale models that do not account for the full complexity of atomic scale models but which can simulate longer timescales and larger doses. One such category of methods is rate theory (RT) models, often referred to as cluster dynamics (CD) models when used to simulate radiation damage evolution.

Description: In a CD model, the population of defects of a given type (for example, vacancies) is treated using a concentration equation $c(t)$. This equation can be in units of m^{-3} or atomic fraction. The evolution of $c(t)$ is given by a rate equation, in the form:

$$\frac{dc}{dt} = \sum_{\mu=1}^{N} \pm r_\mu \tag{3}$$

where r_μ is the rate of reaction μ to occur in the system, and the $\pm$ symbol indicates whether that reaction creates or destroys defects of this type. For example, in the case of a system limited to two species (single vacancies and single interstitials) and two reactions (Frenkel pair creation and vacancy-interstitial annihilation), the rate equations for the population evolution of both vacancies $c_v(t)$ and interstitials $c_i(t)$ are given by:

$$\begin{aligned} \frac{dc_v}{dt} &= K - D_v k_i^2 c_v \\ \frac{dc_i}{dt} &= K - D_i k_v^2 c_i \end{aligned} \tag{4}$$

where K is the Frenkel pair creation rate, D_v and D_i are the diffusivities of vacancies and interstitials, respectively, and k_v^2 and k_i^2 are the sink strengths of vacancies for interstitials and interstitials for vacancies, respectively. This sink strength term k^2 governs the rate at which the two defect types will interact, and is a function of the defect concentrations and diffusivities. The functional form of this sink strength is critical in order to correctly simulate defect evolution, and its form depends on the geometry of each defect type as well as the diffusion type (one, two or three-dimensional diffusion). Sink strengths for point defects interacting with stationary spherical sinks k_s^2 have been developed by Brailsford and Bullough [29, 30], and are given by:

$$k_s^2 = 4\pi c_s r_s \tag{5}$$

where c_s is the concentration of sinks and r_s is the capture radius of the sink. A derivation of equation (5) is given in Section 3.2.2.1. This form has been subsequently expanded to the case of two mobile species with spherical reaction radii, such as the vacancy-interstitial model presented above. Other sink strengths have also been developed for defect-defect interactions including circular dislocation loops that are either glissile in one dimension or

immobile [207, 181, 224] and defects that undergo 1D diffusion with occasional changes in direction [220], as well as defect-dislocation interactions [207].

CD models typically simulate more complicated defect evolution than the model presented in equation (4). These models frequently simulate the populations of vacancy and SIA clusters size n, $c_{vn}(t)$ and $c_{in}(t)$, as well as helium-vacancy clusters [161, 162, 105, 124, 207]. For each allowed reaction between two defect types, a term must be inserted into the rate equations for those defect types as well as the resulting defect type that is created by carrying out that reaction. An example of the rate equation for the evolution of the concentration c_{vn} of vacancy clusters size n in a system in which Frenkel pairs are introduced at a constant rate and vacancy and SIA clusters are allowed to form but only single vacancies and interstitials are mobile is shown below, as adapted from Stoller et al. [207]:

$$\begin{aligned}\frac{dc_{vn}}{dt} &= \omega(n-1)^{1/3} D_v c_{v1} c_{v(n-1)} - \omega n^{1/3}\left(D_i c_{i1} + D_v e^{-\frac{E_b^v(n)}{k_b T}}\right) c_{vn} \\ &\quad - \omega n^{1/3} D_v c_{v1} c_{vn} + \omega(n+1)^{1/3}\left(D_i c_{i1} + D_v e^{-\frac{E_b^v(n+1)}{k_b T}}\right) c_{v(n+1)} \end{aligned} \tag{6}$$

where $\omega = \left(\frac{48\pi^2}{\Omega^2}\right)^{1/3}$ is a geometric constant derived from the sink strength in equation (5), Ω is the atomic volume of a lattice site, D_v and D_i are the diffusivities of single vacancies and single interstitials, c_{v1} and c_{i1} are the concentrations of single vacancies and single interstitials, $E_b^v(n)$ is the binding energy of a vacancy to a vacancy cluster size n, and $k_b T$ is the Boltzmann constant multiplied by the absolute temperature. In equation (6), the first term represents formation of vacancy clusters size n when a single vacancy is absorbed by a cluster size $n-1$, the second term represents shrinkage of vacancy clusters size n to size $n-1$ through annihilation with a single self-interstitial or emission of a single vacancy, the third term represents growth of vacancy clusters size n to size $n+1$ by absorbing a single vacancy, and the fourth term represents shrinkage of vacancy clusters size $n+1$ to size n through annihilation with a single interstitial or emission of a single vacancy. In the work of Stoller et al. [207], a rate equation in this form exists for each vacancy cluster and self-interstitial cluster size n. In addition, the rate equations for the evolution of single vacancies and single interstitials $c_{v1}(t)$ and $c_{i1}(t)$ are considerably more complicated because these defects are mobile, necessitating a term in their rate equations for each possible reaction between single

vacancies or interstitials and every other defect type in the system.

Applications of CD models: Several advancements to cluster dynamics modeling have been made in order to simulate defect evolution in more complicated systems than the example given above. Although CD methods like those presented in equation (6) assume a homogeneous distribution of defects in space, spatial resolution has been added to CD models by solving a simultaneous set of rate equations at a set of material points and allowing diffusion between material points using a finite difference or finite element approximation [124, 64, 245]. This allows simulations of defect evolution in thin films or systems with nonuniform defect creation rates. In addition, cascade damage has been included in CD models by simulating early-stage annealing of displacement cascades using a kinetic Monte Carlo-based method (discussed in Section 2.2.3) and using the surviving defects as a source term in CD [161, 105, 142]. More defect species such as helium have been added to CD models, and more diffusive species such as 2-interstitial clusters and interstitial helium have been included as well [162, 163, 105]. Together, these advancements have enabled CD models to reproduce several experimental studies of radiation damage evolution. Examples include cluster dynamics simulations of defect accumulation in neutron-irradiated iron [161, 105, 142], as shown in Figure 10a in which cluster dynamics simulations are compared to experimental measures of vacancy cluster and interstitial loop concentrations as a function of radiation dose in neutron-irradiated iron [142]. Cluster dynamics models have also simulated helium desorption from pre-implanted and annealed iron [162, 163], as shown in Figure 10b. In this study, experimentally measured helium desorption is plotted as a function of annealing time for three different irradiated and annealed iron thin foils, each with different foil thickness, initial helium content, and annealing temperature. Cluster dynamics simulations show good agreement with experimental measures after adjusting defect migration energies to account for the presence of carbon impuritues [162].

This method has several advantages and drawbacks. The main advantage to CD models is the fact that large radiation doses and timescales can be simulated, up to more than 1 dpa [142]. In addition, due to the time-explicit nature of CD models, parallelization

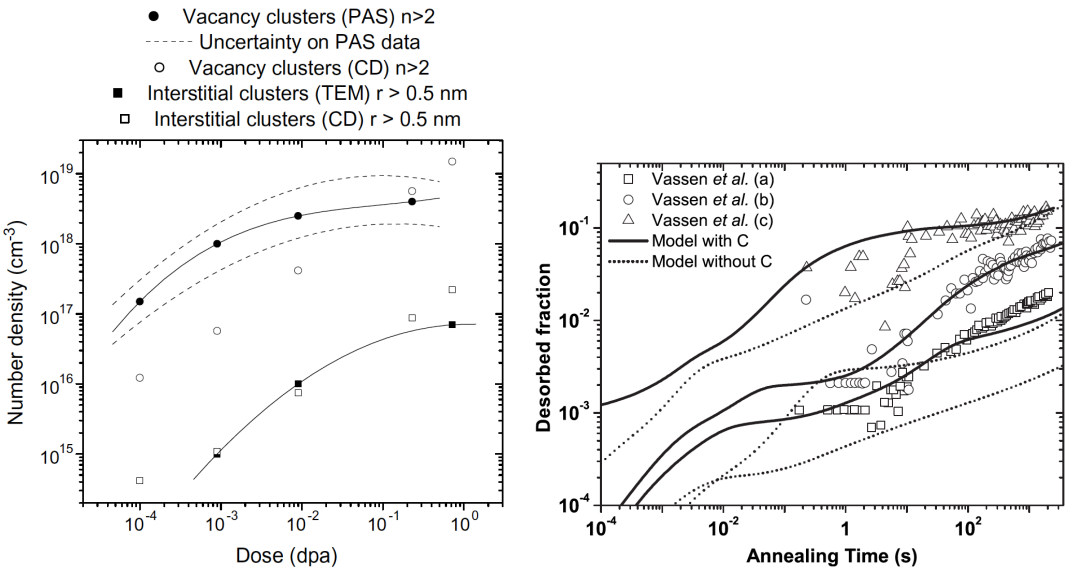

(a) (b)

Figure 10: Comparisons between cluster dynamics models and experimental measurements showing the ability to simulate large radiation doses and long timescales: 10a defect accumulation in neutron irradiated iron (reproduced with permission from Meslin et al. [142]), and 10b helium desorption from implanted and annealed iron thin films (reproduced with permission from Ortz et al. [163])

of these schemes is straightforward. However, the form of the rate equations limits the complexity of the material model that can be applied. For example, in the model of Stoller et al. presented in equation (6), only single vacancies and interstitials are treated as mobile. Atomistic studies have indicated that several sizes of vacancy and interstitial clusters are mobile [75, 74, 198, 197], and in the case of systems with significant concentrations of helium several sizes of interstitial helium and helium-vacancy clusters are mobile as well [216, 64]. The implementation of all of these mobile species in a CD model is a practical impossibility due to the sheer number of reactions that can occur between all of the allowed defects in the system. In addition, the diffusivities of defect types can vary by several orders of magnitude depending on the temperature and migration energy. This can lead to a very stiff problem, or a problem in which the reaction rates of various reactions differ by many orders of magnitude, leading to truncation errors and requiring extremely small timesteps. This problem is especially important in the case of spatially resolved CD methods using finite difference or finite element approximations, as the rate of diffusion between volume

elements may be very dissimilar to the reaction rates between the coupled rate equations at each material point. Overall, CD methods provide computational efficiency at the cost of the complexity of the simulated defect model.

2.2.3 Kinetic Monte Carlo models

In contrast to the coupled concentration rate equations of CD, kinetic Monte Carlo (kMC) methods take a very different approach to simulating radiation defect evolution. In this section, object kinetic Monte Carlo (OKMC) will be described as it is the most common kMC method, but other methods such as lattice kinetic Monte Carlo (LKMC) and event kinetic Monte Carlo (EKMC) operate according to similar principles.

Description: In OKMC, individual defects are placed inside a finite volume element. Each defect is assigned a size and shape as well as a number of reactions that it can carry out. For example, a vacancy cluster in iron may be treated as a spherical object with a diffusivity D and allowed to either diffuse in 3D or to eject a single vacancy and become a smaller vacancy cluster. As in CD, the diffusivity D and the reaction rate for dissociation R_{dis} are given by Arrhenius laws:

$$D = D_0 e^{-\frac{E_m}{k_b T}} \ , \ R_{\text{dis}} = \omega n^{1/3} D_1 e^{-\frac{E_b}{k_b T}} \tag{7}$$

where, as in Section 2.2.2, ω is a geometric constant and the constants D_0 and E_m are the diffusion prefactor and migration energy of the vacancy cluster and E_b is the binding energy of a single vacancy to the vacancy cluster. Here, D_1 is the diffusivity of a single vacancy, also given by a separate Arrhenius relationship. Given the diffusivity D of the defect, if a jump distance d is chosen for diffusion then a jump frequency can be obtained via $\frac{6D}{d^2}$ [197]. Thus, a list of allowed reactions μ with reaction rates R_μ in units of s^{-1} is created, including all defects in the volume. The total reaction rate $R = \sum_\mu R_\mu$ is then compiled, and represents the rate (in reactions per second) for any reaction to occur in the system. The classic kinetic Monte Carlo algorithm can then be applied by selecting two random numbers r_1 and $r_2 \in (0, 1)$ and choosing a reaction μ to carry out and a timestep

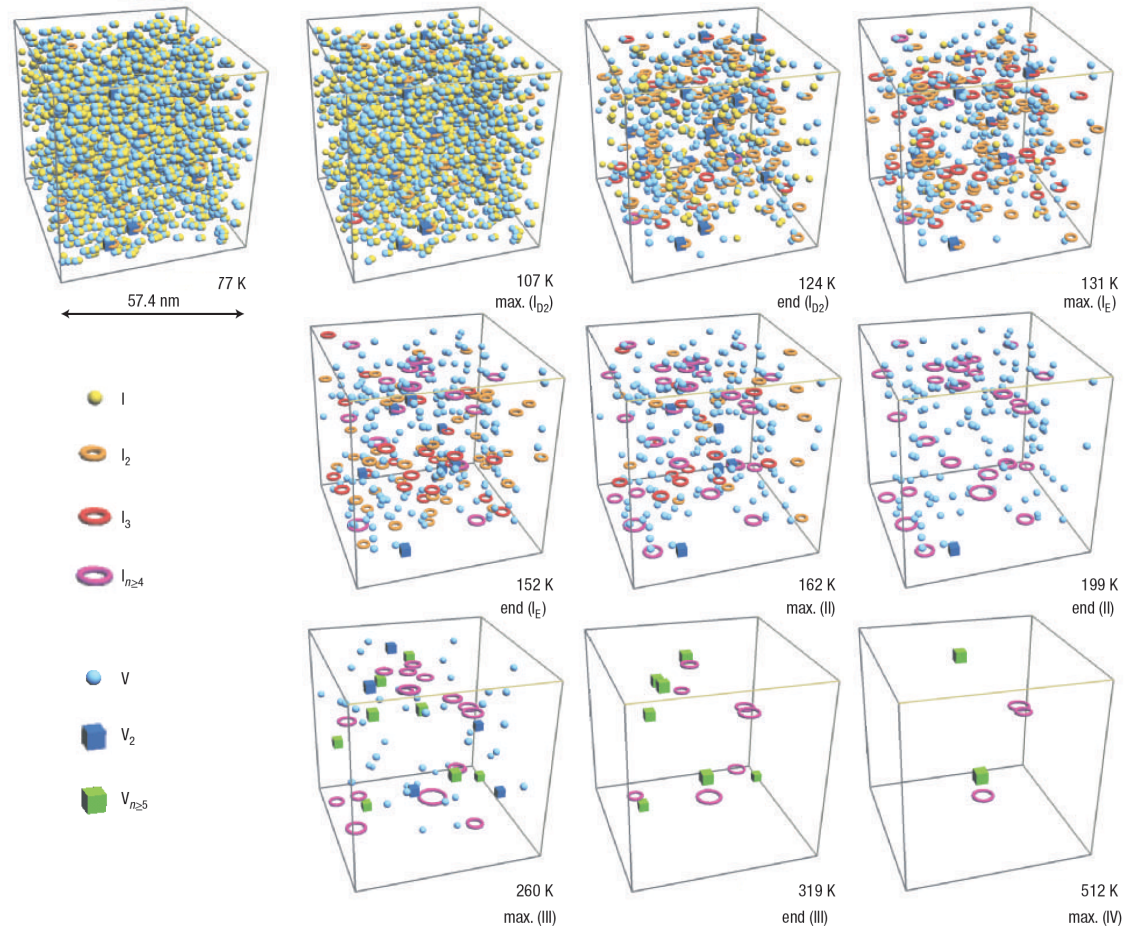

Figure 11: OKMC volume showing defect evolution in a simulation of resistivity recovery of electron beam-irradiated iron thin foils during annealing (reproduced with permission from Fu et al. [74])

τ according to:

$$\tau = \frac{1}{R} \ln\left(\frac{1}{r_1}\right) \ , \ \sum_{\nu=1}^{\mu-1} R_\nu < r_2 R \leq \sum_{\nu=1}^{\mu} R_\nu \tag{8}$$

A derivation of this algorithm can be found in Appendix A and is adapted from the work of Gillespie [83]. Once a reaction is chosen, if two defects overlap as a result of the movement of one of the defects, an instantaneous reaction can occur between the interacting defects (for example, clustering or annihilation). Then the new list of reactions μ and and reaction rates R_μ is compiled and the kMC algorithm is repeated. A schematic showing defect evolution in an OKMC simulation volume is shown in Figure 11.

Applications of OKMC models: OKMC and other kinetic Monte Carlo-based methods are used both to investigate defect behaviors as well as to simulate defect accumulation over large timescales and radiation doses. Examples of studies of defect behaviors using OKMC include analyses of the fraction and types of surviving defects in a displacement cascade after correlated interactions are carried out [197, 105, 161]. OKMC has also been used to compute sink strengths of various sink types including point sinks, line sinks, and grain boundaries and compare those sinks strengths to analytical forms used in CD simulations [127]. Other experimentally observed defect behaviors have been reproduced using OKMC simulations such as dislocation loop raft formation [240] and resistivity recovery of electron-irradiated iron thin foils [74]. The impact of the PKA energy of displacement cascades on long-term defect evolution has also been investigated in detail using OKMC [22, 202].

The largest-scale studies of radiation damage in metals performed using OKMC are simulations of defect accumulation in neutron-irradiated iron [22, 200, 101, 102], in which cascade damage is introduced in simulation volumes with lengths ranging from 100-300 nm at dose rates corresponding to neutron damage in the HFIR reactor [67]. The resulting defect populations are then compared to experimental measures of defect content [67, 259]. Similarly to advanced CD models, OKMC studies of radiation damage accumulation provide a detailed estimate for the numbers and types of defects present in irradiated materials as a function of many variables, such as temperature, dose rate, total dose, and cascade energy.

Methods such as OKMC allow simulation of defect-level spatial resolution and individual defect behaviors that can be quite complex, such as one-dimensional diffusion or defect decoration of dislocation lines [222, 240]. In addition, the material model simulated can be arbitrarily complex without significantly impacting the feasibility of the simulation as reaction rates only need to be calculated for defects present in the system at a given time (in contrast to CD methods, which must calculate all populations of all allowed defect types at each timestep).

The main drawbacks to using OKMC methods to simulate radiation damage accumulation are associated with computation time. Unlike CD models, which have limited

complexity but computational efficiency, OKMC models can simulate very complicated defect behaviors but must take a very large number of timesteps, as only a single reaction (usually diffusion or dissociation) can be chosen from the kMC algorithm at each step. This limits both the total radiation dose as well as the total volume that can be simulated. In addition, parallelization of an OKMC-based model is difficult. If the OKMC volume is split between two processors, the time evolution in each processor may be asynchronous due to the random choice of timestep in each processor, leading to errors with defect movement between processors [136]. Overall, OKMC models present a contrasting set of strengths and drawbacks when compared to CD models.

2.2.4 Comparison of defect evolution in CD and OKMC models

Both CD and OKMC models use results of atomic-scale simulations as a basis for their allowed defect behaviors as well as the diffusion rates and dissociation rates of said defects. Therefore, if radiation damage accumulation is simulated using the same allowed defects in each method, results of CD and OKMC simulations should agree. Several comparisons between OKMC and CD simulations of the same radiation conditions and material model have been made [44, 84, 246, 207, 17], using simplified cases in which both CD and OKMC methods can use the same database of defects and behaviors.

In the model of Stoller et al. [207], OKMC and CD simulations are compared for the case of Frenkel pair implantation, assuming all defects besides single vacancies and single interstitials are immobile. Clusters are allowed to form, using cluster dynamics rate equations given in equation (6). Results showing vacancy concentration as a function of dose for several temperatures are shown in Figure 28. The two methods give similar results for a large range of temperatures and radiation doses. However, limitations to the results of each method are found in this work. Due to the deterministic nature of the CD results, a smooth distribution of large cluster sizes is found in CD while OKMC results tend to have single large defect clusters of a few different sizes. In addition, also due to the deterministic nature of CD, a statistical distribution of defect sizes over several runs cannot be obtained, while this information comes naturally from OKMC results. Finally, the lower limit of

concentration modeled in OKMC simulations is one defect inside the simulation volume, while CD results have no lower limit for concentration.

Another limitation of CD simulations when compared to OKMC is demonstrated in the work of Dalla Torre et al. [44], in which resistivity recovery of iron irradiated with electrons at low temperature and subsequently annealed is simulated. CD and OKMC results of these simulations are shown in Figure 12b. In these simulations, as temperature is slowly increased, different defects are made mobile according to the Arrhenius laws governing their mobility, as given in equation (1). OKMC results are able to identify separate temperatures at which vacancies and self-interstitials from the same Frenkel pairs recombine, after which vacancies and interstitials from separate Frenkel pairs recombine (peaks I_{D2} and I_E in Figure 12b, respectively). CD models cannot include the effects of spatial correlations between vacancy-intestitial pairs in individual Frenkel pairs due to the homogeneous nature of their formulation. Therefore, CD models only match OKMC models if they are initiated after spatially correlated reactions have been carried out.

Due to the different limitations of CD and OKMC models, a need currently exists for modeling techniques that can provide results that use the same inputs as these models, namely diffusion and binding parameters, and can provide the same results in model simulations, but avoid the limitations of each of these methods. In particular, models are needed that can simulate spatially resolved defect behavior such as spatial correlations between defects in Frenkel pairs and cascades or defect diffusion to free surfaces and grain boundaries, that allow complex defect types and behaviors such as mobile helium-vacancy clusters, and that are computationally efficient enough to simulate large doses and simulation volumes.

2.3 Stochastic cluster dynamics as a method for addressing the limitations of CD and OKMC models

As noted in Section 2.2, both CD and OKMC models have advantages and disadvantages to their implementation in studying radiation defect accumulation in metals. An alternate method for simulating radiation defect accumulation in metals has recently been developed by Marian and Bulatov [131]. This method, called stochastic cluster dynamics (SCD), was originally proposed for time evolution of general chemical systems [83] and acts as

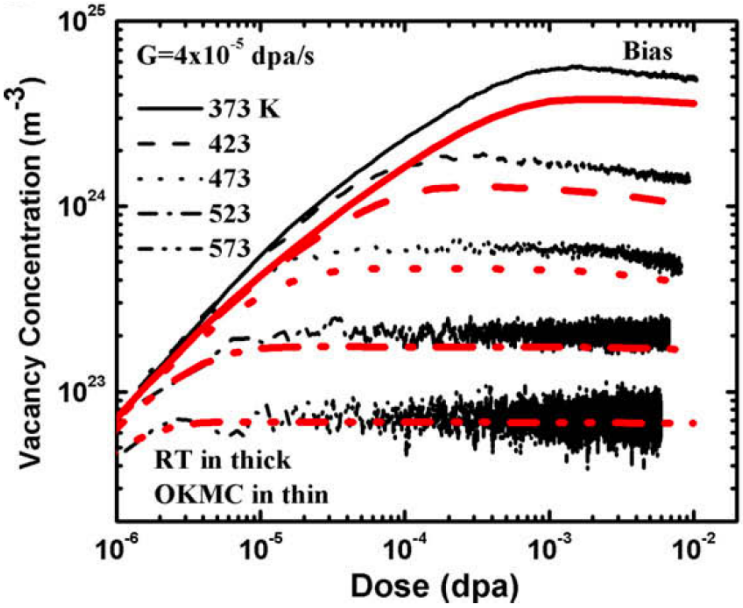

(a)

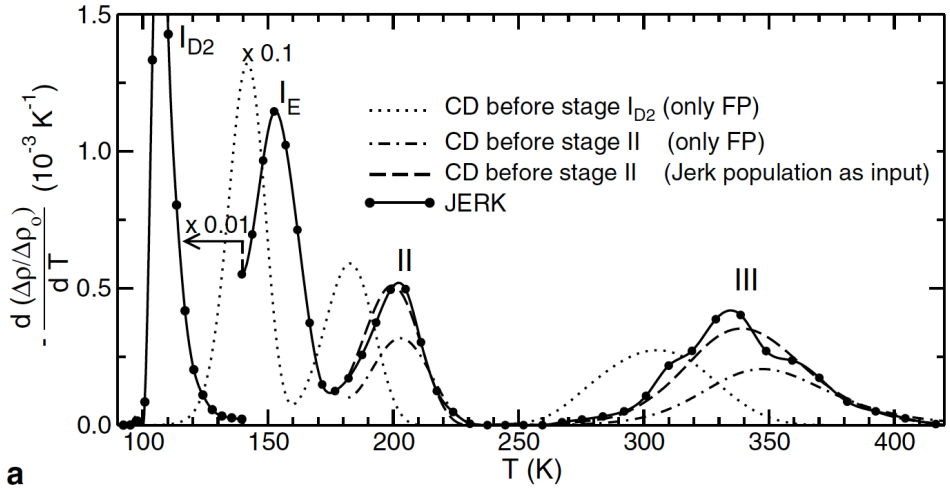

(b)

Figure 12: Simulations comparing CD and OKMC simulation methods. 28 OKMC and CD simulation of defect accumulation in iron implanted uniformly with Frenkel pairs, assuming only single vacancies and single interstitials are mobile (reproduced with permission from [207]). 12b CD simulations of resistivity recovery in electron beam-implanted iron, compared to both OKMC and experimental results (reproduced with permission from [44]).

a compromise between the CD and OKMC methods. Here, space is treated as a finite volume as in OKMC and a finite number of defects populate that volume, but defects are assumed to be homogeneously distributed within the volume. Defect diffusion within the volume is ignored, and instead reactions such as defect creation, clustering, annihilation, and dissociation are chosen at each step. The same kinetic Monte Carlo algorithm used in OKMC is used in SCD to choose a reaction and a timestep during each Monte Carlo step. The rates for these reactions are taken from modified versions of the rate equations found in CD. SCD methods avoid the limitations of CD by allowing arbitrary numbers of chemical species and mobile defects, while maintaining greater computational efficiency than OKMC models. However, several challenges remain in order to use a method such as SCD to simulate defect accumulation in irradiated materials in realistic reactor environments:

1. Reaction rates for complex defect interactions that will be included in SCD but are not typically modeled in deterministic CD - including three-dimensional (3D), one-dimensional (1D), and mixed 3D-1D diffusion of spherical and circular defects - have not yet been derived.

2. SCD, like CD, is a spatially homogeneous method. It therefore does not include spatially resolved effects such as correlated reactions between defects in displacement cascades and the effects of free surfaces in thin foils.

3. The computational efficiency of SCD must be improved to simulate radiation damage in larger volumes and to greater total radiation doses in order to simulate realistic reactor environments and polycrystalline microstructures.

These barriers must be overcome before SCD can be included in a multi-scale framework as a predictive model for defect accumulation in nano-structured metals. Therefore, the model development in this dissertation will focus on developing SCD for use in complex irradiation environments, including adapting SCD to spatially resolved environments, and computational improvements to SCD to allow simulations of realistic reactor and experimental irradiation conditions.

CHAPTER III

SPATIALLY RESOLVED STOCHASTIC CLUSTER DYNAMICS

The goal of this chapter is to introduce the method developed in this dissertation for simulating radiation damage accumulation in metals, called spatially resolved stochastic cluster dynamics (SRSCD). In Section 3.1, the two most commonly used methods for simulating radiation damage accumulation are discussed, and the gap in current computational capabilities that SRSCD is intended to address is defined. The SRSCD algorithm is presented in Section 3.2, along with reaction rates for clustering of defects with various geometries and diffusion behaviors (3D, 1D, mixed 3D-1D, and 2D diffusion on a planar surface) and diffusion between volume elements. Several computational improvements to SRSCD are then described in detail, including approaches for simulating damage accumulation due to displacement cascades in Section 3.3 and the application of a synchronous parallel kinetic Monte Carlo algorithm that enables simulation of larger domains in Section 3.4. Validation of the method is discussed in Section 3.5 by comparing SRSCD results to results of other simulation tools such as rate theory and object kinetic Monte Carlo. Finally, a summary of this chapter is provided in Section 3.6 and conclusions are discussed in Section 3.7.

3.1 Motivation: computational efficiency with complex models

Efforts to model radiation damage evolution using computational tools have been underway for several decades and include many distinct computational techniques [176, 197, 74, 203, 95, 29, 162, 105, 22]. The two commonly used methods for simulating radiation defect accumulation in metals are the object kinetic Monte Carlo method (OKMC) [207, 197, 57, 39] and mean field rate theory (MFRT) methods [161, 162, 124, 64] (sometimes referred to as cluster dynamics, or CD). These methods sometimes use finite element or finite difference algorithms to treat spatial dependence. Each of these approaches presents different challenges when attempting to simulate radiation damage in complex environments, as discussed in Sections 2.2.2 and 2.2.3. OKMC simulations limit the number of assumptions

made about defect evolution by following individual defects as they diffuse stochastically throughout a material. However, due to the fact that each defects diffusion pathway is treated individually, simulations of reactor-relevant irradiation conditions can become computationally prohibitive using this method. Displacement damage in OKMC simulations is typically limited to less than 1 dpa and the minimum concentration of defects that can be simulated is limited to one defect per simulation cell volume [207].

Spatially resolved rate theory (RT), sometimes referred to as cluster dynamics (CD) assumes spatial homogeneity within each volume element and thus does not track individual defect movements. In contrast to OKMC, rate theory simulations can reach dpa levels of 100 or more and can model arbitrarily small defect concentrations [207]. However, the number of rate equations to be solved increases exponentially with the number of species modeled [131]. Increased numbers of mobile defect species, such as glissile interstitial loops, also dramatically increases the complexity of the rate equations to be solved. The effects of impurities, alloying elements, and multispecies gas implantation on microstructural evolution have been shown to be significant in irradiated materials [213, 156, 237, 212], but these simulations are frequently not within the scope of feasible rate theory simulations. Overall, a gap exists in the capabilities of current methods for modeling radiation damage accumulation in complex microstructures, due to limitations in volume and dose of OKMC models and limitations in complexity of CD models. In addition, CD and OKMC methods use fundamentally different approaches to simulate radiation damage evolution and can be directly compared only in limited cases [207]. Therefore, future modeling techniques should reproduce both CD and OKMC results in a variety of irradiation conditions.

An alternative approach to solving spatially homogeneous problems of this type, first proposed for general chemical reactions by Gillespie [83] and developed further for radiation defects in metals by Marian and Bulatov [131], avoids many of these problems. In this approach, called stochastic cluster dynamics (SCD), the rate equations of traditional rate theory are treated in a homogeneous volume element, but the populations of defects are limited to integer populations within the volume. The reactions between defects such

as clustering and dissociation are chosen stochastically, using a kinetic Monte Carlo algorithm. Thus, the migration of individual defects is ignored and the simulation is able to include large numbers of mobile species which can interact without exponentially increasing computational time.

In order to modify this approach to treat problems in which nano- and micro-scale spatial dependence is necessary, in this dissertation the method of stochastic cluster dynamics is amended by creating several volume elements. Inside each element, the population of defects is assumed to be homogeneously distributed, but migration can occur between elements based on diffusion rates, defect concentrations, and element sizes. Gillespie [83] in fact proposes including spatial dependence in this way. Thus, free surfaces, inhomogeneous defect implantation, and other effects can be studied. This approach will be referred to as spatially resolved stochastic cluster dynamics (SRSCD).

3.2 Derivation of the method

In this section, the rate equations of cluster dynamics are converted into forms applicable to SRSCD and then solved using a kinetic Monte Carlo algorithm. A simple rate theory model for defect evolution is first presented in Section 3.2.1, treating only single vacancies and single self-interstitials as mobile defects. This model is used to inform the development of SRSCD, which allows more complex reactions. Due to the complexity of allowed reactions in SRSCD, sink strengths for defect clustering are derived in Section 3.2.2 for several different defect geometries and types of diffusion, including 3D, 1D, and mixed 3D-1D diffusion. Finally, these sink strengths are converted to the various reaction rates for allowed reactions in SRSCD simulations carried out through the course of this dissertation in Section 3.2.3. Spatial resolution is added through the solution of Fick's law in a finite volume setting in Section 3.2.4, and solution of the entire coupled system through use of a kinetic Monte Carlo algorithm is carried out in Section 3.2.5.

3.2.1 Rate theory background

In an infinite, isotropic medium, the evolution of the defect populations can be modeled by tracking individual defect locations and behaviors, or by using a mean field approximation

[207]. The use of a mean field approximation allows the simulation to ignore individual defect behavior, thus reducing the computation time, but assumes spatial homogeneity of defects. In this section, the rate equations for mean field rate theory (MFRT) are described and adapted to the model of the present work using an example case involving only two species of defects - vacancies and self-interstitials.

Here we will present the rate equations for a simple MFRT model containing only two mobile species - single vacancies and single self-interstitials - and immobile clusters of these defects. This model is taken from Stoller et al [207]. The evolution of the atomic fraction of immobile defects such as SIA (i) or vacancy (v) clusters size n ($n > 1$) is given by:

$$\begin{aligned} \frac{dC_{vn}}{dt} &= K_{vn}(t) + J_v(n-1,t) - J_v(n,t) \\ \frac{dC_{in}}{dt} &= K_{in}(t) + J_i(n-1,t) - J_i(n,t) \end{aligned} \tag{9}$$

where K_{vn} and K_{in} are the generation rate of vacancy and self-interstitial clusters of size n, $J_v(n-1,t)$ and $J_i(n-1,t)$ are the rate of vacancy and interstitial clusters of size $n-1$ converting to size n, and $J_v(n,t)$ and $J_i(n,t)$ are the rate of vacancy and interstitial clusters of size n converting to size $n+1$. Care should be taken here to note that $C_{vn}(t)$ and $C_{in}(t)$ are in units of atomic fraction. Other formulations of MFRT use concentration formulated in defects per volume, and constants are adjusted accordingly [161, 131]. In a simple model with only Frenkel pair implantation and no migration of clusters, $K_n = 0$ for all n except $n = 1$. The reactions that are accounted for in the growth and annihilation of vacancy and interstitial clusters are as follows:

1. $V_n + V \rightarrow V_{n+1}$ and $I_n + I \rightarrow I_{n+1}$ cluster growth
2. $V_n \rightarrow V_{n-1} + V$ and $I_n \rightarrow I_{n-1} + I$ thermally activated cluster dissociation
3. $V_n + I \rightarrow V_{n-1}$ and $I_n + V \rightarrow I_{n-1}$ vacancy-interstitial annihilation

Taking these reactions into account, the cluster growth terms in equation (9) are expressed as

$$\begin{aligned} J_v(n,t) &= P_{vn}(t)C_{vn}(t) - Q_{v(n+1)}(t)C_{v(n+1)}(t) \\ J_i(n,t) &= P_{in}(t)C_{in}(t) - Q_{i(n+1)}(t)C_{i(n+1)}(t) \end{aligned} \tag{10}$$

where P_{vn} and P_{in} are the rates of $V_n + V$ and $I_n + I$ clustering respectively, and Q_{vn} and Q_{in} are the rates of recombination (annihilation) and dissociation of vacancy and interstitial clusters of size n. Assuming thermally activated, 3D diffusion, spherical vacancy clusters, and interstitial clusters in the form of circular dislocation loops, the clustering and dissociation rates are given by [207, 107]:

$$\begin{aligned} P_{vn}(t) &= \omega n^{1/3} D_v C_v(t) \\ P_{in}(t) &= Z_{\text{int}} \omega' n^{1/2} D_i C_i(t) \\ Q_{vn}(t) = Q^i_{vn} + Q^v_{vn} &= \omega n^{1/3} \left(D_i C_i(t) + D_v e^{-E^v_b(n)/k_b T} \right) \\ Q_{in}(t) = Q^v_{in} + Q^i_{in} &= \omega' n^{1/2} \left(D_v C_v(t) + D_i e^{-E^i_b(n)/k_b T} \right) \end{aligned} \tag{11}$$

Here, $C_{v,i}$ and $D_{v,i}$ are the concentration and diffusion rates of free vacancies and interstitials, respectively. Z_{int} is a constant reflecting the preference of interstitial clusters to absorb other interstitials, commonly taken as $Z_{\text{int}} = 1.15$. $E_b^{v,i}(n)$ is the binding energy of a vacancy or interstitial to a cluster size $n-1$, k_b is Boltzmann's constant, and T is the temperature. The constants ω and ω' are geometric constants determined by the sink strength of spherical and circular absorbers [207, 30],

$$\begin{aligned} \omega &= \left(\frac{48\pi^2}{\Omega^2} \right)^{1/3} \\ \omega' &= \left(\frac{4\pi}{\Omega b} \right)^{1/2} \end{aligned} \tag{12}$$

where Ω is one atomic volume and b is the Burgers vector of a dislocation loop.

Unlike immobile defects, mobile defects can diffuse and cluster or annihilate with all other defects in the system. Therefore, the rate equations for the time evolution of mobile point defects are more complicated due to the large number of available interactions. The

rate equations for mobile single vacancies and single interstitials are as follows [207]:

$$\begin{aligned}
\frac{dC_v}{dt} &= K_v - \mu_R(D_i + D_v)C_i(t)C_v(t) \\
&\quad - \sum_{n=2}^{\infty}\left[P_{vn}(t)C_{vn}(t) + Q^v_{in}(t)C_{in}(t) - Q^v_{vn}(t)C_{vn}(t)\right] \\
&\quad -2P_{v1}(t)C_v(t) + Q^v_{v2}(t)C_{v2}(t) \\
\frac{dC_i}{dt} &= K_i - \mu_R(D_i + D_v)C_i(t)C_v(t) \\
&\quad - \sum_{n=2}^{\infty}\left[P_{in}(t)C_{in}(t) + Q^i_{vn}(t)C_{vn}(t) - Q^i_{in}(t)C_{in}(t)\right] \\
&\quad -2P_{i1}(t)C_i(t) + Q^i_{i2}(t)C_{i2}(t)
\end{aligned} \tag{13}$$

where μ_R is a coefficient for the recombination of point defects, given by $\mu_R = \frac{4\pi(r_v+r_i)}{\Omega}$. The final terms in each expression are repeated versions of the $n = 2$ terms for the formation and thermal dissociation of divacancy and di-interstitial clusters inside the sum. The repetition of these terms results from the fact that the reactions $v + v \Leftrightarrow 2v$ and $i + i \Leftrightarrow 2i$ add or remove two point defects for each reaction.

Rate equations can vary widely based on the number of defect types present in the model, which defect types are allowed to migrate, and the allowed reactions of the model chosen. As noted by others [131], the number of rate equations required increases exponentially with the number of defect species due to the need to simulate mixed-species clusters. The complexity of the equations also increases as the number of migrating defects of a given species increases. Although grouping schemes exist in rate theory for large clusters in order to speed computation [85], rate theory simulations are commonly limited to a small number of defect species and mobile defects.

3.2.2 Sink strengths in cluster dynamics

In the previous section, the rate equation for concentration evolution of a given species i, $\frac{dC_i}{dt}$, is given as the sum of contributions of several reaction rates representing allowed reactions that either increase or decrease the number of defects of species i in the system, i.e. implantation, clustering, dissociation, trapping at sinks, and annihilation. In SRSCD, instead of explicitly solving these rate equations, defect populations are evolved in time using reaction rates derived from cluster dynamics. However, due to the computational

efficiency afforded by SRSCD, much more complicated reactions can be included in the model and the simple MFRT model presented in the previous section does not consider all types of allowed reactions accounted for in SRSCD. In this section, reaction rates for defect clustering are derived in a more general fashion, including the defects' sizes, geometries (spherical or circular), and geometry of diffusion (3D, 1D, mixed 3D-1D, and 2D diffusion on a surface).

Therefore, in the following sections, it will become useful to discuss the reaction rate of a specific reaction, for example $v + 3v \rightarrow 4v$, instead of the entire rate equation governing the population of a single defect type $\frac{dC_i}{dt}$. As an example, we choose to investigate the reaction rate for clustering between a single mobile vacancy with a vacancy cluster size n. From the previous section, we see that the reaction rate for this particular reaction is given by:

$$\textit{reaction rate} = P_{vn}(t)C_{vn}(t) = \omega n^{1/3} D_v C_v(t) C_{vn}(t) \tag{14}$$

This can be re-written for the interaction of any diffusive species i with an immobile sink, using a sink strength term k^2:

$$\textit{reaction rate} = k^2 D_i C_i(t) \tag{15}$$

where the sink strength k^2 has units $1/m^2$ and represents the inverse of the square of the mean free path travelled by the point defect before it is absorbed by the stationary sink. Therefore, for the example of a single vacancy being trapped by a vacancy cluster size n given above, the sink strength k^2 is given by:

$$k^2 = \omega n^{1/3} C_{vn}(t) \tag{16}$$

It can be seen that all terms representing clustering in the rate equations of the previous section can be expressed in this form, with k^2 depending on many factors, including the size and shape of the sinks, whether the sink is also migrating, and the type of migration (1D vs 3D). The term sink here refers to any object that can interact with a mobile defect, such as other mobile and immobile defects, dislocations, grain boundaries, and impurities. It is therefore important to derive general expressions for sink strength k^2 in order to inform

the reaction rates in SRSCD for defect clustering, annihilation, and trapping at stationary sinks such as dislocations and impurities.

It should be noted that when many sink types are present in a system, sink strengths are not independent and have been shown to increase when other sinks are present in high concentrations [55]. This effect is most likely to be significant in the sink strengths of grain boundaries and free surfaces due to the large number of defects within the grains or metal layers. Large planar sinks such as grain boundaries therefore should not be treated as homogeneously distributed sinks with constant sink strength k^2. In the SRSCD formulation, planar sinks are instead treated as 'primary' sinks. These sinks are simulated using boundary conditions on the system by setting the concentration of all defect types equal to 0 at a free surface or perfectly absorbing grain boundary. All other defects (helium, vacancies, and self-interstitials and their clusters) are simulated as homogeneously distributed 'secondary' sinks with sink strength k^2. This approach has been used in other simulations of sink strength and defect evolution in metals [55, 64, 58].

3.2.2.1 Point defects and spherical sinks

In principle, the idea of sink strengths is to homogenize the true spatially dependent problem of defects diffusing and being trapped at fixed sinks. Therefore, to derive k^2, we consider a problem in which a single mobile defect species is treated by a concentration field c in the presence of fixed sinks s. We then consider two methods for solving such a problem, using concentrations $c_e(t)$ and $c_h(t)$. These equations represent the exact (spatially resolved) and homogeneous distributions of mobile defect concentration c in the presence of sinks type s, respectively. Assuming a constant rate of implantation K (in units of defects$\cdot$m^{-3}s^{-1}), the rate equations for the population evolution of these two formulations for concentration are:

$$\frac{dc_e}{dt} = K + D\nabla^2 c_e \quad , \quad \frac{dc_h}{dt} = K - Dk_s^2 c_h \tag{17}$$

We can see that the rate equation for c_e uses Fick's law and boundary conditions to account for defect absorption at sinks, while c_h uses a homogenized sink strength term k_s^2 to account for the same absorption in a homogenized fashion. Therefore, our goal is to solve the rate equation for c_e explicitly around a single fixed sink and set the two populations

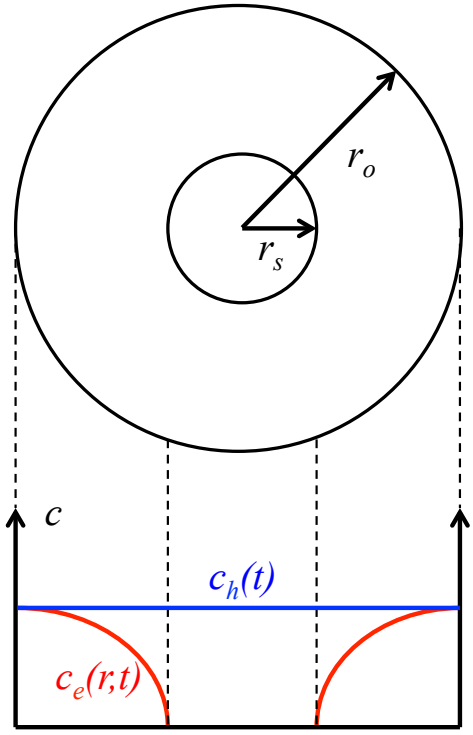

Figure 13: Two-dimensional schematic of computational domain used to derive sink strength k^2 of a spherical sink.

equal in order to find an analytical form for k_s^2. The form of this sink strength depends on the geometry of this defect and its diffusion, and the various functional forms used for the defects modeled in this work are derived in the following sections.

In this section, a derivation of the commonly used functional form for the sink strength of spherical defects diffusing in three dimensions will be given. This is based on the work of Brailsford and Bullough [30], although some deviations are made from their derivation. The method of this derivation will also be applied later to the case of a defect concentration field c on a two-dimensional surface in the presence of a circular sink in Section 3.2.2.5.

We first consider the solution to $\frac{dc_e}{dt}$ around a spherical sink with radius r_s inside a spherical volume with outer radius r_o. A two-dimensional schematic of this problem is shown in Figure 13. The value of r_o is chosen such that the spherical volume V enclosed by r_o, given by $V = \frac{4\pi r_o^2}{3}$, is the inverse of the concentration of sinks in the global medium, $c_s = \frac{3}{4\pi r_o^3}$. Assuming spherical symmetry, the spatial derivatives simplify to:

$$\frac{dc_e}{dt} = K + D\left(\frac{1}{r^2}\frac{d}{dr}r^2\frac{dc_e}{dr}\right) \tag{18}$$

Assuming a perfect sink, the boundary conditions of this equation are $c_e = 0$ at $r = r_s$ (the outer radius of the sink), and $\frac{dc_e}{dr} = 0$ at $r = r_o$ (the outer radius of the volume), assuming that the concentration of point defects is constant far from the sink. This approximation relies on $r_o >> r_s$, because if sinks are very close together, this method of drawing a spherical volume around the sinks and assuming the concentration is constant far from the sinks is not valid.

We next solve this equation at steady-state $\left(\frac{dc_e}{dt} = 0\right)$, giving the following functional form for the spatial distribution of defects $c_e(r)$:

$$c_e(r) = -\frac{Kr^2}{6D} + \frac{\alpha_1}{r} + \alpha_2 \tag{19}$$

where α_1 and α_2 are integration constants. Applying the boundary conditions, we get:

$$c_e(r) = \frac{K}{6D}\left[(r_s^2 - r^2) + 2r_o^3\left(\frac{1}{r_s} - \frac{1}{r}\right)\right] \tag{20}$$

Similarly, we can set $\frac{dc_h}{dt} = 0$ and find:

$$c_h = \frac{K}{Dk_s^2} \tag{21}$$

Requiring that the steady-state homogeneous concentration c_h equals the steady-state exact solution far from the sink $c_e(r = r_o)$, we solve for k_s^2:

$$k_s^2 = \frac{6}{(r_s^2 - r_o^2) + 2r_o^3\left(\frac{1}{r_s} - \frac{1}{r_o}\right)} \tag{22}$$

Next we simplify the above equation by noting that the concentration of sinks $c_s = \frac{3}{4\pi r_o^3}$. Thus, the above equation becomes:

$$k_s^2 = \frac{8\pi c_s r_s}{\left(\frac{r_s^3}{r_o^3} - \frac{r_s}{r_o}\right) + 2\left(1 - \frac{r_s}{r_o}\right)} \tag{23}$$

However, we earlier made the requirement that $r_o >> r_s$, so all terms in the denominator except the unit term are neglected:

$$k_s^2 = \frac{8\pi c_s r_s}{2} = 4\pi c_s r_s \tag{24}$$

This is the classical 3D sink strength of spherical sinks, and gives the following rate equation for $c_h(t)$:

$$\frac{dc_h}{dt} = K - 4\pi D r_s c_s c_h \tag{25}$$

If we then modify this equation to reflect the case of two defect types, for example vacancies and self-interstitials c_v and c_i, in which each defect type can diffuse with diffusivity D_v and D_i and each defect type acts as a sink for the other, we get:

$$\begin{aligned} \frac{dc_v}{dt} &= K_v - 4\pi(D_v + D_i)rc_vc_i \\ \frac{dc_i}{dt} &= K_i - 4\pi(D_v + D_i)rc_vc_i \end{aligned} \tag{26}$$

where here r is the reaction distance between a vacancy and a self-interstitial. This is the well-known result for 3D homogeneous rate theory of vacancies and self-interstitials.

3.2.2.2 Reaction rates for 3D-migrating defects

In order to simplify units, the rate equations in the previous section $\frac{dc}{dt}$ (in units of defects·m^{-3}) are converted here to units of defects per lattice atom or atomic fraction $\frac{dC}{dt}$, with $c = \frac{C}{\Omega}$, where Ω is the volume occupied by one lattice site in the crystal. To calculate the sink strength of defects and defect clusters, it will also be useful to note that for a spherical cluster size n, the radius is given by

$$r = \left(\frac{3n\Omega}{4\pi}\right)^{1/3} \tag{27}$$

and for a circular interstitial dislocation loop size n, the radius is given by

$$r = \left(\frac{n\Omega}{\pi b}\right)^{1/2} \tag{28}$$

where Ω is the atomic volume and b is the Burgers vector.

For a point defect migrating in three dimensions interacting with a spherical (immobile) sink j, the sink strength is given by [30]:

$$k^2 = \frac{4\pi r_j C_j}{\Omega} \tag{29}$$

By applying equation (27) to r_j and substituting k^2 into equation (15), the reaction rate for a point defect species i to interact with a spherical sink species j (in units of reactions per lattice atom per second) is given by:

$$reaction\ rate = \omega n_j^{1/3} D_i C_i C_j \tag{30}$$

where, once again, ω is a geometric constant given by:

$$\omega = \left(\frac{48\pi^2}{\Omega^2}\right)^{1/3} \tag{31}$$

For a point defect interacting with a circular (immobile) sink j, the sink strength is given by [207]:

$$k^2 = \frac{2\pi r_j C_j}{\Omega} \tag{32}$$

Similarly to above, by applying equation (28) to r_j and substituting k^2 into equation (15), the reaction rate for a point defect species i to interact with a circular sink species j (in units of reactions per lattice atom per second) is given by:

$$reaction\ rate = \omega' n_j^{1/2} D_i C_i C_j \tag{33}$$

with ω' given by:

$$\omega' = \left(\frac{4\pi}{\Omega b}\right)^{1/2} \tag{34}$$

The reaction rates presented above correspond to the clustering terms in the rate equations presented in Section 3.2.1.

In the previous equations, interstitial clusters are treated as circular dislocation loops, and their cross-section for interaction with migrating point defects is adjusted accordingly. However, these defects are assumed to be immobile in most rate theory simulations. By contrast, atomistics studies have shown that the small dislocation loops formed by self-interstitial clusters are in fact very mobile, undergoing one-dimensional glide motion with migration energy less than 0.1 eV [197, 166]. The following rate equations will account for interactions of multiple mobile defects of varying geometry and migration dimensionality.

The first modification of equations (30) and (33) occurs when the point defect and the sink are both mobile, spherical defects. In that case, the interaction radius becomes the

sum of the two radii of the spherical objects, and the relative diffusion rate is the sum of the two diffusion rates of each defect. This is the same as the sum of the rate at which mobile defect i encounters stationary defect j and mobile defect j encounters stationary defect i. Thus the reaction rate for two spherical defects interacting is

$$reaction\ rate = \omega \left(n_i^{1/3} + n_j^{1/3} \right) (D_i + D_j) C_i(t) C_j(t) \tag{35}$$

3.2.2.3 1D-migrating defects

Next, we will treat the case of migrating circular dislocation loops. Since these loops can glide in one dimension along the direction of their burgers vector [197, 198], their cross-section for interaction with other defects is different than the case of 3D diffusion. For the case of a point defect migrating in 1D interacting with stationary spherical sinks with absorption cross section σ, the inverse of the average distance travelled before being trapped at a sink type j is given by [181]:

$$\frac{1}{\lambda} = c_j \sigma = \frac{C_j \sigma}{\Omega} \tag{36}$$

where the volume concentration of sinks c has been changed to the atomic concentration divided by atomic volume $\frac{C}{\Omega}$. Using $\sigma = \pi r^2$ for the absorption cross section of a spherical sink, the sink strength $k^2 = \frac{1}{\lambda^2}$ is given by [220]:

$$k^2 = \left(\frac{\pi r_j^2 C_j}{\Omega} \right)^2 \tag{37}$$

We next consider a circular dislocation loop i migrating and interacting with an (immobile) point defect sink j. The interaction radius used here is the radius of the circular dislocation loop. Substituting equation (28) into equation (37), the reaction rate becomes:

$$reaction\ rate = \left(\frac{n_i}{b} \right)^2 D_i C_i(t) C_j(t)^2 \tag{38}$$

Note that the reaction rate is quadratic in concentration of the sinks. This formulation assumes that a reaction between the sink and the dislocation loop occurs whenever the distance between the centers of the two objects are less than the interaction radius r, regardless of the orientation of the loop. Therefore, this formulation is an upper estimate for the reaction radius of this reaction. However, the form of the reaction rate should remain the same and only vary by a constant due to the shape of the defects involved.

In equation (38) we assume that the circular dislocation loop has nonzero radius but the point defect sink is infinitesimally small. Next, we expand this method to the case of a circular dislocation loop i interacting with a sessile spherical cluster j, both with nonzero radius. The reaction rate for this interaction is given by the same formula, using the reaction radius as the sum of the radii of the circular loop and the spherical cluster. This reaction rate is given by

$$reaction\ rate = \left[\left(\frac{n_i}{b} \right)^{1/2} + \left(\frac{9\pi n_j^2}{16\Omega} \right)^{1/6} \right]^4 D_i C_i(t) C_j(t)^2 \tag{39}$$

Note that the form of this reaction is the same as equation (38), with only a change in the radius term accounting for the size of the spherical cluster.

If both the circular dislocation loop i and the spherical defect j migrate, one in 1D and the other in 3D, the reaction rate becomes the sum of the reaction rates for the two types of migration. In this case, we take the sum of the rate for a 1D migrating circular loop to react with a sessile spherical cluster and the rate for a 3D migrating spherical cluster to react with a sessile loop. Thus the reaction rate becomes:

$$\begin{aligned} reaction\ rate = & \left[\left(\frac{n_i}{b} \right)^{1/2} + \left(\frac{9\pi n_j^2}{16\Omega} \right)^{1/6} \right]^4 D_i C_i(t) C_j(t)^2 \\ & + \left(\omega' n_i^{1/2} + \omega n_j^{1/3} \right) D_j C_i(t) C_j(t) \end{aligned} \tag{40}$$

Here, the first term accounts for the migration of the dislocation loop and the second term accounts for the migration of the spherical defect. Both terms use the sum of the radii

of the dislocation loop and the spherical defect as the reaction radius.

Finally, the reaction rate for two 1D-migrating dislocation loops to interact is again found by summing the rates for each individual loop interacting with the other while the other is stationary. Again, the radius used in the reaction is the sum of the radii of the two loops. Thus, the reaction rate for two 1D-migrating dislocation loops i and j to combine is given by:

$$\textit{reaction rate} = \frac{(n_i^{1/2} + n_j^{1/2})^4}{b^2}(D_i C_j(t) + D_j C_i(t))C_i(t)C_j(t) \tag{41}$$

3.2.2.4 Mixed 3D-1D migration

Small SIA clusters have been found to migrate in one dimension along close-packed directions but with occasional changes between equivalent close-packed directions [197]. Direction changes occur according to an Arrhenius law such that the migration behavior transitions between one-dimensional at low temperatures and three-dimensional at higher temperatures. Assuming 1D and 3D sink strengths are known, the sink strength due to a given sink type i for a defect migrating with this mixed 1D-3D character has been derived by Trinkaus et al [220]:

$$k_i^2 = \frac{k_{i(1\mathrm{D})}^2}{2}\left(1 + \left(1 + \frac{4}{\frac{l^2 k_{1\mathrm{D}}^2}{12} + \frac{k_{i(1\mathrm{D})}^4}{k_{i(3\mathrm{D})}^4}}\right)^{1/2}\right) \tag{42}$$

where $k_{1\mathrm{D}}^2 = \sum_i k_{i(1\mathrm{D})}^2$ is the total sink strength for all sinks i using 1D migration, $k_{i(1\mathrm{D})}^2$ and $k_{i(3\mathrm{D})}^2$ are the 1D and 3D sink strengths of sink i, and l is the average distance travelled in one dimension before a direction change.

The sink strength calculated in this way reproduces the 3D sink strength in the limit of frequent direction changes and sparse sinks and reproduces the 1D sink strength in the limit of infrequent direction changes. However, the impact of this functional form for sink strength on defect accumulation has been shown to be relatively minor [63]. Therefore, in this work, sink strengths calculated in this way are only used in the simulations of helium desorption from thin iron films, as discussed in Section 4.3.1.

3.2.2.5 Sink strengths on a planar surface

In order to find reaction rates for defect interactions on two-dimensional surfaces, a similar problem must be solved as in Section 3.2.2.1, but assuming two-dimensional diffusion of concentration c_e on a plane with circular sinks. Therefore, our units of concentration are in m^{-2} instead of m^{-3}. The rate equations for exact and homogeneous concentration evolution, $\frac{dc_e}{dt}$ and $\frac{dc_h}{dt}$, are the same as in equation (17) except for the differences in units and the fact that we are now in cylindrical coordinates rather than spherical coordinates. For boundary conditions of the rate equation $\frac{dc_e}{dt}$, we assume a circular sink with radius r_s and zero concentration on the boundary $c_e(r_s) = 0$. Similarly, we define the outer radius of our circular domain r_o and impose $\frac{dc_e}{dr} = 0$ at $r = r_o$. The size of r_o is defined such that the areal density of sinks c_s is equal to the inverse of the total area in the domain, $c_s = \frac{1}{\pi r_o^2}$.

In cylindrical coordinates, the spatial derivatives in equation (17) simplify to:

$$\frac{dc_e}{dt} = K + D\left(\frac{1}{r}\frac{d}{dr}r\frac{dc_e}{dr}\right) \tag{43}$$

which has steady-state $\left(\frac{dc_e}{dt} = 0\right)$ solution given by:

$$c_e(r) = \alpha_1 \ln(r) + \alpha_2 - \frac{Kr^2}{4D} \tag{44}$$

where α_1 and α_2 are integration constants. By imposing the boundary conditions $c_e(r_s) = 0$ and $\frac{dc_e}{dr}(r_o) = 0$, this equation simplifies to:

$$c_e(r) = \frac{K}{4D}\left[2r_o^2 \ln\left(\frac{r}{r_s}\right) + (r_s^2 - r^2)\right] \tag{45}$$

Again, setting $c_e(r_o) = c_h(r_o)$ at steady-state, where $c_h(r_o) = \frac{K}{Dk_s^2}$ gives:

$$k_s^2 = \frac{4}{2r_o^2 \ln\left(\frac{r_o}{r_s}\right) + (r_s^2 - r_o^2)} \tag{46}$$

Substituting $c_s = \frac{1}{\pi r_o^2}$, this simplifies to:

$$k_s^2 = \frac{4\pi c_s}{2\ln\left(\frac{r_o}{r_s}\right) + \left(\frac{r_s^2}{r_o^2} - 1\right)} \tag{47}$$

Similarly to the previous section, the requirement that $r_o >> r_s$ allows us to neglect the second term in the denominator, giving:

$$k_s^2 = \frac{4\pi c_s}{2\ln\left(\frac{r_o}{r_s}\right) - 1} \tag{48}$$

If we plug the sink strength k_s^2 into the equation $\frac{dc_h}{dt}$ in equation (17), we get the following rate equation for the evolution of the population of defects in a homogeneous medium with sinks:

$$\frac{dc_h}{dt} = K - \frac{4\pi D c_s c_h}{2\ln\left(\frac{r_o}{r_s}\right) - 1} \tag{49}$$

Noting again that $c_s = \frac{1}{\pi r_o^2}$, we can re-write this equation as a function of c_s and c_h only:

$$\frac{dc_h}{dt} = K - \frac{4\pi D c_s c_h}{2\ln\left(\sqrt{\frac{1}{\pi c_s r_s^2}}\right) - 1} \tag{50}$$

Finally, we can generalize this to a two-species system with concentrations of vacancies and self-interstitials, c_v and c_i, with a reaction distance r and diffusivities D_v and D_i, respectively (similarly to equations (25) and (26)):

$$\begin{aligned}
\frac{dc_v}{dt} &= K_v - \frac{4\pi D_v c_v c_i}{2\ln\left(\sqrt{\frac{1}{\pi c_i r^2}}\right) - 1} - \frac{4\pi D_i c_v c_i}{2\ln\left(\sqrt{\frac{1}{\pi c_v r^2}}\right) - 1} \\
\frac{dc_i}{dt} &= K_i - \frac{4\pi D_v c_v c_i}{2\ln\left(\sqrt{\frac{1}{\pi c_i r^2}}\right) - 1} - \frac{4\pi D_i c_v c_i}{2\ln\left(\sqrt{\frac{1}{\pi c_v r^2}}\right) - 1}
\end{aligned} \tag{51}$$

Note that in equation (51), two terms are added to each rate equation - one representing the rate of vacancy diffusion and capture by stationary self-interstitials, and one representing mobile self-interstitial diffusion and capture by stationary vacancies. This method assumes that, when both defect types are mobile, the reaction rate for interaction between mobile defects can be deconvoluted into two reaction rates in which one defect type is mobile and one defect type is stationary.

To test the functional form for the reaction rates between defects diffusing in 2D given in equation (51), the results for vacancy and interstitial concentration given by rate theory using a forward Euler formulation are compared to results for defect concentrations given by an in-house 2D OKMC simulation, using the same diffusivities and reaction distance. These results are shown in Figure 14 and show good agreement over a large range of doses and dose rates. Therefore this functional form for the reaction rate for defect interaction in a 2D diffusion environment is used in simulations of defect diffusion on grain boundaries, as described in Section 4.5.

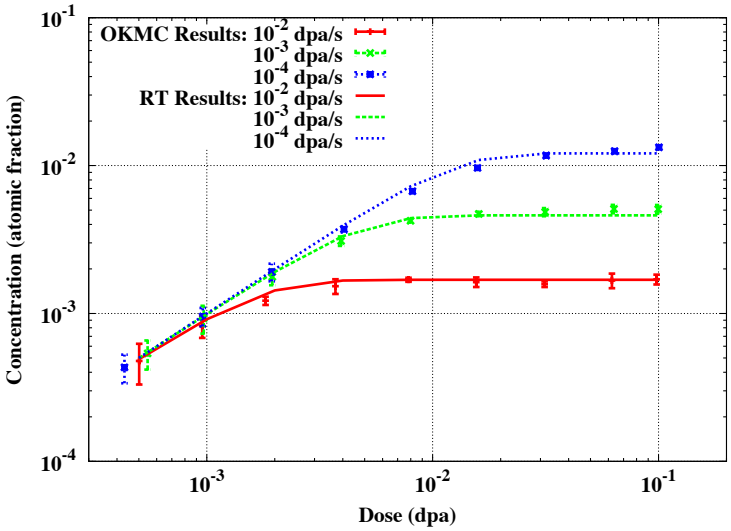

Figure 14: Comparison of 2D OKMC and rate theory results using the rate equations given in equation (51)

3.2.3 Reaction rates in units of s^{-1} inside discrete volume elements

In MFRT models, the reaction rates derived in the previous section are inserted into rate equations for the time evolution of defect concentrations. Therefore, the rate equation for the concentration $C_i(t)$ of defect species i must include the reaction rates for every possible reaction that can occur with defects of type i. By contrast, the central idea of stochastic rate theory is to solve the rate equations described in the previous sections stochastically in a finite volume element, treating only integer numbers of defects. Therefore reaction rates need only be computed for defects present in the volume during a given step, eliminating much of the complexity of MFRT models.

To convert reaction rates into finite-volume form, we solve the rate equations of the previous section inside a single volume element. Given such a volume element with volume V, if the concentration of defects in the volume is C (in atomic fraction), then the total number of defects in that volume is $N = \frac{CV}{\Omega}$. This number is an integer value, and reaction rates for defects not present in the volume are not calculated. Next, given an initial set of defects within a volume element, assuming spatial homogeneity within that element, the reaction rates for any two defects to combine or any one defect to dissociate are given by the same reaction rates as above, which are converted to rates for a finite volume element

by multiplying them by $\frac{V}{\Omega}$:

$$\left(\frac{dC}{dt}\right)\left(\frac{V}{\Omega}\right) = \frac{dN}{dt} \tag{52}$$

Converting concentration C into $\frac{N\Omega}{V}$ and multiplying all reaction rates by $\frac{V}{\Omega}$, we convert all reaction rates to finite-volume rates with units s^{-1}. Table 1 shows these rates for the various reaction types described above, as well as for dissociation reactions (taken from the functional form given by Stoller et al. [207]). Material constants are given for α-Fe in Table 2. It should be noted that other formulations of stochastic rate theory [131] have used concentration rate equations that are in units of defects$\cdot$m^{-3}, so these equations are only multiplied by V.

By converting reaction rates from mean-field to finite-volume form in this way, we have changed the domain of the problem from an infinite domain (in which arbitrarily low concentrations can be computed) to a finite domain with an integer number of defects of each allowed type. This matches more closely the domain of an OKMC simulation rather than an MFRT simulation, but unlike OKMC the defects within the volume element are not assigned a location. Instead, they are assumed homogeneously distributed within the domain and their reaction rates, which are converted from MFRT, reflect that hypothesis. Therefore, spatial resolution is still missing in this formulation of stochastic cluster dynamics. This obstacle is overcome by the division of the domain into several volume elements, as described in the next section.

3.2.4 Spatially resolved rate equations

So far, reaction rates have been derived for a single finite volume element which is assumed to be spatially homogeneous throughout. This is an approximation of an infinite medium. However, a physically representative prediction of defect evolution in a heterogeneous microstructure, e.g. polycrystals, nano-structured materials, and nano-laminates, can only be accessed through a spatially resolved method. Indeed, the behavior of defects in the neighborhood of grain boundaries, dislocations, and hetero-interfaces is known to be different from the bulk [255, 178, 96, 94, 52, 64, 49, 91, 252]. While traditional approaches

Table 1: Reaction rates for vacancy and interstitial reactions in a finite volume element, size V. N_i indicates the absolute number of species i present in the volume. All rates are in units of s^{-1}. 3D SIA indicates that the SIA cluster is approximated as a sphere that migrates in three dimensions, 1D SIA indicates that the SIA cluster is approximated as a circular dislocation loop that migrates in one dimension. In the migration reaction, species X migrates from volume element i to j, with boundary surface area A_{ij} and separation L_{ij}.

Reaction	Reaction rate (s^{-1})	Equation
Clustering reactions		
$V_n + V_m \rightarrow V_{n+m}$	$\omega(n^{\frac{1}{3}} + m^{\frac{1}{3}})(D_{Vn} + D_{Vm})N_{Vn}(t)N_{Vm}(t)\frac{\Omega}{V}$	(35)
$V_n + I_m \rightarrow V_{n-m}$ or I_{m-n} (3D SIA)	$\omega(n^{\frac{1}{3}} + m^{\frac{1}{3}})(D_{Vn} + D_{Im})N_{Vn}(t)N_{Im}(t)\frac{\Omega}{V}$	(35)
$V_n + I_m \rightarrow V_{n-m}$ or I_{m-n} (1D SIA)	$\left[\left(\frac{m}{b}\right)^{\frac{1}{2}} + \left(\frac{9\pi n^2}{16\Omega}\right)^{\frac{1}{6}}\right]^4 D_{Im}N_{Im}(t)N_{Vn}(t)^2\frac{\Omega^2}{V^2}$ $+ \left(\omega' m^{\frac{1}{2}} + \omega n^{\frac{1}{3}}\right) D_{Vn}N_{Im}(t)N_{Vn}(t)\frac{\Omega}{V}$	(40)
$I_n + I_m \rightarrow I_{n+m}$ (3D + 3D SIA)	$Z_{\text{int}}\omega(n^{\frac{1}{3}} + m^{\frac{1}{3}})(D_{In} + D_{Im})N_{In}(t)N_{Im}(t)\frac{\Omega}{V}$	(35)
$I_n + I_m \rightarrow I_{n+m}$ (3D + 1D SIA)	$Z_{\text{int}}^4\left[\left(\frac{m}{b}\right)^{\frac{1}{2}} + \left(\frac{9\pi n^2}{16\Omega}\right)^{\frac{1}{6}}\right]^4 D_{Im}N_{Im}(t)N_{In}(t)^2\frac{\Omega^2}{V^2}$ $+ \left(\omega' m^{\frac{1}{2}} + \omega n^{\frac{1}{3}}\right) D_{In}N_{Im}(t)N_{In}(t)\frac{\Omega}{V}$	(40)
$I_n + I_m \rightarrow I_{n+m}$ (1D + 1D SIA)	$Z_{\text{int}}^4\frac{\left(n^{\frac{1}{2}} + m^{\frac{1}{2}}\right)^4}{b^2}\times$ $\left(D_{In}N_{Im}(t) + D_{Im}N_{In}(t)\right)N_{In}(t)N_{Im}(t)\frac{\Omega^2}{V^2}$	(41)
2D Diffusion on a surface		
$i + j$ (clustering or annihilation)	$\frac{4\pi N_i N_j}{A}\times$ $\left[\frac{D_i}{2\ln\left(\sqrt{\frac{A}{\pi N_j}}\left(\frac{1}{r_i + r_j}\right)\right) - 1} + \frac{D_j}{2\ln\left(\sqrt{\frac{A}{\pi N_i}}\left(\frac{1}{r_i + r_j}\right)\right) - 1}\right]$	(51)
Dissociation reactions		
$V_n \rightarrow V + V_{n-1}$	$\omega n^{\frac{1}{3}} D_V e^{-\frac{E_b(n)}{k_b T}} N_{Vn}(t)$	(11)
$I_n \rightarrow I + I_{n-1}$ (3D SIA)	$\omega n^{\frac{1}{3}} D_I e^{-\frac{E_b(n)}{k_b T}} N_{In}(t)$	(11)
$I_n \rightarrow I + I_{n-1}$ (1D SIA)	$\omega' n^{\frac{1}{2}} D_I e^{-\frac{E_b(n)}{k_b T}} N_{In}(t)$	(11)
Migration reactions		
$X^i \rightarrow X^j$ (volume element i to j)	$D_X A_{ij}\frac{N_X^i(t) - N_X^j(t)}{V L_{ij}}$	(56)
Implantation reactions		
$0 \rightarrow V + I$	(dpa rate) $\left(\frac{V}{\Omega}\right)$	
$0 \rightarrow (cascade)$	$\left(\frac{\text{dpa rate}}{N_{\text{displaced}}}\right)\left(\frac{V}{\Omega}\right)$	

Table 2: Constants used in Table 1 for calculating reaction rates in SRSCD. Material constants for α-Fe are given.

Constant	Meaning	Value (α-Fe)
Ω	atomic volume	1.182×10^{-2} nm^{-3}
V	single element volume	(variable)
b	Burgers vector	0.287 nm
Z_{int}	SIA absorption bias	1.2 (SIA), 1.0 (V)
k_b	Boltzmann's constant	8.617×10^{-5} eV/K
T	temperature	(variable)

use averaging arguments to treat the impact of grain boundaries and dislocations in homogeneous models, in nano-structured materials this approximation can no longer be made. In addition, defect populations resulting from cascade implantation have been shown to depend on the spatial resolution of the initial cascade state [197, 39, 161]. It is therefore necessary to develop a method that can simulate both large timescales and the spatially resolved structures of nano-structured materials.

It was noted by the original author of stochastic rate theory [83] that the system could approximate spatial resolution by creating several volume elements instead of a single one. Within each volume element, the system is assumed to be 'well-mixed' and therefore spatially homogeneous, but differences in numbers of defects occur between elements. The reaction rates of combination and dissociation are calculated within each element according to the rate equations presented above. To calculate the reaction rates of migration between elements, we begin with a standard gradient-driven diffusion equation (in units of atomic fraction):

$$\frac{dC}{dt} = \nabla \cdot (D \cdot \nabla C) + f(x,t) \tag{53}$$

where $f(x,t)$ accounts for all of the terms discussed in the previous sections.

To convert this equation to a reaction rate for a finite volume, we first integrate over the volume element and apply the divergence theorem. Neglecting $f(x,t)$, this gives:

$$\int_V \frac{dC}{dt} dV = -\oint_S (D \cdot \nabla C) \cdot \vec{n} dS \tag{54}$$

where the second integral is now a surface integral over the boundary of the element.

Multiplying by $\frac{1}{\Omega}$, the left hand side of equation (54) is now $\frac{dN}{dt}$ where N is the absolute number of defects of this type in the volume element. We will refer to this element as i and its neighbors as j, with $j \in [1, 6]$. Assuming the element is rectangular, diffusion is isotropic and constant, and approximating ∇C using the neighboring volume elements, we approximate the surface integral and get:

$$\frac{dN_i}{dt} = \sum_{\text{neighbors}} \left(\frac{DA_{ij}(N_j - N_i)}{VL_{ij}} \right) \tag{55}$$

where A_{ij} is the area of the facet connecting elements i and j and L_{ij} is the distance between the centers of the two elements. Thus the reaction rate for a defect migrating from from element i to element j is given by

$$\textit{reaction rate} = DA_{ij}\frac{N_i - N_j}{VL_{ij}} \tag{56}$$

This reaction is treated similar to all other reactions listed above, with a rate (in units of s^{-1}) for a single defect to migrate from volume element i to j. This approach mirrors that of a finite-element or finite-difference approximation for spatial resolution of mean field rate theory equations, which has been carried out for some systems [161, 162, 64, 247]. The reaction rate associated with inter-element diffusion is included in Table 1.

Using spatially resolved finite volumes in this way, materials such as thin films with free surfaces can be approximated by holding the concentration of defects outside the material equal to zero at the boundaries on one axis and applying periodic boundary conditions on other axes. Cascade implantation can also be simulated using various methods described in Section 3.3. The optimal method for representing cascade damage in this scheme is still an open question, since cascades are not spatially homogeneous and the local density of defects in a cascade is very high. Simulation of cascade damage is discussed in Section 3.3.

3.2.5 Application of the kinetic Monte Carlo algorithm

In order to solve the rate equations presented here in a stochastic way, reactions are chosen and time is iterated in a stochastic manner, instead of using a standard finite-difference

time iteration formulation as in the case of rate theory. It has been proven [83] that this approach correctly solves the master equation for the time evolution of the entire system.

Given an initial set of defects in the system, all possible reactions and their rates can be calculated using the rates in Table 1. Thus, unlike mean field rate theory, only reaction rates for defects present in the system are calculated and only integer numbers of defects are treated. Each reaction μ has a reaction rate a_μ in the system. Therefore, the total reaction rate for the system (in reactions per second) for all reactions is

$$a = \sum_{\mu} a_\mu \tag{57}$$

Thus, as in standard Monte Carlo techniques, the probability that the first reaction after time t in the system will occur between time $t + \tau$ and $t + \tau + \delta\tau$ is given by [83]:

$$P_1(\tau)\delta\tau = ae^{-a\tau}\delta\tau \tag{58}$$

and the probability that the next reaction will be reaction μ is

$$P_2(\mu) = \frac{a_\mu}{a} \tag{59}$$

Therefore, in the simulation, the amount of time that passes before the next reaction is carried out is chosen stochastically by choosing a random number $r_1 \in (0, 1)$ and iterating time by timestep

$$\tau = \frac{1}{a} \ln\left(\frac{1}{r_1}\right) \tag{60}$$

and reaction μ is carried out, with μ chosen by choosing a second random number $r_2 \in (0, 1)$ and finding μ such that

$$\sum_{\nu=1}^{\mu-1} a_\nu < r_2 a < \sum_{\nu=1}^{\mu} a_\nu \tag{61}$$

A derivation of this algorithm can be found in [83] and in Appendix A. A demonstration of the equivalence of the Monte Carlo and traditional deterministic solutions to problems of this type can be found in Appendix B. After each timestep, the number of defects in the

cell is updated for each defect type involved in the reaction chosen. The reaction rates for all relevant reactions are subsequently updated. Thus, if a defect type disappears from the cell during a reaction, all reaction rates associated with that defect type are removed from the list of possible reactions that the system can choose. This greatly reduces the amount of computation required compared to mean field rate theory, and allows arbitrarily sized defects to migrate without creating rate equations that are unmanageable.

Due to the spatial resolution of the system, rates for reactions are calculated within each cell and between each adjacent cell for migration reactions. However, the time iteration is carried out for the entire system at once. Thus, only one possible reaction is chosen from among all volume elements in the system per timestep. A modification of this technique using a synchronous parallel kinetic Monte Carlo formulation is presented in Section 3.4.

3.3 Simulating radiation damage in the form of displacement cascades

Although the basic implementation of SRSCD has been described in Section 3.2, several outstanding challenges remain before simulations of realistic damage conditions can be carried out. Chief among these challenges is the inclusion of displacement cascades into SRSCD simulations. Displacement cascades, produced by PKA atoms with energy large enough to displace many other lattice atoms in their vicinity, are important to defect evolution in irradiated metals because of the spatial correlation between defects in the cascades and the formation of clusters directly in cascades [161, 105, 142, 206, 165, 46, 235, 10, 203]. Therefore, models of radiation damage that simulate cascade implantation conditions must account for these factors. In this work, three methods for simulating cascade implantation in irradiated metals have been developed. In all three methods, displacement cascades are first taken from atomistic simulations and annealed for a very short time (10 ps) in an OKMC simulation in order to allow all reactions automatically triggered by proximity to occur. The resulting stable defects are then implanted into SRSCD simulations using the techniques described below. This methodology is described further in [59].

In Section 3.3.1, an entire cascade is implanted in an SRSCD volume element. The results are shown to be dependent on the volume element size due to the spatial correlations

between defects in the cascade. In Section 3.3.2, cascades are distributed between several smaller volume elements, so that the initial defect densities are correct for a range of volume element sizes. This method shows more stable defect accumulation results as a function of volume element size for small elements. Finally, in Section 3.3.3, an adaptive meshing scheme is developed for efficient simulation of cascade implantation in bulk materials with the goal of simulating large doses and volumes.

3.3.1 Method 1: Single volume element implantation

The first and most direct method of simulating cascade damage in SRSCD is to simply place all stable defects generated by atomistic simulations into a single volume element in SRSCD. However, when using this method, care must be taken to choose the appropriate volume element length. A 20 keV cascade in α-Fe has a diameter of approximately 10 nm. The spatial proximity of defects inside the cascade determines the likelihood of spatially correlated reactions between defects as they diffuse after initial implantation. However, SRSCD assumes that all defects inside a volume element are homogeneously distributed and their spatial correlation is not accounted for beyond the length scale of the volume element. Therefore, the volume element size chosen must roughly match the size of the cascade in order to produce the correct probability of spatially correlated reactions between cascade defects. Elements that are too large will assume a low initial density of defects and too few spatially correlated reactions, and elements that are too small will assume a high initial density of defects and too many spatially correlated reactions. Thus, mesh convergence cannot be obtained using this method for cascade implantation.

To demonstrate the lack of mesh convergence of this method of cascade implantation, simulated cascade implantation in Cu is carried out using a variety of mesh sizes. Defect parameters and allowed reaction are described in Section 3.5.2. The effect of changing the size of the volume element on the profile of vacancy cluster concentrations is shown in Figure 15, and results are compared to the results of Caturla et al. [39] generated using OKMC simulations. For large meshes, the size of a volume element is much larger than the size of a cascade and the simulation produces mesh-independent results that do not match

the results of OKMC. As the mesh gets smaller, the initial defect concentration increases dramatically, changing the initial clustering and annihilation rates for the defects in a given cascade. The optimal mesh size for this simulation is found to be approximately 10 nm, which is similar to the size of a 20 keV cascade. Although this method is used successfully in this dissertation to simulate cascade damage, its limiting influence on mesh size is not desirable and therefore other techniques to cascade implantation have been pursued, as discussed in the following sections.

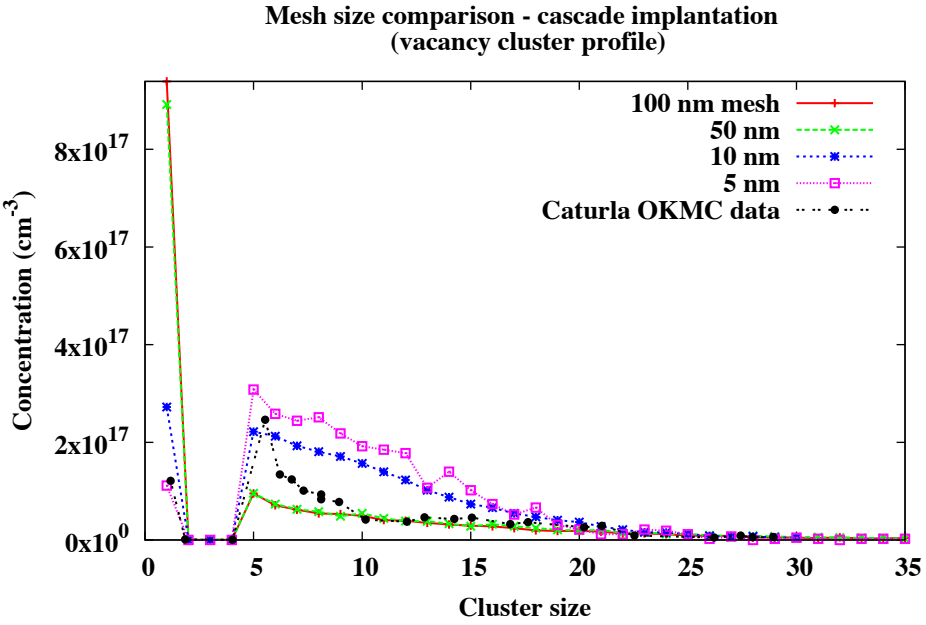

Figure 15: Comparison of vacancy cluster profiles with varying mesh sizes at 8×10^{-4} dpa. The mesh size is critical in determining the initial concentration of defects in a cascade, and thus the mesh must match the cascade size to produce qualitatively correct results.

3.3.2 Method 2: Distributed cascade implantation

The method of implanting cascades in single volume elements has two main drawbacks: first, the spatial distribution of defects within the cascade (with vacancies near the center and self-interstitials near the boundary) is lost. Second, the volume element size needs to be approximately the same as the cascade size in order to achieve the correct initial concentration of defects. This method results in the inability to achieve convergence of results as the mesh size decreases as shown in Figure 15.

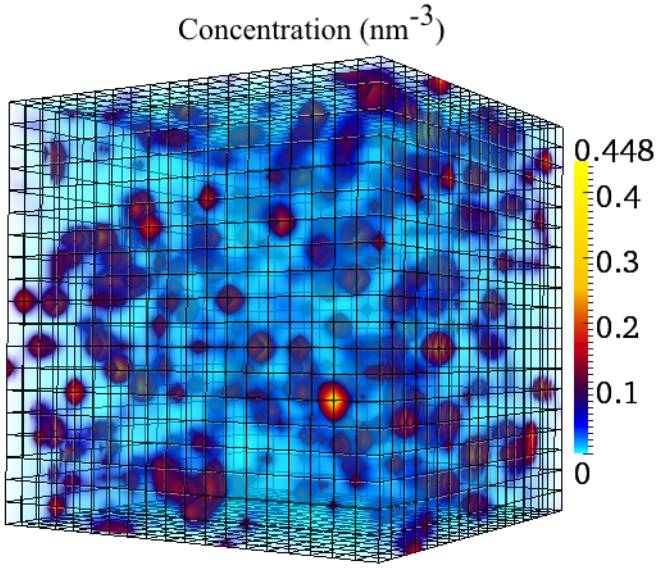

Figure 16: Vacancy cluster distribution inside bulk Fe under cascade implantation to 10^{-3} DPA at 273 K using SRSCD. Volume elements (shown with grid lines) are cubes with side length 5 nm.

In order to more accurately simulate cascade implantation in metals, a new 'multi-element' method is proposed in this work. Here, the coordinates of each defect in the cascade relative to the center of the cascade are recorded. The center of the cascade is randomly placed within the volume of the simulation. The coordinates of each defect in the cascade are then used to identify which volume element each defect is implanted into. Thus, as the mesh size decreases, the cascade is spread among more volume elements and the concentration of defects within each element remains approximately constant. This method allows both stability of the solution and the ability to distribute the defects in the cascade in a non-homogeneous manner throughout the simulation volume. Note that within each volume element, defect distribution is still assumed to be homogeneous and defects do not have individual positions. An example of the spatial distribution of vacancy clusters generated using this method for cascade implantation to 10^{-3} DPA in α-Fe is shown in Figure 16.

The dependence of cascade implantation results on mesh size is shown for the single-element and multi-element methods in Figure 17. At large mesh sizes, both methods under-estimate the concentration of defects in the cascades after initial implantation and SRSCD

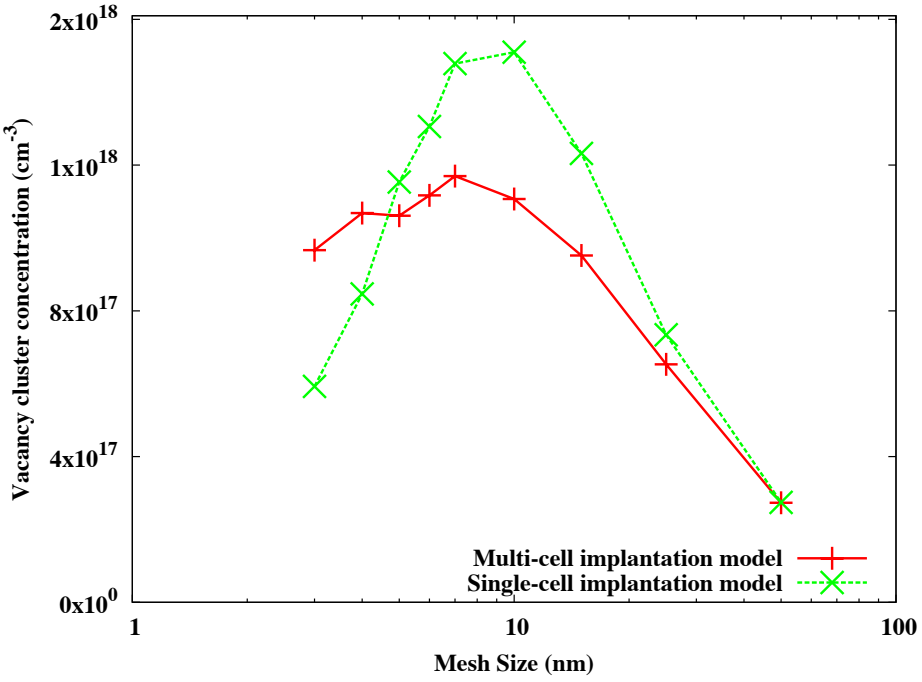

Figure 17: Mesh convergence using the 'multi-cell' cascade implantation method compared 'single-cell' method. Results shown are for 20 keV cascade implantation in Fe at 373 K to 10^{-3} DPA.

results are similar for both methods. As mesh size decreases, the single-element method first overestimates then underestimates the vacancy cluster concentration, while the multi-element method provides a much more stable solution. The differences between the two methods are due to the fact that in the single-element method, defect density within the cascade increases as mesh size decreases while in the multi-element method, defect density remains relatively constant once the mesh size is smaller than the cascade size.

The lack of true convergence of the multi-element method is due to the fact that the reaction rates presented above are derived for a continuous distribution of defects, and therefore some systematic errors occur when the number of defects in a given volume element approaches zero. However, this method does successfully simulate cascade implantation with a range of volume element sizes over a large range of DPA.

3.3.3 Method 3: Adaptive meshing

Both of the previous methods for modeling cascade damage are unsuccessful when the mesh size is greater than the cascade, as the initial density of defects in the cascade is too low in these cases. However, simulations with larger volume elements typically have fewer total reactions and take less computation per step than simulations with many smaller volume elements. Unfortunately, as described previously, fine spatial resolution is necessary to adequately simulate displacement cascade implantation in metals due to spatially correlated reactions between defects in cascades. In this section, an adaptive meshing method is implemented to allow both computational efficiency for simulations of larger volumes and accurate treatment of cascade implantation.

3.3.3.1 Computation as a function of mesh size

It is first useful to understand how computation time can depend on the number and type of defects present in a volume element. The amount of computation per step in the SRSCD algorithm is strongly dependent on the number of possible reactions in the system. An estimate of the upper bound for the number of reactions in a volume element containing n total mobile defect types and m total stationary defect types can be obtained for each of the four broad classes of reactions treated in this simulation: clustering, dissociation, trapping at sinks and traps (with k sink/trap types treated), and element-to-element diffusion.

For binary clustering reactions, there are at most $\binom{n}{2}$ possible reactions between distinct mobile defect types, n possible reactions representing two defects of the same type combining, and mn possible reactions between mobile defect species and immobile defect species. Therefore, the number of clustering reactions dramatically increases when several mobile species are present because the number of clustering reactions varies quadratically with n and linearly with m. Dissociation reactions are typically limited to $m + n$ total reactions, as each defect type has at most one possible dissociation reaction associated with it. The number of reactions representing sinks and traps is typically kn, representing one reaction for each mobile defect type interacting with each sink or trap type. Finally, diffusion of mobile defects between volume elements leads to at most $6n$ reactions, representing six

diffusion directions for each mobile defect species. Table 3 shows the upper bound estimate of the number of reactions present in a volume element.

Table 3: Maximum number of reactions in SRSCD inside a single volume element with n mobile defect types and m stationary defect types.

Reaction type	Number of reactions
Clustering	$\binom{n}{2} + n + mn$
Dissociation	$n + m$
Sinks/traps (k sink/trap types)	kn
Diffusion	$6n$

If a large number of mobile defect species are present within a volume element, most reactions are associated with defect clustering. Conversely, if a small number of defects are spread out over many elements, diffusion, dissociation, and trapping at sinks are the most common reactions. The number of mobile defect species in a given simulation depends strongly on both the parameter set used to characterize defect behavior and the simulated irradiation conditions.

For a simulation consisting of a single volume element with n mobile and m immobile species, clustering reactions dominate the number of available reactions. By contrast, a simulation with the same total volume and defect content consisting of d domains (volume elements) has fewer mobile defects in the same domain and therefore diffusion, dissociation, and trapping at sinks dominate the number of available reactions. In the limit that many volume elements are either completely empty or have only a few defects in them, the number of additional diffusion reactions in the system far outweighs the number of clustering reactions in the single-volume element simulation. In addition, reaction rates for diffusion increase with decreasing volume element length, so that the average timestep is also decreased in these simulations. Therefore, simulations with small volume element sizes required to simulate cascade damage using the previous methods are much more computationally intensive than simulations with large volume element sizes. This motivates an adaptive meshing scheme for cascade implantation, in order to achieve better computational efficiency. Reaction rates and numbers of reactions in adaptive and non-adaptive meshing simulations are compared in more detail in Section 3.3.3.4.

3.3.3.2 Adaptive meshing: formulation

Figure 18 shows a two-dimensional schematic of the adaptive meshing scheme used here in a single volume element. The simulation is carried out using a coarse mesh with volume elements of length $L_c = 80 - 125$ nm. When a cascade implantation event is chosen, a separate fine mesh is created with element length $l_f = 5$ nm. In this work, the fine mesh created contains 6 volume elements per side. The size of the fine mesh was chosen to best reproduce the results given by the uniform meshing method while maintaining reasonable computation times and keeping the size of the fine mesh significantly smaller than the size of a coarse mesh volume element.

This fine mesh is first populated with existing defects from the coarse mesh randomly so that the concentration of defects of various types is the same in the fine mesh and the coarse mesh. The cascade defects are then introduced into the fine mesh, using the coordinates of the cascade defects relative to the cascade center to choose which volume element in the fine mesh each defect is implanted into. This way the spatial correlation between the defects in the cascade is preserved with resolution determined by the fine mesh element length.

After implantation, the entire system (both fine mesh and coarse mesh) is simultaneously evolved in time using the Monte Carlo algorithm, allowing defects to diffuse between the fine mesh and coarse mesh. Once the total reaction rate for all reactions within the fine mesh reaches a low threshold, all of the remaining defects in the fine mesh are deposited into the coarse mesh and the fine mesh is subsequently deleted. At this point, the spatial correlation between defects in the cascade provided by the fine mesh is lost and all defects are assumed to be homogeneously distributed within the coarse mesh. This model therefore assumes that all spatially correlated reactions have already occurred by the time that the fine mesh is deleted. This is the principal tradeoff for the increased numerical efficiency of the adaptive meshing scheme.

The threshold reaction rate for the removal of the fine mesh is treated as a parameter and chosen in order to provide results that most closely match those of the uniform mesh simulation. In this work, the threshold reaction rate within a fine mesh for removal and insertion back into the coarse mesh is 10 times the cascade implantation rate. Note that

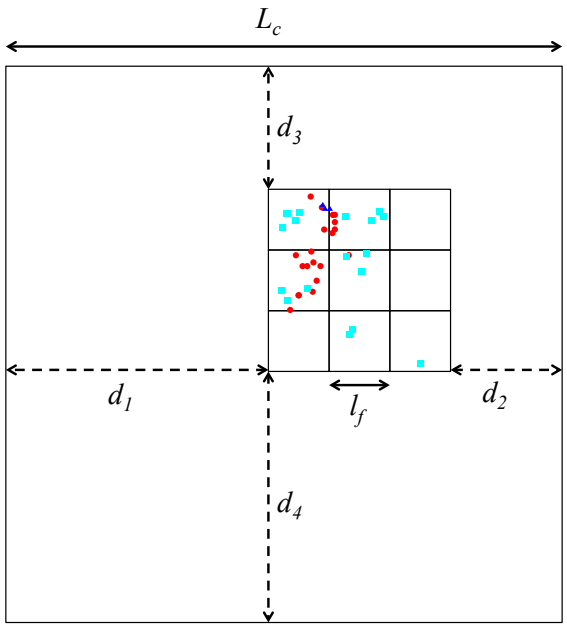

Figure 18: Two-dimensional schematic of a single coarse mesh element with a fine mesh inside. The coarse mesh element is divided into virtual elements for the sake of computing the diffusion between the fine and coarse meshes. The fine mesh is assumed to be randomly placed within the coarse mesh element.

at any given time, several fine meshes can exist in this simulation, but multiple cascades cannot exist within the same fine mesh. At the damage rates studied in this work, the effect of interacting cascades is considered negligible.

A critical parameter in this simulation is the diffusion length used in the reaction rate for diffusion between the fine mesh and the coarse mesh. The fine mesh is assumed to be placed randomly within the coarse mesh, and an effective length $\overline{L}$ is used to find the reaction rate for diffusion between the two meshes. To derive this length, we consider a fine mesh placed randomly in the interior of a coarse mesh element, as shown in Figure 18. The coarse and fine mesh element lengths are labelled L_c and l_f, respectively. The total fine mesh has length nl_f, where n is the number of elements along the length of the (cubic) fine mesh. The distances from the edges of the fine mesh to the edges of the coarse mesh element are labelled d_i, with $i \in [1, 6]$ (only two dimensions shown in Figure 18). The area of a single face of a fine mesh element is a_f, and the total area of the fine mesh is $A_f = 6n^2 a_f$.

In general, the diffusive flux of a single defect species with diffusivity D between rectangular volume elements i and j sharing a face area A_{ij} is given by:

$$flux = \frac{DA_{ij}(c_i - c_j)}{L_{ij}} \tag{62}$$

where L_{ij} is the distance between the centroids of i and j perpendicular to the normal of the shared face. Therefore, the flux from a fine mesh element on the exterior of the fine mesh to the coarse mesh is given by:

$$flux = \frac{Da_f(c_f - c_c)}{\overline{L}} \tag{63}$$

where c_f is the concentration of a given defect species in the fine mesh element, c_c is the concentration in the coarse mesh element, and $\overline{L}$ is an effective length to be determined.

To determine this effective length, we refer back to Figure 18. We will temporarily assume that the concentration of defects in the fine mesh, c_f, is constant over all fine mesh elements. In this case, using equation (62), the total flux of defects from all fine mesh elements on the outer surface of the fine mesh into the coarse mesh element is given by:

$$flux = D(n^2 a_f)(c_f - c_c)\left(\sum_{i=1}^{6} \frac{2}{l_f + d_i}\right) \tag{64}$$

where d_i are determined by the (random) location of the fine mesh inside the coarse mesh such that $d_1 + d_2 + nl_f = L_c$ (and similarly for the other d_i). Therefore equation (64) can be rewritten as:

$$flux = D(n^2 a_f)(c_f - c_c)\left(\sum_{i=1,3,5} \frac{2}{l_f + d_i} + \frac{2}{l_f + d_{i+1}}\right) \tag{65}$$

where, from above, $d_{i+1} = L_c - d_i - nl_f$ for $i \in [1, 3, 5]$. Integrating from $d_i = 0$ to $d_i = L_c - nl_f$, the maximum value for d_i, the average value for the diffusive flux over all possible placements of the fine mesh within the coarse mesh is given by:

$$flux = \frac{D(n^2 a_f)(c_f - c_c)}{(L_c - nl_f)^3} \times \sum_{i=1,3,5} \int_0^{L_c - nl_f} \iiint \left(\frac{2}{l_f + d_i} + \frac{2}{L_c - (n-1)l_f - d_i} \right) dd_1 dd_3 dd_5 \tag{66}$$

This reduces to:

$$flux = \frac{D(6n^2 a_f)(c_f - c_c)}{L_c - nl_f} \log \left(\frac{(L_c - (n-1)l_f)^2}{l_f^2} \right) \tag{67}$$

Dividing by $6n^2$ to find the flux out of a single fine mesh face, we can compare this equation to equation (63) to find $\overline{L}$:

$$\overline{L} = \frac{L_c - nl_f}{\log \left(\frac{(L_c - (n-1)l_f)^2}{l_f^2} \right)} \tag{68}$$

In all subsequent simulations, the reaction rate for the flux of defects of a given species out of the fine mesh and into the coarse mesh is given by equation (63) with $\overline{L}$ given by equation (68). Note that the concentrations of defects c_f and c_c are given by the number of defects in the fine and coarse mesh elements divided by the fine and coarse element volumes, respectively, where the coarse element volume has been adjusted to subtract the fine mesh volume.

For the case of diffusion from the coarse mesh into the fine mesh, calculating the diffusion rate from the coarse mesh into each element on the outer surface of the fine mesh using $\overline{L}$ given by equation (68) is computationally expensive due to the large number of volume elements on the surface of the fine mesh. Therefore, when calculating flux from the coarse mesh to the fine mesh, the entire fine mesh is treated as a single element and equation (68) becomes:

$$\overline{L} = \frac{L_c - nl_f}{\log \left(\frac{L_c^2}{(nl_f)^2} \right)} \tag{69}$$

When a defect diffuses from the coarse mesh element into the fine mesh in this way, it is randomly placed within one of the fine mesh elements. This procedure allows computation

of only one reaction rate for each defect type diffusing into the fine mesh.

The effective length $\overline{L}$ given in equation (68) is similar to the value given by simply placing the fine mesh in the center of the coarse mesh element, $\overline{L}_{\text{center}}$, for the simulation parameters chosen in this work. However, as the coarse mesh length L_c becomes large (assuming constant fine mesh length l_f), the ratio $\overline{L}/L_c$ approaches 0 while the ratio $\overline{L}_{\text{center}}/L_c$ approaches 1/4. Therefore, using the value of $\overline{L}$ presented here instead of $\overline{L}_{\text{center}}$ would have a significant impact on results in cases where the coarse mesh is much larger than the fine mesh.

3.3.3.3 Adaptive meshing: performance

Three metrics are used to study the effectiveness of the adaptive meshing procedure. First, 20 keV cascade implantation in bulk Fe is carried out at various temperatures to 10^{-4} DPA. The percent of implanted vacancies retained and annihilated by recombination with self-interstitials are computed at each temperature using both the adaptive meshing procedure and a uniform 5 nm mesh. Second, 20 keV cascade implantation is again carried out at 353 K up to 10^{-2} DPA using both the adaptive meshing procedure and a uniform 5 nm mesh. The concentration of vacancies and vacancy clusters is compared between the two methods. Third, the cluster profiles produced in SRSCD are compared between the uniform and adaptive mesh simulations at a dose of 10^{-4} DPA with an elevated density of traps for SIA loops compared to the density used in other simulations in this work (100 ppm instead of 30 ppm, see Section 4.4.4 for discussion). The reason for this choice is that the increased concentration of SIA loops provided by the increased trap density allows better comparison between the two methods. The results of all three metrics are shown in Figure 19. The results show good agreement over the range of temperatures and doses studied. The difference between the vacancy concentrations given by the two methods at high doses seen in Figure 19b is likely due to the loss in spatial correlations between defects in the adaptive meshing algorithm when fine meshes are deleted from the system, as discussed previously. This is a limitation of the adaptive meshing method.

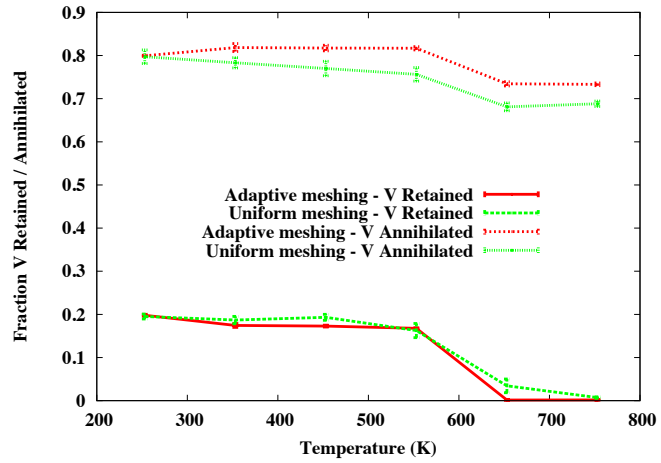

(a)

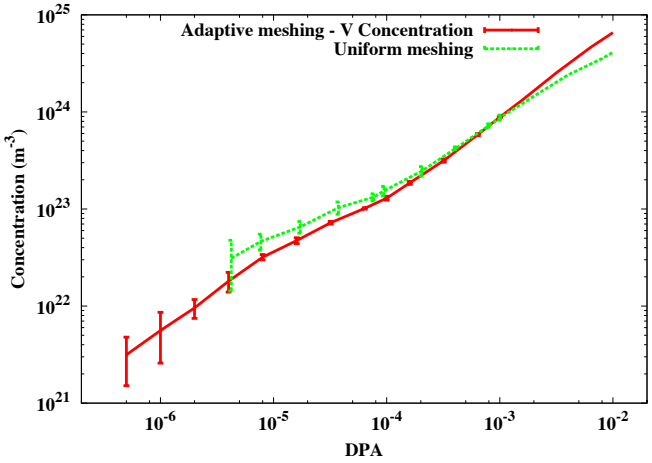

(b)

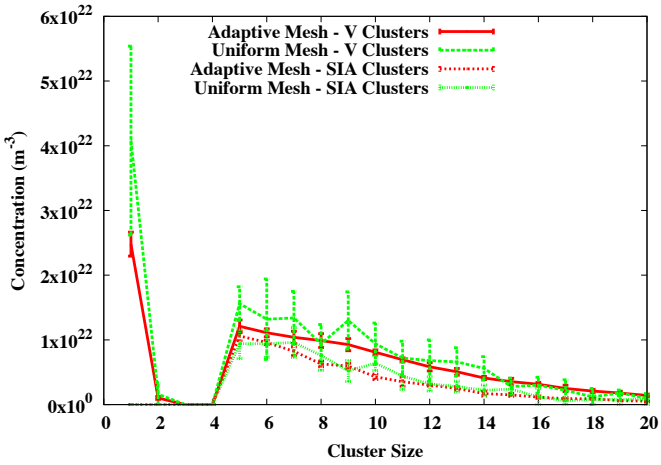

(c)

Figure 19: Comparison of adaptive meshing and uniform meshing procedures with 20 keV cascade implantation in Fe: 19a percent vacancies retained and annihilated with self-interstitials at various temperatures after 10^{-4} DPA implantation, 19b concentration evolution of vacancies and vacancy clusters at 353 K, and 19c density profiles for SIA and vacancy clusters at 10^{-4} DPA.

3.3.3.4 Computation time

The use of adaptive meshing in this study is a key factor in reaching total doses and simulated volumes that allow these simulations to be compared directly to experiments. To demonstrate the computational efficiency gained with this procedure, 20 keV cascade implantation is carried out to 10^{-4} DPA at 343 K inside a 300 nm cube using adaptive meshing and inside a 100 nm cube using a uniform 5 nm mesh. For the case of the uniform mesh, all counts of reactions and reaction rates are multiplied by 27, the volume difference between the two simulations. The total numbers of reactions of each type listed in Table 3 and the average reaction rates are shown in Figure 20. Figure 20a shows that the reaction rates in the simulation with the uniform 5 nm mesh are greater than for the adaptive meshing method for all reaction types listed in Table 3, and in some cases more than an order of magnitude greater. Figures 20b and 20c show the evolution of the number of reactions of each type as a function of dose in both methods. Again, the uniform mesh has a higher total number of reactions. In addition, the fraction of clustering reactions in the uniform 5 nm mesh is significantly lower than in the adaptive meshing method because of the lower probability that multiple defects are in the same volume element. Both methods show a maximum in the number of diffusion and dissociation reactions as the number of diffusive species saturates and more defects become immobile as larger clusters grow.

When comparing computation times of the two methods, the computational gain provided by the adaptive meshing method varied from a factor of approximately 24 at 10^{-4} DPA to 7.5 at 10^{-3} DPA. Note however that the relative speed of each method depends strongly on the numbers and rates of reactions of the various types shown in Figure 20 so that the speedup may not be constant as factors such as simulation volume, temperature, and other variables change. This can be seen Figures 20b and 20c, as the number of reactions of different types evolves differently in the adaptive and uniform mesh simulations as dose increases. In particular, the number of clustering reactions is very low in the simulations with a 5 nm uniform mesh, while the number of these reactions increases significantly in the adaptive meshing simulations due to the greater likelihood that multiple mobile defects will occupy the same volume element in these simulations.

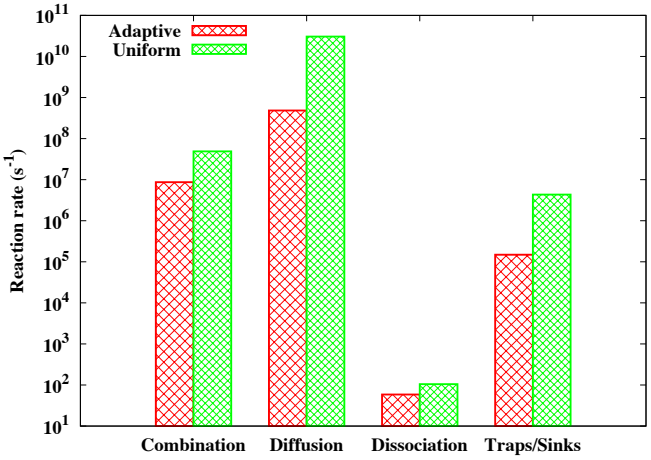

(a)

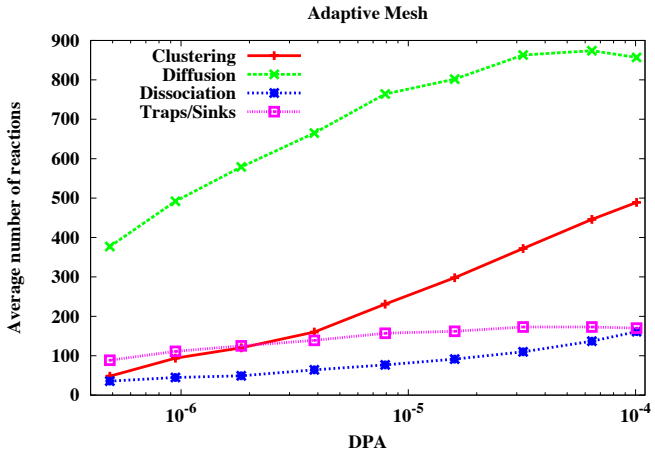

(b)

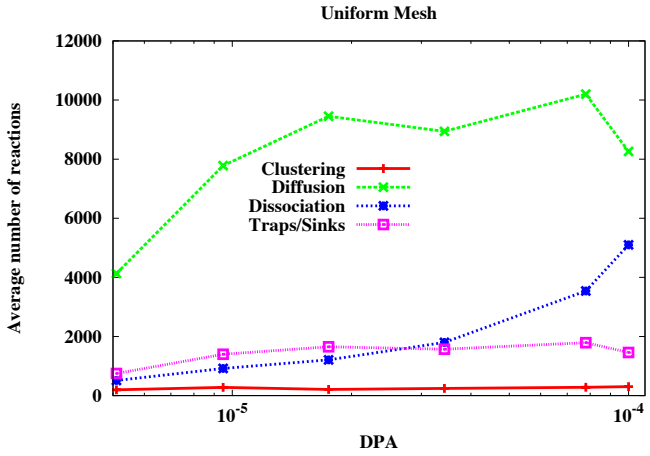

(c)

Figure 20: Comparison of SRSCD simulations of 20 keV cascade implantation in a 300 nm cube to 10^{-4} DPA using adaptive and uniform meshing methods. 20a: comparison of total reaction rates from the four types of reactions modeled in this work. 20b and 20c: comparison of numbers of reactions of each reaction type as a function of DPA using the adaptive and uniform meshing methods.

Trends for computation time in SRSCD using the adaptive meshing scheme as a function of total dose, dose rate, and volume element length are shown in Figure 21, using a total dose of 10^{-3} DPA in Figures 21b and 21c. These results are dependent on both the specific implementation of the SRSCD algorithm used in this study as well as the computational power available to the authors. Therefore, the results shown in Figure 21 should be thought of as trends only.

Computation time increased in a consistent fashion as a function of both total dose and volume element length, as shown in Figures 21a and 21c. The dependence of computation time on dose rate is much more complex, as shown in Figure 21b. This is due to the fact that many competing effects change occur simultaneously as dose rate changes. From 7×10^{-13} to 7×10^{-7} DPA/s, two competing processes occur: lower dose rates mean mobile defects can take more diffusive steps in between cascade implantation events, which serves to increase the computation time. However, at lower dose rates the number of mobile defects is also lower on average, decreasing the number of clustering reactions and making computation faster. For the set of parameters chosen here, these effects result in a slightly increasing computation time with dose rate, although this trend may change as other parameters such as temperature change. From 7×10^{-6} to 7×10^{-4} DPA, a different trend dominates: at higher dose rates, fewer large vacancy clusters are formed. This indicates fewer clustering reactions and therefore faster computation times. Finally, at 7×10^{-3} DPA, the computation is dominated by the fact that new cascades are formed so quickly that the number of fine meshes present in the simulation is high. This causes additional computation as the program has to search both fine and coarse meshes for reactions.

Overall, computation time is more strongly effected by total dose than dose rate, as changing the dose rate by several orders of magnitude changes the computation time by less than an order of magnitude. In addition Figure 21b shows that, the dependence of computation time on simulation parameters is very complex as several effects can increase or decrease computation time.

The average timestep is relatively constant for a given simulation in SRSCD because diffusivities of the various defects modeled here differ by many orders of magnitude and

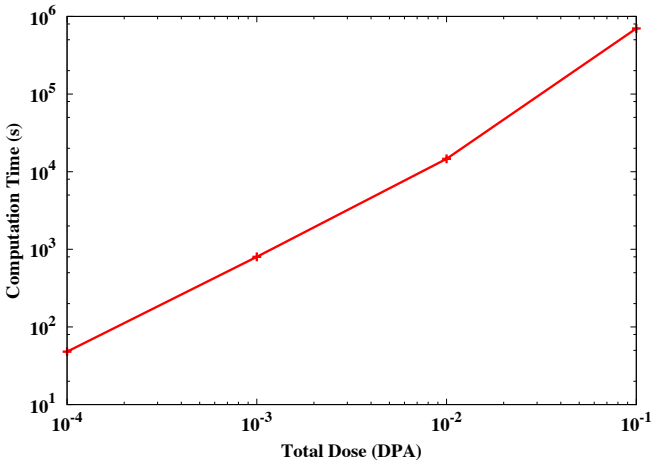

(a)

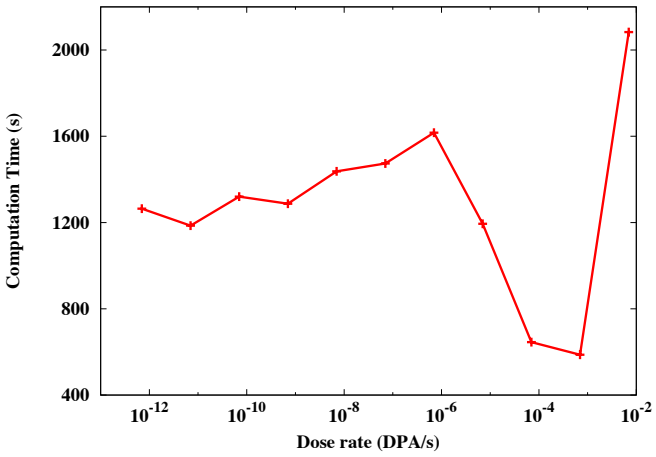

(b)

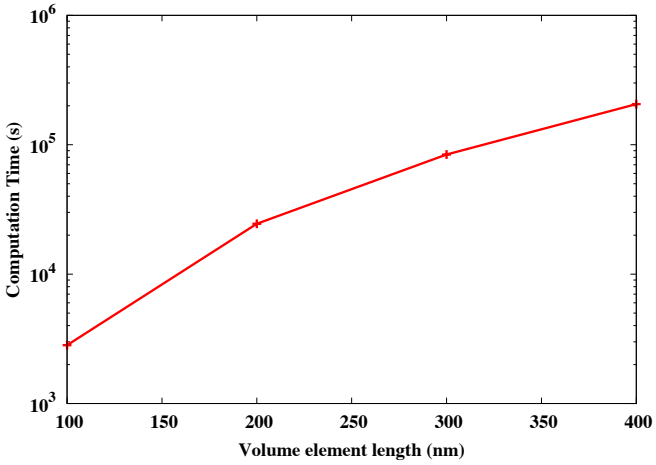

(c)

Figure 21: Computation time in SRSCD using adaptive meshing as a function of total dose (21a), dose rate (21b), and volume element length (21c). A total dose of 10^{-3} DPA is used in Figures 21b and 21c.

Table 4: Comparison of simulation box sizes, computation times, and number of steps of SRSCD simulations using the adaptive meshing algorithm. Results of these simulations are presented in the following sections.

Final dose (DPA)	Simulation size (nm)	Computation time (s)	Number of steps
10^{-4}	$300 \times 300 \times 300$	6.7×10^2	4×10^6
10^{-3}	$200 \times 200 \times 200$	2.2×10^3	9×10^6
10^{-2}	$160 \times 160 \times 160$	1.5×10^4	4×10^7
10^{-1}	$160 \times 160 \times 160$	7.0×10^5	3×10^8

therefore the timestep is largely determined by the fastest reaction in the system, in this case diffusion of small SIA loops. Therefore a large number of reactions may be required to simulate experimentally relevant doses. The number of reactions required to reach these doses is given in Table 4.

Using the adaptive meshing scheme described here, simulations of cascade implantation in bulk α-iron are computationally feasible up to a total dose of 10^{-1} DPA. The simulation volumes of the SRSCD simulations performed in Section 4.4 are varied depending on the total dose in each simulation, in order to achieve greater volume at lower doses and greater computational efficiency at higher doses. The box sizes and computation times for the simulations used to generate the data in Section 4.4.5 are given in Table 4. For comparison, OKMC simulations of the same experimental conditions have been carried out using simulation volumes of $100 \times 100 \times 100$ nm [200] and $100 \times 115 \times 130$ nm [102, 101], but computation times are not reported.

3.4 Synchronous parallel SRSCD

To reach large simulation volumes one necessarily needs to implement tools such as SRSCD, OKMC, and cluster dynamics in parallel. In a deterministic model (cluster dynamics), such implementation is straightforward as each parallel domain will explicitly march in time with the same time step. However, in the case of kinetic Monte Carlo approaches the problem is far more complex because the time increment at each step is a weighted random choice based on the allowed reactions in the system. Therefore, domains running in parallel may become asynchronous, making reactions such as defect diffusion from one to the other difficult to properly carry out. In order to address this problem, a synchronous parallel

kinetic Monte Carlo algorithm has been developed by Martínez et al. [136] in which a single time increment is chosen for all processors and the possibility of choosing null events is added to the KMC algorithm. Although this algorithm has been implemented for OKMC and lattice kinetic Monte Carlo (LKMC) systems [136, 137, 134], it has not been applied to the SRSCD methodology.

The synchronous parallel kinetic Monte Carlo method of Martínez et al. [136] has been developed to avoid asynchronous time evolution in multiple domains which can occur in parallel kinetic Monte Carlo methods. In this method, the total volume is divided between D domains. Therefore, X_i^d and A_μ^d represent the population of species X_i in domain d and the reaction rate of reaction R_μ^d in domain d, respectively, with $\mu \in \{1, ..., M\}$, $i \in \{1, ..., N\}$, and $d \in \{1, ..., D\}$. Similarly to the kinetic Monte Carlo algorithm presented in Section 3.2, the total reaction rate A^d is computed in domain d:

$$A^d = \sum_{\mu=1}^{M} A_\mu^d \tag{70}$$

The maximum total reaction rate is then found among all domains:

$$A_{\max} = \max_d \{A^d\} \tag{71}$$

In order to carry out the synchronous parallel kinetic Monte Carlo algorithm, a null event R_0^d is then added to the list of reactions in each domain. This reaction represents the possibility of no reaction being carried out in a given domain during a global time step. The reaction rate of the null event A_0^d is defined in each domain as the difference between the total reaction rate in domain d and the maximum reaction rate among all domains:

$$A_0^d = A_{\max} - A^d \tag{72}$$

Therefore the rate of R_0^d is nonzero in all domains with total reaction rate $A^d < A_{\max}$. By adding null events to each domain in this way, each domain has a new total reaction rate A^{*d} with value given by:

$$A^{*d} = \sum_{\mu=0}^{M} A_\mu^d = A_{\max} \tag{73}$$

where here $\mu = 0$ is included in the sum in order to include the null event in the list of reactions. Since the total reaction rate A^{*d} is the same in each domain, the kinetic

Monte Carlo algorithm can choose a single time step for the global system while choosing an independent reaction in each system. This is done by choosing independent random numbers r_1 and $r_2^d \in (0,1)$. These are used to choose a single time step τ for all domains and a separate reaction R_μ^d in each domain d:

$$\tau = \frac{1}{A_{\max}} \log\left(\frac{1}{r_1}\right) \ , \ \sum_{\nu=0}^{\mu-1} A_\nu^d < r_2 A_{\max} \leq \sum_{\nu=0}^{\mu} A_\nu^d \tag{74}$$

The main difference between equations (8) and (74) is the fact that τ is treated as a global time step and that in each domain the possibility of choosing a null event now exists. The addition of null events to the kinetic Monte Carlo algorithm in this way has been proven not to alter the overall time evolution of the system [136], while allowing the choice of a single time step and multiple reactions per step in the entire system. A demonstration that adding null events R_0^d to the system does not alter the time evolution of the system is given for an example problem in Appendix C.

An example simulation of Frenkel pair implantation in 100 nm thin films of α-Fe is carried out to verify the correctness of the synchronous parallel algorithm using a mesh of $10 \times 10 \times 5$ volume elements with element length 20 nm. The free surfaces of the thin film are treated as perfect sinks and boundary conditions are periodic in all other directions. This thin film is implanted with Frenkel pairs at room temperature to 10^{-3} dpa at a dose rate of 7×10^{-7} dpa·s^{-1} using the serial and parallel (64 domains) implementations of SRSCD. Parameters for allowed defects, reactions, diffusivities, and binding energies are the same as in Section 3.4.1.1 and can be found in [60]. Figure 22 shows the evolution of the concentration of vacancies and vacancy clusters in this simulation. No differences can be seen between the simulation results of the two methods.

The term 'domain' used above describes a sub-volume of the simulation volume within which one choice of reaction is made during each step. The smallest size this domain can take in SRSCD is a single volume element, such that a separate reaction is chosen inside each volume element during each step, and the largest size that this domain can take is all of the volume elements ascribed to a single processor. Choosing smaller domains increases the number of reactions at each step but makes null events more likely, and the optimal choice

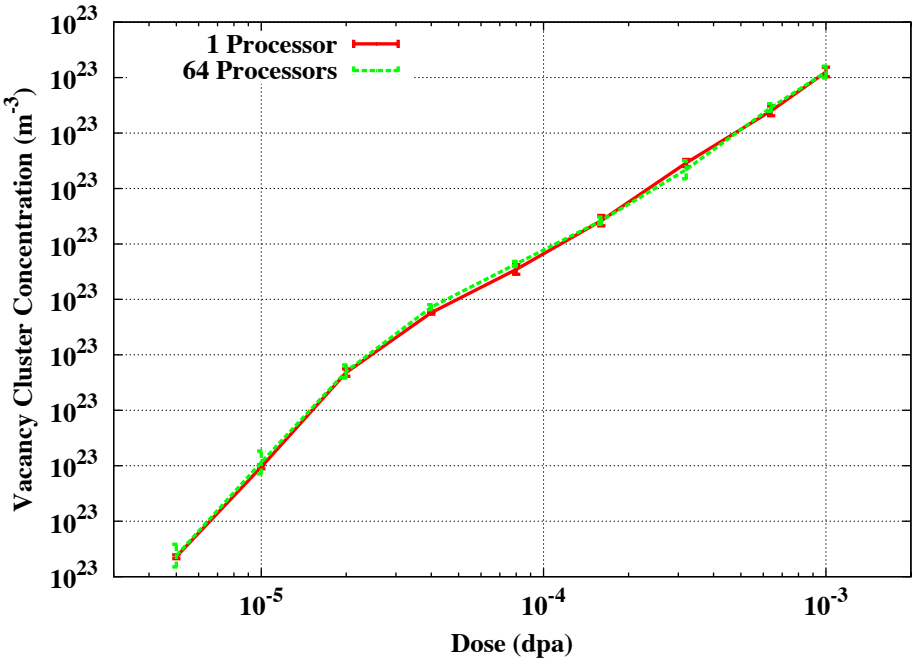

Figure 22: Comparison of the concentration evolution of vacancies and vacancy clusters in a simulated α-Fe 100 nm thin film implanted with Frenkel pairs at room temperature. No differences are seen between the serial and parallel (64 domains) implementations of SRSCD.

of domain size can vary depending on the simulation. Therefore, the parallel performance of SRSCD is analyzed in Section 3.4.1 for the case of one KMC domain per processor, and the impact of this choice is investigated further in Section 3.4.2.

The parallel kinetic Monte Carlo algorithm presented here can cause boundary errors in OKMC methods when two reactions are chosen during the same step in neighboring domains such that two defects move within a pre-defined interaction distance of each other [136]. In SRSCD, boundary errors are caused when defects in neighboring volume elements in different domains exchange positions during the same step. In doing so, the defects are unable to interact because they are never located in the same volume element. However, these errors are extremely unlikely except for unusual cases, for example in a system with two volume elements and two domains only. Therefore, these errors are considered negligible in the simulations performed in this work. Indeed, no difference between defect populations were found in serial and parallel implementations of SRSCD, even in cases with very small total volume per domain.

3.4.1 Scaling of synchronous parallel SRSCD

In this section, the performance of the synchronous parallel SRSCD methodology implemented in this dissertation is compared to serial SRSCD simulations. If a kinetic Monte Carlo simulation with total reaction rate A is divided among D domains using the synchronous parallel algorithm presented in Section 3.4, the best-case scenario for scaling (assuming zero probability of null events in any domain) gives $A_{\max} = \frac{A}{D}$. Therefore, the best-case increase in time step is $\tau_{\text{parallel}} = D \cdot \tau_{\text{serial}}$. Any deviation from this is due to uneven distribution of total reaction rates A^p among the domains, leading to non-zero probabilities of null events being chosen inside some domains at each step. When simulating very stiff problems, defined as problems in which reaction rates A_μ vary by orders of magnitude for different reactions, total reaction rates A^d are likely to vary as well due to heterogeneous distributions of fast-reacting defects in the system. Because of the large number of defect types modeled in simulations of damage accumulation and ion implantation of metals such as α-Fe, as well as the fact that their diffusivities can vary by many orders of magnitude, this problem occurs frequently in simulations of radiation damage accumulation in metals. Therefore, it is important to quantify the computational scaling of both model systems and typical metal irradiation simulations in order to understand the practicality of using parallel SRSCD for simulating radiation defect accumulation in large volumes.

The following scaling simulations were performed on Sandia's High Performance Computing Sky Bridge cluster from Cray, Inc. The cluster has 16 processors and 64GB of RAM per node with 2.6 GHz Intel Sandy Bridge:2S:8C processors. Processor communication is handled through a fully connected QDR InfiniBand interconnect.

3.4.1.1 Damage accumulation in characteristic simulations of irradiated α-Fe: allowed defects and reactions

In Sections 3.4.1.2 and 3.4.1.3, the parallel performance of SRSCD is investigated for two cases: an idealized case in which clustering is not allowed and the only reactions are Frenkel pair formation, diffusion, and recombination, and a case representing realistic defect behaviors. In the latter case, vacancy and self-interstitial clusters are allowed to form, and

displacement cascades are introduced in Section 3.4.1.4. Parameters for defect migration and binding energies are taken from ab-initio and atomistic simulations in α-Fe [74, 198] and can be found elsewhere [60]. Vacancy clusters are assumed to take a spherical shape while clusters of self-interstitials are assumed to form circular dislocation loops. The diffusivity of small vacancy and interstitial clusters is assumed to be three-dimensional, while larger dislocation loops are assumed to glide in one dimension in the direction parallel to their Burgers vector [197, 198]. The reaction rates A_μ for the various allowed reactions between defects depend on the diffusivity of the various defects, their geometry, and the character of their diffusion. Reaction rates for all allowed reactions in this work are found in [60].

In Sections 3.4.1.2-3.4.1.4, scaling is investigated using the case of one KMC domain per processor only. Simulations with one KMC domain per volume element are less efficient when defect clustering is allowed due to the large number of null events chosen when the parameters presented above are applied. Further discussion of the scaling of simulations with one KMC domain per volume element can be found in Section 3.4.2.

3.4.1.2 Weak scaling during Frenkel pair implantation

In this work, weak scaling is used as the principal metric for parallel performance of SRSCD. In weak scaling, the change in computation time is measured as the simulation volume per processor is held constant while the total simulation volume is varied. This metric indicates how effectively the parallel algorithm enables simulations of larger volumes than are feasible using the serial algorithm. The metric used in this work for parallel performance associated with weak scaling, $\eta_w(p)$, is defined as:

$$\eta_w(p) = \frac{t_s}{t_p} \ , \tag{75}$$

where p is the number of processors, t_s is the computation time for a standard serial simulation, and t_p is the computation time for a parallel simulation with p processors and total volume p times the volume of the serial simulation. When $\eta_w = 1$, the system exhibits perfect weak scaling, indicating that the addition of simulation volume and processors does not increase computation time. If $\eta_w < 1/p$, the parallel simulation is slower than the equivalent

simulation in serial, indicating that the parallel algorithm does not allow efficient simulation of large volumes.

In this section, the weak scaling performance of synchronous parallel SRSCD is characterized for two categories of simulations: (1) simulations in which the only allowed reactions in the system are Frenkel pair implantation, vacancy and self-interstitial diffusion, and vacancy-interstitial recombination and (2) simulations in which defect clustering is also allowed, as described in Section 3.4.1.1. All simulations include volume elements with 20 nm length and periodic boundary conditions. Weak scaling simulations are performed with 1000 volume elements per processor.

In order to compare scaling in simulations with different allowed reactions, simulations with and without clustering are started from the same initial defect state. The initial defect state chosen corresponds to the steady-state population of single vacancies and interstitials found when clustering is not allowed for a given dose rate (in dpa·s^{-1}). Steady-state populations of defects are reached before 10^{-4} dpa for all dose rates studied here, and therefore all simulations are started from an initial dose of 10^{-4} dpa. Simulations with no clustering remain at this steady state population while simulations in which clustering is allowed deviate from steady-state as clusters form. Although the latter case does not represent a true physical problem, it was chosen in order to better compare scaling between problems with different allowed reactions. The steady-state population of vacancies and interstitials is shown in Figure 23a for the various dose rates used in this study.

Weak scaling results are shown in Figures 23b and 23c for the cases of no clustering and clustering, respectively. The final dose in all weak scaling simulations is 10^{-3} dpa. In all cases, scaling remains above the $1/p$ limit, indicating that significant computational gains are achieved by using the synchronous parallel SRSCD algorithm. When no clustering is allowed (23b), η_w is almost independent of dose rate indicating that very few null events were chosen in these simulations and the distribution of reaction rates is fairly homogeneous between KMC domains. Therefore all decreases in η_w with increasing numbers of processors are due to increased communication time between processors. By contrast, when clustering is allowed (23c), η_w decreases with decreasing dose rate until 10^{-3} dpa·s^{-1} and then increases

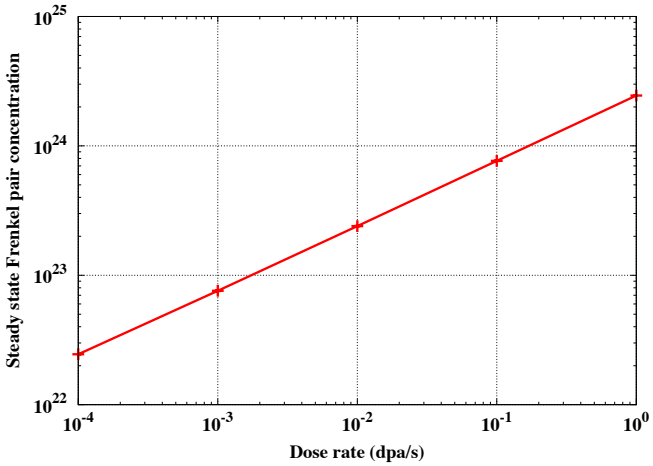

(a) Steady-state concentrations (no clustering)

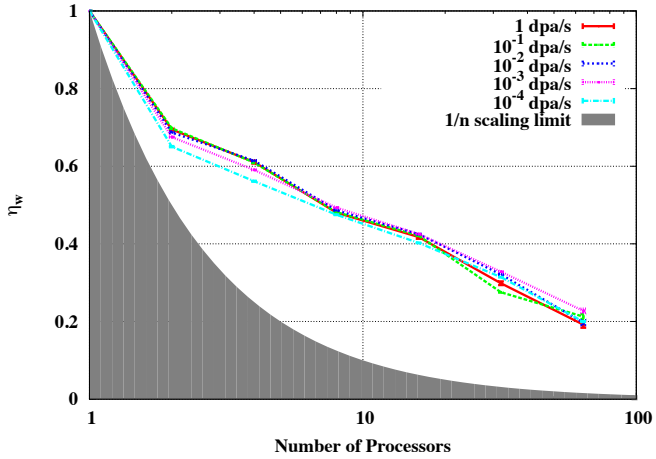

(b) Weak scaling: no clustering

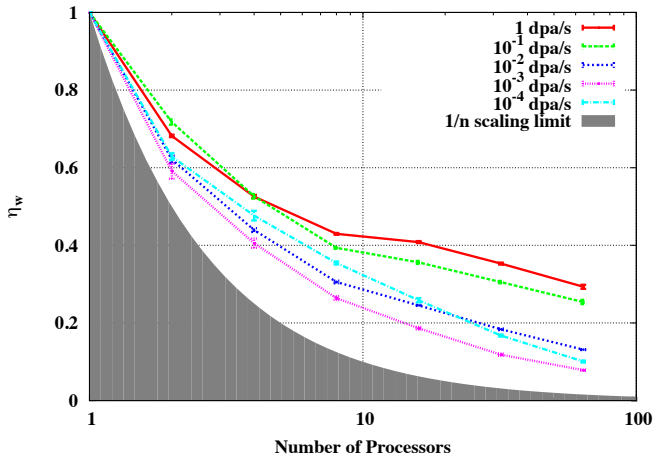

(c) Weak scaling: clustering

Figure 23: Parallel performance associated with weak scaling using several different dose rates corresponding to different initial concentrations of Frenkel pairs. The initial concentration of Frenkel pairs in each simulation is given by the steady-state concentration with no clustering allowed for various dose rates (23a). Results are compared for the cases of no defect clustering (23b) and clustering (23c).

slightly between 10^{-3} and 10^{-4} dpa·s^{-1}. The initial decrease in η_w is due to the increased heterogeneity of reaction rates between processors due to the lower number of defects and the presence of small numbers of fast-diffusing defects like dislocation loops. Below 10^{-3} dpa·s^{-1}, fast-moving loops become scarce again and the population of immobile loops grows, leading to improved scaling as reaction rates become more homogeneous between processors once again.

In summary, weak scaling simulations show that for the simplified system studied here, fast computation of defect evolution is made possible by the synchronous parallel algorithm even for very large total simulation volumes. The scaling of any given SRSCD simulation is dependent on the heterogeneity of reaction rates among processors as well as factors such as the amount of computation time expended choosing reactions and the amount of time spent communicating information between processors.

3.4.1.3 Strong scaling during Frenkel pair implantation

Strong scaling can be used as an additional measure of parallel performance, in order to show the decrease in computation in a simulation with a fixed total volume and an increasing number of processors. In this case, the volume per processor decreases as number of processors increases, and the metric used for parallel performance associated with strong scaling, $\eta_s(p)$, is defined as:

$$\eta_s(p) = \frac{t_s}{pt_p} \ , \tag{76}$$

where, t_s and t_p are the computation time expended in serial and parallel simulations of p processors, using the same total volume. Again, $\eta_s = 1$ indicates perfect strong scaling in which the computation time is decreased by a factor of p when the number of processors is increased by a factor of p. Similarly, $\eta_s < 1/p$ indicates that the simulation is slower in parallel than in serial and thus parallel operation does not improve performance.

The metric $\eta_s(p)$ used to measure the performance of the parallel SRSCD code developed in this work can take values of $\eta_s > 1$. This indicates that when increasing the number of processors by a factor of p the computation time decreases by more than a factor of p, due

to a strong decrease in search time when the number of processors increases accompanied by a relatively small increase in communication time. Here we will discuss the limiting case, in which communication time is zero and reaction rates are homogeneously distributed across volume elements. When m volume elements with n possible reactions per element are present in a single KMC domain, the implementation of synchronous parallel SRSCD used in this study uses an optimized search algorithm for choosing reactions that requires $\mathcal{O}(m)$ computation time to choose a volume element and $\mathcal{O}(n)$ computation time to choose a reaction within that element. In a strong scaling simulation, in which there are m total elements divided among p processors, then the search time per step is $\mathcal{O}(\frac{m}{p})$ to choose a volume element and $\mathcal{O}(n)$ to choose a reaction. In addition, in this ideal case the timestep will scale with p due to the reduction of the total reaction rate in each processor as the number of processors increases. Therefore, we substitute in equation (76): $t_s = \mathcal{O}(m+n)$ and $t_p = \frac{1}{p} \cdot \mathcal{O}(\frac{m}{p} + n)$, giving:

$$\eta_s(p) = \frac{m+n}{\frac{m}{p}+n} \tag{77}$$

In the limiting case that $\frac{m}{p} \gg n$, this reduces to $\eta_s(p) = p$. This represents the maximum scaling behavior of $\eta_s(p)$ for the case of one KMC domain per processor, and demonstrates the possibility of achieving strong scaling greater than 1 seen in Figure 24. As the number of processors increases, this approximation deviates from the ideal case and eventually the increased communication time causes η_s to decrease. In addition, at lower initial defect concentrations the distribution of reaction rates in the system is more heterogeneous and the measured value of η_s decreases. Note that this analysis is only valid for the case of one KMC domain per processor. In the case of one KMC domain per volume element in the idealized system described above the search time per step is $\mathcal{O}(\frac{mn}{p})$ and the timestep is independent of the number of processors, leading to a limiting case of $\eta_s(p) = 1$.

The same simplified test case as shown in Figure 23 is used to investigate strong scaling, in a total simulation volume with 64000 elements. The results of this simulation are shown in Figures 24a and 24b for the cases of single defects only and clustering, respectively. The parallel efficiency is greater than 1 for both the cases initially, but decreases as the

computational loss increases with larger numbers of processors. Similar to the weak scaling results in Figure 23, better strong scaling is seen in the case of diffusion and point defect recombination only than in the case when clustering is allowed.

3.4.1.4 Weak scaling during displacement cascade implantation

Simulations of cascade damage in SRSCD use a pseudo-adaptive meshing scheme [60] in which a fine mesh is introduced when cascade implantation events are chosen in the kinetic Monte Carlo algorithm, allowing spatially correlated reactions between defects in the cascade to occur. When all such spatially correlated reactions have occurred, the fine mesh is discarded and the simulation continues with a coarser mesh. This scheme was developed in order to enable simulations of larger volumes and greater radiation doses than feasible in past SRSCD simulations, as described in Section 3.3.

This methodology causes simulations of cascade damage to exhibit poor parallel performance, as the total reaction rate when a cascade is present can be as much as seven orders of magnitude greater than after the spatially correlated reactions in the cascade have been carried out. This is shown in Figure 25a, which depicts the total reaction rates inside each processor in a two-processor simulation of cascade implantation in α-Fe at room temperature. The total reaction rate inside each processor in the simulation oscillates between 10^9 s^{-1} while a cascade is present and 10^2 s^{-1} otherwise. Due to the Monte Carlo nature of cascade implantation, this oscillation leads to a situation where a cascade is typically present in only one processor at a time, and during that time the other processor chooses null events. Thus weak scaling of this method leads to values of η_w close to the $1/p$ limit, as only a single processor typically chooses a reaction at each step.

In order to mitigate this problem, an explicit cascade implantation scheme has been implemented. In this case, cascade implantation is not treated as a reaction that can be chosen with the Monte Carlo algorithm. Instead, cascades are regularly implanted into all processors simultaneously at regular time intervals. The frequency of cascade implantation is chosen such that the overall dose rate remains the same. Thus, spatially correlated reactions between defects in the cascades can be carried out simultaneously for several

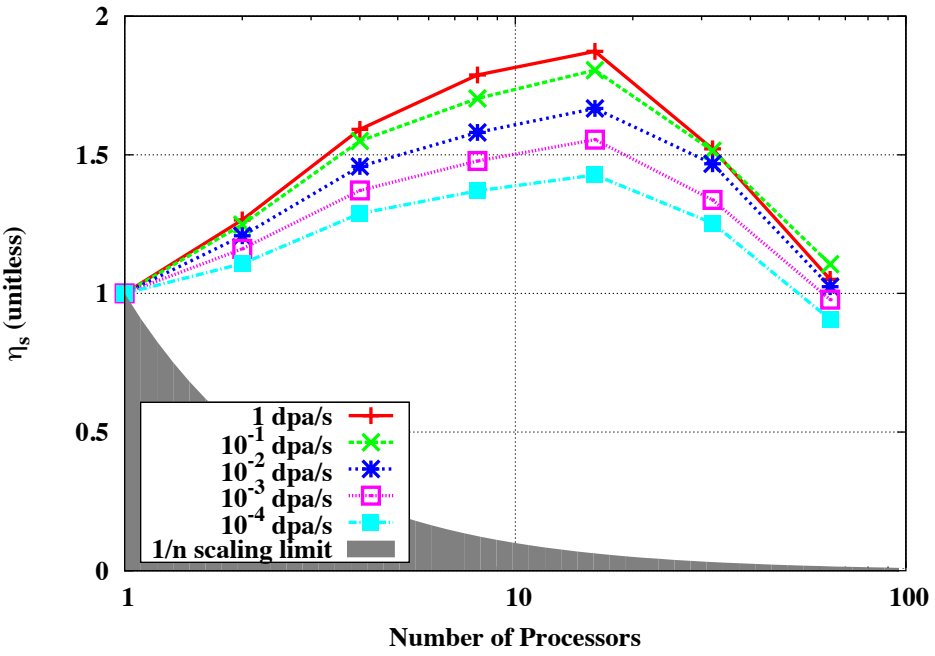

(a) Strong scaling: no clustering

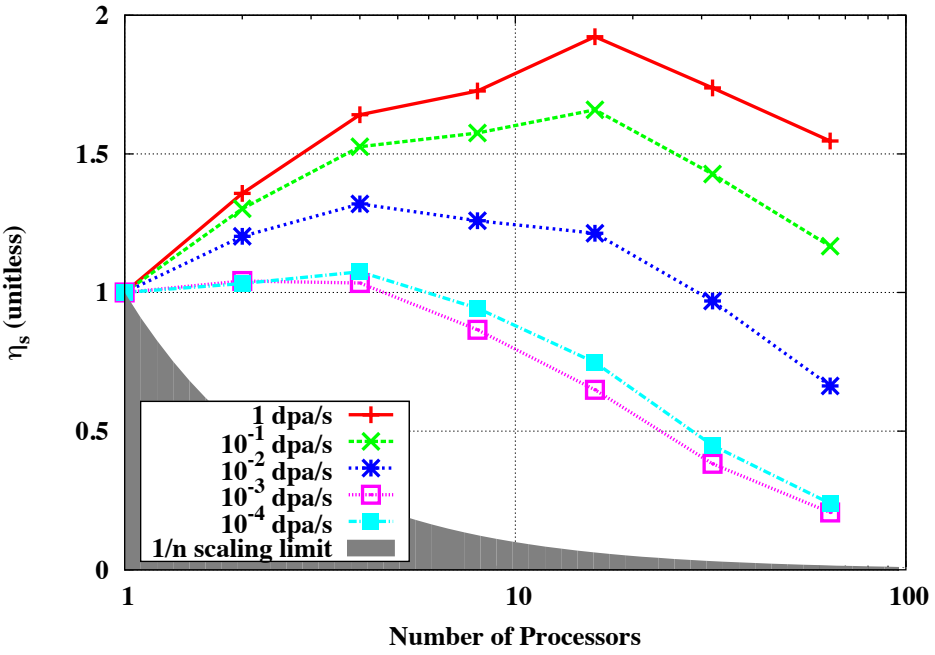

(b) Strong scaling: clustering

Figure 24: Parallel performance associated with strong scaling using several dose rates corresponding to initial concentrations of Frenkel pairs. Results are compared for the cases of no defect clustering (24a) and clustering (24b).

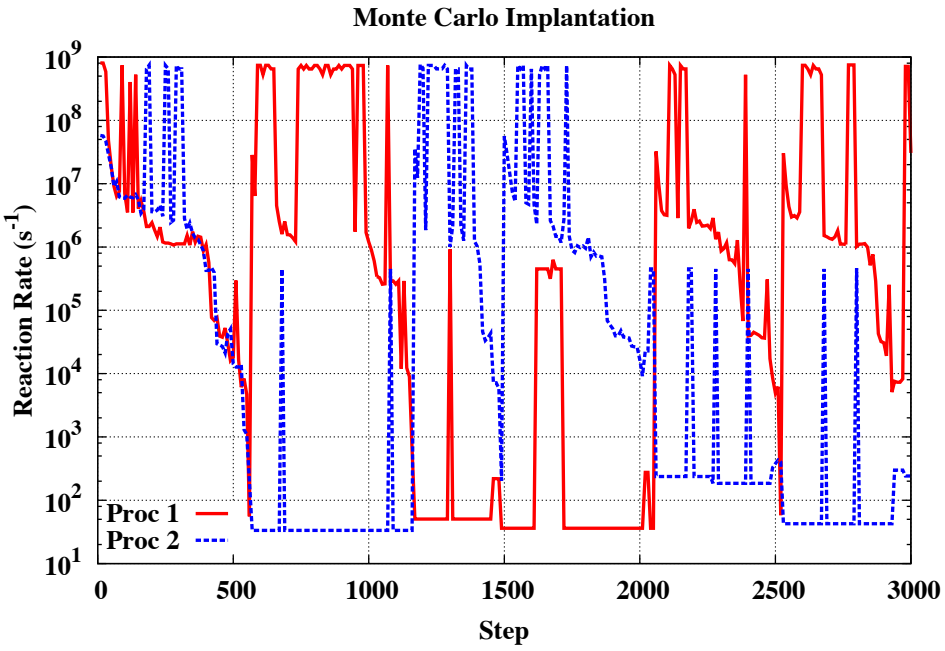

(a)

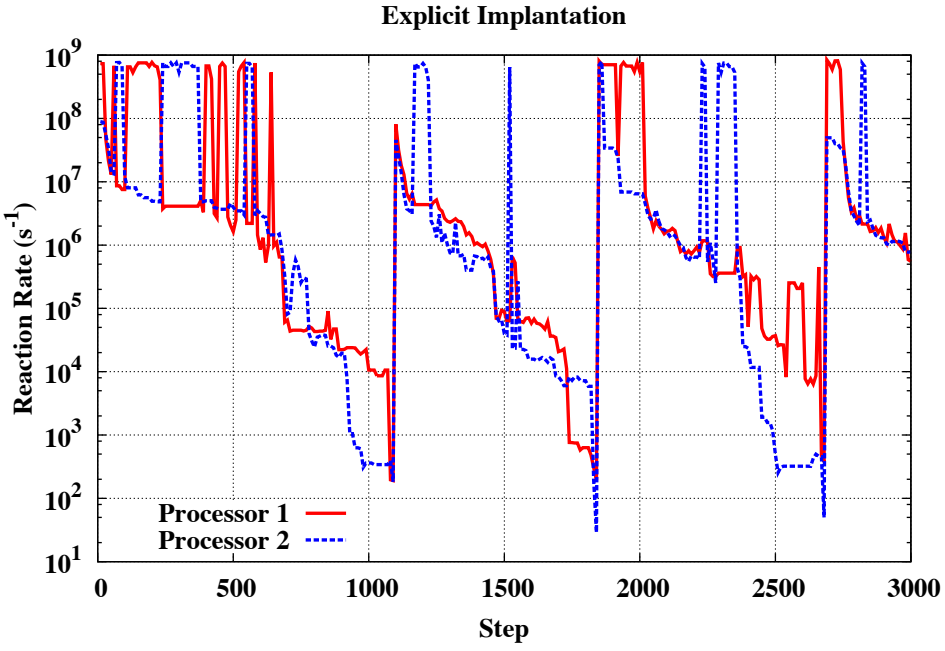

(b)

Figure 25: Total reaction rates inside each processor during the first 3000 Monte Carlo steps in a two-processor cascade implantation simulation, using the Monte Carlo algorithm for cascade implantation (top) or using an explicit implantation scheme at the same dose rate (bottom). Increasing overlap of reaction rates allows for better scaling of parallel SRSCD simulations.

cascades in multiple processors, decreasing the probability that a null event will be chosen. This is shown in Figure 25b, in which the total reaction rates for each processor inside a two-processor system are once again shown. Since cascades are implanted simultaneously in both processors, the amount of overlap between the reaction rates in each processor increases, allowing for better weak scaling.

To demonstrate the computational gain provided by this explicit cascade implantation scheme, the speedup gained by using the explicit method has been calculated for both computation time and number of kinetic Monte Carlo steps:

$$\text{Speedup} = \frac{t_{\text{MC}} - t_{\text{exp}}}{t_{\text{MC}}} \ , \tag{78}$$

where t_{exp} and t_{MC} are the computation time in explicit or Monte Carlo cascade implantation mode, respectively. These simulations are performed with 8 coarse volume elements per processor due to computational constraints with length 80 nm and periodic boundary conditions, and displacement cascades are implanted up to 10^{-3} dpa at 7×10^{-7} dpa·s^{-1} and room temperature. Figure 26 shows the speedup calculated in this way as a function of the size of the simulated system (keeping volume per processor constant as in weak scaling simulations).

Although the explicit implantation scheme does provide a decrease in computation time and number of steps as the system becomes larger, the computational gain from additional processors is not as strong as seen in Sections 3.4.1.2 and 3.4.1.3. This is due to the fact that fast-moving interstitial clusters are more likely to form as a result of the spatial correlation between defects in the cascades, and these defects cause the system to exhibit poor scaling due to their extremely high diffusivities even when the explicit cascade implantation scheme is used. A different choice of material parameters in which dislocation loops are assumed to be immobile, such as in the work of Fu et al. [74], or a first-passage Monte Carlo algorithm [160] could be used to remove these fast-diffusing clusters and would significantly improve the scalability of the explicit implantation method.

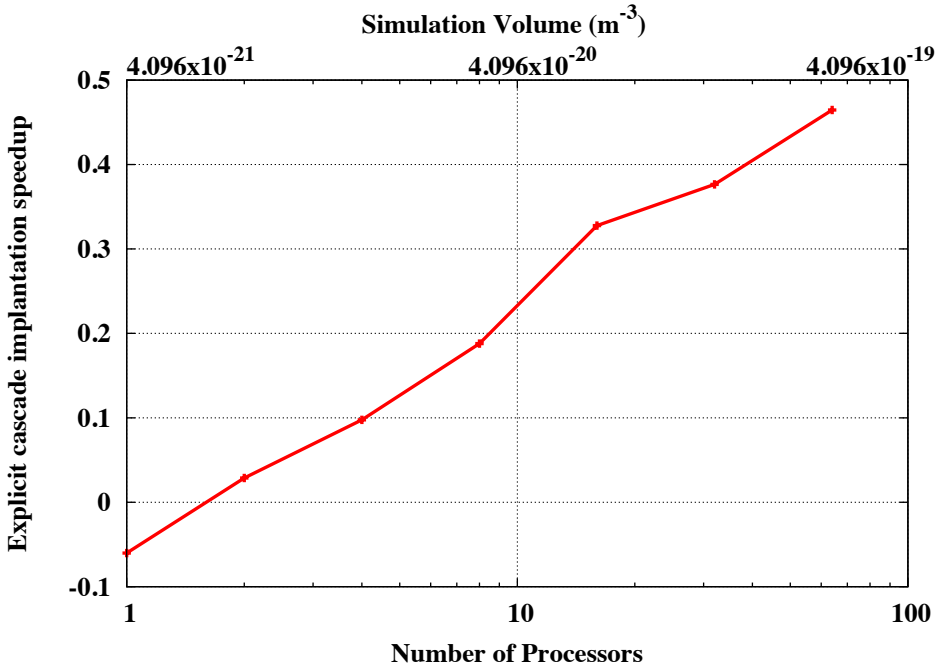

Figure 26: Speedup in computation time using the explicit cascade implantation method vs Monte Carlo cascade implantation for simulations of cascade damage in α-Fe.

3.4.2 Limiting cases of kinetic Monte Carlo domains

In parallel SRSCD simulations, two competing factors can influence computation time: the amount of communication carried out between processors and the time spent searching for which reaction to choose in each KMC domain. Both of these factors are influenced by choosing the size of the KMC domain. Here we discuss the limiting cases of KMC domain sizes: one KMC domain per processor ($\mathrm{KMC_P}$, the choice made for all simulations in Section 3.4.1) and one KMC domain per volume element ($\mathrm{KMC_E}$). These two choices of KMC domain will be investigated under two limiting cases: (1) homogeneously distributed reaction rates, and (2) strongly heterogeneously distributed reaction rates, in which only one fast-moving defect is active in the entire simulation at a time. For simplicity, we assume an ideal case for this analysis: p processors with m volume elements per processor and n possible reactions per volume element. In case (1), we assume that n is equal for all volume elements and therefore the probability of null events is zero. We also assume that the same amount of time T_c is spent in communication between processors each step.

We first investigate case (1). When using the $\mathrm{KMC_P}$ domain, the implementation of

synchronous parallel SRSCD used in this study uses an optimized search algorithm for choosing reactions that requires $\mathcal{O}(m)$ computation time to choose a volume element and $\mathcal{O}(n)$ computation time to choose a reaction. By contrast, when using the $\mathrm{KMC_E}$ domain, the search time for a reaction in that domain is $\mathcal{O}(n)$ but m such searches are made.

In addition to differences in computation required to search for reactions, the average timestep taken by each method is different. In case (1), the timestep chosen when using the $\mathrm{KMC_P}$ domain scales with $\frac{1}{m}$ while the timestep when using the $\mathrm{KMC_E}$ domain is independent of the size of the domain. Therefore, the computation times $T(\tau)_\mathrm{P}$ and $T(\tau)_\mathrm{E}$ required in order to allow the same amount of simulated time τ to pass in the cases of $\mathrm{KMC_P}$ and $\mathrm{KMC_E}$, respectively, are:

$$\begin{aligned} T(\tau)_\mathrm{P} &= m\left[T_c + \mathcal{O}(m+n)\right] \\ T(\tau)_\mathrm{E} &= T_c + \mathcal{O}(mn) \end{aligned} \tag{79}$$

where the first equation has been multiplied by m to indicate that m steps are required for $\mathrm{KMC_P}$ to reach the same simulated time τ reached in by $\mathrm{KMC_E}$ in a single step. In the limiting case of negligible communication time and $n \gg m$, equation (79) gives the same computation time using either method, while in the limit that $n \ll T_c$ or $n \ll m$, $\mathrm{KMC_E}$ is faster. In a typical simulation, $n \ll m$, and therefore $\mathrm{KMC_E}$ is the preferred method in case (1).

This advantage disappears in the case of very stiff problems, or problems in which a few fast-moving defects are heterogeneously distributed throughout the volume (case (2)). This is frequently realized in simulations of defect accumulation in α-Fe, in which a fast-moving SIA loop with diffusivity several orders of magnitude higher than single vacancies and interstitials can form. In this case, for $\mathrm{KMC_P}$ simulations, the reaction chosen at each step will most likely include the fast-moving defect. By contrast, in $\mathrm{KMC_E}$ simulations, the volume element containing the fast-moving defect will choose a reaction involving that defect and all other volume elements will choose null events. Therefore, the average timestep of the two methods is the same as it is dominated by the reaction rates associated with the fast-moving defect. As the probability of the system including such a fast-moving defect

is proportional to m, the timestep of each method scales with $\frac{1}{m}$ in this case. Therefore, assuming equal communication time per step, the total computation times $T(\tau)_{\mathrm{P}}$ and $T(\tau)_{\mathrm{E}}$ required in order to allow simulated time τ to pass are:

$$\begin{aligned} T(\tau)_{\mathrm{P}} &= m\left[T_c + \mathcal{O}(m+n)\right] \\ T(\tau)_{\mathrm{E}} &= m\left[T_c + \mathcal{O}(mn)\right] \end{aligned} \tag{80}$$

where both equations have been multiplied by m due to the $\frac{1}{m}$ scaling of the timestep. In this case, the choice of $\mathrm{KMC_P}$ is superior.

To demonstrate the different scaling situations described in equations (79) and (80), the impact of the choice of KMC domain on computation is compared using weak scaling simulations of Frenkel implantation and clustering shown in Figure 23c. Only two implantation rates are chosen for the sake of comparison, 1 dpa·s^{-1} and 10^{-4} dpa·s^{-1}. At 1 dpa·s^{-1}, the high dose rate causes the reaction rates in the system to remain relatively homogeneous, and the system more closely resembles the one described by equation (79). At 10^{-4} dpa·s^{-1}, reaction rates are more heterogeneously distributed and the system more closely resembles the one described by equation (80). Although the scaling behavior described in equations (79) and (80) represents limiting cases not achieved in these simulations, results still agree with the trends predicted by these equations. This can be seen in Figures 27a and 27b as the weak scaling is higher and computation time is lower for $\mathrm{KMC_E}$ than for $\mathrm{KMC_P}$ at 1 dpa·s^{-1}, while the opposite is true at 10^{-4} dpa·s^{-1}. Figure 27c shows the ratio N_E/N_P of the number of steps in $\mathrm{KMC_E}$ simulations (N_E) to the number of steps in $\mathrm{KMC_P}$ simulations (N_P). At 1 dpa·s^{-1}, $\mathrm{KMC_E}$ simulations take two orders of magnitude fewer steps, allowing a significant reduction in communication time. By contrast, at 10^{-4} dpa·s^{-1}, $\mathrm{KMC_E}$ take less than an order of magnitude fewer steps than $\mathrm{KMC_P}$ simulations while expending significantly more computation time searching for reactions during each step. This is due to the high fraction of null events chosen at 10^{-4} dpa·s^{-1} for $\mathrm{KMC_E}$ simulations.

Due to the fact that SRSCD simulations typically include significant heterogeneity of reaction rates among volume elements, the scaling described in equation (80) more closely describes the typical performance of the algorithm than the scaling described in equation

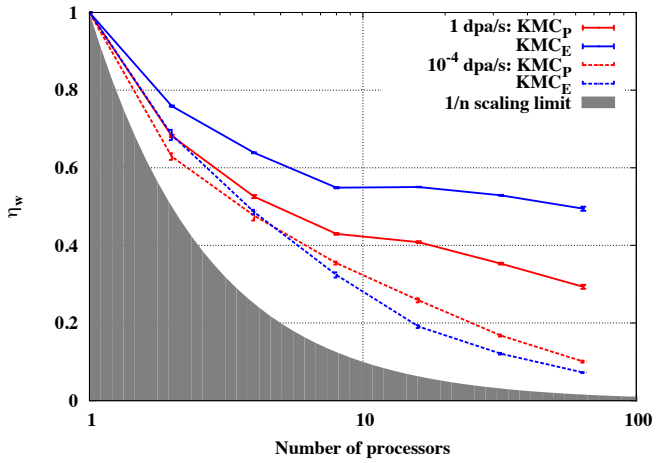

(a)

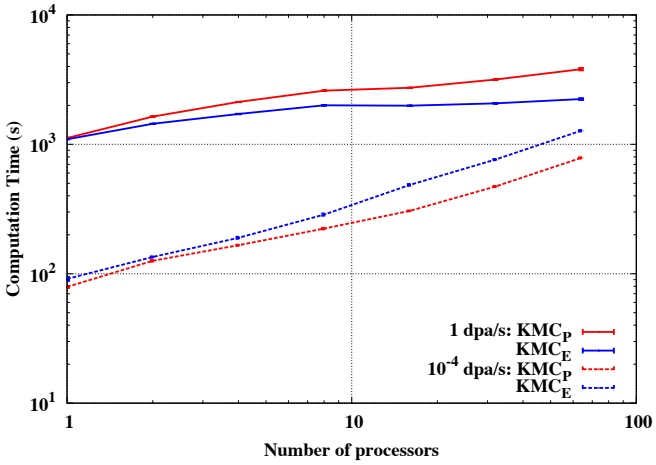

(b)

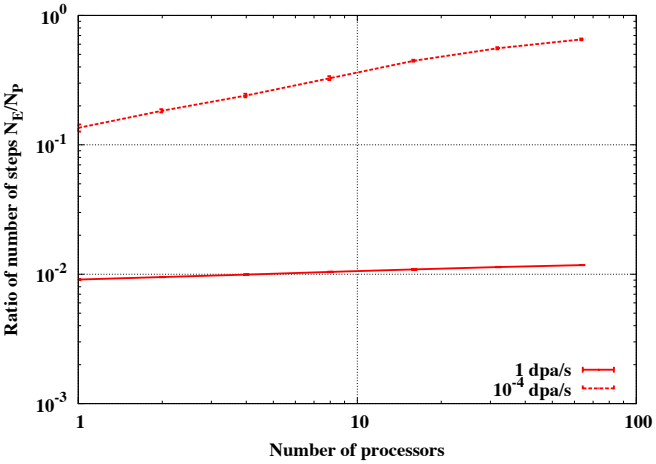

(c)

Figure 27: Weak scaling (27a), computation time (27b), and number of steps (27c) compared between SRSCD simulations with one KMC domain per volume element (KMC_E) and one KMC domain per processor (KMC_P). Results are shown for two dose rates: 1 dpa·s^{-1} and 10^{-4} dpa·s^{-1}, corresponding to cases of homogeneous and heterogeneous reaction rate distributions, respectively. In Figure 27c, the ratio between the number of steps for KMC_E and KMC_P simulations is shown.

(79). Therefore, all results presented in Section 3.4.1 reflect the choice of the KMC_P domain as this is expected to be the most frequently used scheme for implementing synchronous parallel SRSCD. However, this analysis is dependent on many factors such as allowed reactions, temperature, and dose rate. The choice of optimal KMC domain size may vary depending on these factors, as seen in Figure 27. Overall, a combination of increased communication time, deceased time spent searching for reactions, and increased timestep all influence the total computation time when increasing the number of processors for a given simulation of fixed size. Therefore, the best choice of simulation volume per processor and size of KMC domains depends on the particular simulation parameters. In an ideal case, volume elements are subdivided among KMC domains and processors such that the number of null events is minimized while keeping the number of volume elements per KMC domain low enough to avoid computation-intensive searches for reactions.

3.5 Validation of SRSCD by comparison to other simulation techniques

The SRSCD method presented in the previous section acts as an intermediate method between OKMC methods, which are completely spatially resolved, and cluster dynamics/MFRT methods, which are typically spatially homogeneous in nature. It is therefore interesting to compare the results provided by SRSCD to simulations using the same irradiation conditions, allowed defects, and reaction rates as both other methods. In Section 3.5.1, SRSCD is shown to be equivalent to rate theory in simple examples with a limited number of defect types. In Section 3.5.2 and 3.5.3 SRSCD is compared to published results and in-house simulations of damage evolution using OKMC. Finally, comparison with MFRT, OKMC, and experiments are achieved through resistivity recovery simulations of electron-irradiated iron in Section 3.5.4.

3.5.1 Comparison with rate theory: Frenkel pair implantation

The first model chosen for comparison with SRSCD is that of Stoller et al. [207] which compares the results of MFRT with OKMC. In order to simplify the rate equations used, this model treats only single vacancies and single interstitials as mobile. Circular SIA clusters are immobile in this model, so all migration is in 3D and only the corresponding

Table 5: Material and experimental parameters used in the simulation of Stoller et al. [207]. Interstitials were assumed perfectly bound to interstitial clusters and could not dissociate.

Parameters used		
Temperature	373 K	
Atomic volume	$1.189 \cdot 10^{-2}$ nm^3	
Burgers vector	0.2876 nm	
dpa rate	$4 \cdot 10^{-7}$ dpa/s	
Diffusion and binding parameters		
v formation energy	E_f^v	1.6 eV
v diffusion prefactor	D_0^v	$6.02 \cdot 10^{10}$ nm^2/s
v migration energy	E_m^v	0.65 eV
v_n binding energy	$E_b^v(n)$	$E_f^v + (0.2 - E_f^v)\left(\frac{n^{\frac{2}{3}} - (n-1)^{\frac{2}{3}}}{2^{\frac{2}{3}} - 1}\right)$
i diffusion prefactor	D_0^i	$6.02 \cdot 10^{10}$ nm^2/s
i migration energy	E_m^i	0.3 eV

reaction rates with 3D migration are used (see Table 1). In this simulation, Frenkel pairs are implanted homogeneously in an infinite, initially defect-free medium at a constant rate. The vacancy and vacancy cluster populations are recorded as a function of dose (in dpa).

To further validate the results of SRSCD, the simulation is carried out here using both SRSCD and MFRT to verify that the rate equations and constants are being applied correctly. The diffusion and binding parameters for this simulation are shown in Table 5. The concentration of vacancies and vacancy clusters is plotted as a function of dpa and compared to the results of Stoller et al. [207]. Note that spatial resolution is disregarded in the SRSCD model in this simulation due to the spatial homogeneity of the problem. The results of these simulations are shown in Figure 28.

All three sets of results (SRSCD, in-house MFRT, and published MFRT results) are in good agreement. Due to the fact that the MFRT and SRSCD results carried out in this work agree, any differences between these results and the results of Stoller et al. are assumed to be minor. The details of matching these results to the published results of Stoller et al. are considered out of the scope of this work and were not pursued further.

In this simulation, error bars represent simple standard deviations of the result. The variation of the result between simulations depends on the total volume simulated, so standard deviation should not be interpreted as a physical result here. The choice of simulation

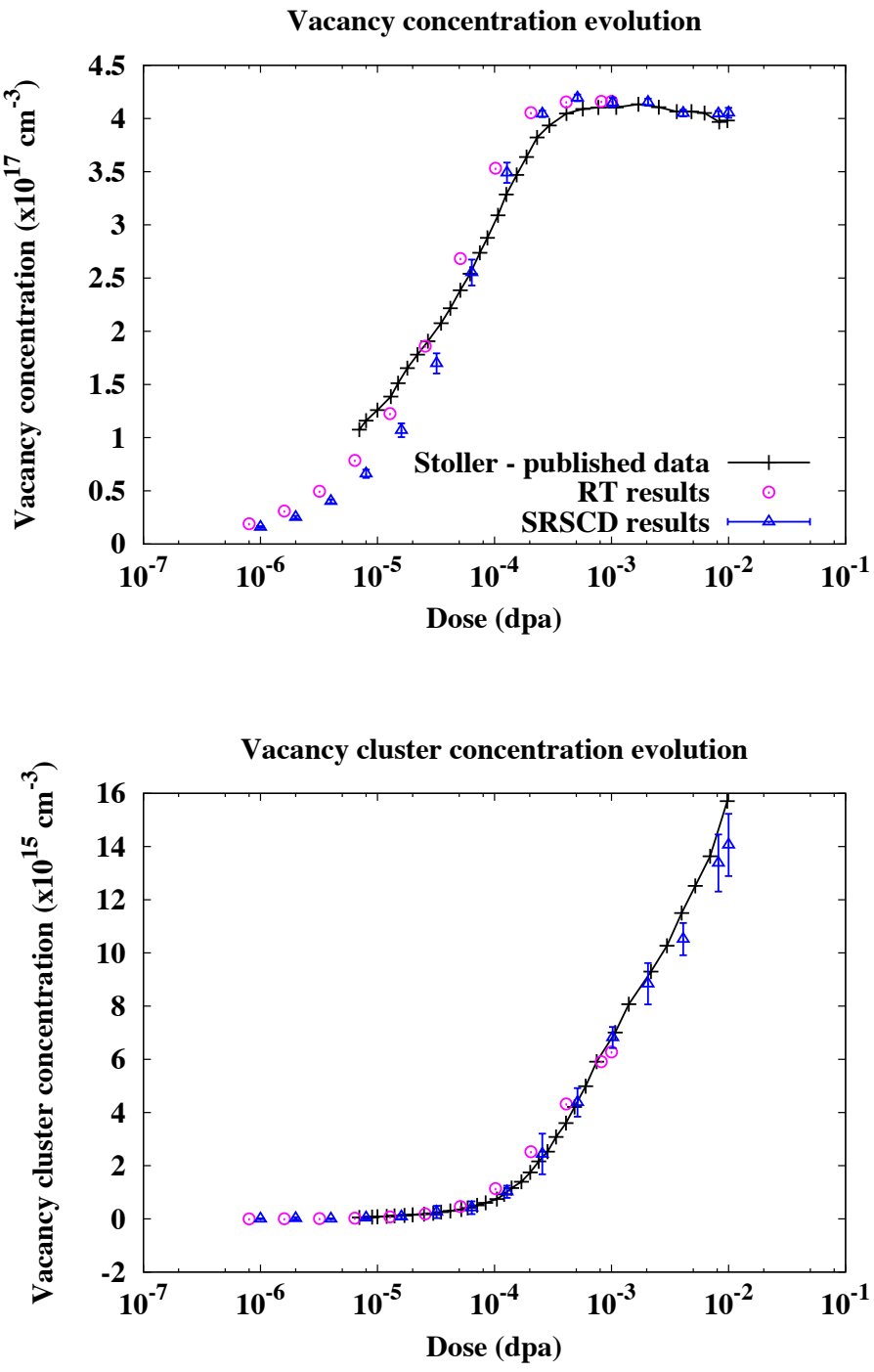

Figure 28: Vacancy and vacancy cluster concentrations as a function of dpa given by Stoller et al. [207], in-house MFRT, and SRSCD.

volume was made in each case to balance computational time with precision of results. It should also be noted that the rate theory results carried out in this study are not extended beyond 10^{-3} dpa, because of computational limitations. The stochastic method, due to its increased computational efficiency, is able to easily reach the larger 10^{-2} dpa range.

Demonstration of the spatially resolved capabilities of the SRSCD model developed here is also carried out by modifying the simulation from an infinite medium to a single-crystal layer of material with thickness 400 nm and free surfaces on either side. The free surfaces are treated as infinite sinks for all migrating defects, so that any defect that migrates out of the free surface is lost from the system. This spatially-resolved system is evolved to a much smaller dpa of 10^{-6} due to computational limitations of MFRT. The spatial resolution in the rate theory model is carried out through the use of a finite difference approximation, and in the SRSCD model through the use of the method described above. The spatially resolved profiles of self-interstitial and vacancy concentrations are shown in Figure 29.

It can be seen that the results of SRSCD and spatially resolved rate theory agree. Again, the ability of the rate theory results to reach large doses and timescales was severely limited by the need for small enough timesteps for the solution to converge. However, timesteps are generated intrinsically in the SRSCD algorithm and rates are not computed for cluster populations that are not present in the material, this method easily reaches much larger doses.

3.5.2 Comparison with OKMC: cascade damage in Cu

One of the main benefits of SRSCD is the ability to allow many species to migrate and cluster, instead of limiting the number of mobile species as in rate theory. Unlike MFRT methods, OKMC simulations also have the ability to take into account the migration of larger defects and one-dimensional migration. Therefore, the performance of SRSCD compared to OKMC is of interest, as SRSCD is significantly faster but necessitates more approximations.

To compare the performance of this method to OKMC, the results of cascade implantation in Cu are compared to those of Caturla et al [39]. In these simulations, 20 keV cascades from a database produced using molecular dynamics simulations are implanted into copper

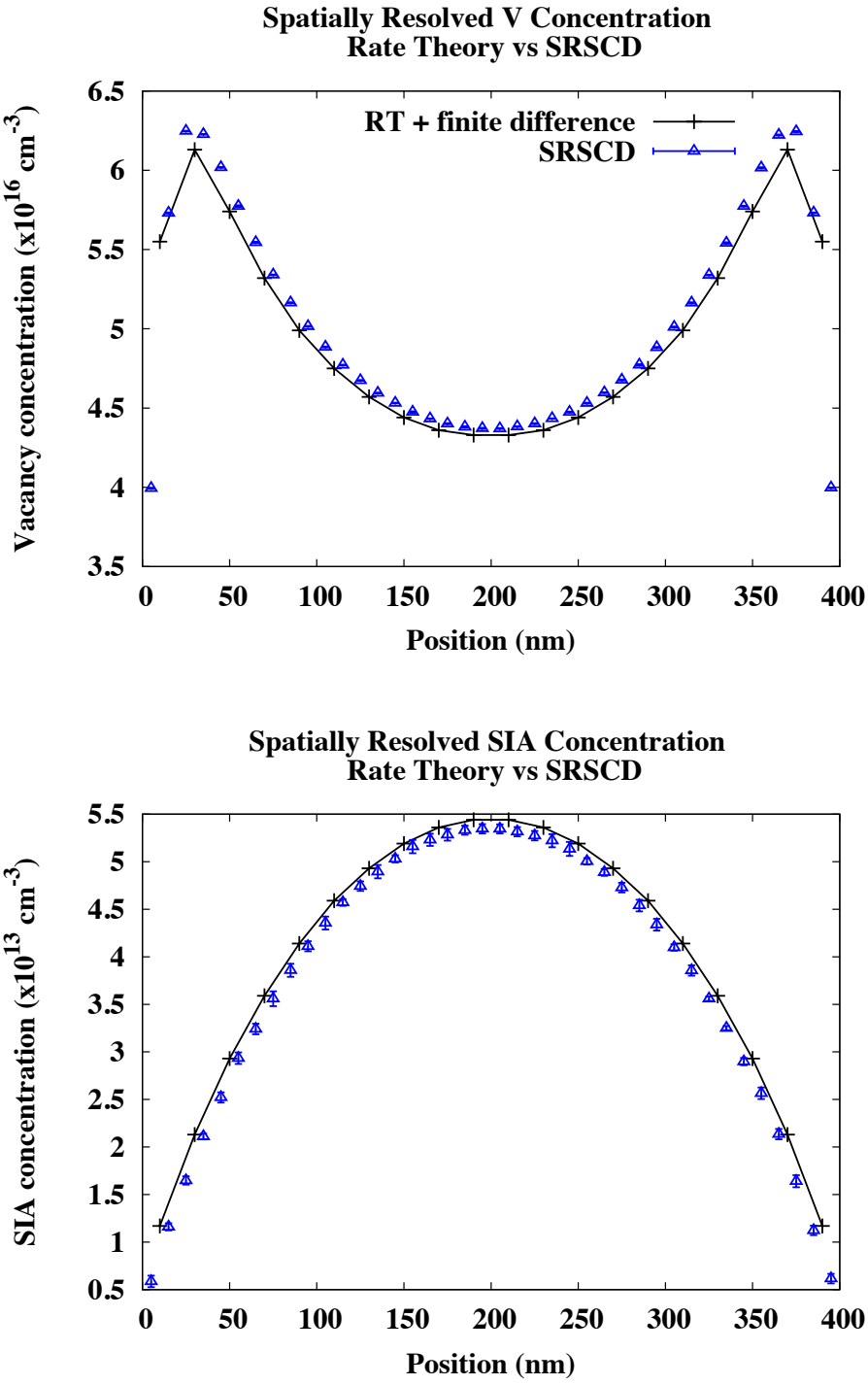

Figure 29: Spatially resolved vacancy and interstitial concentration profiles at 10^{-6} dpa using in-house RT coupled with a finite difference algorithm and SRSCD.

at 10^{-4} dpa·s^{-1}. Unlike the simulations described in the previous section, vacancy clusters up to size 4 and SIA clusters up to size 60 are mobile, with large self-interstitial clusters migrating in one dimension. Additionally, implanted cascades have spatial distributions that impact the clustering properties of the defects produced in the cascades. This is important early in the annealing of a given cascade, as the spatial correlation of defects in the cascades impacts the subsequent time evolution of the system.

The simulation parameters for this study are listed in Table 6. All simulation parameters used in this work are the same as reported by Caturla et al [39]. Migration energies of vacancy clusters are taken Sabochick et al. [180], single-interstitials from Corbett et al. [42], and small SIA clusters from Schober and Zeller [183]. Larger interstitial clusters are assumed to maintain the same migration energy but decrease their diffusion attempt frequency as the size of the cluster grows. The binding energy of vacancy clusters is found by fitting the values for small vacancy clusters from Sabochick et al. [180] to a fitting function, using the formation energy of a vacancy as the binding energy of an infinite sized cluster. The binding energy of small SIA clusters is taken from Schober and Zeller [183], while the binding energy of larger SIA clusters is assumed to be the formation plus migration energy of a single SIA.

In accordance with Caturla et al, interstitial clusters of size $n = 1 - 4$ are treated as spherical defects that migrate in 3D, while larger interstitial clusters are treated as circular dislocation loops that migrate in 1D. This dimensionality applies only to the reaction rates between defects and not the actual migration between volume elements in the simulation. In this case, only 3D migration can be considered. Since FCC and BCC metals have 6 and 4 options for close-packed migration directions ($\langle 110 \rangle$ and $\langle 111 \rangle$ respectively) but only 3 independent axes for migration directions exist, migration between volume elements cannot be restricted such that each face of a volume element permits only one direction of migration. True one-dimensional migration could be achieved in a simple cubic crystal, which has close-packed directions in the $\langle 100 \rangle$ directions, but this is not within the scope of this work.

The limitation of long-range migration to 3D is a main limitation of the SRSCD model

Table 6: Material and experimental constants used in the simulation of Caturla et al. [39] for Cu.

Parameters used	
temperature	340 K
atomic volume	$1.17 \cdot 10^{-2}$ nm^3
Burgers vector	0.36 nm
dpa rate	$1 \cdot 10^{-4}$ dpa/s
grain size	1 μm
Diffusion rates	$D = D_0 e^{-\frac{E_m}{k_b T}}$
single vacancy	$E_m = 0.72$ eV, $D_0 = 2.5 \cdot 10^{13}$ nm^2/s
2-v cluster	$E_m = 0.55$ eV, $D_0 = 3.6 \cdot 10^{13}$ nm^2/s
3-v cluster	$E_m = 0.56$ eV, $D_0 = 1.2 \cdot 10^{13}$ nm^2/s
4-v cluster	$E_m = 0.38$ eV, $D_0 = 1.4 \cdot 10^{13}$ nm^2/s
larger vacancy cluster ($n > 4$)	(immobile)
single interstitial	$E_m = 0.13$ eV, $D_0 = 2 \cdot 10^{11}$ nm^2/s
2-i cluster	$E_m = 0.11$ eV, $D_0 = 1 \cdot 10^{11}$ nm^2/s
3-i cluster	$E_m = 0.2$ eV, $D_0 = 6.6 \cdot 10^{10}$ nm^2/s
4-i cluster	$E_m = 0.1$ eV, $D_0 = 5 \cdot 10^{10}$ nm^2/s
larger interstitial cluster ($n > 4$)	$E_m = 0.1$ eV, $D_0 = \frac{2 \cdot 10^{11}}{n}$ nm^2/s
Binding energies	
2-v cluster	$E_b^v(2) = 0.05$ eV
3-v cluster	$E_b^v(3) = 0.15$ eV
4-v cluster	$E_b^v(4) = 0.28$ eV
5-v cluster	$E_b^v(5) = 0.65$ eV
larger vacancy cluster ($n > 5$)	$E_b^v(n) = 1.2 - 2.121(n^{\frac{2}{3}} - (n-1)^{\frac{2}{3}})$ eV
small interstitial cluster	$E_b^i(2-4) = 1.16$ eV
larger interstitial cluster ($n > 4$)	$E_b^i(n) = 2.62$ eV

compared to OKMC. The effect of this limitation is expected to be more strongly felt in systems that are spatially anisotropic, such as thin films, than systems that are spatially homogeneous over large distances such as the simulation of Caturla et al. In the latter case, the reaction rates between defects are more important than whether defects migrate from one cell to another in a given direction because the overall arrangement of defects is homogeneous.

In the simulation of Caturla et al., the effect of grain boundaries on stopping the long-range migration of fast-moving SIA clusters is accounted for by removing 1D-migrating SIA clusters that migrate a distance greater than 1 μm from the simulation cell [39]. To match this in the SRSCD simulation, interstitial clusters that migrate from one volume element to another are removed from the system with a probability given by the ratio of the volume element size to the grain size. The results obtained are only weakly dependent on the grain size chosen.

This approximation for the effects of grain boundaries was tested by comparison with two other models of grain boundary behavior. In the first model, all defect types can be removed from the system when migrating from one volume element to another, instead of only 1D-migrating SIA clusters. Allowing the simulation to remove all defect types in this way did not significantly change the results, due to the fact that the vast majority of defect migration is in the form of 1D-migrating SIA clusters. In the second model, the grain boundary was simulated by placing free surfaces 1 μm apart (assuming the grain boundary acts as an infinite absorber), which trapped all incident defects. Using free surfaces to simulate a grain boundary decreased the concentration of vacancy clusters slightly compared to the results obtained by simply removing the defects from the system, but the results remained similar. The results reported here represent the grain boundary model in which 1D-migrating SIA clusters are removed from the system as described above in order to match most closely the parameters of Caturla et al.

Glissile dislocation loops of SIAs with unequal Burgers vectors can interact to form immobile clusters or larger glissile dislocation loops, depending on the temperature and the geometry of the interaction [167]. In order to reproduce the simulation parameters of

Caturla et al., this simulation assumes that if two mobile SIA dislocation loops undergo a clustering reaction they are assumed to form a junction and thus become immobile. These immobile interstitial clusters remain in the system and can act as sinks for other defects but cannot migrate.

In order to reproduce this simulation using SRSCD, 20 keV cascades from Caturla et al [39] have been converted into a list of initial defects for each cascade. These are then implanted into the volume elements in the simulation with a rate given by the dpa rate and the number of defects in the cascade, according to the equation in Table 1. The entire cascade is implanted at the same time into a single volume element, according to the method described in Section 3.3.1 using a 10 nm mesh. Because SRSCD assumes that defects are homogeneously distributed within a volume element, the size of the volume elements used determines the local concentration of defects in a cascade. Therefore, the spatial resolution of this method is necessary because the volume element size must match approximately the size of the cascade to provide the correct initial concentration of defects.

Simulated cascade implantation in Cu is carried out using the parameters listed in Table 6. Vacancy and cluster populations are found as a function of dpa. The results of SRSCD and the comparison to the results of Caturla et al. [39] are shown in Figure 30. The quantitative results of this simulation differ from those of Caturla, but the qualitative trends match. In agreement with published OKMC results, the vacancy cluster concentration increases linearly with dpa and the single vacancy concentration reaches an early saturation before decreasing slowly. The concentration of TEM-visible clusters, defined as clusters with diameter greater than 1 nm, also increases linearly with dpa. The vacancy cluster population profile also qualitatively matches the results of Caturla et al., although the concentration of small vacancy clusters of size < 10 differs from the results of Caturla et al.

The differences between the results of this model and the OKMC simulation are due to the spatial correlations that exist in 20 keV cascades in Cu that cannot be included in such a model. Specifically, Cu cascades have the property that a core region of vacancy clusters is surrounded by interstitials [46]. This model cannot simulate this type of spatial correlation, and thus some information about the initial annealing of Cu cascades may be

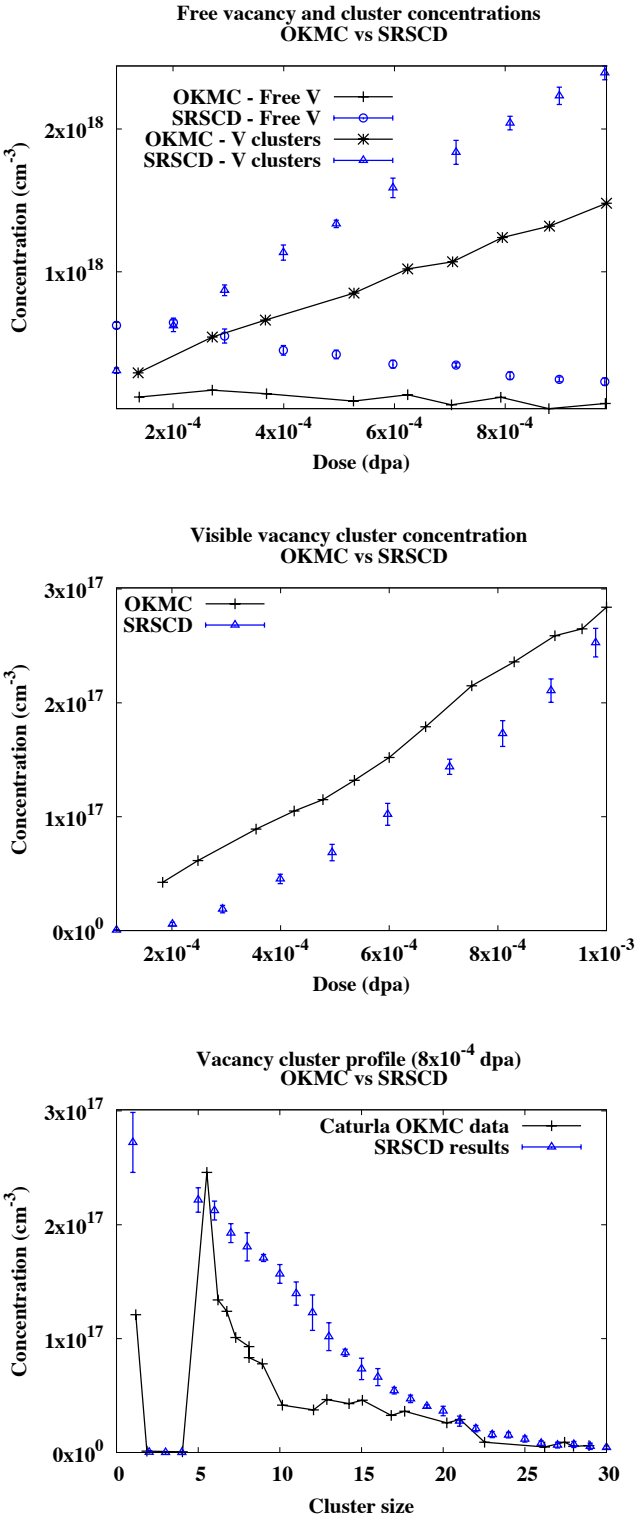

Figure 30: SRSCD results compared to the OKMC results of Caturla et al [39] for 20 keV cascades implanted in Cu at a dpa rate of 10^{-4} dpa/s.

lost. However, the results obtained here match the results of OKMC more closely than any results that can be obtained by traditional rate theory or non-spatially resolved stochastic cluster dynamics. Both the stochastic nature and the spatial resolution of this simulation allow it to reproduce many aspects of this much more computationally intensive OKMC simulation.

3.5.3 Comparison with OKMC: Frenkel pairs and helium in α-Fe

To further test the ability of SRSCD to reproduce the results of OKMC, simulations of damage accumulation in iron are compared to in-house OKMC simulations. The use of in-house OKMC simulations allows for precise determination of all defect and simulation parameters in both methods, ensuring that differences between the methods are not due to differences in inputs as may be the case when comparing to published results. To compare SRSCD to OKMC, two simulations are carried out at 373 K over a large range of damage: 20 keV cascade implantation (without helium) in bulk iron and helium implantation with 20 keV cascades in an iron thin film. OKMC simulations are performed using the code `MMonCa` [135]. The simulations are carried out using both techniques with all other implantation conditions set to the default conditions listed in Table 10. As the simulations described here have been used as a verification step before studying effective helium diffusion in Frenkel pair and cascade-irradiated iron thin films, the majority of the description of the simulation conditions can be found in Section 4.3.3, where those results are presented.

Bulk iron is simulated here using a simulation volume with periodic boundary conditions in all directions. In bulk iron, the ability of grain boundaries to absorb $\langle 111 \rangle$ mobile self-interstitial clusters is simulated by removing such clusters from the simulation after migration over 1 μm. As described in the previous section, only $\langle 111 \rangle$ clusters need be removed in this way due to their greater mobility compared to other defects in the material [63]. Material parameters are given in Table 2.

Defect concentrations are shown for both cascade damage and cascade+helium implantation simulations in Figure 31. In the case of cascade damage in bulk iron, the population

of single vacancies reaches an early maximum and then decreases as more defects are concentrated within larger vacancy clusters. In the case of cascade+helium implantation in iron thin films, this effect is seen again while the growth of HeV and He_nV_m clusters is observed. In all cases, the results of SRSCD good agreement with OKMC over four orders of magnitude of radiation dose. Remaining differences between the defect populations found in OKMC and SRSCD were shown to not significantly impact the desired results of this study, the simulated effective diffusivity of helium. The sources of these differences are therefore considered to be out of the scope of this work.

As in Figure 28, the computational efficiency of SRSCD allows simulation of greater total doses than was achieved by OKMC, as shown in Figure 31. This reflects the main goal of the creation of this method: development of a simulation method that can reach large total doses and which can simulate larger volumes than methods such as OKMC, but which can include much more complicated defect behaviors and spatially resolved effects than MFRT or cluster dynamics methods.

3.5.4 Resistivity recovery in electron-irradiated iron: comparison with OKMC, MFRT, and experiment

The use of an adaptive meshing scheme allows SRSCD to model spatially correlated interactions between defects in cascades while maintaining correct rates between uncorrelated defects in the bulk. To demonstrate the ability of SRSCD to model spatially correlated reactions, as well as the necessity of choosing correct volume element sizes, simulations of resistivity recovery in electron-irradiated iron are carried out and compared to experimental and OKMC studies [211, 74]. In these studies, Frenkel pairs are implanted into low temperature (4.5 K) iron and the temperature is subsequently increased in increments, allowing various reactions to occur as they become thermodynamically feasible. The change in resisitivity is related to the derivative of defect density with respect to temperature, $\frac{d\rho}{dT}$. Peaks in this curve indicate temperatures at which a significant amount of defect recombination is occurring. Therefore, each peak represents a temperature at which a different defect type becomes mobile, allowing for experimental estimation of defect parameters such as migration energies E_m.

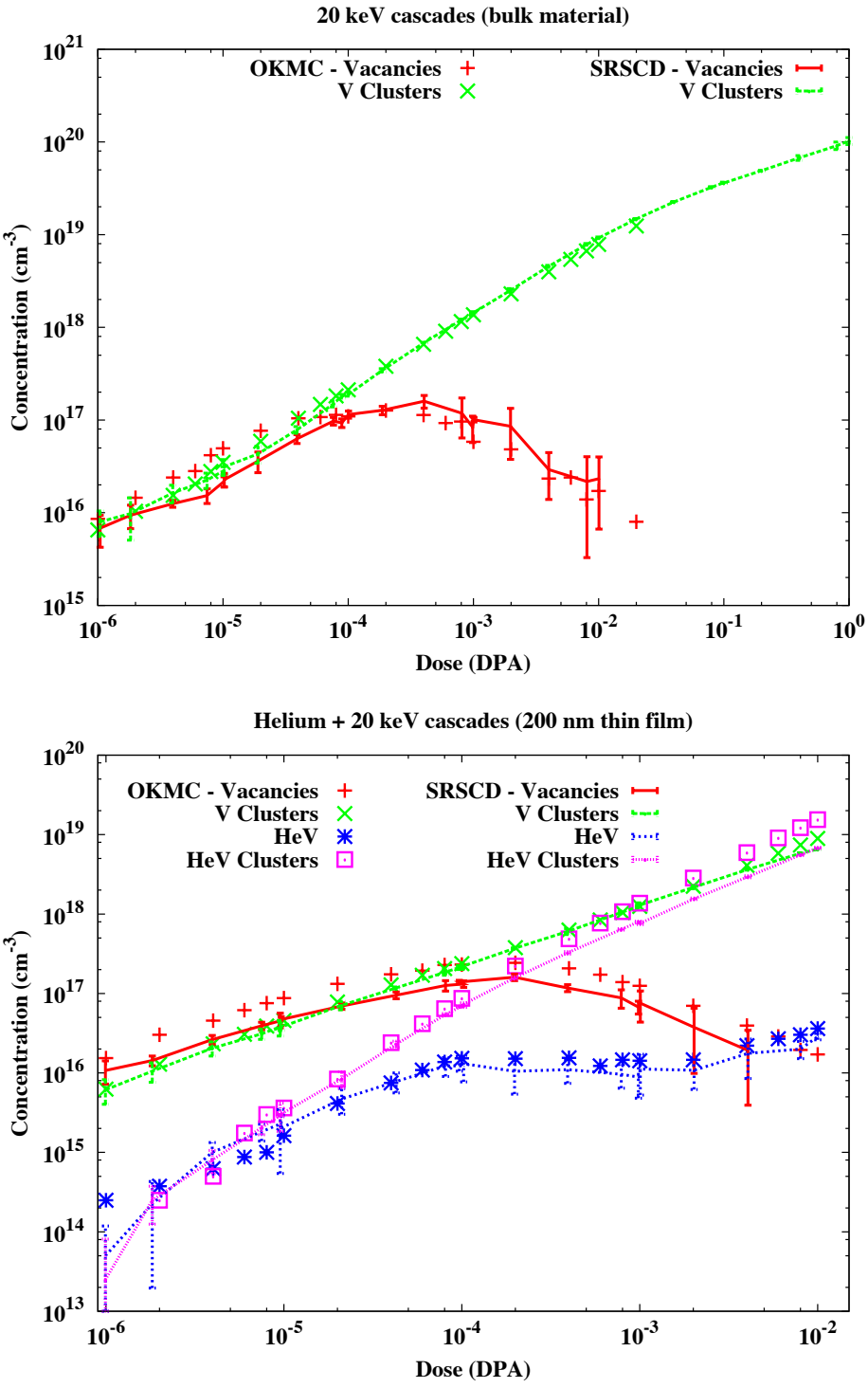

Figure 31: Species populations in an infinite Fe medium implanted with 20 keV cascades (top) and a Fe thin film implanted with helium and 20 keV cascades (bottom). Results are shown for OKMC and SRSCD. The two methods are in good agreement for the range of DPA shown.

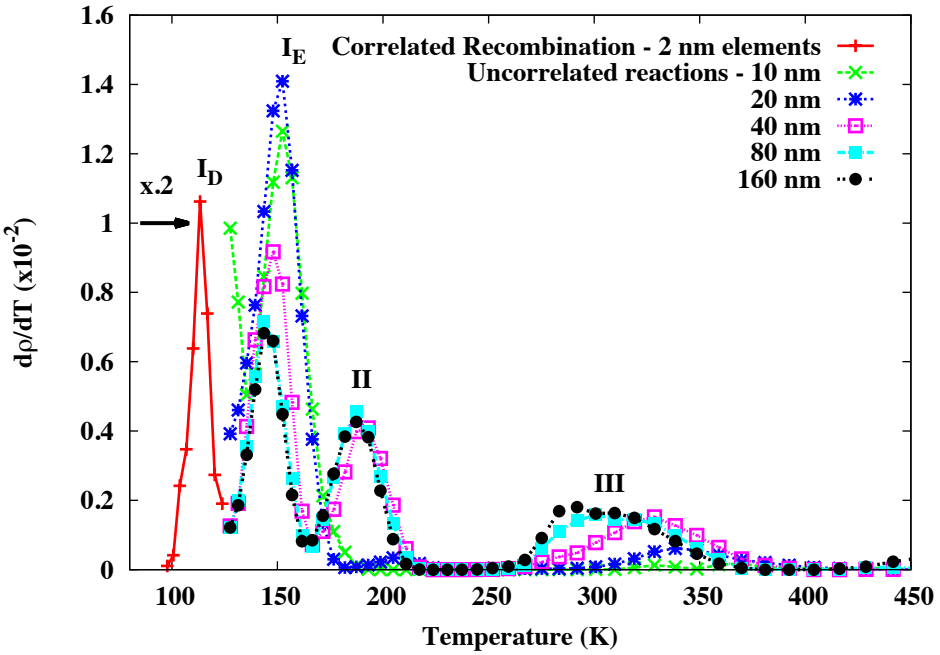

Figure 32: Resistivity recovery simulations in electron-irradiated Fe to 2×10^{-6} DPA using SRSCD. Peak locations correspond to stages in resistivity recovery identified in experimental and OKMC simulations [211, 74]. A mesh size of 2 nm is used to simulate correlated recombination (peak I_D) and larger mesh sizes are used for uncorrelated peaks.

The simulation parameters used are the same as reported by Fu et al. [74] and Dalla Torre et al. [44], who carried out this simulation using OKMC and MFRT, respectively. Electron irradiation (in the form of Frenkel pairs) is first carried out in a periodic mesh of iron to a total dose of 2×10^{-6} DPA at low temperature. Annealing is carried out in 300 second increments, starting at 77.2 K and increasing the temperature by a factor of 1.03 at each increment. The derivative of the concentration of vacancies with respect to temperature is plotted in Figure 32, and results are compared to OKMC and experimental results. The labeled stages in Figure 32 correspond to correlated recombination of Frenkel pairs (stage I_D), uncorrelated recombination of single vacancies and interstitials (stage I_E), migration of di-interstitial pairs (stage II) and migration of single vacancies (stage III), in agreement with both OKMC and experiment [211, 74].

Due to the close proximity of the vacancy-interstitial pairs in these studies, a correlated

recombination peak occurs at approximately 107K [74]. This peak represents vacancy-interstitial pairs from the same Frenkel pair recombining with each other as single self-interstitials become mobile. In this work a 2 nm mesh is used to reproduce this correlated recombination peak. This mesh size is on the order of the separation between the vacancy-interstitial pair (1.148 nm). If a larger mesh size is used to simulate stage I_D of resistivity recovery, peaks I_D and I_E merge into a single peak and the correlated recombination behavior is lost. This behavior is noted by Dalla Torre et al. [44] in MFRT simulations of the same resistivity recovery experiments. This indicates that in SRSCD, the amount of spatial correlation between defects is limited by the size of the volume elements used in the simulation as defects are assumed to be homogeneously distributed within volume elements.

After stage I_D is passed, the remaining reactions in the system occur between uncorrelated defects. Therefore, the defect population produced by the simulation with a 2 nm mesh is input into several simulations with mesh sizes ranging from 10 nm to 160 nm. In this work, the location of peaks I_E, II, and III best match those of OKMC simulations [74] for 40 nm volume elements. In the case of truly uncorrelated reactions, one would expect a best match at the largest volume element size. This indicates that some level of spatial correlation may remain in the system during peak I_E. In addition, the use of elements that are much smaller than the spatial correlation present in the system causes SRSCD to produce incorrect results here.

The simulations presented in Figure 32 represent a procedure analogous to the adaptive meshing scheme presented in Section 3.3.3, applied to the case of Frenkel pair evolution during resistivity recovery simulations. These results show that such a scheme is necessary to reproduce peak locations found in OKMC studies [74]. The sensitivity to mesh size shown in Figure 32 is magnified by the low concentration of Frenkel pairs in the system caused by the low total dose and high fraction of defect recombination. Note here that although the height of the I_D peak using a 2 nm mesh matches the height found in OKMC, other peak heights do not match.

The results of these simulations demonstrate the ability of SRSCD to serve as an intermediate method between the defect-level spatial resolution of OKMC and the spatial

homogenization of MFRT. The resistivity recovery simulations carried out here delineate the importance of choosing mesh sizes in SRSCD so that reaction rates match those of OKMC.

3.6 Summary of Chapter 3

Chapter 3 describes the main tool used for simulating damage evolution in this dissertation, spatially resolved stochastic cluster dynamics (SRSCD). This chapter begins by presenting the mathematical basis for SRSCD)as derived by Gillespie et al. [83] for general chemical systems and expanded by Marian and Bulatov [131] for modeling damage accumulation in irradiated metals. This derivation is motivated by classical models for damage accumulation using mean field rate theory (MFRT), such as the model presented by Stoller et al. [207]. However, these models typically only include a few types of mobile defects and simple reaction rates using 3D diffusion; therefore, these reaction rates must be extended to larger defects and more complicated diffusive behavior for implementation in SRSCD. Reaction rates for clustering between various diffusive species are therefore derived in Section 3.2.2 using a standard formulation, where the reaction rate for defect species i to interact with sink j is governed by a sink strength k_{ij}^2:

$$reaction\ rate = k_{ij}^2 D_i C_i \tag{81}$$

The sink strength k_{ij}^2 represents the inverse of the square of the mean free path of defect i when interacting with sink j. Sink strengths are derived for several cases that extend this definition, including clustering between two mobile defect species, clustering between dislocation loops that diffuse in one dimension, and clustering between defects on planar surfaces, which are used to represent grain boundaries in later applications.

The fundamental principle behind SRSCD is the ability to solve the coupled rate equations of MFRT using a stochastic approach, by modeling the number of defects inside a finite volume and choosing reactions using a kinetic Monte Carlo algorithm. Therefore, the conversion of reaction rates from concentration rates (units of $\mathrm{s}^{-1}\mathrm{m}^{-3}$) to true reaction rates (units s^{-1}) is demonstrated in Section 3.2.3. After including reaction rates for diffusion between discrete volume elements, thus introducing spatial resolution into SRSCD,

the implementation of the kinetic Monte Carlo algorithm using the reaction rates derived in the earlier sections is presented in Section 3.2.5. In this implementation, a list of nonzero reaction rates a_μ is compiled for each allowed reaction μ. The total reaction rate $a = \sum_\mu a_\mu$ is calculated, and two random numbers r_1 and $r_2 \in [0, 1]$ are generated. A timestep τ and reaction choice μ are made using the classical kMC algorithm:

$$\tau = \frac{1}{a} \ln\left(\frac{1}{r_1}\right) \ , \ \sum_{\nu=1}^{\mu-1} a_\nu < r_2 a < \sum_{\nu=1}^{\mu} a_\nu \tag{82}$$

After choosing a reaction, the defect numbers are updated based on the reaction chosen, reaction rates are recalculated, and the process is repeated.

The implementation of displacement cascade damage in SRSCD is a particular challenge for several reasons. First, cascade damage is a common phenomenon in irradiated materials when the PKA atom has great enough energy that it can displace multiple other lattice atoms. This occurs frequently during heavy ion irradiation and neutron irradiation. Second, displacement cascades create high concentrations of defects and defect clusters within a small volume, usually on the order ten nanometers, indicating that the 'well-mixed' hypothesis of MFRT and SRSCD does not apply. Instead, spatially correlated reactions such as clustering and annihilation are expected between defects created in a displacement cascade. Therefore, in Section 3.3 three techniques for simulating cascade damage implantation using SRSCD are discussed. The first technique simply implants all of the defects generated in the cascade inside a single volume element, which is effective only when the size of the volume element is similar to the size of the cascade. The second technique distributes the cascade defects over several volume elements, which allows for somewhat improved mesh convergence. The final technique uses a pseudo-adaptive meshing scheme to create a fine mesh into which cascades are implanted while treating the rest of the system with a coarse mesh. This allows for simulating total doses and volumes large enough to compare directly to experimental measures of defect accumulation [67, 259].

In order further improve computational efficiency and simulate large domains such as polycrystals, SRSCD is implemented using a synchronous parallel kinetic Monte Carlo algorithm developed by Martínez et al. [136] for OKMC simulations and expanded in this

dissertation to SRSCD in Section 3.4. The parallel scaling of this methodology is investigated from the perspective of both weak scaling, in which the volume per processor is held constant and the number of processors is increased, and strong scaling, in which the total simulation volume is held constant and the number of processors is increased. Using both of these measures, synchronous parallel SRSCD is shown to provide significant computational gains compared to serial SRSCD.

One challenge to the scalability of the synchronous parallel SRSCD implementation is very stiff problems, in which the total reaction rate in one processor is so much greater than its neighbors that the neighboring domains are idle as the domain with the fast reaction rates chooses reactions. This is a common problem when damage is in the form of displacement cascades, as the reaction rates between domains can vary by several orders of magnitude. An explicit method for improving the parallel scaling of simulations that include displacement cascades is therefore implemented and shown to provide significant computational advantages compared to the standard method.

In order to validate the SRSCD method developed in this dissertation, several comparative studies are carried out in Section 3.5 between SRSCD and MFRT, OKMC, and published experimental results. These studies demonstrate that SRSCD is computationally equivalent to MFRT and spatially resolved RT models when the same defects, reactions, and reaction rates are allowed. In addition, comparison to OKMC shows good agreement for the case of complicated damage accumulation models outside the scope of MFRT, such as helium and cascade damage accumulation inside bulk iron. Finally, resistivity recovery simulations show agreement with OKMC, MFRT, and experimental measures of resistivity recovery during annealing of electron-irradiated iron.

3.7 Conclusions

This chapter describes the development and implementation of spatially resolved stochastic cluster dynamics (SRSCD) for modeling radiation damage accumulation. SRSCD is shown to avoid some of the pitfalls of both traditional MFRT and OKMC models, by allowing computational efficiency while including complicated defect reactions and spatial

resolution. By implementing techniques such as adaptive meshing for simulating cascade damage and using a synchronous parallel kinetic Monte Carlo algorithm, SRSCD is capable of simulating damage accumulation at doses, dose rates, and temperatures that are outside the range of previous methods while including highly spatially resolved phenomena such as cascade damage and simulating spatially resolved microstructures such as thin films and polycrystals. Therefore, SRSCD meets the requirements for innovative modeling techniques developed in this dissertation and uniquely enables investigation of the scientific questions posed in Section 1.2. It should also be noted that the kinetic Monte Carlo solution of coupled initial value problems implemented in this dissertation can be applied generally to arbitrary initial value problems, even when the problem does not represent the evolution of concentrations of chemical species. In particular, this algorithm can be applied to problems in which populations are not conserved and reaction rates can be positive or negative, by making some minor adjustments. A discussion of the application of this method to generic initial value problems is presented in Appendix D.

CHAPTER IV

THE INFLUENCE OF IRRADIATION CONDITIONS AND MATERIAL MICROSTRUCTURE ON DEFECT ACCUMULATION

4.1 Irradiation and microstructural regimes of interest

The goal of this chapter is to apply the SRSCD methodology to problems of radiation damage in a variety of contexts, in order to answer the first two scientific questions addressed in this dissertation:

How do radiation conditions such as temperature, dose rate, and damage type influence radiation defect accumulation in irradiated metals? (Q1)

How does the presence of interfaces, grain boundaries, free surfaces, and other micro-structural elements influence radiation defect accumulation in irradiated metals? (Q2)

Therefore, the various studies performed in this chapter address a variety of radiation conditions and material microstructures. Particular emphasis is placed on three main microstructural and irradiation regimes, which are chosen due to their significance to the radiation damage community:

1. Ion irradiation of thin films is a technique frequently used in experimental studies of radiation damage due to the relative speed and cost-effectiveness of such techniques [231, 114, 186, 92]. Thin films are used in these experiments due to their application to microscopy tools such as TEM and the short penetration depth of ion beams in metals. In order to study mechanisms that are relevant in neutron-irradiated materials (which can contain helium through transmutation reactions), helium implantation is also frequently combined with displacement damage in such thin film studies. Therefore,

in Section 4.3 the influence of a wide variety of irradiation conditions and helium implantation on damage evolution in thin films is studied.

2. When neutron irradiation experiments are carried out, in contrast to ion irradiation, the implantation depth is large enough that bulk metals can be irradiated [38]. These experiments also typically occur over much larger timescales than ion irradiation experiments. Therefore, in Section 4.4 neutron damage in coarse-grained microstructures is simulated using reported experimental irradiation conditions [67].

3. Finally, grain boundaries and interfaces have been shown to influence the accumulation of radiation damage [210, 118, 144, 50]. In nanocrystalline materials, these effects can dominate damage evolution due to the high ratio of interface surface area to volume. Therefore, to study damage evolution in nanocrystalline materials, simulations must both explicitly account for the polycrystalline microstructure of such materials as well as correctly treat the impact of grain boundaries on damage accumulation, including the possibility of certain grain boundaries acting as imperfect sinks [90, 218, 188, 56]. In Section 4.5, both of these modeling needs are addressed for nanocrystalline microstructures.

In addition to investigating the scientific questions posed above in this chapter, the outputs of SRSCD simulations are used to investigate the various mechanisms responsible for defect accumulation and evolution in irradiated materials. Examples of such mechanisms include the interaction between vacancies and helium atoms in controlling helium migration, the interaction between displacement cascades and defects already present in the material, and the impact of the presence of impurities on the population of dislocation loops.

To close the loop, the use of ion implantation to reproduce damage accumulation similar to that produced during neutron irradiation is investigated in Section 5.3. Here, temperatures must be adjusted to account for the change in dose rate between the two experimental methods [239, 170, 129, 2]. Quantification of this equivalence between temperature and dose rate is important in designing experiments that avoid the cost and difficulty of neutron damage while remaining confident that the results correctly reproduce damage accumulation

due to neutron irradiation. A novel methodology is presented in Section 5.3 to estimate the temperature needed in ion irradiation experiments to provide defect accumulation results relevant to the neutron irradiation conditions of interest.

4.2 Allowed defects and migration/binding energies in α-Fe

In this dissertation, most SRSCD simulations are performed using α-Fe as a model material. This choice is motivated by the fact that a large body of atomistic data exists for the binding and migration of various defect cluster types inside iron, including helium-vacancy clusters. Therefore, in all simulations carried out in the remainder of this chapter, the same list of parameters for defect behaviors is applied to the various microstructures and irradiation conditions under consideration. The allowed defects, their geometries, and the energetics of their migration and binding behaviors are below and in Table 7, unless otherwise noted for a specific simulation.

The defects modeled in the following sections of this chapter are:

1. *Single defects:* these are self-interstitial atoms (SIA), vacancies (V) or interstitial helium atoms (He). These defects migrate in three dimensions and can cluster or annihilate with other defects.

2. *Vacancy clusters:* these are treated as spherical clusters in SRSCD. Small vacancy clusters are mobile and can migrate, cluster, and annihilate. Single vacancies can dissociate from vacancy clusters.

3. *Helium clusters:* these are treated similarly to vacancy clusters, but are only allowed to form up to size 4. These can migrate in 3D as well.

4. *Helium-vacancy clusters:* these are treated as spherical clusters in SRSCD as well, with the size of the cluster given by the vacancies in the He_mV_n cluster. Some small He_mV_n clusters are allowed to migrate and cluster with other defects (see Table 7).

5. *Self-interstitial clusters size 2-4:* these SIA clusters migrate in three dimensions and are treated as spherical clusters in SRSCD.

6. *Larger mobile self-interstitial clusters:* these SIA clusters are treated in as circular dislocation loops that lie on a <111> plane and glide in the direction of their Burgers vector. In SRSCD, individual <111> planes cannot be resolved but their reaction rates for interaction with other defects are adjusted to reflect 1D migration and circular geometry (see Table 1).

7. *Larger immobile self-interstitial clusters:* these SIA clusters are formed when two <111> clusters meet and form a junction. In SRSCD, these are treated as immobile circular clusters.

Note that He-SIA clusters are not allowed to form in this dissertation. Although some studies have included such clusters [131, 23], the problem of He-SIA binding is not frequently addressed in the literature. The effect of He-SIA clusters on helium desorption from thin iron foils has been shown to be minor [63].

The behavior of interstitial helium clusters size greater than 4 is not well-parameterized in the literature. As limiting cases, simulations were carried out allowing arbitrary interstitial helium cluster size using the same binding energy as 4-He clusters (0.98 eV) and compared to simulations in which 4-He clusters are the largest such clusters allowed to form. No changes in effective diffusivity behavior were seen between these two methods, and the results presented here correspond to simulations in which 4-He clusters are the largest interstitial helium clusters allowed in the simulation.

4.3 Helium and displacement damage under ion irradiation conditions: application to thin films

In this section, mechanisms of radiation damage evolution are investigated inside iron thin films, with an emphasis on the interaction between displacement damage and helium. Thin films are a frequently used microstructure in experimental studies of radiation damage because damage caused by light and heavy ions typically only penetrates hundreds of nanometers to a few microns into a material. As studies of radiation damage using ion beams to create damage are much simpler and cost-effective to operate than neutron damage, structures such as thin films that can be investigated with ion irradiation are commonplace. In

Table 7: Migration and binding parameters used in SRSCD simulations. The diffusion of HeV and HeV_3 clusters are taken from the values found for Nb, which is assumed to be similar to the behavior of Fe. He_mV_n clusters with $m/n \leq 0.5$ are assumed to act as vacancy clusters only, and do not allow He dissociation. Vacancy and helium binding energies in He_mV_n for $m/n > 0.5$ are taken from [216].

Migration parameters	$D = D_0 e^{-\frac{E_m}{k_b T}}$	
Single vacancy	$E_m = 0.67$ eV, $D_0 = 8.2 \times 10^{11}$ nm$^2/s$	[74]
2-v cluster	$E_m = 0.62$ eV, $D_0 = 8.2 \times 10^{11}$ nm$^2/s$	[74]
3-v cluster	$E_m = 0.35$ eV, $D_0 = 8.2 \times 10^{11}$ nm$^2/s$	[74]
4-v cluster	$E_m = 0.48$ eV, $D_0 = 8.2 \times 10^{11}$ nm$^2/s$	[74]
Larger v clusters	(immobile)	
Single interstitial	$E_m = 0.34$ eV, $D_0 = 8.2 \times 10^{11}$ nm$^2/s$	[74]
2-i cluster	$E_m = 0.42$ eV, $D_0 = 8.2 \times 10^{11}$ nm$^2/s$	[74]
3-i cluster	$E_m = 0.43$ eV, $D_0 = 8.2 \times 10^{11}$ nm$^2/s$	[74]
4-i cluster	$E_m = 0.43$ eV, $D_0 = 8.2 \times 10^{11}$ nm$^2/s$	[74]
n-i cluster (1D)	$E_m = .06 + .11(n^{-1.6})$, $D_0 = (3.5 \times 10^{10} + 1.7 \times 10^{11} n^{-1.7})$ nm$^2/s$	[198]
Single-He	$E_m = 0.077$ eV, $D_0 = 5 \times 10^{11}$ nm$^2/s$	[216]
2-He cluster	$E_m = 0.055$ eV, $D_0 = 3 \times 10^{10}$ nm$^2/s$	[216]
3-He cluster	$E_m = 0.062$ eV, $D_0 = 1.5 \times 10^{10}$ nm$^2/s$	[216]
4-He cluster	$E_m = 0.062$ eV, $D_0 = 5 \times 10^{9}$ nm$^2/s$	[216]
HeV (value for Nb)	$E_m = 2.57$ eV, $D_0 = 1.15 \times 10^{12}$ nm$^2/s$	[64]
HeV_2	$E_m = 0.27$ eV, $D_0 = 4.1 \times 10^{10}$ nm$^2/s$	[75]
HeV_3 (value for Nb)	$E_m = 1.42$ eV, $D_0 = 1.15 \times 10^{12}$ nm$^2/s$	[64]
He_2V	$E_m = 0.33$ eV, $D_0 = 1.16 \times 10^{11}$ nm$^2/s$	[216]
He_3V	$E_m = 0.31$ eV, $D_0 = 2 \times 10^{10}$ nm$^2/s$	[216]
He_4V	$E_m = 0.28$ eV, $D_0 = 2.36 \times 10^{9}$ nm$^2/s$	[216]
He_2V_3	$E_m = 0.55$ eV, $D_0 = 7.82 \times 10^{9}$ nm$^2/s$	[216]
Binding energies		
$V_2 \rightarrow V+V$	$E_b = 0.3$ eV	[74]
$V_3 \rightarrow V_2+V$	$E_b = 0.37$ eV	[74]
$V_4 \rightarrow V_3+V$	$E_b = 0.62$ eV	[74]
Vacancy clusters ($n > 4$)	$E_b^v(n) = 2.07 - 3.01(n^{\frac{2}{3}} - (n-1)^{\frac{2}{3}})$	[74]
$I_2 \rightarrow I+I$	$E_b = 0.8$ eV	[74]
$I_3 \rightarrow I_2+I$	$E_b = 0.92$ eV	[74]
Interstitial clusters ($n > 3$)	$E_b^i(n) = 3.77 - 5.05(n^{\frac{2}{3}} - (n-1)^{\frac{2}{3}})$	[74]
$He_2 \rightarrow He+He$	$E_b = 0.43$ eV	[161]
$He_3 \rightarrow He_2+He$	$E_b = 0.95$ eV	[161]
$He_4 \rightarrow He_3+He$	$E_b = 0.98$ eV	[161]
Small He_mV_n clusters ($m, n \leq 4$)	E_b taken from Ortiz and Caturla	[161]
He_mV_n (He binding, $\frac{m}{n} \leq 0.5$)	(does not dissociate)	
He_mV_n (He binding, $\frac{m}{n} > 0.5$)	$E_b^{\mathrm{He}} = 2.2 - 1.55 \log\left(\frac{m}{n}\right) - .53 \log\left(\frac{m}{n}\right)^2$	[216]
He_mV_n (V binding, $\frac{m}{n} \leq 0.5$)	$E_b^v(n) = 2.07 - 3.01(n^{\frac{2}{3}} - (n-1)^{\frac{2}{3}})$	[74]
He_mV_n (V binding, $\frac{m}{n} > 0.5$)	$E_b^v = 1.55 + 3.19 \log\left(\frac{m}{n}\right) + 3.0 \log\left(\frac{m}{n}\right)^2$	[216]

Table 8: Material parameters used in experiment [231] and rate theory [162] studies of helium desorption from Fe foils

Anneal temp	He concentration	Sample thickness
559 K	1.39 ppm	2.5 μm
577 K	0.013 ppm	20.6 μm
667 K	0.109 ppm	2.6 μm

addition, thin films allow for other experimental techniques such as measurement of helium desorption [231] and TEM investigation of damage accumulation [92].

In Section 4.3.1, SRSCD is used to simulate helium and Frenkel pair implantation in iron thin films and the subsequent desorption caused by annealing. Results are compared to experimental results [231] and mechanisms of helium mobility are investigated in Section 4.3.2. Finally, more in-depth study of the impact of various microstructural and irradiation conditions on helium migration in irradiated iron thin films is carried out in Section 4.3.3.

4.3.1 Helium desorption from low-temperature implanted and annealed iron thin films

Helium desorption experiments can be used to investigate the mobility of implanted helium in irradiated metals. In these experiments, helium is implanted in thin foils, causing simultaneous displacement damage in the form of Frenkel pairs. After allowing the system to equilibrate, the thin foil is annealed in a vaccuum and the fraction of implanted helium that is released as a function of time is measured. This has been studied previously in experimental studies [231] and using spatially resolved rate theory developed by Ortiz et al. [162]. In these studies, three iron foils varying in width from 2.5 μm to 20.6 μm are implanted with helium to a variety of initial concentrations and subsequently annealed at a variety of annealing temperatures. The irradiation and annealing parameters for this experiment, which are also used as simulation parameters, are given in Table 8.

To simulate the experimental conditions, Ortiz et al. first implanted helium, vacancies, and self-interstitials homogeneously in the material to the concentrations listed in Table 8, with 200 Frenkel pairs per helium atom introduced. The system was then allowed to reach steady-state at 300 K and subsequently annealed at high temperature. The boundaries of the iron foil were treated as free surfaces (infinite sinks for all mobile point defects) and the

amount of helium released from the system as a function of time was tracked.

In the rate theory simulation by Ortiz et al. [162], the mobile species were limited to He, single vacancies, single interstitials, and 2-interstitial clusters. It is important to note that the rate equations used by the authors differ from the rate equations presented in this dissertation, and can be found in [161]. Using rate theory, Ortiz et al. [162] were able to achieve good agreement between simulation results and experiment, assuming some modified defect mobilities due to the effect of impurities in the material.

4.3.1.1 Defect parameters and reaction rates

To simulate this experiment using SRSCD, the same material parameters are used, but all species which have been found to be mobile in iron are allowed to migrate. In addition, HeV and HeV_3 clusters have been studied in Nb [64] but do not have migration data available in Fe. For this simulation the migration values from Nb are used for HeV and HeV_3, but since these defects have relatively high migration energy the impact of their migration on the simulation results is negligible. In order to best match the simulation parameters used by Ortiz et al. [162], some vacancy and interstitial diffusivity parameters used in this simulation differ from the values used in the majority of the simulations in this chapter, and therefore the parameters in Table 7 are not used. Instead, the migration and binding energies of all cluster types used in this simulation are given in Table 9. In addition, in these simulations small SIA clusters are assumed to migrate with mixed 1D-3D character as discussed in Section 3.2.2.4. Therefore, the sink strength for interaction between these defects is given by equation (42), and the parameters used to determine the frequency of direction changes are also given in Table 9.

In order to include helium in the reaction rates for defect clustering, HeV clusters are assumed to be spherical with radius given by the number of vacancies in the cluster. Helium clusters are also assumed to be spherical, but the population of interstitial helium clusters is never significant. Thus reaction rates for He+HeV, V+HeV, HeV+HeV, and SIA+HeV (with the number of V greater or equal to the number of SIA) are found using the same methods as described in Chapter 3.

Table 9: Migration and binding parameters used in spatially resolved stochastic rate theory simulation of Helium desorption from Fe foil. The diffusion of HeV and HeV_3 clusters are taken from the values found for Nb, which is assumed to be similar to the behavior of Fe. For the binding energy of vacancies to large He_mV_n clusters, the He was not taken into account. A functional form for this binding energy exists [216] but does not apply to clusters where $m << n$. Most large HeV clusters in this simulation are of this type.

Migration parameters	$D = D_0 e^{-\frac{E_m}{k_b T}}$	
Single vacancy	$E_m = 0.6$ eV, $D_0 = 7.9 \times 10^{11}$ nm$^2/s$	[131]
2-v cluster	$E_m = 0.66$ eV, $D_0 = 3.5 \times 10^{10}$ nm$^2/s$	[131]
Larger v clusters	(immobile)	
Single interstitial	$E_m = 0.25$ eV, $D_0 = 1.3 \times 10^{10}$ nm$^2/s$	[131]
2-i cluster	$E_m = 0.36$ eV, $D_0 = 3.516 \times 10^{12}$ nm$^2/s$	[131]
3-i cluster	$E_m = 0.14$ eV, $D_0 = 1.21 \times 10^{11}$ nm$^2/s$	[131]
4-i cluster	$E_m = 0.15$ eV, $D_0 = 1.32 \times 10^{11}$ nm$^2/s$	[131]
n-i cluster	$D_i(n) = \frac{8.98 \times 10^{11}}{n^{-.61}} e^{-\frac{.06+.07(n^{-1.3})}{k_b T}}$ nm$^2/s$	[132]
Single-He	$E_m = 0.077$ eV, $D_0 = 5 \times 10^{11}$ nm$^2/s$	[216]
2-He cluster	$E_m = 0.055$ eV, $D_0 = 3 \times 10^{10}$ nm$^2/s$	[216]
HeV	$E_m = 2.57$ eV, $D_0 = 1.15 \times 10^{12}$ nm$^2/s$	[64] (value for Nb)
HeV_2	$E_m = 0.27$ eV, $D_0 = 4.1 \times 10^{10}$ nm$^2/s$	[75]
HeV_3	$E_m = 1.42$ eV, $D_0 = 1.15 \times 10^{12}$ nm$^2/s$	[64] (value for Nb)
He_2V	$E_m = 0.33$ eV, $D_0 = 1.16 \times 10^{11}$ nm$^2/s$	[216]
He_3V	$E_m = 0.31$ eV, $D_0 = 2 \times 10^{10}$ nm$^2/s$	[216]
He_4V	$E_m = 0.28$ eV, $D_0 = 2.36 \times 10^{9}$ nm$^2/s$	[216]
He_2V_3	$E_m = 0.55$ eV, $D_0 = 7.82 \times 10^{9}$ nm$^2/s$	[216]
1D-3D direction change	$v = v_0 e^{-\frac{E_v}{k_b T}}$	
2-i cluster	$E_v = 0.088$ eV, $v_0 = 2.86 \times 10^{11}$ s^{-1}	[197]
3-i cluster	$E_v = 0.271$ eV, $v_0 = 4.54 \times 10^{11}$ s^{-1}	[197]
Binding energies		
Small clusters ($n \leq 4$)	E_b taken from Ortiz	[162]
Vacancy clusters	$E_b^v(n) = 2.07 - 3.01(n^{\frac{2}{3}} - (n-1)^{\frac{2}{3}})$	[74]
Interstitial clusters	$E_b^i(n) = 3.77 - 5.05(n^{\frac{2}{3}} - (n-1)^{\frac{2}{3}})$	[74]
He_mV_n (He binding)	$E_b^{\mathrm{He}} = 2.2 - 1.55 \log\left(\frac{m}{n}\right) - .53 \log\left(\frac{m}{n}\right)^2$	[216]
He_mV_n (V binding)	$E_b^v(n) = 2.07 - 3.01(n^{\frac{2}{3}} - (n-1)^{\frac{2}{3}})$	(same as v clusters)

The binding of helium to single interstitials and self-interstitial clusters is a problem that has not been fully addressed in the literature. Marian et al. [131] and Becquart et al. [23] have studied defect evolution including He-SIA cluster formation, while the work of others such as Ortiz et al. [162] neglects this effect. In general, the availability of parameters governing the behavior of He-SIA clusters is low. Therefore, this simulation was carried out using only He-V clustering. In order to test the significance of this choice, identical helium desorption simulations were performed using the He-SIA parameters reported by Marian et al. [131], assuming that He-SIA clusters are stable and immobile. Although a large number of He-SIA clusters appeared at the beginning of the annealing stage of the simulation, the change in the overall desorption results was minor. In addition, the physical mechanisms responsible for helium desorption do not change in this case. A larger study of the effect of He-SIA binding on defect accumulation in metals, with an improved set of parameters such as binding and migration energies of these defects, is warranted but outside the scope of this work.

In agreement with the results of Soneda [197], self-interstitial clusters of size 2 and 3 are assumed to migrate with mixed 1D-3D character, and their reaction rates for combining with other defects are calculated using the sink strength from equation (42). Although the frequency for direction changes is taken from the work of Soneda, in order to keep the parameter set as consistent as possible, the interstitial migration energies used are the same as those used by Marian [131]. These vary significantly from the migration energies for small interstitial clusters found by Soneda. However, when the simulation was repeated with the migration energies of Soneda for small interstitial clusters, the results did not change significantly. In addition, allowing only 3D migration for small interstitial clusters also produced similar results, although the migration energy of single vacancies had to be adjusted to 0.68 eV to achieve agreement with experimental results. This value is well within the range of values reported for the migration of a single vacancy in Fe [131, 197]. It is therefore expected that the mixed 3D-1D migration behavior of small interstitial clusters does not have a major impact on the results of this study.

4.3.1.2 Description of simulations and results

After implanting helium and Frenkel pairs in the simulated thin foil (200 Frenkel pairs per helium atom, in agreement with Ortiz et al. [162]), the system is evolved for 1 second at 300 K and subsequently annealed for 2×10^4 seconds at the higher temperature, with the boundaries of the system free surfaces for the entire simulation. The boundary conditions of the system during the low-temperature annealing part of the simulation were shown to not strongly impact the results of the simulation. The amount of helium released from the system and the types of helium clusters that leave the system are recorded as a function of the annealing time.

Figure 33 shows helium desorption for the 559 K sample using SRSCD compared to experiment. The results provided by SRSCD differ from the experimental results when using the parameters listed in Table 9. Although the qualitative results match, the model predicts significantly more helium release than was measured in experiment or simulated in the rate theory model of Ortiz et al. [162]. The reason for this difference is hypothesized to be the long-range mobility of SIA clusters in this simulation, which increases annihilation with helium-vacancy clusters, causing increased helium mobility. Assuming that the material has some impurity content, interstitial clusters could be trapped and become immobile when interacting with impurity atoms [99]. In the work of Ortiz et al. [162], the migration energy of vacancies was used as a fitting parameter in order for the rate theory results to match experiment. This variation of vacancy migration energy is explained by Ortiz to be the result of the presence of impurities in the iron foil. In this work, vacancy migration energies are not modified but SIA cluster pinning by impurities is treated instead. Therefore, in this simulation, the mean free path for interstitial clusters to become immobile is varied to fit the simulation results to experimental results. The simulation results are shown to depend only weakly on the actual value of the mean free path chosen and thus an optimal value of mean free path is not found. Nonetheless, when this method is applied the SRSCD results match the experiment more closely.

It is interesting to note that if, instead of the mean free path described above, interstitial diffusion is simply eliminated for all clusters greater than size 2 in SRSCD, desorption results

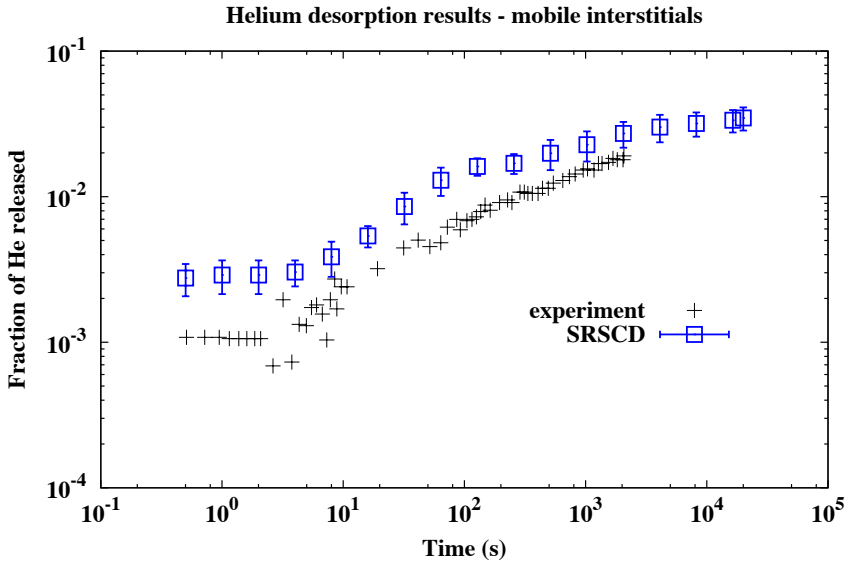

Figure 33: Fraction of He released, 559 K anneanling. Interstitial clusters are assumed to be mobile until interacting with a second interstitial cluster, at which point they form a junction and become immobile. These results predict more helium release than measured experimentally by Vassen et al. [231].

are almost identical to results obtained by using of a mean free path for interstitial cluster migration. Thus the approach of Ortiz et al. [162], which only considers single SIAs and 2-interstitial clusters as mobile, treats interstitial migration in much the same way as this simulation. This is due to the fact that one-dimensionally migrating SIA clusters have a low cross-section for interacting with other defects and are therefore likely to reach the end of their mean free path and become sessile before interacting with other defects. Therefore the main difference between the models is the mobility of small He_mV_n clusters.

The helium desorption results of the SRSCD simulation compared to experiment after including SIA cluster pinning by impurities are shown in Figure 34. A reasonable fit is achieved when comparing simulation to experimental results, even though these simulations represent a range of 100 K in annealing temperature, two orders of magnitude in initial helium content, and one order of magnitude in layer thickness. It should be noted that SRSCD necessarily depends on a large number of binding and migration energies and prefactors, some of which are not agreed upon in the literature. The simulation results are most sensitive to binding and migration energies of small clusters such as V_2 and HeV_2.

Changing any of these parameters changes the quantitative results of the simulation while (generally) keeping the qualitative results the same.

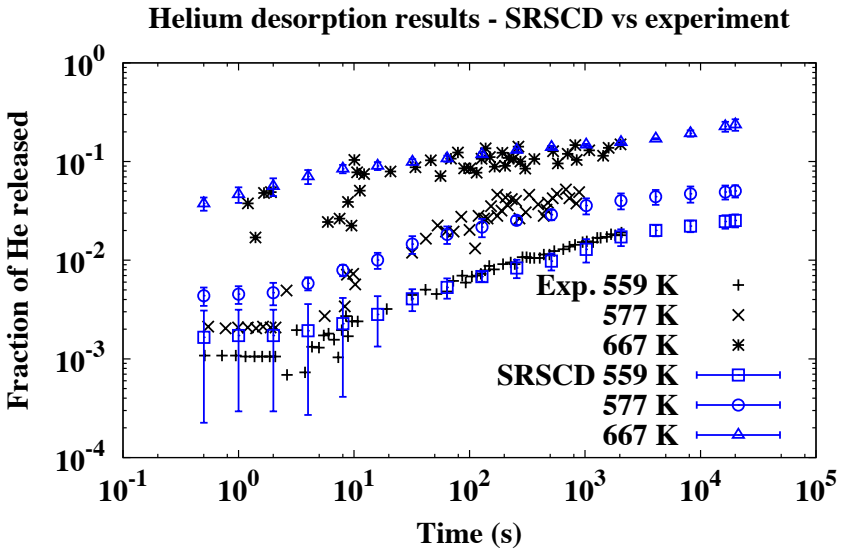

Figure 34: Fraction of helium released in desorption simulations, using experimental parameters given in Table 8.

4.3.2 Mechanisms of helium desorption through He_mV_n cluster migration

Unlike rate theory simulations, the capabilities provided by the SRSCD methodology allow for precise quantification of the mechanisms responsible for helium migration during the desorption process. In the rate theory simulations of Ortiz et al. [162], He_mV_n clusters are not mobile. Helium desorption therefore occurs either by substitutional replacement by interstitials SIA+HeV$\rightarrow$ He, which leaves a mobile interstitial helium atom behind, or by helium dissociation from HeV clusters. In either case, only mobile He interstitials can leave the free surface of the material. By contrast, studies of He_mV_n migration have shown that small clusters are in fact mobile [64, 216, 75, 28]. Helium release from the free surfaces of a thin Fe foil through He_mV_n cluster migration is a problem particularly well-suited to SRSCD, due to the size and timescale of the system and the number of mobile species involved. By allowing small He_mV_n clusters to migrate, new regimes during which the dominant mechanism of helium desorption changes can be found using SRSCD.

To study helium release from the free surface of the foil, every instance of helium leaving

the system through the free surface is recorded, along with the type of defect that carried the helium out and the simulated time. The simulated annealing time is then divided into intervals representing an order of magnitude increase in annealing time. The rate of helium desorption per cm^2 of surface area for each of the three main mobile defects containing helium (interstitial He, HeV_2, He_2V_3) is then plotted for each interval. The results of this analysis are shown in Figure 35.

The mechanism for helium release from the free surface of iron foils in this simulation is dependent on both temperature and time. In all simulations, HeV_2 clusters dominate initial helium release from the system. Mobile HeV_2 clusters are created first as vacancies combine with HeV clusters at early times (before 10^{-3} seconds at 559 K) and then as HeV_3 clusters release vacancies (up to tens of seconds at 559 K). Interstitial helium is very unlikely to reach the free surface before interacting and combining with vacancy clusters, preventing the release of interstitial helium at the free surfaces early in the simulation.

As time evolves and average cluster sizes increase, the number of HeV_3 defects present in the system decreases and the creation of HeV_2 becomes less common. At this point, the presence of He_mV_n clusters with $m > n$ becomes likely enough that dissociation of helium directly from these defects causes interstitial helium to be once again present in the material. This helium diffuses out of the material more easily than before, because the total defect density is less and interstitial helium is more likely to reach the free surface before being interacting with a vacancy or He_mV_n cluster. The intermediate presence of He_2V_3 clusters comes about in a similar manner to HeV_2, as the timescale becomes longer and more clustering and dissociation reactions become feasible. The mechanism and timescale of helium release varies from sample to sample due to the differences in initial defect density and temperature of annealing. In the 667 K simulations, a small number of He_2V clusters also dissociate from the free surface near the end of the simulation.

The migration and binding energies of small HeV clusters used in this simulation likely vary from the actual values somewhat. This is due to the fact that values for migration in Nb are used in place of Fe for HeV and HeV_3 clusters, and due to the fact that other cluster types not allowed to migrate here may be mobile (HeV_4, for example). Because the

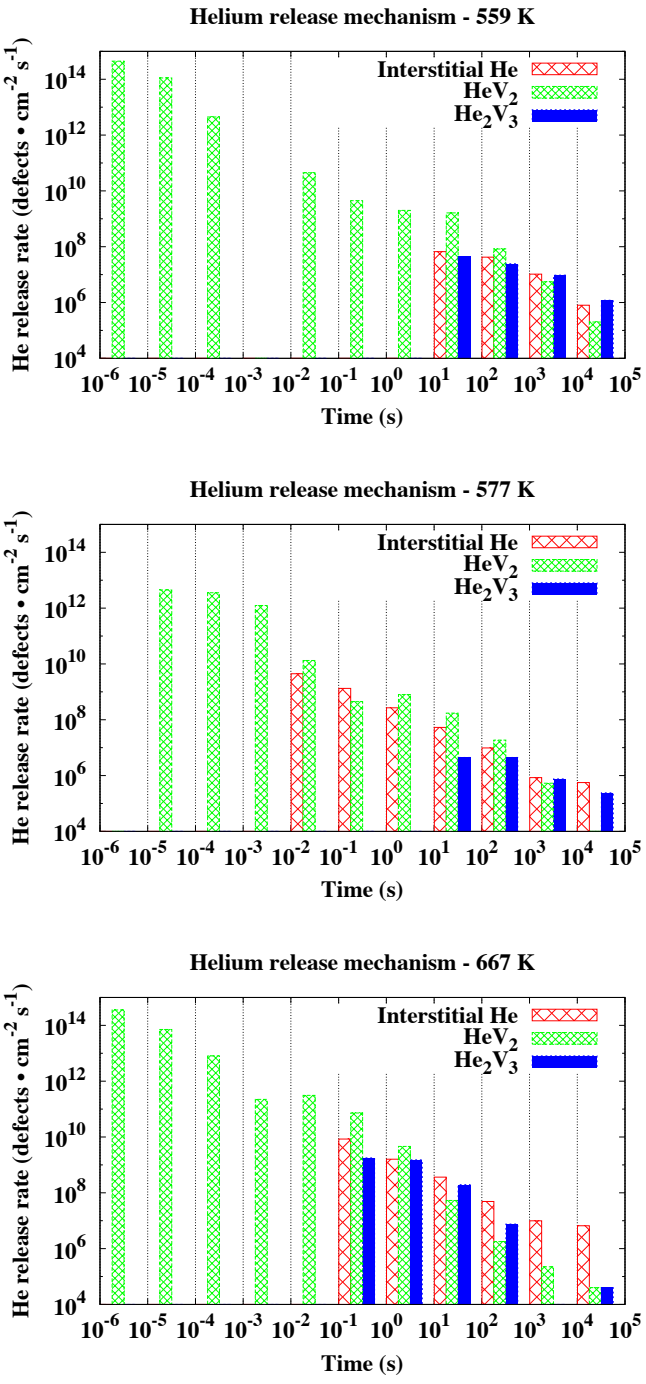

Figure 35: Release rates for time intervals of annealing of interstitial He, HeV_2, and He_2V_3 from iron foils for the three samples listed above. As time evolves, the mechanism of helium release shifts from HeV_2 to interstitial He and He_2V_3.

rate of He desorption is very dependent on the energetics of small HeV and V clusters, the qualitative results of this simulation should be emphasized over the quantitative results. As the parameters describing the behavior of helium, vacancies, and interstitials improve, the results of such simulations should match reality more closely.

In the analysis of Ortiz et al. [162], the initial helium release is caused by interstitial clusters dissociating at the annealing temperature and creating interstitial helium through substitution replacement reactions with HeV clusters. The subsequent, long-time annealing behavior is then caused by helium dissociation from He_mV_n clusters. However, their rate theory simulation does not account for mobility of small HeV clusters and therefore may not capture some of the effects described here.

4.3.3 Effective helium diffusivity in irradiated α-Fe thin films

The results of the simulations described in Sections 4.3.1 and 4.3.2 indicate that helium migration in irradiated materials is a complicated phenomenon, as helium-vacancy clusters have a range of mobilities depending on their content and the irradiation temperature. Therefore, in this section a more systematic study of the role of various irradiation and microstructural parameters on helium mobility is performed. These results can aid in the design of radiation-resistant materials by describing ideal grain sizes (using a thin film as a proxy for a single grain in this study) in engineered materials in order to enhance defect recombination and remove helium from the system.

Helium can occur in metals due to (n, α) reactions or direct implantation. Its subsequent behavior within the metal has a significant impact on the mechanical properties of the metal. In particular, the formation of helium bubbles can lead to effects such as hardening, embrittlement, and accelerated crack growth [112, 230, 179]. It is therefore important to understand the mechanisms responsible for helium diffusion and clustering in a variety of environments to predict the microstructural evolution and mechanical behavior of materials that operate in environments that expose them to helium damage.

The dominant mechanism for helium transport in metals depends on many variables, such as irradiation conditions (i.e. dpa, dpa rate), temperature, helium concentration, and

other defects present in the material [71, 221]. In irradiated metals, previous work [71, 221] has identified three temperature regimes in which different mechanisms dominate helium diffusivity, with each regime providing greater diffusivity than the previous: (1) cascade mixing at low temperatures $T < 0.2\ T_m$, (2) helium trapping at vacancies and subsequent replacement by self-interstitial atoms at intermediate temperatures $0.2\ T_m < T < 0.5\ T_m$, and (3) helium trapping at vacancies and diffusion with the assistance of a second vacancy at high temperatures $T > 0.5\ T_m$ (T_m being the melting temperature). Bubble formation is both a function of effective helium diffusivity and the density of potential bubble nucleation sites such as grain boundaries, bi-material interfaces, or clusters of impurities [230, 51].

These mechanisms suggest that effective helium diffusivity may not remain constant throughout the lifetime of a material as radiation damage accumulates. This effect has been observed in studies estimating the ages of natural minerals zircon and apatite, which contain naturally occurring uranium and helium from (n, α) reactions. Such studies depend on the effective diffusivity of helium in these materials, which decreases over time as the radiation damage accumulates and helium is trapped at damage sites [187, 88].

Models of effective helium diffusivity at intermediate temperatures in metals have focused on a substitutional mechanism of helium migration [221, 81, 173]. In these models, helium is trapped at vacancy sites and helium migration is characterized by jumps from vacancy to vacancy either through replacement with a self-interstitial or thermal dissociation. These mechanisms are thought to apply to all metals [221]. Such models for helium transport do not account for more complex damage states and helium-vacancy clustering. Molecular dynamics studies have shown that small helium-vacancy clusters such as HeV_2 and He_2V_3 are in fact mobile in iron [75, 216], while molecular statics simulations have determined the migration energy of HeV_2 and HeV_3 in Cu and Nb to be slightly higher than that of a single vacancy [64]. However, the relative importance of these migration mechanisms compared to the ones described above in controlling effective helium diffusivity are not known.

The present work focuses on the relationship between effective helium diffusivity in thin iron foils and total dpa, temperature, dpa rate, helium-to-dpa ratio, foil thickness, and

implantation type (Frenkel pair implantation vs cascade damage). To this end, two different methods are used: (1) object kinetic Monte Carlo (OKMC) [135], which is used here primarily for the sake of validation, and (2) spatially resolved stochastic cluster dynamics (SRSCD) [63]. As OKMC simulations track each defect within a given volume they provide atomic scale spatial resolution of complex systems at the expense of relatively large computational cost. OKMC is therefore used here to study helium diffusivity within a baseline set of implantation conditions (see Table 10) and the results are compared to simulations using SRSCD. Stochastic cluster dynamics has been shown to efficiently simulate radiation damage in systems with multiple chemical species and timescales greater than 10^4 seconds in thin foil annealing simulations [131, 63]. This method results in loss of spatial resolution below the scale of the volume elements chosen but, given an appropriate choice of simulation volume, can result in shorter computation times than OKMC, allowing for the study of effective helium migration over a large spectrum of conditions.

Effective helium diffusivity is found in this study to be strongly dependent on implantation conditions. Diffusivity decreases with increasing total dpa and decreasing dpa rate. Layer thickness, He-to-dpa ratio, and implantation type (cascade vs Frenkel pair) are also shown to impact helium diffusivity to varying degrees. Both the chemical species responsible for the majority of helium migration and the presence of barriers to helium migration vary with temperature, implantation rate, total dose, and implantation type. Therefore, helium diffusivity does not follow a traditional Arrhenius law with a constant effective migration energy. The physical mechanisms responsible for these changes in diffusivity are investigated in the following sections under a range of implantation conditions.

4.3.3.1 Material parameters and irradiation conditions

In this study, helium diffusivity in thin iron foils is studied under a range of implantation conditions. The effect of temperature, total dpa, dpa rate, He/dpa ratio, layer thickness, and implantation type (20 keV cascades vs Frenkel pairs) on effective helium diffusivity is quantified. Irradiation conditions used in this study are given in Table 10.

Allowed defects and reaction rates are the same as listed in Section 4.2 and in Table 1,

Table 10: Table of implantation conditions used in simulations. The effect of changing each parameter on effective diffusivity of helium was studied.

Default implantation	
Thickness	200 nm
dpa rate	10^{-4} dpa·s^{-1}
Helium to dpa ratio	2×10^{-2}
Total dpa	10^{-5} to 10^{-2} dpa
Implantation type	20 keV cascades
Quantities varied	
Temperature	273 K to 673 K
dpa rate	10^{-6} to 10^{-2} dpa·s^{-1}
Helium to dpa ratio	2×10^{-1} and 2×10^{-2}
Thickness	50 nm, 200 nm, and 800 nm
Implantation type	Frenkel pairs and 20 keV cascades

respectively. These represent the standard set of defect parameters for radiation damage evolution in α-Fe used in the majority of this dissertation. Migration and binding parameters for Fe used in the OKMC and SRSCD simulations are found in Table 7. The migration and binding parameters used here for vacancies, self-interstitials and their clusters have previously been shown to successfully reproduce experimental results [39].

4.3.3.2 Calculating effective He diffusion - methodology

The effective diffusivity of helium is calculated differently in OKMC and SRSCD simulations, due to their different treatment of spatial resolution. The OKMC simulation calculates effective diffusivity D of each helium atom using the Einstein formula [157]:

$$D = \frac{1}{6}\frac{(\vec{r}_{\mathrm{f}} - \vec{r}_{\mathrm{i}})^2}{N\triangle t}, \tag{83}$$

where $\vec{r}_{\mathrm{i}}$ and $\vec{r}_{\mathrm{f}}$ are the original and the final coordinates, respectively, of each helium atom, N is the total number of He atoms in the simulation box and $\triangle t$ is the elapsed time. The results are then averaged to find the overall effective diffusivity of helium in the system. Note that this method accounts for the helium atoms that still remain in the simulation box when the simulation finishes, regardless of the type of defects they belong to. He atoms released from the free surface are not included in the calculation of effective diffusivity.

In SRSCD, effective diffusivity of helium is calculated using the fraction of implanted

helium retained in the material after irradiation. This percentage is then fitted to a gradient-driven diffusion model that ignores the effects of various helium-defect interactions and instead assumes all helium has constant (effective) diffusivity D. To calculate effective diffusivity using a simple gradient-driven diffusion model, we first solve the relevant diffusion equation for the concentration of helium C in our thin film:

$$\frac{dC}{dt} = \nabla \cdot (D \cdot \nabla C) + f_0 \tag{84}$$

where f_0 is the source term for helium, a known constant in these simulations. Given a thin film with thickness L, normal in the $x-$direction and zero concentration at $x = 0$ and $x = L$, this equation becomes one dimensional by symmetry and (assuming constant effective diffusion D) has a solution given by:

$$C(x,t) = -\frac{4f_0}{DL}\left(\sum_{n\in\text{odd}}\left(\frac{L}{n\pi}\right)^3 \sin\left(\frac{n\pi x}{L}\right) e^{-\frac{n^2\pi^2 D}{L^2}t}\right) + \frac{f_0(Lx - x^2)}{2D} \tag{85}$$

To solve for the effective diffusivity, we state that the helium remaining in the system must equal the fraction helium retained F as calculated in the full SRSCD simulation at time t_0. Therefore, we have:

$$F\int_0^{t_0} f_0 AL dt = \int_0^L C(x,t_0) A dx \tag{86}$$

where A is the cross-sectional area of the sample. Integrating, we get the equation for the effective diffusion D of helium:

$$t_0 F = \frac{L^2}{12D} - \frac{8L^2}{D}\left(\sum_{n\in\text{odd}}\left(\frac{1}{n\pi}\right)^4 e^{-\frac{n^2\pi^2 D}{L^2}t_0}\right) \tag{87}$$

All constants in this equation are known, and it can be solved numerically for the effective diffusion rate. In this work, the number of terms in the series expansion used is varied to assure convergence of the solution.

Due to the difference in methodology for measuring effective helium diffusion between OKMC and SRSCD methods, it is important to verify that the effective diffusion D given

by each method is equivalent. The effective diffusivity of helium in a simulated 200 μm iron foil at 273 K and 373 K implanted using the default implantation conditions given in Table 10 is shown as a function of dpa in Figure 36 using both OKMC and SRSCD. Both methods are in good agreement in the range of dpa used in this simulation. This indicates that the methodology developed in this work for estimating effective helium diffusivity using SRSCD is both computationally efficient and reliable.

In the following sections, combined helium and Frenkel pair or cascade damage is carried out in SRSCD using the implantation conditions given in Table 10 in α-Fe thin films, and the effective diffusivity is estimated using the SRSCD methodology described above. The impact of various microstructural and irradiation conditions on effective diffusivity is investigated and mechanisms for helium migration are discussed.

4.3.3.3 Effective diffusivity with increasing total dose

The effect of total radiation dose (in dpa) on the effective diffusivity of helium in samples with implantation conditions given in Table 10 is first investigated. Temperatures from 273 K - 673 K are used to create Arrhenius plots in which the logarithm of effective diffusivity D is plotted as a function of the inverse temperature, with the total dose ranging from 10^{-5} to 10^{-2} dpa. The results are shown in Figure 37. A standard thermally activated process, such as the diffusion of interstitial helium in α-Fe, has functional form:

$$D = D_0 e^{\frac{-E_m}{k_b T}} \tag{88}$$

An Arrhenius plot of a functional form of this type will appear as a straight line, with the y-intercept given by D_0 and the slope of the line given by $-E_m$. Unlike the Arrhenius plots for standard thermally activated processes, the Arrhenius plots for diffusivity D generated by SRSCD are nonlinear at high temperatures, and increasingly so for higher displacement doses. This indicates a change in the migration mechanism of helium at high temperatures. The physical nature of this amplified helium diffusivity at high temperatures is discussed in Section 4.3.3.6.

As the total total displacement dose is increased, the effective diffusivity of helium

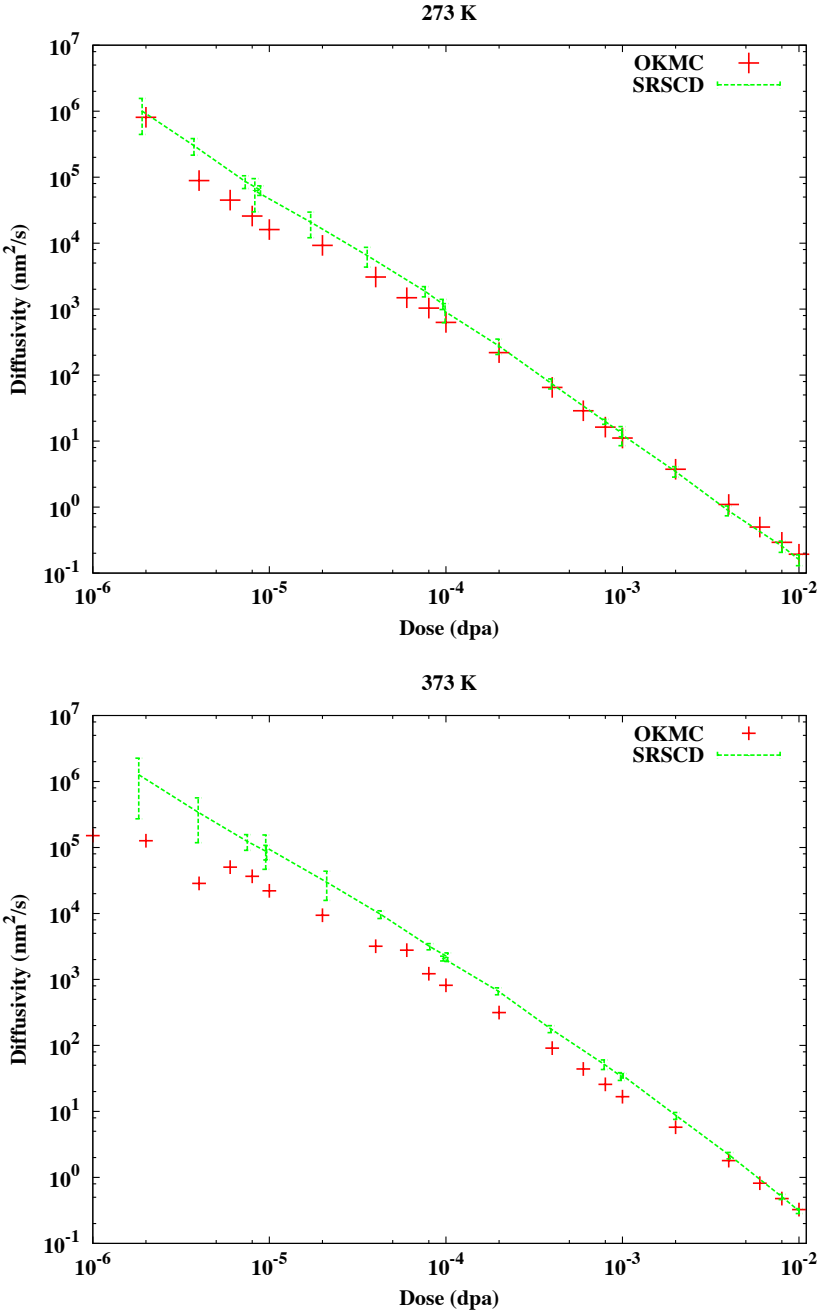

Figure 36: Effective helium diffusivity in a simulated 200nm iron sample implanted to 10^{-2} dpa at 273 K and 373 K. OKMC and SRSCD provide good agreement in effective helium diffusivity over the range of dpa simulated here.

decreases significantly at all temperatures studied here. As dpa increases, more vacancies and clusters are present in the material. These act as sinks for implanted interstitial helium and decrease its range of migration, thus decreasing effective diffusivity.

In the low temperature linear regions of the Arrhenius plots, effective migration energies are between 0.02 - 0.06 eV, indicating that the process that governs helium migration is dominated by a low activation energy mechanism. Most mobile helium is in the form of interstitial helium implanted in the material before it is trapped by a vacancy or vacancy cluster. This mobile helium has a migration energy of 0.077 eV (see Table 7), and is thought to be the dominant species responsible helium mobility at low temperatures. The effective migration energy for helium found here is even lower than the migration energy of interstitial helium because the population of small, mobile He_mV_n clusters decreases and larger immobile clusters form as temperature increases. The increase in diffusivity at higher temperatures is also discussed in Section 4.3.3.6.

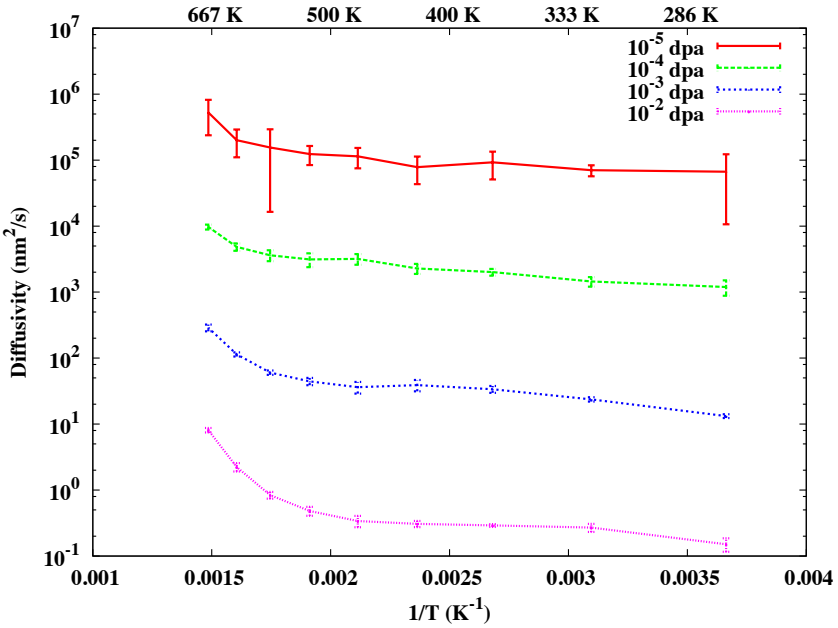

Figure 37: Arrhenius plots for effective helium diffusivity for several values of total dose. Other implantation conditions are given in Table 10.

4.3.3.4 Effective diffusivity with increasing dose rate

The effect of dpa rate on the effective diffusivity of helium was also studied. Dose rates from 10^{-12} to 10^{-2} dpa·s^{-1} are investigated. The results shown here correspond to a total dose of 10^{-2} dpa. All other implantation conditions are listed in Table 10. The dpa rates simulated represent the damage rates spanning fission, fusion, and ion implantation [37, 121, 190, 35, 66, 193]. At low dpa rates, no defects are left in the simulated volume at the end of the simulation and therefore effective diffusion could not be quantified using SRSCD. The results of estimated helium diffusivity as a function of dpa rate for rates ranging from 10^{-6} to 10^{-2} dpa·s^{-1} are shown in Figure 38.

As the damage rate decreases, the effective diffusivity of helium also decreases for all temperatures in this simulation except in cases where the material is completely defect-free at the end of the simulation. This is a somewhat counter-intuitive result, as the lower dpa rate simulations result in less total damage in the system, indicating that more defects travel to the free surface. However, since most helium diffusivity occurs immediately after implantation in the material, the amount of time that helium is trapped at sinks increases as dpa rate decreases. Therefore, decreasing the implantation rate also decreases the effective diffusivity of helium.

Here, as in the previous section, the Arrhenius plots of effective diffusivity are not linear with temperature, indicating a shift in the dominant migration mechanism for helium as temperature increases. Results are not shown in Figure 38 for the lowest dpa rate (10^{-6} dpa·s^{-1}) at the highest temperature (673 K) because the material became completely annealed at this particular choice of implantation conditions, causing an effective vertical asymptote in helium diffusivity between 623 K and 673 K. The physical mechanism causing these behaviors is discussed in Section 4.3.3.6.

4.3.3.5 Effects of layer thickness, He/dpa ratio, and implantation type

The effect of varying layer thickness, He/dpa ratio, and damage in the form of Frenkel pairs or cascades on the effective diffusivity of helium was also studied. Values of implantation conditions used are shown in Table 10. Arrhenius plots showing effective diffusivity for

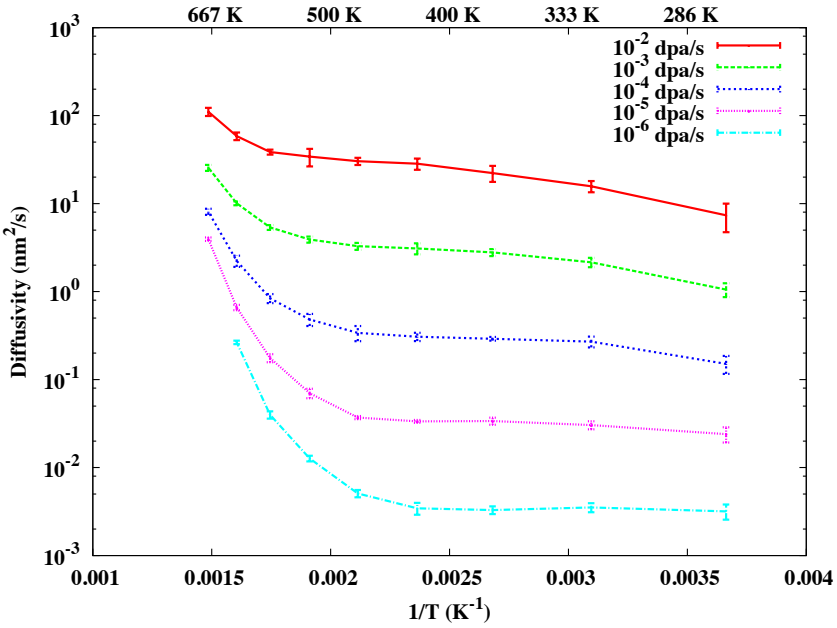

Figure 38: Arrhenius plots for effective helium diffusivity at a dose of 10^{-2} dpa for several values of implantation rate. Implantation conditions are given in Table 10.

these various simulated implantation conditions are shown in Figure 39.

At low temperatures, effective helium diffusivity is independent of layer thickness. However, narrower layers accumulate fewer defects due to the larger interface to volume ratio. Above 675 K, first the 50 nm layer and then the 200 nm layer become completely annealed as temperature increases, creating a vertical asymptote in effective diffusivity similar to the one seen at low dpa rates and high temperatures. The values for effective diffusivity in the 50 nm and 200 nm layers at very high temperatures shown in Figure 39 are only rough estimates due to the very small number of helium atoms (less than one on average) remaining in the simulation volume. The temperature at which this completely annealed behavior occurs increases with layer thickness.

Helium to dpa ratio is not shown to strongly influence helium diffusivity when increased by an order of magnitude from the value in typical helium implantation experiments. The number of stable sinks for helium is dependent on the vacancy content of the system and not the helium content. Therefore, the introduction of a greater quantity of helium in the system with the same number of vacancies and self-interstitials simply resulted in $\mathrm{He}_m\mathrm{V}_n$

clusters with a larger ratio of m to n without changing the density of sinks for interstitial helium.

Frenkel pair implantation is shown to have a strong effect on helium diffusivity at both high and low temperatures. Due to the tendency of thin foils implanted with Frenkel pairs to release all defects from the free surface at high temperatures, a lower temperature range of 173 K - 423 K was studied with Frenkel pair implantation. Unlike the cascade results (which are shown from 273 K - 673 K in Figure 39), the Arrhenius plot of helium diffusivity with Frenkel pair implantation seems to display three major regimes for effective diffusivity: (1) a low-temperature region where the effective helium diffusivity is low but the slope of the Arrhenius plot is relatively high, (2) an intermediate region where effective helium diffusivity remains relatively constant, and (3) a high-temperature region where diffusivity increases with temperature, similar to the high-temperature region of the cascade implantation Arrhenius plot. The mechanisms responsible for the changing diffusivity in each of these three regions will be discussed in the next section.

4.3.3.6 Migration mechanisms with cascade implantation

In order to study the physical mechanisms responsible for the nonlinear behavior observed in the Arrhenius plots, the species of helium or helium-vacancy cluster that migrates out of the free surface of the thin iron foil is recorded in the SRSCD simulations. This provides information on the species responsible for the majority of helium migration at various times and temperatures.

At all temperatures and times studied with cascade implantation, the dominant species responsible for helium release at the free surface is interstitial helium. A non-negligible fraction of helium released at low temperatures and high dpa are in the form of mobile HeV_2 and He_2V, but as temperature increases these defects become less common. Mobile He_mV_n clusters are therefore not responsible for the strongly increased helium diffusivity at high temperatures. In addition, the rate of helium dissociation from He_mV_n clusters is never high enough for this to be a significant contributor to mobile interstitial helium in the system, and recombination of He_1V_1 clusters with self-interstitial atoms (releasing

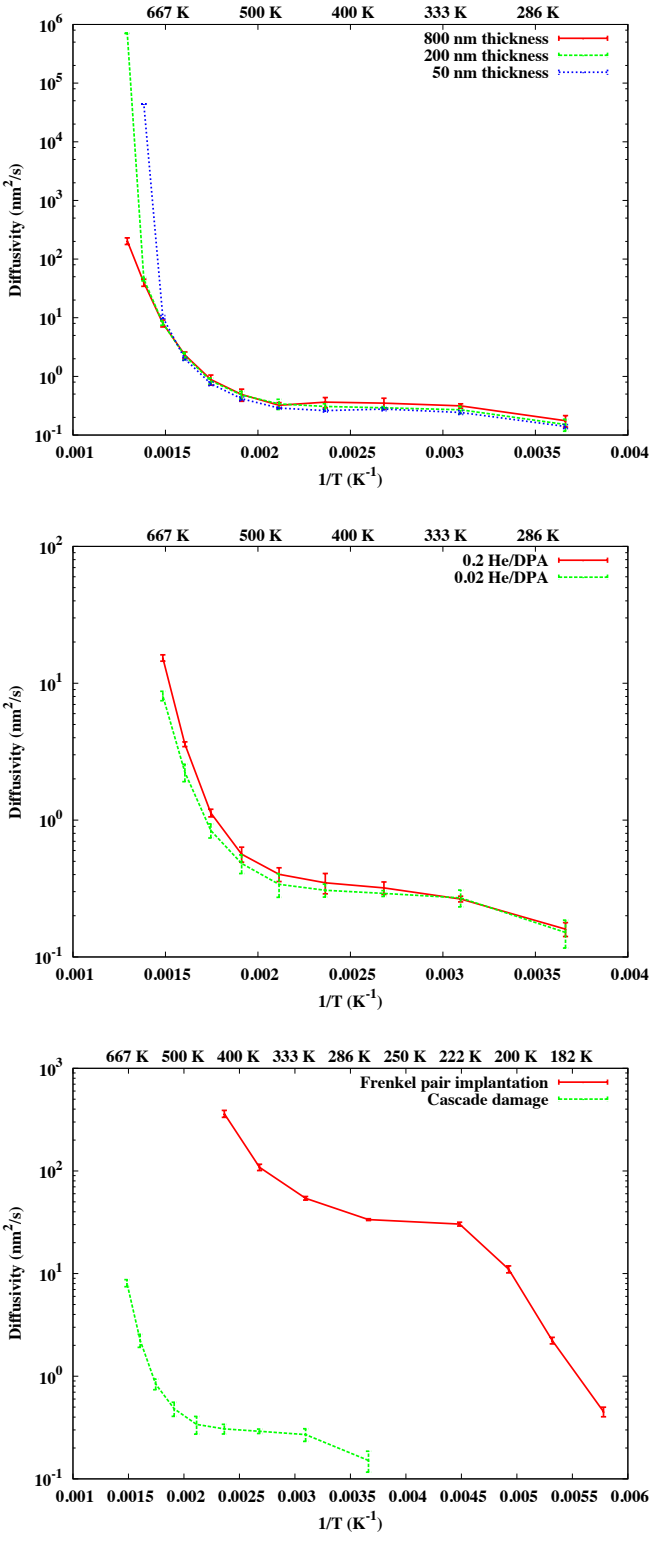

Figure 39: Effect of changing layer thickness thickness, He/dpa ratio, and implantation type on effective He migration in thin Fe films. All simulations represent 10^{-2} dpa at 10^{-4} dpa·s^{-1}.

an interstitial helium) also becomes less likely as temperature increases. Therefore the dominant source of mobile helium in these simulations is interstitial helium immediately after it is implanted in the material, before it has been trapped at a vacancy cluster or released from the free surface.

This observation is in agreement with effective diffusivity decreasing both with increasing dpa and decreasing dpa rate. As the total dpa increases, the number and size of sinks for helium increases, limiting its mean free path before it becomes trapped and immobile. As dpa rate decreases, assuming other helium in the system is trapped and immobile, the amount of time between implantation events of mobile interstitial helium atoms is greater. Therefore, the ratio of trapped helium to interstitial helium is higher at lower dpa rates, and the effective helium diffusivity decreases.

At high temperatures, greatly increased helium diffusivity is observed, especially at low dpa rates and high total dpa. However, as previously stated, the dominant mechanism for helium diffusion in these simulations is still interstitial helium directly after implantation, before trapping at a sink (usually a He_mV_n cluster). The cause of this greatly increased helium diffusivity can instead be seen by comparing the rate of helium release from the material to the volume density of defects in the material. This comparison is shown in Figure 40. The volume density of defects in the material greatly decreases at 673 K, due to the activation of vacancy dissociation from V_n and He_mV_n clusters. At this temperature, vacancies are able to quickly escape the system or become trapped at the relatively small number of large He_mV_n clusters. Therefore, few V_n clusters remain and interstitial helium atoms can migrate long distances before they are trapped, greatly increasing the effective diffusivity of the system.

This effect is most pronounced at low dpa rates and low layer thicknesses because vacancy clusters can more easily dissociate and escape through the free surface in between helium implantation events. In the extreme case, all defects are released at the free surface and no implanted helium is trapped in the material. At high temperatures, low dpa rates, and low layer thicknesses, these materials could remain essentially defect-free within the

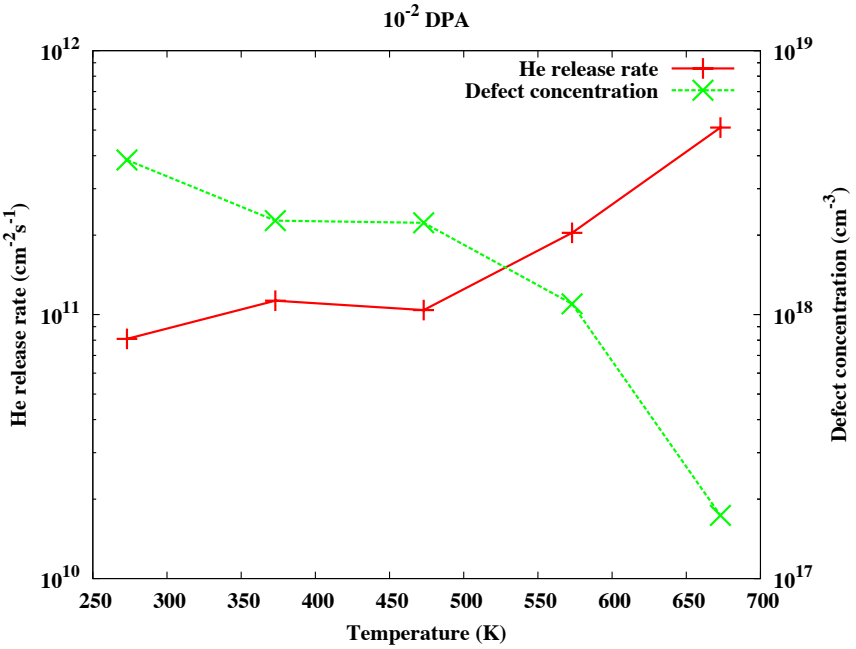

Figure 40: Release rate of interstitial helium from the free surface of thin iron foils compared to the density of defects contained in the foils as a function of temperature. Results are shown at 10^{-2} dpa.

limit of the approximation that the free surface acts as a perfect sink. It is therefore interesting to note that the dpa rates expected in fusion first walls and fission pressure vessel chambers are lower than in the simulations presented here [193, 37, 121, 190, 35, 66]. Simulations at those dpa rates resulted in no defects in the material at the end of the simulation and were unable to estimate effective diffusivity.

4.3.3.7 Migration mechanisms with Frenkel pair implantation

Frenkel pair-implanted thin films show significantly different effective diffusion behavior than cascade damage given the same dpa rate, He/dpa ratio, and other implantation conditions. In the previous section, three regions of temperature were shown to exhibit three types of effective diffusion behavior. By analyzing the types of helium clusters escaping through the free surface of the material as a function of temperature, we can study the mechanisms responsible for effective helium migration in these three regions. Figure 41 shows the rate of release of interstitial helium and small He_mV_n clusters at 173 K, 273 K, and 373 K. In all cases, the mechanism for effective helium diffusivity is more complex

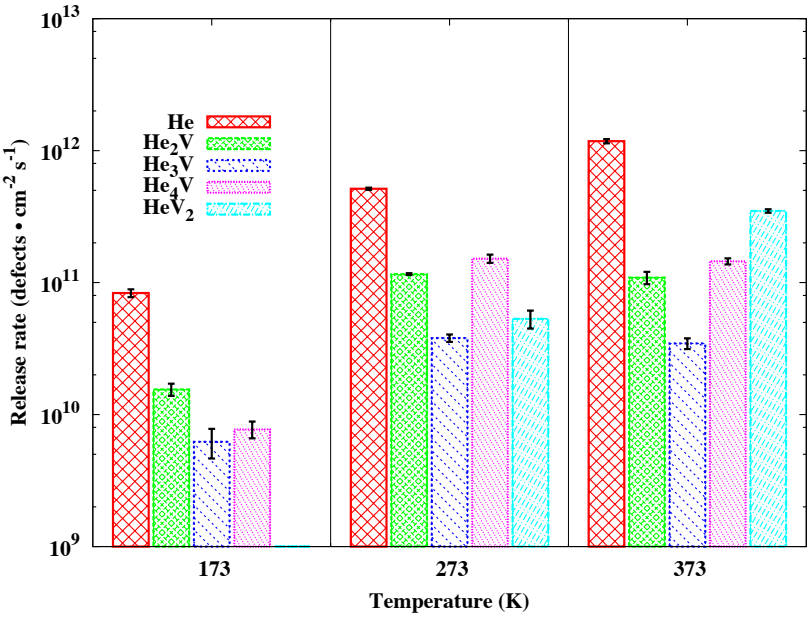

Figure 41: Mechanisms of He release from the free surface of a 200 nm Fe thin foil during implantation to 10^{-2} dpa with Frenkel pairs and interstitial He.

than in the case of cascade implantation. By studying both helium release and the density and type of defects in the material, we arrive at the following conclusions about helium diffusivity under Frenkel pair implantation:

1. At 173 K, helium release is mixed between interstitial helium and small clusters such as He_2V_1, He_3V_1, and He_4V_1. Most immobile helium at these temperatures is in the form of He_1V_1, He_2V_2, He_3V_2, or He_4V_2 clusters. Thus, helium mobility is governed by substitutional replacement of immobile He_mV_n clusters to form mobile He_mV_{n-1} clusters. The effective migration energy of helium at this stage, given by the slope of the Arrhenius plot, is approximately 0.33 eV.

2. At 273 K, the substitutional replacement mechanisms for helium release are still significant, but the overall density of defects in the material has decreased. In addition, the fraction of helium trapped in clusters that cannot easily become mobile has increased at this temperature range. Therefore, a greater fraction of implanted helium is either released immediately from the material or is trapped permanently at a sink,

and the effective migration energy in this region is greatly reduced to approximately 0.02 eV.

3. At 373 K, as in cascade simulations at high temperatures, vacancy dissociation and escape through the free surface allows the material to 'clean up' internally, decreasing the total defect concentration in the material. This leads to an increase in effective helium diffusivity that is nonlinear on the Arrhenius plot. The fact that this effect occurs at lower temperatures in Frenkel pair implantation than cascade implantation is due to the smaller average size of vacancy clusters, which have lower binding energies. Note also that the increased diffusivity of vacancies has made the HeV_2 mechanism a viable release mechanism at this temperature, contributing to the increased effective migration energy as well.

4.3.4 Summary

In Section 4.3, SRSCD simulations of helium implantation and subsequent evolution inside α-Fe thin films are used to demonstrate the complicated nature of helium mobility in irradiated metals. Implantation and desorption results show that the species responsible for helium desorption from implanted α-Fe thin films evolves as a function of implantation conditions and annealing time. A more detailed study of the effective diffusivity of helium implanted in α-Fe thin films under a variety of microstructure and irradiation conditions confirms this observations, and several regimes are identified in which helium migration is dominated by various effects such as substitutional replacement, migration of small HeV clusters, and so on.

These results highlight the benefits of simulation techniques such as SRSCD, which can efficiently compute effective diffusivity over a wide range of input parameters while including complicated defect behaviors in the model such as HeV_2 diffusivity and reaction rates for clustering of defects that diffuse in a mixed 1D-3D fashion. These capabilities allow simulation of a larger range of input space than traditional models, including damage content at radiation doses that can be compared directly to experiments, as discussed in

the following section.

4.4 Neutron damage accumulation over long timescales: application to bulk materials

In this section, SRSCD is used to simulate radiation damage accumulation in neutron-irradiated coarse-grained α-Fe. These simulations are used to investigate aspects of cascade damage at intermediate and high doses, such as the impact of the interaction between displacement cascades and defects already present in the material. In addition, the computational efficiency of SRSCD allows direct comparison between simulated defect populations and experimentally measured populations using TEM and PAS techniques [67, 259]. In Section 4.4.1, the irradiation conditions and simulation parameters used in this study are defined. Next, three aspects of damage accumulation in neutron-irradiated coarse-grained iron are investigated: (1) the effect of interactions between displacement cascades and defects already present in the material (Section 4.4.2), (2) the impact of the PKA energy of a displacement cascade on damage production and subsequent accumulation (Section 4.4.3), and (3) the impact of impurities such as carbon that act as pinning points for SIA loops on defect statistics (Section 4.4.4). Finally, using the information gained in the previous three sections, neutron damage is simulated using irradiation conditions that best match experimentally reported iron irradiation conditions [67] and damage accumulation is compared to experimental results in Section 4.4.5.

4.4.1 Description of simulation and methodology

In this study, damage accumulation is simulated using the material and irradiation conditions reported by Eldrup et al. [67]. Cascade damage accumulation is simulated in SRSCD using the adaptive meshing scheme described in Section 3.3.3. The relevant irradiation conditions are shown in Table 11. Two parameters are varied to study their effect on the damage microstructure: the cascade energy (in keV) and the concentration of traps for mobile 1-D SIA loops (in ppm). In the latter case, when SIA loops encounter traps, they become immobile permanently. In addition, two mobile SIA loops that join to form a cluster are assumed to create an immobile SIA loop [217].

Table 11: Simulation parameters for neutron irradiation of coarse-grained iron. Parameters are chosen to match the experiment of Eldrup et al. [67]. Cascade energy and SIA loop trap density are treated as parameters and their effect on defect microstructure is discussed in the next section.

Simulation Parameters		
Temperature	343	K
Dose rate	7×10^{-7}	dpa·s^{-1}
Grain size	33	μm
Initial dislocation density	1×10^{-5}	nm^{-2}
Cascade energy	1-50	keV
SIA loop trap density	5-120	ppm

Damage is introduced in the form of surviving defects formed in displacement cascades. These displacement cascades are taken from atomistic simulations performed by Stoller et al. [204, 203]. The cascades are first annealed for 10 ps in the OKMC code MMonCa [135] in order to allow only reactions triggered automatically by proximity to occur. By doing so, the defects input into SRSCD include all clusters formed during the cascade itself. Radiation dose (in dpa) is calculated directly from the number of surviving displaced atoms in the cascade after the thermal spike phase divided by the number of lattice atoms in the simulated volume.

The defects modeled in these simulations are:

1. *Single defects:* these are self-interstitial atoms (SIA) or vacancies (V). These defects migrate in three dimensions and can cluster or annihilate with other defects [207, 74].

2. *Vacancy clusters:* these are treated as spherical clusters in SRSCD. Small vacancy clusters are mobile and can migrate [74], cluster, and annihilate with self-interstitial atoms. Single vacancies can dissociate from vacancy clusters.

3. *Self-interstitial clusters size 2-4:* these SIA clusters migrate in three dimensions [74] and are treated as spherical clusters in SRSCD.

4. *Larger mobile self-interstitial clusters:* these defects are treated as 1D diffusing circular dislocation loops [198]. Diffusion of larger SIA clusters between volume elements cannot be restricted to a single crystallographic diffusion direction due to the mean-field formulation of SRSCD. However, their reaction rates for interaction with other

defects reflect 1D migration and circular geometry (see Table 1).

5. *Larger immobile self-interstitial clusters:* these SIA clusters are formed when two mobile SIA clusters meet and form a junction [217] or a mobile SIA cluster encounters a trap. In SRSCD, these defects are treated as immobile circular clusters.

The parameters for migration and binding energies and diffusion prefactors for vacancies and self-interstitials and their clusters in iron used in this study are the same as in [59] and are given in Table 7.

Due to the stochastic nature of SRSCD, significant variation can occur between simulations using the same input parameters. In this study, most simulations are carried out 5 times and the average result is plotted along with the standard deviation for each data point. At high values of dpa (above 10^{-2} dpa), only one simulation is carried out due to computational limitations.

4.4.2 Investigation of interactions between displacement cascades and defects

Cascade damage in metals involves temporary displacement of many more atoms during the cascade's thermal spike than are finally present as stable defects at the end of the cascade event [199]. If a defect already present in the region in which lattice atoms are displaced during the thermal spike, that defect may interact with the cascade causing the formation of larger clusters. Therefore, the direct interaction of cascades with defects already present in the material should influence the evolution of point defect concentrations in such materials. Although cluster dynamics models typically include schemes for introducing cascade damage [22, 245, 123], direct cascade-defect interactions during the thermal spike phase are generally not taken into account. Instead, in SRSCD, all interactions occur by diffusive mixing. At low amounts of accumulated damage, the probability of an implanted cascade overlapping spatially with an existing defect is low. As the dose increases, however, direct cascade-defect interactions become more likely. Therefore, the effective size for interaction of the cascade and the behavior of the defects that encounter cascades are important parameters for accurately simulating displacement cascades at intermediate and high doses in SRSCD.

The effect of a cascade interacting with point defects present in a material has not

been fully characterized in the literature. Cascade-defect interactions may cause complex behaviors such as cluster breakup in a real material [248]. In SRSCD, interactions between pre-existing defects with cascades cannot be directly simulated. Instead, in this work an assumption is made about how cascades interact with defects during the thermal spike: all defects that lie within the volume of the cascade during the thermal spike phase are assumed to combine with cascade defects randomly. Therefore, although cascade-defect interactions are not considered in the OKMC simulations used to anneal cascades for use as inputs in SRSCD, the treatment of cascade-defect interactions in SRSCD is intended to approximate these interactions.

To carry out this approximation using the adaptive meshing technique for cascade implantation discussed in Section 3.3.3, the probability p for a given defect in the fine mesh to combine with the cascade is given by:

$$p = \frac{V_{\text{casc}}}{V_{\text{fine}}} \tag{89}$$

where V_{casc} and V_{fine} are the cascade and fine mesh volumes, respectively. Note here that V_{fine} represents the volume of the entire fine mesh. When a cascade event is chosen by the SRSCD algorithm, existing defects in the fine mesh are first randomly combined with defects in the cascade according to the probability above, and the resulting modified cascade is then added to the fine mesh. The cascade volume V_{casc} is taken to be the effective volume of the cascade for interacting with defects present in the metal, and is treated as a parameter here.

The cascade mixing procedure is carried out such that the correct number of pre-existing defects is combined with the cascade according to the assumption above. However, the distribution of pre-existing defects left over after the cascade mixing procedure is carried is still homogeneous throughout the fine mesh, instead of combining those defects with the cascade preferentially towards the center of the fine mesh where the cascade is implanted. The effect of this approximation is likely to be significant only when the number of pre-existing defects in the fine mesh is large, at high doses.

The cascade volume V_{casc} is taken to be the approximate volume of the cascade during

Table 12: Cascade energies (in keV) and volumes (in nm^3) used in this simulation. Cascade volumes were used to determine the probability of ballistic mixing of defects in the cascade with defects already present in the material.

Energy (keV)	Volume (nm^3)
1	35
5	350
10	700
20	1000
50	4000

the thermal spike phase. This volume is estimated for smaller cascades by placing a rectangular box around all of the surviving defects in the cascade. The cascade is assumed to have occupied the entire volume of the box during the thermal spike phase, allowing it to interact with any defects already present within that volume. For larger cascades, due to their sub-cascade structure, volume is estimated by fitting smaller cubic boxes around the cascade defects. To verify this method of estimating cascade volume, defect accumulation to 10^{-1} dpa is simulated using 20 keV cascades at several values of V_{casc}. By varying V_{casc}, a value is chosen so that the results best fit the experimental results of Eldrup et al. [67]. The cascade volume obtained in this way was similar to the results of the geometric estimation of cascade volume. The volumes obtained in this way are considered to be first approximations of the cascade volumes. Table 12 shows the cascade energies and volumes used in this study.

The evolution of the concentration of vacancy and interstitial clusters as a function of dpa is shown in Figure 42a with and without cascade-defect interactions. Two main conclusions can be reached from this figure: first, vacancy concentrations more closely match experimental results [67] when cascade-defect interactions are taken into account (see Section 4.4.5 for comparison with experimental results). Second, the effect of cascade recombination on the defect microstructure using this method is significant above 10^{-2} dpa. The sensitivity of defect accumulation results to cascade size is shown in Figure 42b, using vacancy concentration as a metric to compare the impact of cascade volume on defect concentration. The approach taken here should be thought of as a first attempt at capturing the effect of cascade-defect interactions and needs more refinement to accurately capture

defect evolution at high doses. The preliminary nature of this model is a likely cause for the early saturation of the defect concentrations and decrease in SIA concentrations at high doses shown in Figure 42. Further atomistic studies on cascade-defect interactions are necessary to inform future iterations of this model.

4.4.3 The impact of PKA energy on damage accumulation

When a metal is subjected to neutron irradiation, the displacement damage that is created results from a wide variety of PKA energies [2, 116]. By contrast, simulations of damage accumulation with displacement cascades typically use only a single cascade energy. Therefore, it is important to understand the role of varying the PKA energy of displacement cascades on damage accumulation [54]. In this work the effect of cascade energy on damage accumulation is studied by introducing displacement cascades in iron at PKA energies from 1-50 keV at a constant dpa rate. For each PKA energy the average vacancy and SIA cluster sizes are shown as a function of dose in Figure 43 and the evolution of the concentration of vacancy clusters and SIA clusters with dose is shown in Figure 44.

Except for the case of 1 keV cascades, in which self-interstitial clusters dominate in the defect evolution, all other cascade energies produce qualitatively similar results for both defect size and concentration in the studies performed here. This is in agreement with the work of others [22, 202], which concludes that the long-term damage microstructure is not sensitive to the initial cascade conditions. Increasing concentrations of defects were found for larger cascade sizes, indicating greater defect recombination in smaller cascades; however, it is expected that for cascades larger than those studied here, this trend will not continue as high-energy cascades are typically composed of several smaller sub-cascades [204]. Thus, although cascades created by neutron irradiation are present in a distribution of PKA energies [22], experimental irradiation of iron is compared in this study to SRSCD simulations using a single cascade energy of 20 keV.

4.4.4 The effect of traps for SIA loops on microstructure

SIA clusters in the form of $\frac{1}{2}\langle 111\rangle$ dislocation loops diffuse much more rapidly in iron than other defect types [198]. In this simulation, SIA loops have diffusivity approximately three

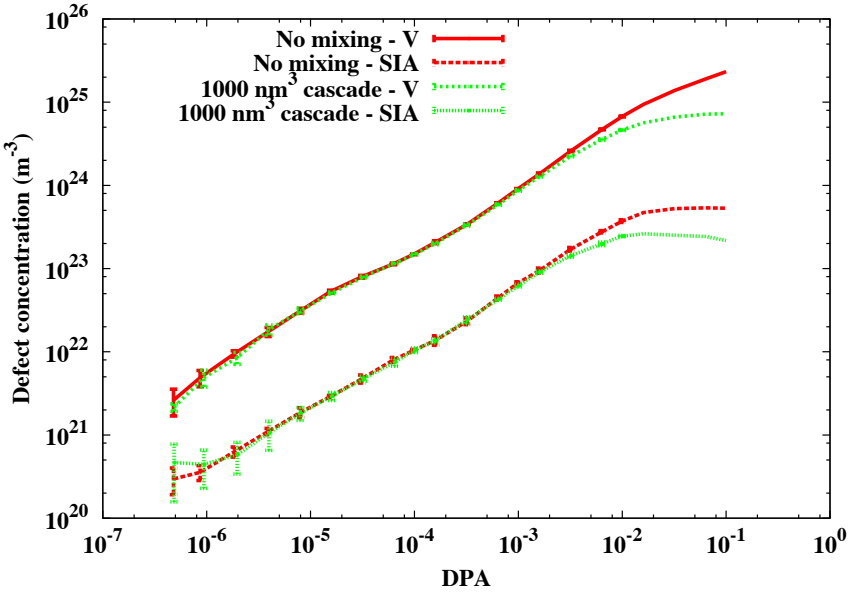

(a)

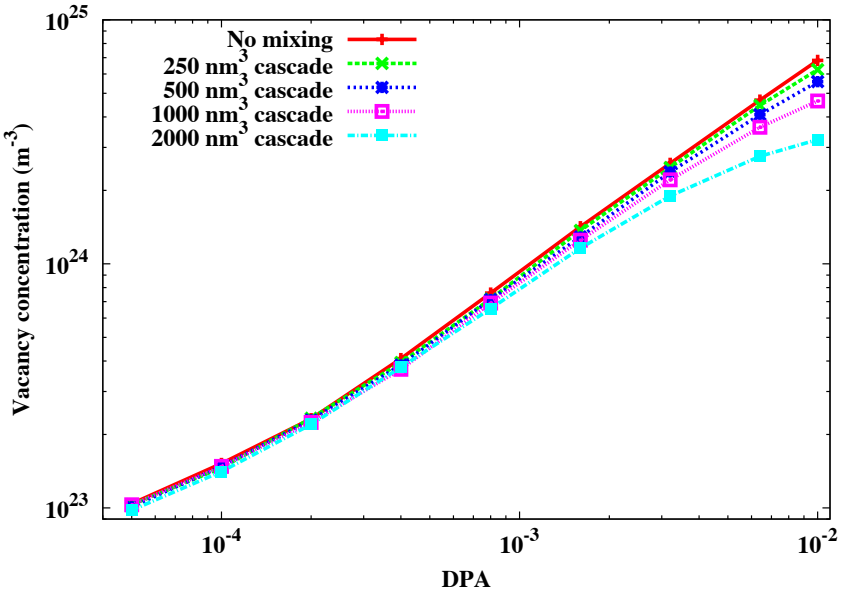

(b)

Figure 42: (42a) Concentration of vacancy and self-interstitial clusters with and without cascade mixing (assuming 1000 nm^3 cascades) as a function of dpa, using 20 keV cascades. (42b) Effect of cascade volume V_{casc} on vacancy concentration as a function of dpa, using 20 keV cascades

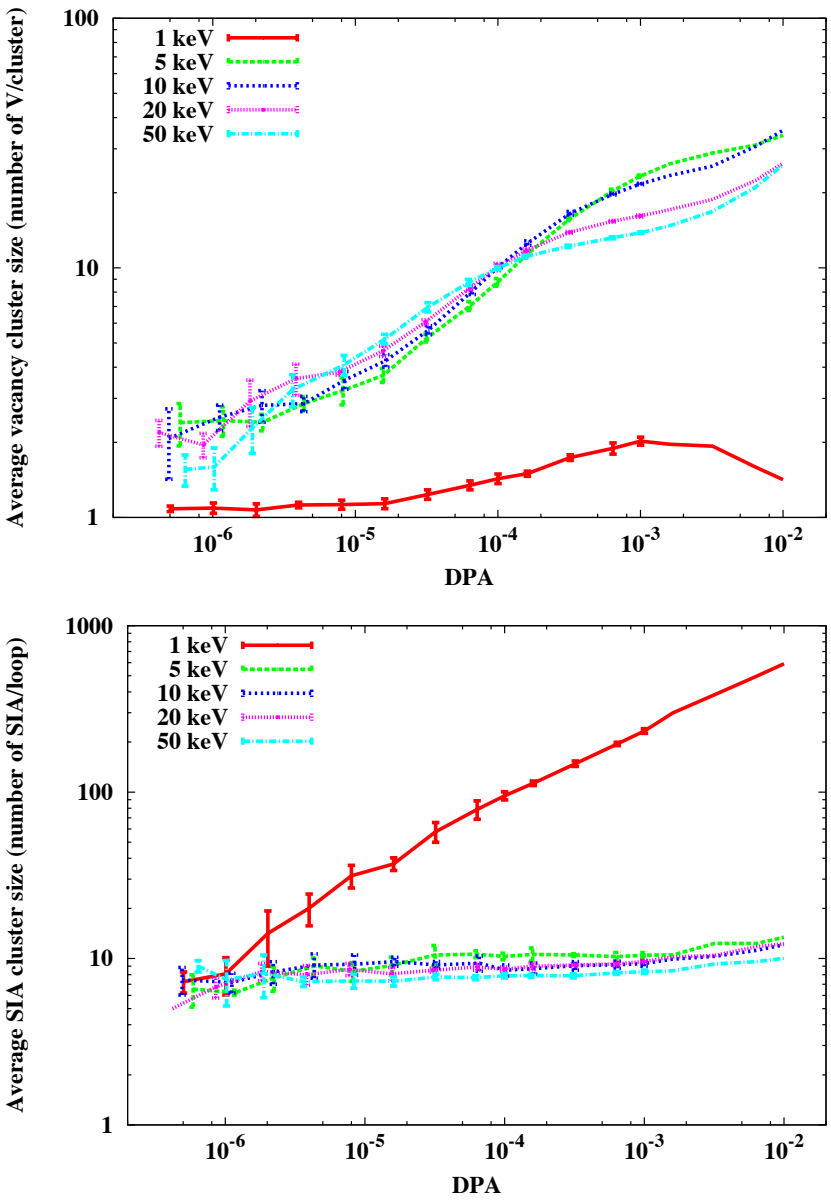

Figure 43: Evolution of average vacancy (top) and self-interstitial cluster (bottom) sizes for several cascade energies.

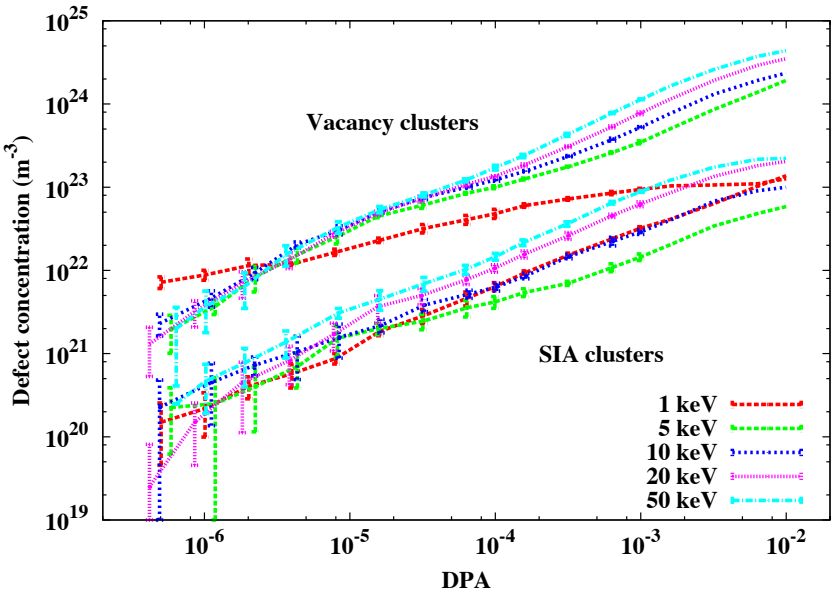

Figure 44: Evolution of average vacancy and self-interstitial cluster concentrations for several cascade energies.

orders of magnitude greater than a 3-vacancy cluster (the fastest diffusing species of vacancy cluster) at 343 K. Therefore, traps that stop their diffusion can impact microstructure evolution and damage accumulation even at low concentrations. Some impurities such as carbon may act as traps for self-interstitial loops, for example through the formation of carbon-vacancy complexes that trap SIA loops [215, 101]. In the experiments of Eldrup et al. [67] and Zinkle et al. [259] using 99.995% Fe, several impurities including carbon are present in concentrations of a few ppm to tens of ppm. It is therefore important when attempting to reproduce experimental damage accumulation with SRSCD to ensure that the impact of such impurities on defect populations, especially SIA loop populations, is treated correctly.

To study the impact of traps for SIA loops on defect populations, the concentration of traps for SIA loops is treated here as a parameter and varied from 5 ppm to 120 ppm. The reaction rate for interaction between these impurity traps, which are artificially included in the simulation, and SIA loops is given by the same reaction rate for interaction between an SIA loop and a stationary spherical point sink, from equation (39), which is converted into units of s^{-1} for SRSCD:

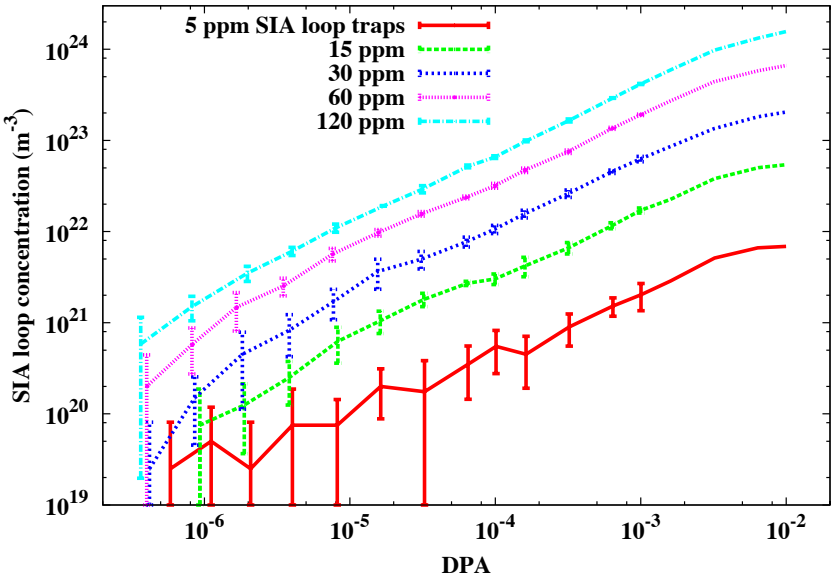

Figure 45: Evolution of self-interstitial concentrations with dose for several concentrations of SIA loop traps.

$$reaction\ rate = \left[\left(\frac{m}{b}\right)^{\frac{1}{2}} + \left(\frac{9\pi}{16\Omega}\right)^{\frac{1}{6}}\right]^4 D_{Im} N_{Im}(t) N_{\text{trap}}(t)^2 \frac{\Omega^2}{V^2} \tag{90}$$

where m is the number of SIAs in the dislocation loop, D_{Im} is the diffusivity of the dislocation loop, N_{Im} is the number of dislocation loops in the simulation volume, and N_{trap} is the number of traps for SIA loops in the simulation volume. In this formulation, the trap is assumed to take the volume of a single lattice site.

The results of these simulations show that the vacancy cluster concentration and size distribution changes only slightly over the range of trap concentrations studied here, from 5 - 120 ppm, but the evolution of the concentration of sessile SIA loops is strongly effected by the density of traps for SIA loops. Figure 45 shows the evolution of the concentration of self-interstitial loops with dose for each trap density studied. Increasing the population of these traps by only a few tens of ppm is shown to change the concentration of dislocation loops by up to an order of magnitude. The results of this simulation suggest that the density of impurities or other traps for mobile SIA loops could be a primary factor in determining the content of SIA loops in the material after significant accumulation of radiation damage.

In order to best fit the experimental results, a trap density of 30 ppm was chosen in

Section 4.4.5, similar to the impurity content reported [259]. The results presented in the next section use this value for the density of traps for SIA loops.

4.4.5 Damage accumulation in neutron-irradiated α-Fe: comparison to experimental results

Using the information gained from the previous three sections, simulation of neutron damage in coarse-grained iron is performed using the same irradiation conditions as reported in experiments [67, 259]. The evolution of the concentration of vacancy and self-interstitial clusters predicted by SRSCD is compared to the experimental results of Eldrup and Zinkle [67, 259] up to 10^{-1} dpa. These simulations are carried out using 20 keV cascades and assuming a 30 ppm concentration of traps for SIA loops as discussed previously.

In these experiments, vacancy cluster concentration is measured by positron annihilation spectroscopy (PAS) and therefore includes even very small defects such as single vacancies. Therefore, the results reported in this section include all vacancies and vacancy clusters, including single vacancies. Conversely, self-interstitial loop concentration is measured by transmission electron microscopy (TEM) and therefore a lower threshold on the detection limit of this method must be included in the computation of SIA loop densities. In this study, results are shown assuming SIA loops are visible above 1 nm in diameter, with the range of results representing a detection limit of 0.9-1.1 nm shown as well. The large variation in SIA cluster concentration observed when changing the threshold diameter for detection indicates that these results are very sensitive to the actual threshold SIA loop size for detection using TEM.

Results for TEM-visible SIA loop and vacancy concentrations using SRSCD are shown in Figure 46. The results of SRSCD show a qualitative match to experimental results at low doses (below 10^{-2} dpa). At high doses, SRSCD predicts a saturation and eventual decrease in visible SIA loop density that is not seen in experimental results. The cause of the difference between SRSCD and experimental results is likely related to the treatment of cascade-defect interactions as noted in Section 4.4.2. In particular, the assumption of random combination between cascade defects and pre-existing defects during cascade events does not account for effects that may occur in irradiated metals such as the break-up of

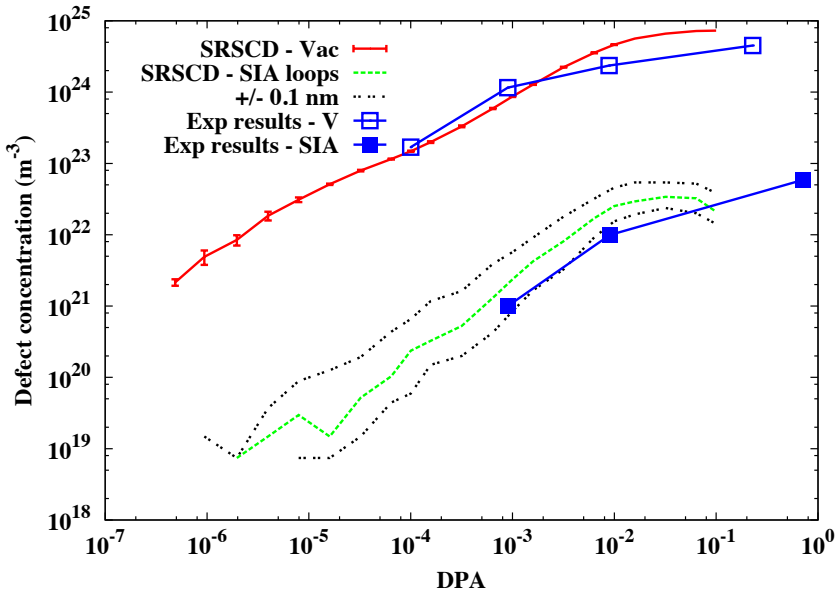

Figure 46: Match of SRSCD results with experimental results of Eldrup et al. [67]. The concentration of SIA clusters is given assuming visible (in TEM) clusters of diameter greater than 1 nm, with black dotted lines indicating detection limits of 0.9 and 1.1 nm.

large defect clusters by cascades.

4.4.6 Summary

In this study, spatially resolved stochastic cluster dynamics (SRSCD) is used to reproduce vacancy and self-interstitial defect concentrations measured experimentally by Eldrup and coworkers [67, 259]. A numerically efficient scheme has been developed in this work to allow simulations of radiation damage accumulation in bulk to 10^{-1} DPA, including adaptive meshing, interactions between cascades and existing defects, and the effect of cascade energy on damage microstructure. As noted in Section 3.3.3.3, the volume of simulated material is larger than previous OKMC studies of the same experimental conditions [22, 101, 102, 200], allowing greater resolution of defects with low concentrations, especially at low irradiation doses. The conclusions of this study are:

1. Defect microstructure is not strongly dependent on the cascade energy used, in agreement with OKMC studies.

2. The concentration of SIA loops is strongly dependent on the presence of traps for

these loops, even at trap concentrations on the order of tens of ppm.

3. Inclusion of cascade-defect interactions in the model for damage accumulation improves the match between simulated and measured vacancy concentrations above 10^{-2} DPA. However, inclusion of cascade-defect interactions also causes premature saturation and decrease of SIA loop populations at high doses. This effect is assumed here to be a result of the method by which cascade-defect interactions are carried out. Further study of these complex interactions could result in a model that more accurately reproduces experimental results.

4. After taking these factors into account, SRSCD simulations of damage accumulation in neturon-irradiated iron show a reasonable qualitative and quantitative match to experimental results, with the exception that at high doses SRSCD predicts greater saturation of defect populations than measured experimentally.

In this study, SRSCD is shown to be a suitable method for simulating long-term irradiation damage accumulation in bulk materials due to its ability to reproduce experimentally measured defect concentrations while maintaining computational efficiency. Such a method could be applied as an important tool in a multi-scale framework for predicting material behavior under various experimentally and industrially relevant irradiation conditions, as discussed in Chapter 5.

4.5 The impact of grain boundaries on defect accumulation: application to nanocrystalline metals

Materials with microstructure length scales on the order of tens to hundreds of nanometers have shown increased resistance to radiation damage compared to coarse-grained materials. Examples such as nano-grained and nano-laminate materials show higher radiation tolerance with increasing interface-to-volume ratio [210, 118, 144, 50]. Grain boundaries and bi-material interfaces can act as recombination sites for point defects, thereby reducing the amount of radiation damage in an irradiated metal [25, 50, 15, 225]. Several types of advanced materials have been developed with this property in mind for potential use in nuclear environments, such as oxygen dispersion-strengthened steels [229, 154], nanoscale laminate

materials [144, 48], nanoporous metals [33, 76], and nanocrystalline metals [210, 118]. All of these materials have a high interface surface area to volume ratio compared to bulk metals, and show increased resistance to radiation damage. However, models that can explicitly represent nanoscale microstructures and can simulate radiation damage accumulation to doses and timescales that are directly comparable to experiments have not yet been developed.

For the case of nanocrystalline metals, the ability of grain boundaries to act as efficient sinks for radiation defects significantly impacts their radiation tolerance. Experiments of defect accumulation and defect denuded zone formation in the vicinity of grain boundaries have shown a dependence on grain boundary character [90, 218, 188, 56], indicating differences in grain boundary sink efficiency between various grain boundary types. At the atomic scale, grain boundary sink efficiency has been investigated by measuring the binding energies of single vacancies and SIAs to a variety of different grain boundaries [225, 227]. However, the length and time scales of such simulations are too small to simulate defect accumulation in the grain interior or inside grain boundaries, making comparisons between such modeling efforts and experimental results challenging.

Multi-scale modeling tools are necessary to bridge the gap between atomic-scale studies of grain boundary energetics and experimental evidence of grain boundary-dependent radiation damage tolerance. Several methods for modeling radiation defect accumulation have been developed for such a purpose, including cluster dynamics (CD) and object kinetic Monte Carlo (OKMC) [207, 161, 105, 142, 22, 200, 101, 102] methods as well. However, in the absence of input parameters such as defect migration and binding energies in grain boundaries taken from atomic scale studies, such simulations are typically limited to bulk materials or thin films [124, 64, 245, 162, 22, 200, 101, 102, 142].

In this section, radiation damage inside polycrystals is simulated and the influence of grain boundary properties on damage accumulation is investigated inside nanocrystalline α-Fe. SRSCD is shown to be capable of simulating polycrystalline domains in Section 4.5.1 due to the increased computational efficiency provided by the synchronous parallel kinetic Monte Carlo algorithm implemented in Section 3.4. To the knowledge of the authors, this capability is currently unique to SRSCD and represents a step towards predictive

modeling of the radiation-resistant behavior of new materials in damage environments that are difficult to achieve in experiments, such as fast fission and fusion neutron irradiation. Next, in Sections 4.5.2, 4.5.3, and 4.5.4 a detailed sensitivity analysis of the various defect migration and binding parameters on grain boundaries is carried out and used to describe the dependence of void denuded zones on grain boundary character. Simulation parameters varied and the layout of the SRSCD simulations used are described in Section 4.5.2. The impact of changing the various grain boundary simulation parameters on grain boundary vacancy content, sink efficiency, and defect profiles inside the grain is investigated in Section 4.5.3. Finally, principal component analysis is performed on a large number of simulations using randomly chosen grain boundary parameters in Section 4.5.4 in order to determine the most influential groups of parameters on grain boundary defect accumulation. Discussion of the results and conclusions of the work performed in this section are presented in Section 4.5.6.

4.5.1 The effect of grain size on damage content in nanocrystalline α-Fe

The synchronous parallel SRSCD algorithm presented in Section 3.4 allows simulation of explicitly represented polycrystalline microstructures with grain sizes on the order of tens of nanometers. To demonstrate this capability, Frenkel pair implantation in nano-grained polycrystalline α-Fe is simulated using two representative polycrystalline structures with 15 grains and 30 grains generated using Sandia National Laboratories' Material Point Method (MPM) code [20]. This polycrystalline microstructure is obtained by means of a 3D Potts model of grain evolution [250]. The simulated grain evolution used to generate the representative microstructure employs a Monte Carlo Potts model using a non-physical kinetic Monte Carlo temperature with isotropic grain boundary energy and mobility. The dimensions of each representative volume are $400 \times 100 \times 100$ nm, and spatial resolution is achieved using 5 nm cubic volume elements in SRSCD. The polycrystalline grain structures are shown in Figures 47a and 47b.

Radiation damage in these polycrystals is simulated with uniform Frenkel pair implantation at a dose rate of 7×10^{-7} dpa$\cdot$s^{-1}. As a first approximation, grain boundaries are

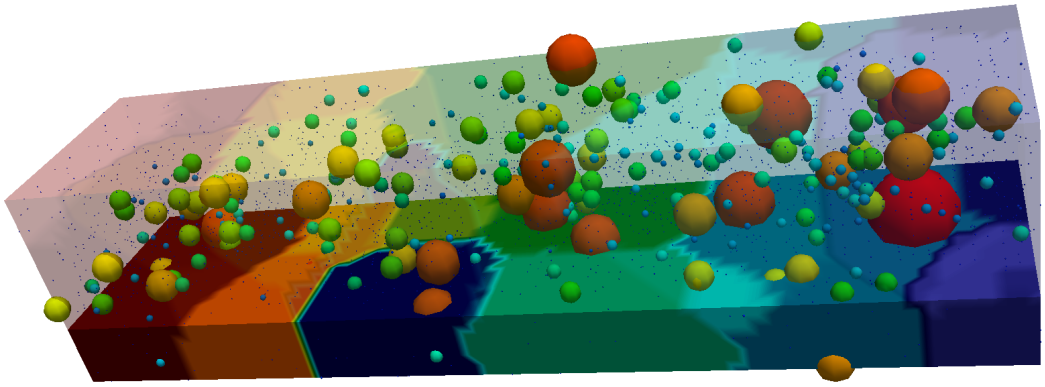

(a) 15 Grains

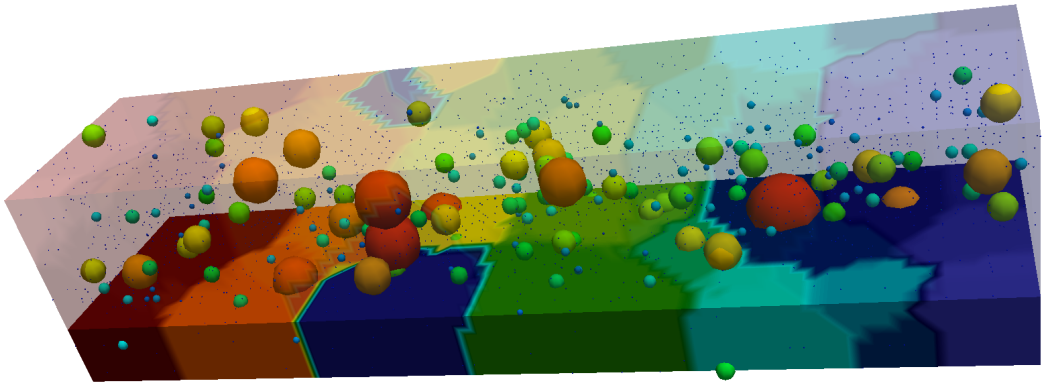

(b) 30 Grains

Figure 47: Grain structure and vacancy clusters (spheres) in simulated polycrystals implanted with Frenkel pairs to 10^{-2} dpa. Fewer total defects are found in the case of 30 grains due to the smaller average grain size and corresponding higher grain boundary sink strength. The total simulation volume is $400 \times 100 \times 100$ nm.

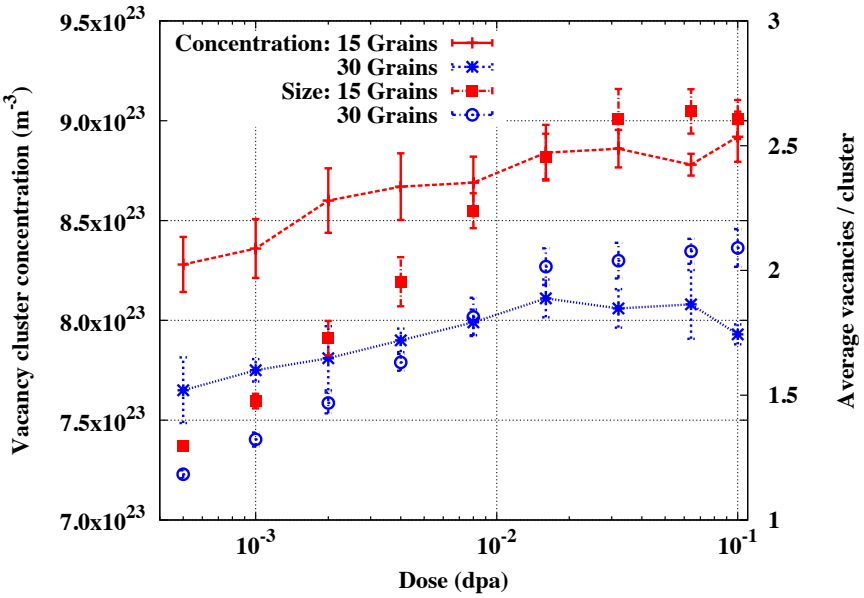

Figure 48: Average vacancy cluster concentration (in m^{-3}) and average number of vacancies per cluster as a function of dose for a polycrystals implanted with Frenkel pairs to 10^{-1} dpa. Two polycrystals were simulated, with 15 and 30 grains, respectively. The total simulation volume is $400 \times 100 \times 100$ nm.

treated as perfect sinks for defects and more complex behaviors such as defect diffusion along grain boundaries and grain boundaries acting as imperfect sinks are not accounted for. Damage accumulation is simulated up to a total dose of 10^{-1} dpa. The final population of vacancy clusters inside the grains at 10^{-1} dpa is shown for the 15-grain and 30-grain representative volume elements in Figures 47a and 47b. Self-interstitial populations are not shown because their high diffusivity causes the majority of self-interstitials to be absorbed by grain boundaries, which are treated as perfect sinks. The difference in damage content in terms of vacancy cluster concentration and average cluster size, in units of vacancies per cluster, between the two grain sizes is shown as a function of dose in Figure 48. The effect of increasing the number of grains (and therefore decreasing the average grain size) is shown to be decreased vacancy cluster concentration and average size, in agreement with experimental trends [210, 118].

The treatment of grain boundaries as perfect sinks in this simulation represents an upper bound for the removal and recombination of radiation damage due to the nanocrystalline

microstructure. In a real nanocrystal, some grain boundaries may have greater sink efficiencies than others, leading to deviations in damage accumulation from the results predicted by this model. Therefore, in the following sections, the ability of grain boundaries to act as efficient sinks is investigated as a function of the various parameters for defect migration and binding inside grain boundaries.

4.5.2 Investigating defect behaviors inside grain boundaries: methodology

In order to extend multi-scale modeling efforts to complex materials such as nano-grained metals, a wide range of information describing defect properties and behaviors inside grain boundaries is needed. Atomistic studies investigating a limited set of grain boundaries have obtained some defect migration energies for several metals [120, 16, 201, 227, 226], and multi-scale studies using OKMC have been implemented for limited cases using atomistic predictions of binding and migration energies as inputs [227]. However, defect behaviors in grain boundaries depend on the specific atomic scale structure of the material interface (misorientation, defect content, etc.) such that a comprehensive quantification of these variables is not amenable to atomistic scale simulations. Therefore, it is important to identify the defect behaviors within grain boundaries that have the greatest impact on damage accumulation, in order to inform future atomic-scale studies.

In this work, SRSCD is applied to the problem of radiation damage accumulation in nanocrystalline α-Fe near grain boundaries. In order to identify key parameters governing defect accumulation, defect migration and binding energies are are varied for each defect type present in the boundary. The impact of varying these energies is measured using three metrics: (1) the density and size of vacancy clusters that accumulate inside the grain boundary, (2) the sink efficiency of the grain boundary for both vacancies and self-interstitials (SIAs), and (3) the profile of vacancy clusters in the grain interior as a function of distance from the grain boundary. These sensitivity analyses are first carried out by changing two variables at a time inside the grain boundary, in order to identify regimes of damage accumulation that can occur near grain boundaries ranging from damage suppression to amplification of vacancy cluster formation. Next, a multivariate statistical analysis is

used to investigate correlations between grain boundary variables and damage accumulation metrics when many defect behaviors are changed simultaneously.

4.5.2.1 Defect parameters in the bulk and inside grain boundaries

The defects modeled in the grain interior are:

1. *Single defects:* these are self-interstitial atoms (SIA) or vacancies (V). These defects migrate in three dimensions and can cluster or annihilate with other defects [207, 74].

2. *Vacancy clusters:* these are treated as spherical clusters in SRSCD. Small vacancy clusters (size 2-4) are mobile in three dimensions [74] and can cluster and annihilate with self-interstitial atoms. Larger vacancy clusters are treated as immobile, but can still interact with other mobile defects. Single vacancies can dissociate from vacancy clusters of all sizes.

3. *Small self-interstitial clusters (size 2-4):* these SIA clusters migrate in three dimensions [74] and are treated as spherical clusters in SRSCD.

4. *Larger mobile self-interstitial clusters:* these defects are treated as circular dislocation loops which diffuse in one dimension along their Burgers vector [198]. Diffusion of larger SIA clusters between volume elements cannot be restricted to a single crystallographic diffusion direction due to the mean-field formulation of SRSCD. However, their reaction rates for interaction with other defects reflect one dimensional migration and circular geometry [60].

5. *Larger immobile self-interstitial clusters:* these SIA clusters are formed when two mobile SIA clusters meet and form a junction [217] or a mobile SIA cluster encounters a trap. In SRSCD, these defects are treated as immobile circular clusters.

The diffusivity and binding energies of the various defect types listed here are taken from ab-initio and atomistic simulations [74, 198] and are listed in Table 7. These inputs have been used in previous SRSCD simulations which have successfully reproduced experimental results for damage accumulation in neutron-irradiated coarse-grained iron [60].

Unlike in bulk α-Fe, defect behaviors and energetics in α-Fe grain boundaries have not been predicted in sufficient detail using ab-initio or atomistic techniques. Defect diffusivities depend on migration energies E_m, which represent energetic barriers for defect motion and are typically treated using an Arrhenius relationship:

$$D = D_0 e^{-\frac{E_m}{k_b T}} \tag{91}$$

where D_0 is a diffusion prefactor determined by the attempt frequency for diffusion, typically on the order of 8×10^{11} nm^{2}s^{-1} [74], k_b is Boltzmann's constant, and T is the absolute temperature. Due to the exponential relationship between migration energy and diffusivity, small changes in E_m can affect diffusivity by several orders of magnitude. Molecular dynamics (MD) studies using the empirical Johnson potential [103] have estimated that in symmetric $\Sigma5(210)\,[001]$ (36.9°) tilt boundaries, the migration energy for vacancies is 0.51 eV while self-interstitial migration energies are at least 1.26 eV [120, 16], rendering them essentially immobile at room temperature due to the Arrhenius relationship described above. This contrasts with migration energies in the grain interior of 0.67 eV for vacancies and 0.34 eV for self-interstitials [74], indicating accelerated vacancy diffusion but decelerated interstitial diffusion in these boundaries. This result is qualitatively similar to results for point defect diffusivity in some Cu boundaries [201], although intra-grain boundary diffusivity is expected to be dependent on the grain boundary character and the concentration of defects in the grain boundary.

Due to the unknown nature of various defect energetics inside grain boundaries, in this study all allowed reactions and energetics not treated as free variables inside the grain boundary during a given set of simulations are set as equal to their values in bulk α-Fe unless otherwise noted. An exception to this rule is that all vacancy and SIA clusters inside the grain boundary are assumed to be spherical, unlike large SIA clusters in the grain interior which are assumed to form dislocation loops. In addition, large SIA clusters (greater than 4 SIAs) inside the grain boundary are assumed to be immobile.

The following defect properties are treated as variables inside the grain boundary and their impact on defect accumulation is tested through sensitivity analyses in Section 4.5.3:

1. The migration energy E_m of single vacancies and single SIAs inside grain boundaries
2. The migration energy E_m of small (size 2-4) vacancy and SIA clusters inside grain boundaries
3. The binding energy E_b of a single vacancy to a vacancy cluster or a single SIA to an SIA cluster inside grain boundaries
4. The binding energy E_b of single vacancies and SIAs to the grain boundary

The binding energies of single vacancies and SIAs to grain boundaries in α-Fe has also been investigated by Tschopp et al. [225] using atomistics. Although these binding energies are not uniform throughout the grain boundary, their averages have been computed for a range of common grain boundaries as well as twist and asymmetric tilt grain boundaries. These results are shown in Table 13. Note here that although these values are used to give the reader a qualitative understanding of where various boundary types are located in the results of Section 4.5.3.5, a large number of unknowns remain inside each grain boundary such as the diffusion and clustering behaviors of various defects. Therefore, the results presented in Section 4.5.3 are meant to serve as a qualitative guide rather than predictions for defect accumulation in specific grain boundaries.

4.5.2.2 Simulation details

In the following sections, SRSCD is used to simulate uniform Frenkel pair implantation in nanocrystalline α-Fe, including the effect of grain boundary trapping and re-emission of defects. In the proposed approach, the geometry considered is as follows: the grain and grain boundary system is approximated by a simulation volume that is 100 nm thick in the x-direction and infinite in the y and z-directions. The size of the total simulated volume is 105 nm $\times$ 50 nm $\times$ 50 nm, so that the grain is 100 nm thick and the boundary is represented by one additional layer of volume elements. All volume elements are 5 nm in length and periodic boundary conditions are applied in all directions, as shown in Figure 49. Therefore, only a single grain boundary is modeled, as periodic boundary conditions allow it to capture defects diffusing in both the $+x$ and $-x$ directions.

Table 13: Average binding energies for single vacancies and single interstitials on a variety of grain boundary types in α-Fe (from Tschopp et al. [225]). All binding energies are given in eV.

Grain boundary	E_b(V) (avg)	E_b(SIA) (avg)
$\Sigma3\{112\}\langle110\rangle$	0.13	0.25
$\Sigma3\{111\}\langle110\rangle$	1.03	1.34
$\Sigma3\{011\}\langle111\rangle$	0.13	0.45
$\Sigma5\{012\}\langle100\rangle$	0.26	1.29
$\Sigma5\{013\}\langle100\rangle$	0.27	1.52
$\Sigma7\{123\}\langle111\rangle$	0.44	1.86
$\Sigma9\{114\}\langle110\rangle$	0.46	2.31
$\Sigma9\{221\}\langle110\rangle$	0.55	2.37
$\Sigma11\{332\}\langle110\rangle$	0.42	1.97
$\Sigma11\{113\}\langle110\rangle$	0.41	1.88
$\Sigma13a\{023\}\langle100\rangle$	0.24	1.08
$\Sigma13a\{015\}\langle100\rangle$	0.26	1.20
$\Sigma13b\{134\}\langle111\rangle$	0.55	2.04
$\langle100\rangle$ STGBs $\Sigma > 13$	0.27	1.36
$\langle110\rangle$ STGBs $\Sigma > 13$	0.60	1.91
$\langle111\rangle$ STGBs $\Sigma > 13$	0.35	1.92
All Twist GBs	0.44	1.73
All ATGBs	0.63	2.17

Allowed reactions and reaction rates inside the grain interior are the same as in previous studies, and can be found elsewhere [62]. As defect diffusion inside the grain boundary is assumed to be two dimensional, reaction rates for defect clustering and diffusion between elements while inside the grain boundary are altered. The functional form for the reaction rate for defect clustering and annihilation is computed using the same method as three dimensional clustering rates [63, 30], and can be found in 3.2.2.5.

A defect trapping and emission model for grain boundaries is implemented in this work in order to investigate the impact of grain boundary parameters on defect accumulation and sink efficiency. Defects are allowed to migrate from the grain into the grain boundary using a reaction rate that treats the grain boundary as a perfect sink for defects diffusing from the bulk, regardless of the concentration of defects inside the grain boundary. However, defect emission from the grain boundary is allowed for single vacancies and single self-interstitials. The reaction rate used for vacancy or SIA emission from the grain boundaries is the same

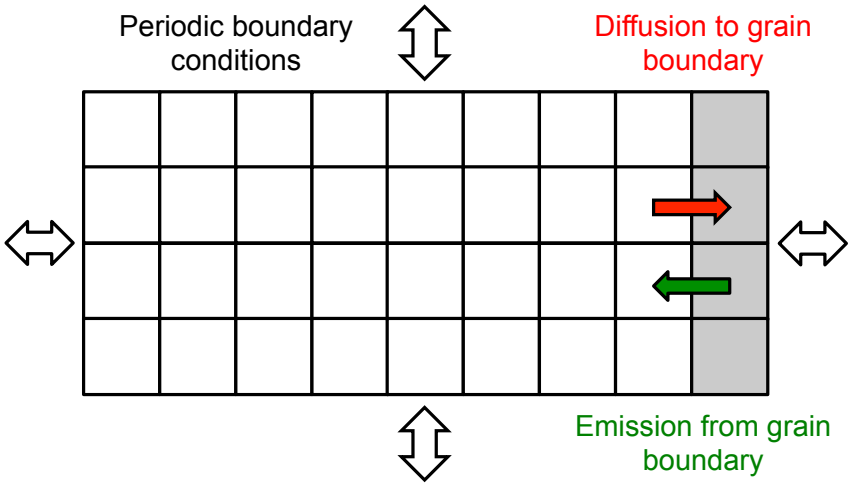

Figure 49: Two dimensional schematic of layout of SRSCD simulations. The grain is simulated with a 100 nm thin film using 5 nm volume elements (white), with a grain boundary acting as a barrier in the $+x$-direction (gray). All boundary conditions are periodic, so that diffusion in the $-x$-direction also leads to trapping on the grain boundary. Defect trapping and emission from the grain boundary are depicted with colored arrows.

as the reaction rate used for point defect dissociation from defect clusters [63]:

$$\text{reaction rate} = \omega D_{\text{V,I}} e^{-\frac{E_b(\text{V,I})}{k_b T}} N_{\text{V,I}} \tag{92}$$

where ω is a geometric constant, E_b(V,I) is the binding energy of vacancies or SIAs to the grain boundary, $N_{\text{V,I}}$ is the number of vacancies or SIAs inside the grain boundary element, and $D_{\text{V,I}}$ is the diffusivity of vacancies or SIAs inside the grain. The diffusivity of point defects in bulk α-Fe rather than inside the grain boundary is used here because the total energy required for emission from the grain boundary is equal to the binding energy to the grain boundary plus the energy required to move the defect one additional diffusive step away from the boundary. Since this final step is taken within the grain, $D_{\text{V,I}}$ is taken to be the diffusivity in the grain interior.

Grain boundaries are therefore not perfect sinks in this work, and instead have a sink efficiency η defined as the probability that a defect trapped in the grain boundary will remain in the grain boundary. The probability that a defect will be emitted from the grain boundary is given by the ratio of the number of defects emitted from the grain boundary N_{emit} to the number of defects trapped at the grain boundary N_{trap}. Therefore η is given

by:

$$\eta = 1 - \frac{N_{\text{emit}}}{N_{\text{trap}}} \tag{93}$$

Using this formulation, a grain boundary with sink efficiency $\eta = 0$ will not trap any defects, while a grain boundary with sink efficiency $\eta = 1$ will trap all defects that diffuse towards it and will act as a perfect sink. This sink efficiency depends on the grain boundary binding energy as well as many other factors, such as the implantation conditions and the allowed defects and reactions between defects in the grain boundary. In addition, the sink efficiencies for vacancies and self-interstitials, η_{V} and η_{I}, are in general not equal. In Sections 4.5.3.5 and 4.5.3.6, values for sink efficiency are reported along with populations of defects in the grain boundary and in the grain interior for the irradiation conditions investigated here. It should be noted that due to the implantation conditions and allowed defects chosen in this study, a steady-state defect population is not achieved during irradiation. Therefore, sink efficiencies η_{V} and η_{I} reported in Section 4.5.3.5 and 4.5.3.6 may change as a function of irradiation dose.

In all simulations in this study, Frenkel pairs are implanted uniformly into the grain at room temperature to a total dose of $10^{-3}-10^{-2}$ dpa and at a dose rate of 10^{-7} dpa·s^{-1}. This dose rate was chosen to maximize the fraction of vacancies that reach the grain boundary as single vacancies rather than small mobile clusters. This rate corresponds to dose rates in neutron irradiation experiments [67, 35], although displacement cascades formed during neutron irradiation are not considered here. The populations of SIA clusters are not reported in the results of this work because the concentrations of these defects are very low in the simulation results. This is mainly due to their fast diffusivity in the grain interior as well as the fact that all defects are initially introduced as Frenkel pairs, so the formation of large dislocation loops is unlikely.

4.5.3 Impact of grain boundary defect energetics on damage accumulation

In order to investigate the impact of the various defect behaviors listed in Section 4.5.2.1 on damage accumulation in the vicinity of the grain boundary, several sensitivity analyses are performed in this section. The goal of these analyses is to find, within a limited input space,

regimes in which different trends for defect accumulation can be observed. In Section 4.5.3.1, defect behaviors inside the grain boundary are varied while leaving the binding energies of defects to the grain boundary constant. The parameters varied in this section are point defect and cluster migration energies (Sections 4.5.3.2 and 4.5.3.3) and the binding energies of point defects to clusters within the grain boundary (Section 4.5.3.4). In Section 4.5.3.5, the effect of changing the binding energy of vacancies and SIAs to the grain boundary is investigated. Finally, in Section 4.5.3.6, the potential impact of cluster emission from the boundaries on defect accumulation within this system is studied. As a reference, Table 14 shows the various grain boundary properties varied throughout this section.

Table 14: Grain boundary properties varied in sensitivity analyses carried out in this section

Quantity varied	Range		Section
Point defect migration energies	E_m(V)	$0.3 - 1$ eV	4.5.3.2
	E_m(SIA)	$0.2 - 1.3$ eV	
Cluster migration energies	E_m(V clusters)	$0.2 - 1$ eV	4.5.3.3
	E_m(SIA clusters)	$0.2 - 1.3$ eV	
Parameter A in cluster binding energies	A(V clusters)	$0.3 - 3.9$ eV	4.5.3.4
(see equation (94))	A(SIA clusters)	$0.8 - 4.4$ eV	
Point defect - grain boundary binding energies	E_b(V)	$0 - 1.2$ eV	4.5.3.5
	E_b(SIA)	$0 - 2.5$ eV	
Cluster - grain boundary binding energies	E_b(V clusters)	$0 - 1.2$ eV	4.5.3.6
	E_b(SIA clusters)	$0 - 2.5$ eV	

4.5.3.1 Defect binding and diffusion inside grain boundaries

In this section, SRSCD is used to simulate Frenkel pair implantation as described in Section 4.5.2.2 to a total dose of 10^{-3} dpa. The metrics used to quantify the impact of changing various defect behaviors in this section are the concentration of vacancies and vacancy clusters inside the grain boundary (in units of atomic fraction) and the average size of vacancy clusters inside the grain boundary. In all simulations in this section, vacancies are assumed bound to the grain boundary with energy $E_b = 0.26$ eV and self-interstitials are assumed bound to the grain boundary with energy $E_b = 1.29$ eV, corresponding to the average defect binding energies in a $\Sigma 5$ grain boundary [225]. This choice was made because the mobility of defects inside this grain boundary has been investigated in atomistic simulations [120, 16] and it represents an intermediate case for point defect binding to the

grain boundary, as studied by Tschopp et al. [225].

4.5.3.2 Single vacancy and SIA mobility

Figure 50 shows the vacancy concentration (in atomic fraction) and average vacancy cluster size inside the grain boundary as a function of single vacancy and SIA migration energies E_m inside the grain boundary. The migration energies E_m for point defect diffusivity in the grain interior (0.67 eV for vacancies and 0.34 eV for SIAs) as well as the values predicted by atomistic results inside $\Sigma 5$ grain boundaries [120, 16] (0.51 eV for vacancies and 1.26 eV for SIAs) are indicated on Figure 50 with + symbols as a reference.

Note that in Figure 50b, some local variations in average cluster size are seen in regions where the vacancy concentration is low due to poor statistics in these regions. This is demonstrated in Figure 51, where the standard deviation in average vacancy cluster size for five simulations at each value of E_m(V) and E_m(SIA) is shown. The standard deviation is seen to be higher where the average concentration of vacancies is low, contributing to the inhomogeneity in Figure 50b.

The results shown in Figure 50 can be divided roughly into four quadrants, which represent different regimes of defect accumulation:

1. For low values of vacancy migration energy E_m(V) and self-interstitial migration energy E_m(SIA), both single vacancies and single self-interstitials are very mobile within the grain boundary. In this case, a low number of vacancies remain inside the grain boundary at the end of the simulation due to annihilation between the two defect types.

2. For low values of E_m(V) but high values of E_m(SIA), vacancies are mobile but self-interstitials are relatively immobile. In this case, vacancies either annihilate with self-interstitials or form larger, immobile clusters. Therefore the density of vacancy clusters is low but the average size is high in this quadrant.

3. For high values of E_m(V) and low values of E_m(SIA), immobile vacancies and mobile self-interstitials create a regime of intermediate vacancy content but very low average

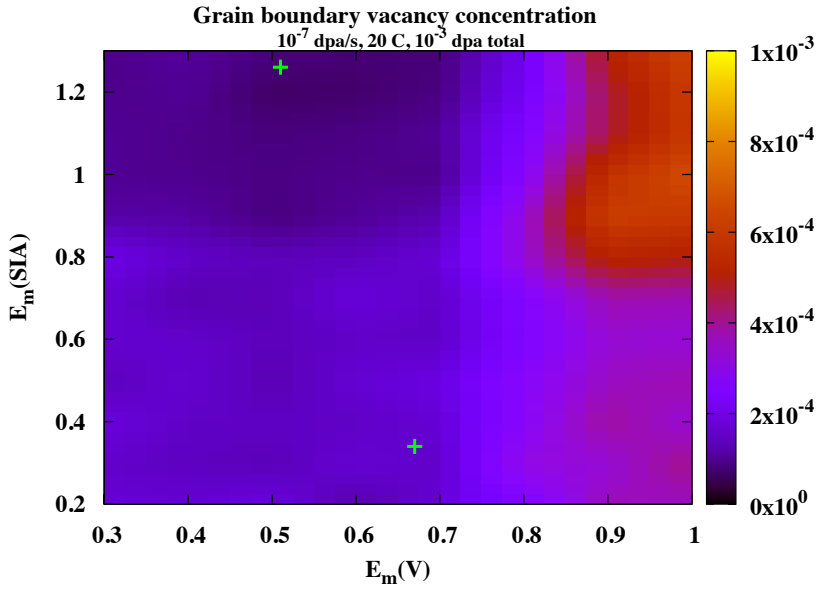

(a)

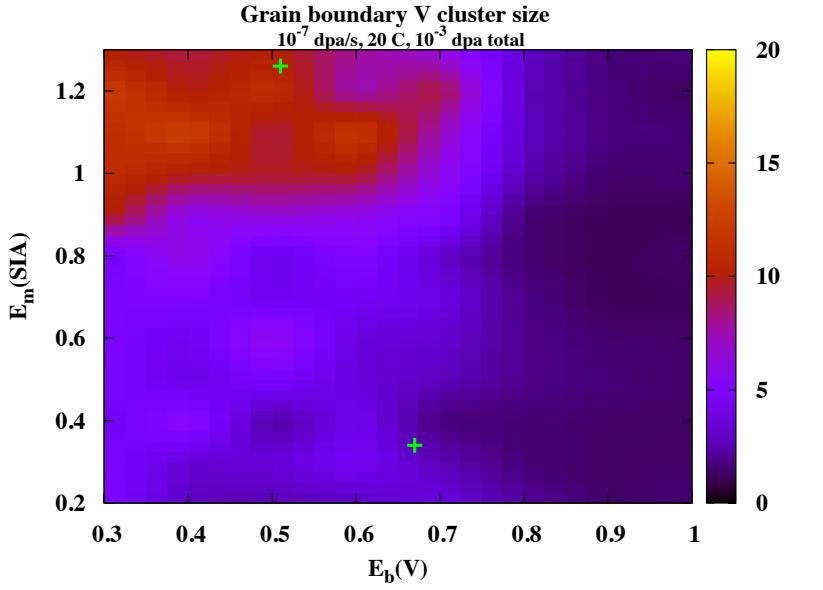

(b)

Figure 50: Grain boundary vacancy concentration (50a) and average cluster size (50b) for several different values of migration energies E_m(V) and E_m(SIA) inside the grain boundary. Marked points represent the V and SIA migration energies in bulk (0.67 and 0.34 eV, respectively [74]) and on $\Sigma 5$ grain boundaries (0.51 and 1.26 eV, respectively [120, 16]).

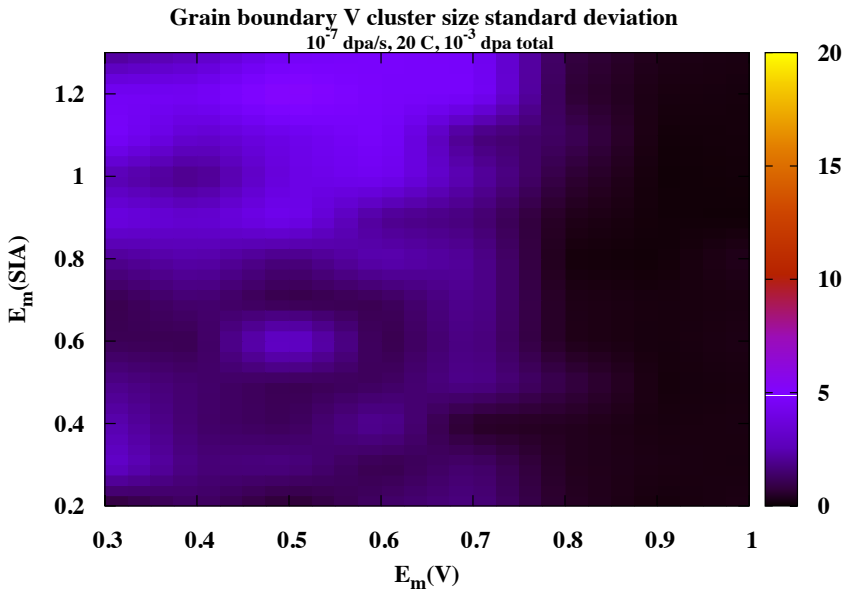

Figure 51: Standard deviation of average vacancy cluster sizes computed over five simulations in Figure 50b, in order to demonstrate the source of the statistical variation in vacancy cluster size seen in Figure 50b.

vacancy cluster size in the grain boundary.

4. For high values of both E_m(V) and E_m(SIA), neither defect type is mobile inside the grain boundary and thus very little interaction between vacancies and self-interstitials occurs. In this case, a large concentration of single vacancies is trapped in the grain boundary but the average size is low.

Overall, the migration energies of single vacancies and self-interstitials inside the grain boundary both have strong impacts on defect accumulation inside the grain boundary. Therefore, predicting these values using atomistic methods is important in designing models to accurately simulate radiation damage in the vicinity of various grain boundaries.

4.5.3.3 Defect cluster mobility

The growth and annihilation of defect clusters depends on the mobility of point defects (treated in the previous section) as well as small defect clusters. Therefore, in this section the diffusivities of small clusters of vacancies and SIAs (size 2-4) inside the grain boundary are also investigated while leaving single vacancy and SIA migration energies constant. Due

to the large number of parameters that could be independently varied in such a study, the migration energies of vacancy clusters size 2-4 are set to the same value and varied together. The migration energy of SIA clusters size 2-4 is varied in the same way. Results showing vacancy concentration inside the grain boundary as a function of cluster migration energies within the grain boundary are shown in Figure 52. Two cases for single defect migration energies were chosen, corresponding to the + symbols in Figure 50: In Figure 52a, single V and SIA migration energies are 0.51 and 1.26 eV, respectively, corresponding to atomistic results for $\Sigma 5$ boundaries [120, 16]. In Figure 52b, single vacancy and SIA diffusion is the same as in bulk α-Fe. The average size of vacancy clusters inside the grain boundary was also investigated but is not shown in Figure 52 as results were relatively constant for both cases studied here.

The migration energy of small vacancy clusters strongly influences the vacancy concentration predicted by SRSCD on the grain boundary above 0.7 eV, but the migration energy of SIA clusters is a less significant variable here. This is due to the fact that such SIA clusters are relatively rare on the grain boundary in these simulations.

4.5.3.4 Defect cluster binding energy

Finally, the competition between defect cluster growth by capture of mobile defects and dissociation of point defects from clusters can play a role in defect accumulation. The stability of defect clusters is a function of the binding energy E_b of point defects to those clusters, which represents the energetic barrier for emission of a point defect from a cluster within the grain boundary. The effect of changing the binding energy for dissociation of vacancy and self-interstitial clusters inside the grain boundary is also investigated. Note that this energy represents the energy barrier for point defect emission from a defect cluster while remaining inside the boundary, rather than the binding energy of those defects to the boundary itself. As a first approximation, we assume that the binding energy of defects to clusters size n inside the grain boundary follows the same law as in the grain interior, given by a functional form [74]:

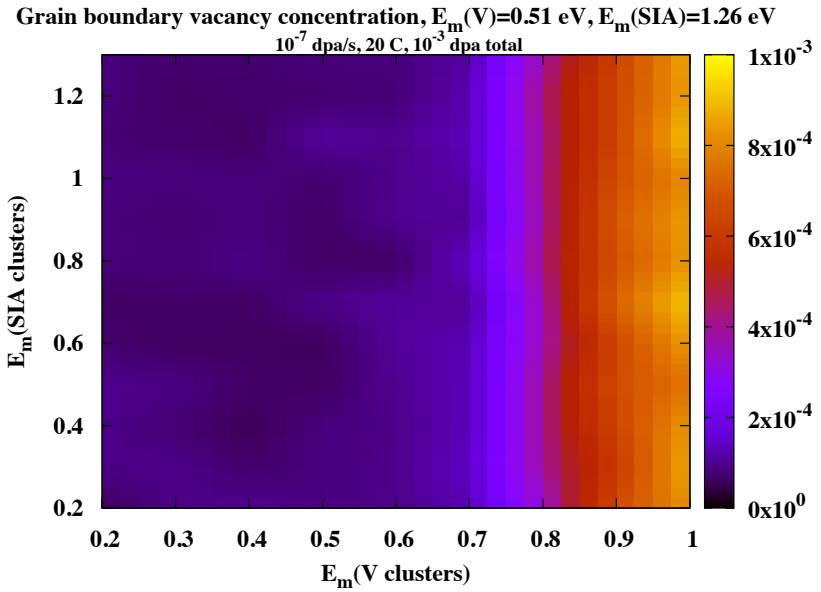

(a)

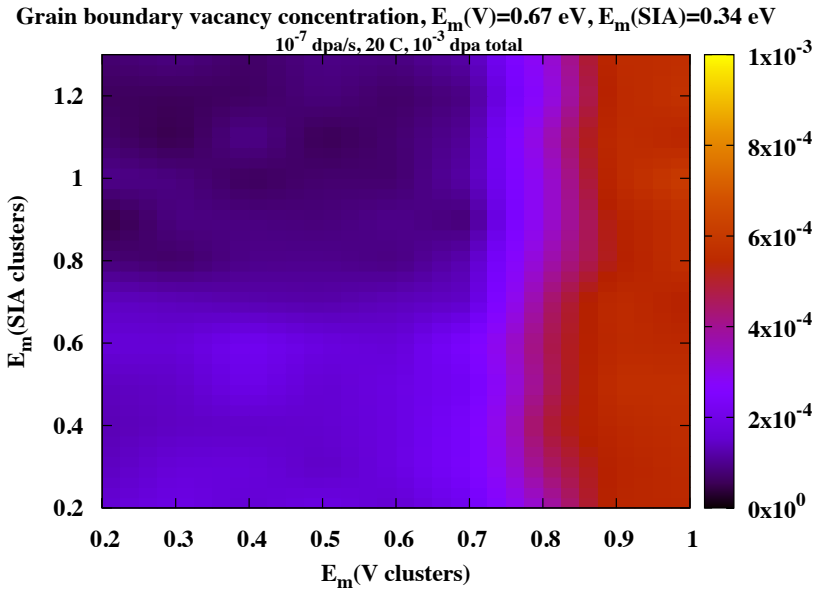

(b)

Figure 52: Grain boundary vacancy concentration for several different interfacial values of cluster migration energy. (52a) Single vacancy and SIA migration energies are fixed at 0.51 eV and 1.26 eV, respectively, in accordance with atomistic simulations of $\Sigma 5$ grain boundaries [120, 16]. (52b) Single vacancy and SIA migration energies are fixed at 0.67 eV and 0.34 eV, respectively, their values in bulk α-Fe [74].

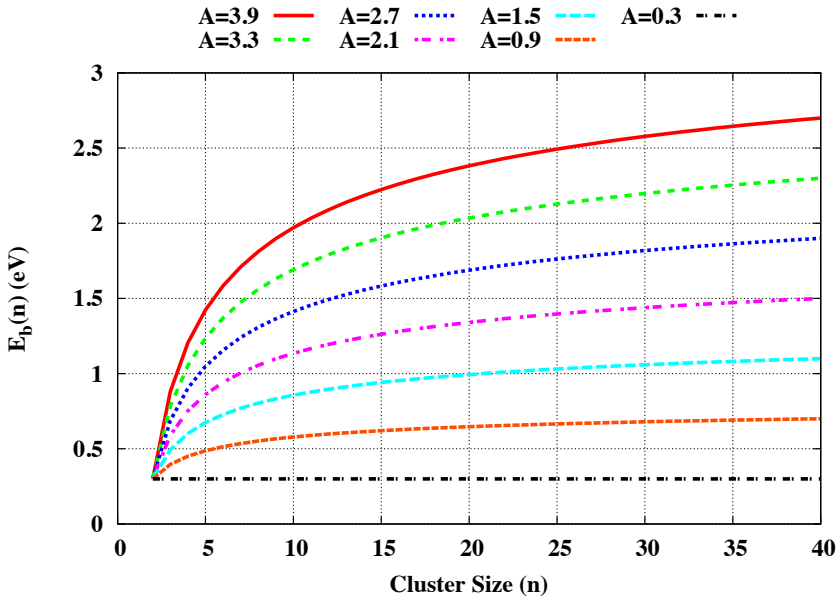

Figure 53: Effect of parameter A in equation (94) on the binding energy E_b(V) of a single vacancy to a vacancy cluster size n, with parameter $B = 0.3$ eV.

$$E_b(n) = A + (B - A)\left[\frac{n^{\frac{2}{3}} - (n-1)^{\frac{2}{3}}}{2^{\frac{2}{3}} - 1}\right] \tag{94}$$

where A and B are constants representing the limiting binding energy as $n \to \infty$ and the binding energy when $n = 2$, respectively. The effect of changing parameter A is investigated here, with B equal to 0.3 eV for vacancies and 0.8 eV for SIAs, the values for 2-V and 2-SIA binding energies inside the grains (see Table 7). The impact of parameter A in equation (94) on the binding energy of a vacancy cluster size n is shown in Figure 53. Note that in bulk α-Fe, values for binding energies of small vacancy (size 2-4) and SIA (size 2-3) clusters are given separately from the functional form of equation (94), but in this parameter study the functional form is applied to clusters of all sizes inside the grain boundary.

Average vacancy cluster sizes are shown in Figure 54 for the same two cases of vacancy and SIA diffusion inside the grain boundary shown in Figure 52. As in Figure 50b, some statistical variation in cluster sizes is seen in Figure 54 due to low overall vacancy concentration. However, it is still possible to identify regions of different defect accumulation due to different grain boundary defect binding energies. For the case of E_m(V)= 0.51 eV and E_m(SIA)= 1.26 eV, parameter A in vacancy cluster binding energy is significant below

$A = 1$ eV, with decreasing cluster size as A decreases. For the case of E_m(V)= 0.67 eV and E_m(SIA)= 0.34 eV, parameter A in vacancy cluster binding energy is significant below $A = 0.5$ eV, causing decreasing cluster size as A decreases. The average concentration of vacancy clusters inside the grain boundary was also investigated but is not shown in Figure 54 as results were relatively constant for both cases studied here.

4.5.3.5 Binding energy of point defects to grain boundaries

In this section, the ability of grain boundaries to act as efficient sinks for radiation-induced defects is investigated as a function of E_b(V) and E_b(SIA), the binding energy of vacancies and SIAs to the grain boundary. Three types of results are obtained here: (1) vacancy concentration and average size inside the grain boundaries, (2) grain boundary sink efficiency for both vacancies and self-interstitials, and (3) the profile of vacancy clusters in the interior of the grain. Using these three measures, a more complete picture of defect accumulation at and near grain boundaries is obtained for a variety of different grain boundary behaviors.

The binding energies of single vacancies and SIAs to grain boundaries in α-Fe have been investigated by Tschopp et al. using atomistics [225]. Although these binding energies are not uniform throughout the grain boundary, their averages have been computed for a range of common grain boundaries as well as twist and asymmetric tilt grain boundaries. As a guide for the reader, these values are overlaid on the results shown in this section. Clearly, the various other defect behaviors have not been parameterized on each of these grain boundaries and therefore these results are meant to serve as a qualitative guide rather than predictions for defect accumulation in specific grain boundaries. Therefore, the results of this section can be interpreted as investigating one aspect of changing grain boundary character, while leaving other parameters such as defect diffusivity constant. These results demonstrate the range of binding energies of point defects to grain boundaries and the resulting different regimes of damage accumulation that could be expected in a real material.

To study the effect of binding energies E_b to the grain boundary, uniform Frenkel pair implantation in the grain interior is simulated with irradiation conditions as described in Section 4.5.2.2. All results are shown for a total dose of 10^{-3} dpa. Vacancy and SIA

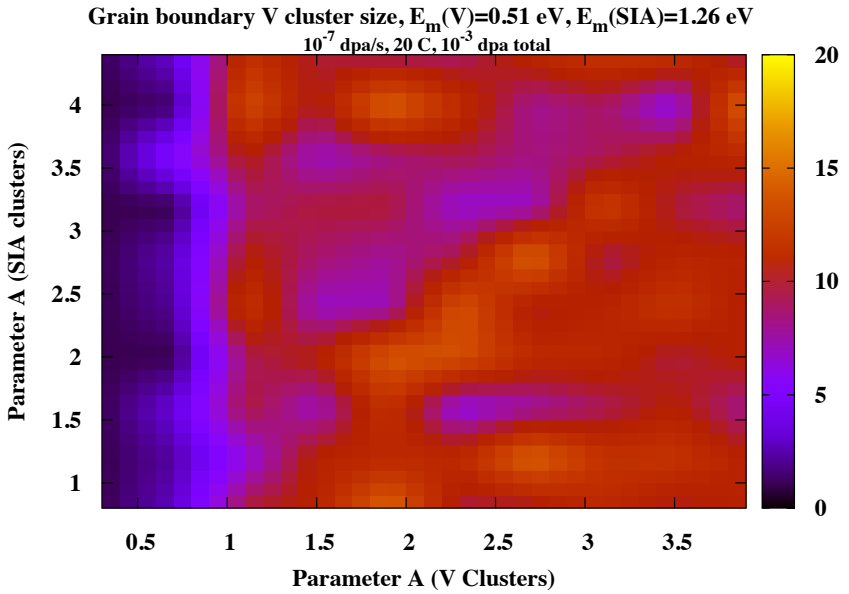

(a)

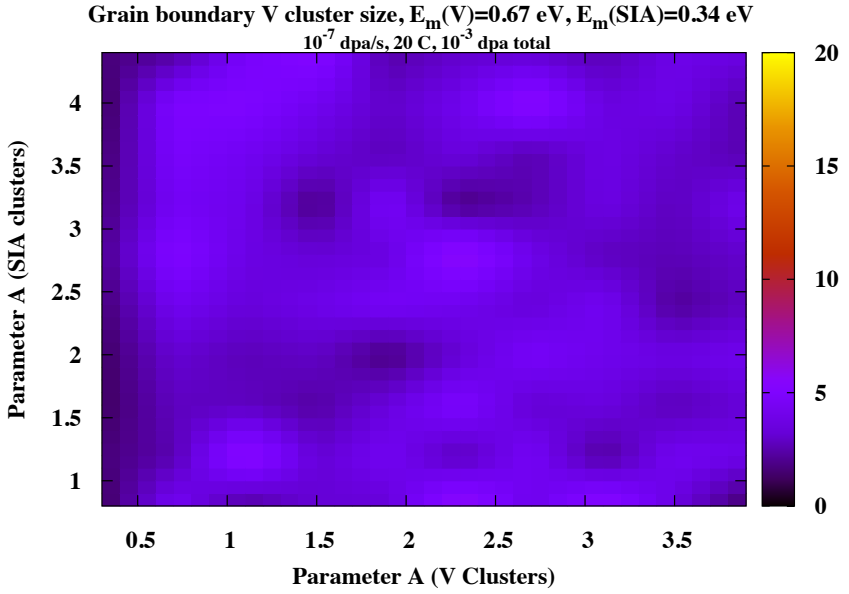

(b)

Figure 54: Grain boundary average cluster size for several different interfacial values of A in equation (94). (54a) Single vacancy and SIA migration energies are fixed at 0.51 eV and 1.26 eV, respectively, in accordance with atomistic simulations of $\Sigma 5$ grain boundaries [120, 16]. (54b) Single vacancy and SIA migration energies are fixed at 0.67 eV and 0.34 eV, respectively, their values in bulk α-Fe [74].

migration energies inside the grain boundary in these simulations are given by E_m(V)= 0.51 eV and E_m(SIA)= 1.26 eV, similar to atomistic results for Σ5 grain boundaries [120, 16]. Results of this sensitivity study are shown in Figures 55, 56, and 57. Although not shown here, results analogous to those shown in Figures 55, 56, and 57 were also obtained for the case of E_m(V)= 0.67 eV and E_m(SIA)= 0.34 eV, their values in bulk α-Fe (similar to Figures 52 and 54). These results do not change the qualitative analysis of the impact of point defect binding energies to grain boundaries on defect accumulation, and are therefore not included here.

In Figures 55a and 55b, the vacancy concentration and average size, respectively, are shown on the grain boundary as a function of E_b(V) and E_b(SIA). Both vacancy concentration and average size on the grain boundary are strongly dependent on E_b(V) and E_b(SIA). To better understand the mechanisms behind defect accumulation, Figures 56a and 56b show the sink efficiencies η_{V} and η_{I} as a function of the same binding energies E_b(V) and E_b(SIA). Together these maps of defect accumulation and sink efficiency can be roughly divided into four regions:

1. E_b(V)$<$ 0.2, E_b(SIA)$<$ 0.5: In this region, neither vacancies not SIAs are strongly bound to the grain boundary and η_{V} and η_{I} are nearly zero. However, a few immobile vacancy clusters are trapped on the grain boundary. Therefore, the concentration of vacancies on the grain boundary is very low, but the vacancy clusters that are trapped on the grain boundary are large.

2. E_b(V)$>$ 0.2, E_b(SIA)$<$ 0.5: In this region, vacancies are trapped by the grain boundary but SIAs are not, giving $\eta_{\mathrm{V}} \simeq 1$ and $\eta_{\mathrm{I}} \simeq 0$. Therefore, the boundary accumulates a surplus of vacancies, although the size of clusters found on the boundary is smaller than in the first region. Note that none of the grain boundaries studied by Tschopp et al. [225] fall into this region.

3. E_b(V)$<$ 0.2, E_b(SIA)$>$ 0.5: In this region, vacancies are not strongly bound to the grain boundary, with $\eta_{\mathrm{V}} < 1$ but SIAs are strongly bound, with $\eta_{\mathrm{I}} \simeq 1$. Therefore, there is a surplus of SIAs on the grain boundaries and both the size and concentration

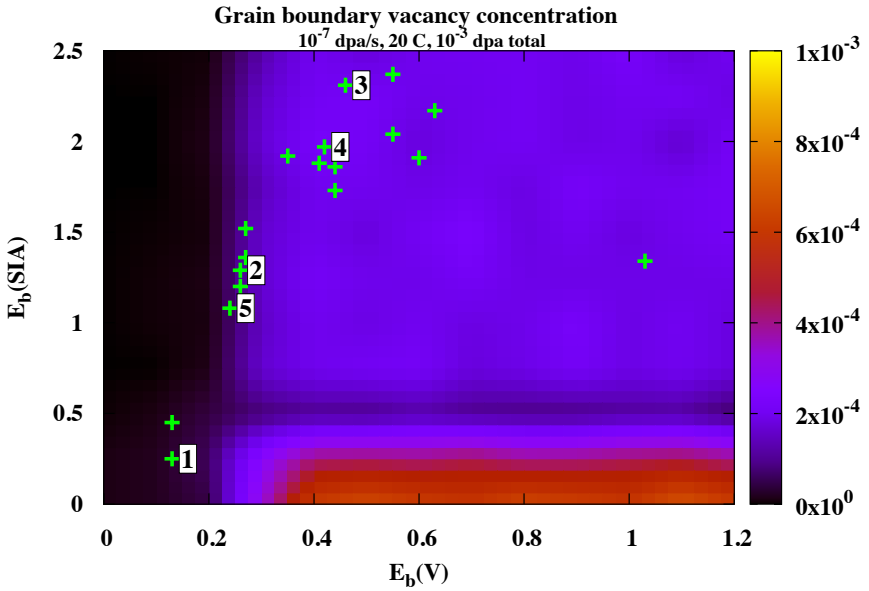

(a)

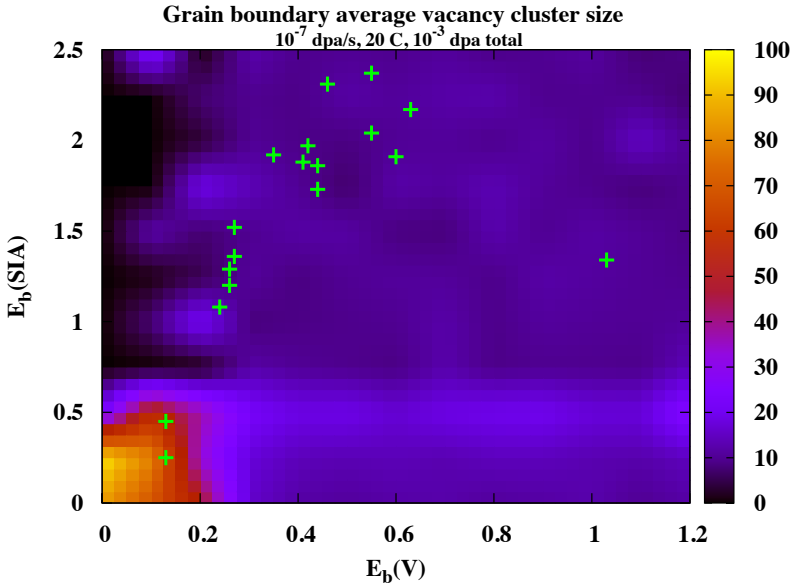

(b)

Figure 55: Maps of void concentration (55a) and average size (55b) on the grain boundary as a function of binding energy of vacancies and self-interstitials to the grain boundary, at a total dose of 10^{-3} dpa. Marked points indicate average binding energies of defects to grain boundaries found by Tschopp et al. [225].

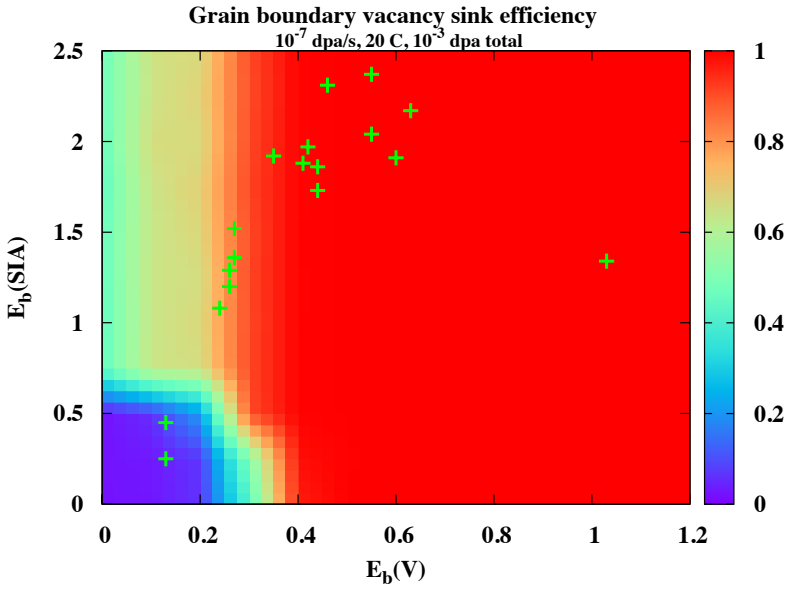

(a)

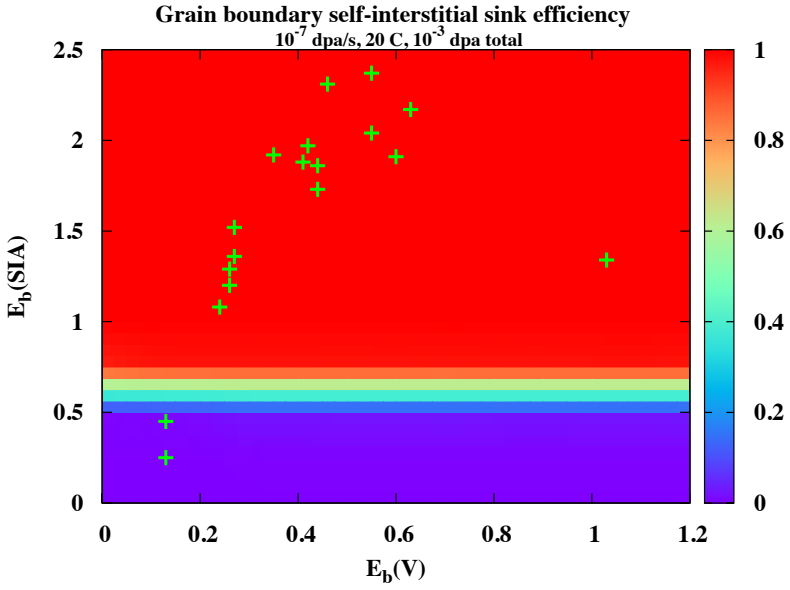

(b)

Figure 56: Maps of sink efficiencies η_V (56a) and η_I (56b) on the grain boundary as a function of binding energy of vacancies and self-interstitials to the grain boundary, at a total dose of 10^{-3} dpa. Marked points indicate average binding energies of defects to grain boundaries found by Tschopp et al. [225].

of vacancy clusters on the grain boundary is very small.

4. E_b(V)$>$ 0.2, E_b(SIA)$>$ 0.5: In this region, both vacancies and self-interstitials are strongly trapped by the grain boundary and $\eta_{\mathrm{V}} \simeq \eta_{\mathrm{I}} \simeq 1$. In this region, vacancies tend to form clusters in the grain boundary because of their greater diffusivity relative to that of SIAs inside the grain boundary. However, the average size of vacancy clusters on these grain boundaries is still small compared to the first region.

The results of Tschopp et al. [225], overlaid on Figures 55 and 56, indicate that a wide range of grain boundary behaviors could be expected inside a nanocrystalline material, as a wide range of binding energies of defects to grain boundaries have been found in atomistic results. Although these points are not intended to simulate actual grain boundary behavior due to the lack of knowledge of other parameters, they are used to choose some points lying within Regions 1, 3, and 4 listed above for which the vacancy cluster profiles inside the grain interior can be investigated. These points are indicated with numbers in Figure 55a. The vacancy cluster profiles created using these binding energies are shown in Figures 57a and 57b at a higher dose of 10^{-2} dpa along with the vacancy cluster profiles created using two limiting cases: (1) a 100 nm thin film with free surfaces that act as perfect sinks and (2) a bulk medium with no grain boundaries and periodic boundary conditions in all directions.

For the sake of illustration, we choose several points in Figure 55a, indicated by numbers 1-5, to investigate defect accumulation within the grain interior. Anecdotally, points 1-5 correspond to the binding energies of vacancies and self-interstitials to $\Sigma 3$, $\Sigma 5$, $\Sigma 9$, $\Sigma 11$, and $\Sigma 13a$ grain boundaries found in the work of Tschopp et al. [225], respectively. The defect profiles and average sizes shown in Figures 57a and 57b show a variety of different damage accumulation trends, depending on which region listed above the grain boundary binding energies E_b(V) and E_b(SIA) fall into:

1. For case 1, the grain interior is almost completely defect-free. This is due to the slight bias of the grain boundary to trap vacancy clusters, and contradicts experimental observations of coherent twin boundaries [90, 47]. This difference may be explained by grain boundary emission of small vacancy clusters, as discussed in Section 4.5.3.6.

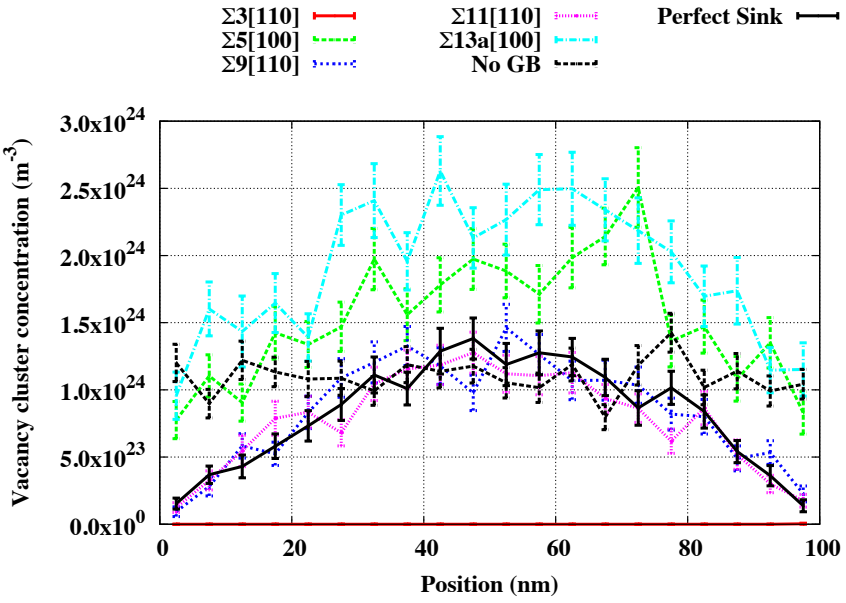

(a)

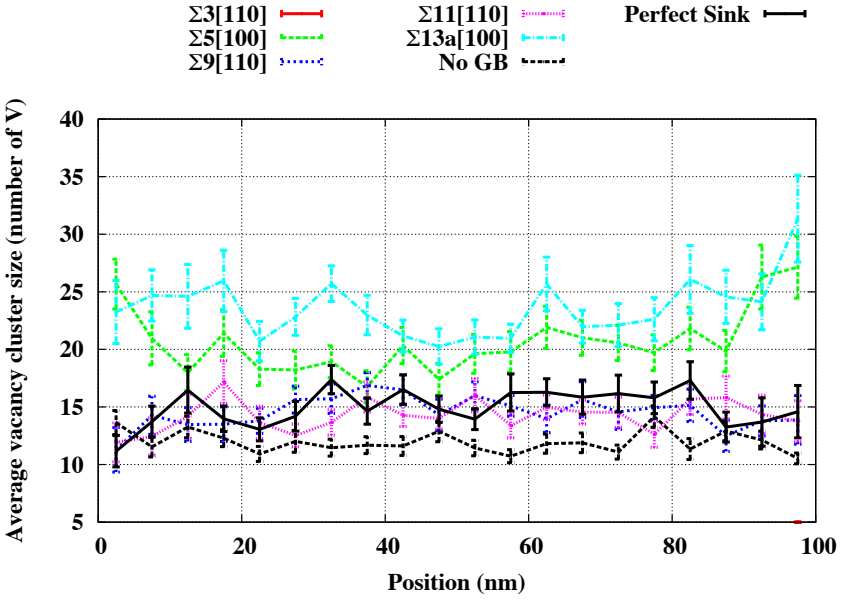

(b)

Figure 57: Profiles showing vacancy cluster concentration and average size inside the bulk for several chosen values of E_b(V) and E_b(SIA), corresponding to values for specific grain boundaries found by Tschopp et al. [225].

2. For cases 2 and 5, the grain boundary is biased towards trapping self-interstitials, and the resulting surplus of vacancies in the grain interior leads to the opposite effect. In this case, both the average vacancy concentration and size are higher than for the case of a system with no grain boundaries.

3. For cases 3 and 4, both vacancies and SIAs are trapped on the grain boundary and the defect accumulation profile resembles that of a perfect sink.

These results indicate that the effects of grain boundaries on defect accumulation can vary widely, with behaviors ranging from strong suppression of defect formation inside some grains to amplification of vacancy cluster formation inside others. Therefore, the binding energies E_b(V) and E_b(SIA) of defects to grain boundaries are primary variables necessary for correctly modeling defect accumulation in a nanocrystalline metal, in agreement with Uberuaga et al. [227]

4.5.3.6 Cluster emission from grain boundaries

For case 1 in Figure 57a, the defect profile inside the grain is in qualitative disagreement with experimental results. In this case, grain boundary binding energies for single vacancies and self-interstitials corresponding to the $\Sigma 3[110]$ grain boundary [225] are found to cause decreased vacancy accumulation inside the grain. This contrasts with experiments in helium-irradiated copper [90, 47] and quenched gold [188], in which defect accumulation near twin boundaries proceeded as if the boundary was not present, indicating a low sink efficiency for defects. Indeed, the sink efficiency η_{V} for vacancies in this grain boundary as shown in Figure 56a is on the order of 10^{-3}. However, the sink efficiency η_{I} for self-interstitials in this grain boundary is on the order of 10^{-5}, even lower than η_{V}. Therefore, there is a slight surplus of SIAs in the grain interior, causing annihilation of the majority of vacancies and vacancy clusters and decreasing the defect concentration in the grain. This behavior was found to persist even when decreasing the values of E_b(V) and E_b(SIA) to 0 eV.

The discrepancy between these results and experimental results is likely due to the need for inclusion of additional defect behaviors in the model, such as defect cluster emission

from the grain boundary. In Sections 4.5.3.1 and 4.5.3.5, sensitivity analyses are used to investigate the variability in defect accumulation caused by different migration and binding energies of defects in the grain boundary while keeping the allowed defect behaviors and reactions the same. However, this model is based on assumptions such as the ability of the grain boundary to emit only single vacancies and SIAs, rather than clusters of such defects. To demonstrate the necessity of identifying the correct defect behaviors that should be included in such a model, the analysis of Section 4.5.3.5 is repeated here while allowing all vacancy and SIA clusters size 1-4 to dissociate from the grain boundary and move back into the bulk with the same binding energy E_b(V) and E_b(SIA). Results of this analysis are shown in Figures 58, 59, and 60. When comparing results to Figures 55, 56, and 57, results show several significant differences including no vacancy cluster formation on the grain boundary at very low binding energies, a broader Region 3 (described in Section 4.5.3.5 above), and a smoother transition from Region 1 to Region 2.

Defect accumulation in the grain interior after irradiation to a higher dose of 10^{-2} dpa, shown in Figures 60a and 60b, is also shown to change significantly as a result of changing the allowed reactions in the system. Overall, using this model, higher populations of vacancy clusters are present in the grain interior and their average sizes are greater when compared to the results of the previous model shown in Figures 57a and 64b. Importantly, the qualitative disagreement with experiments of damage accumulation near twin boundaries described above is smaller for case 1 in Figure 60a than in Figure 57a and disappears entirely for values of $E_b(V) < 0.1$ eV.

This analysis indicates that for certain grain boundaries such as $\Sigma 3$ boundaries, the ability for defect clusters to emit from the boundary may be a critical factor in predicting their impact on damage accumulation. This phenomenon has not been investigated extensively in atomistic studies of binding energies of defects to grain boundaries [225, 227].

4.5.4 Analysis of correlations between grain boundary defect behaviors and damage accumulation

In Section 4.5.3, maps of damage accumulation and sink efficiency are shown for two-point correlation studies of binding and migration energies governing defect behavior on

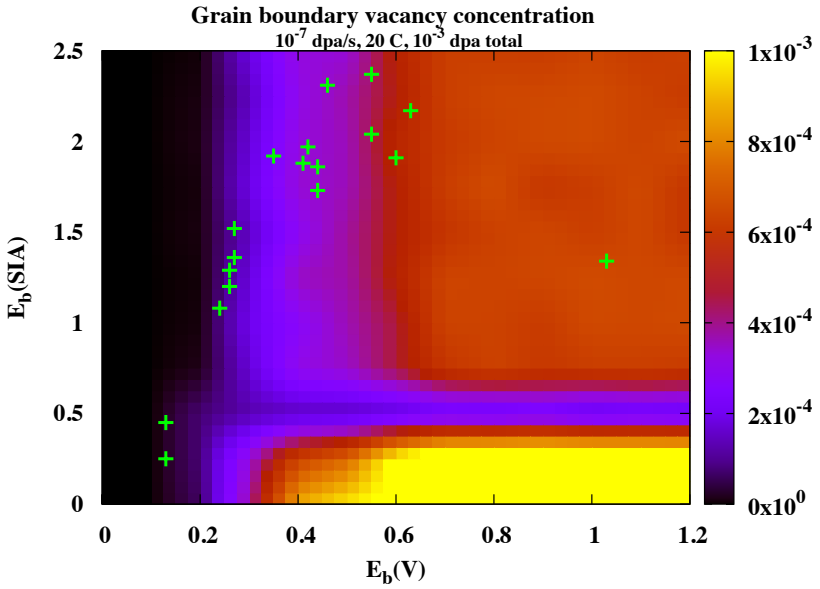

(a)

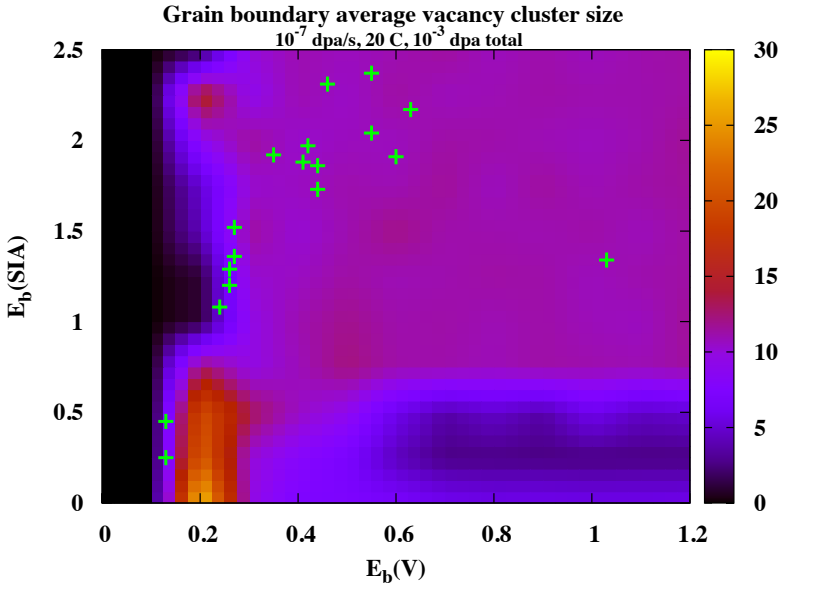

(b)

Figure 58: Maps of void concentration (55a) and average size (55b) on the grain boundary as a function of binding energy of vacancies and self-interstitials to the grain boundary, at a total dose of 10^{-3} dpa. Marked points indicate average binding energies of defects to grain boundaries found by Tschopp et al. [225].

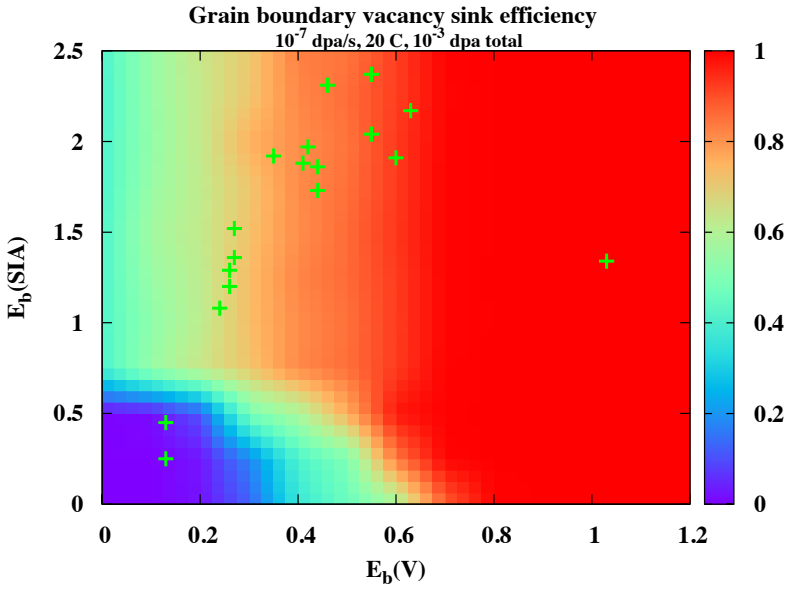

(a)

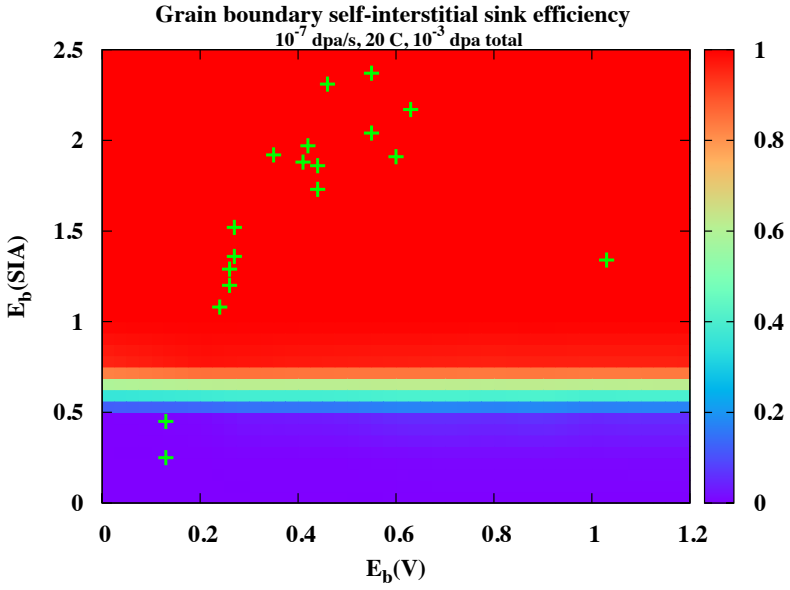

(b)

Figure 59: Maps of sink efficiencies η_V (56a) and η_I (56b) on the grain boundary as a function of binding energy of vacancies and self-interstitials to the grain boundary, at a total dose of 10^{-3} dpa. Marked points indicate average binding energies of defects to grain boundaries found by Tschopp et al. [225].

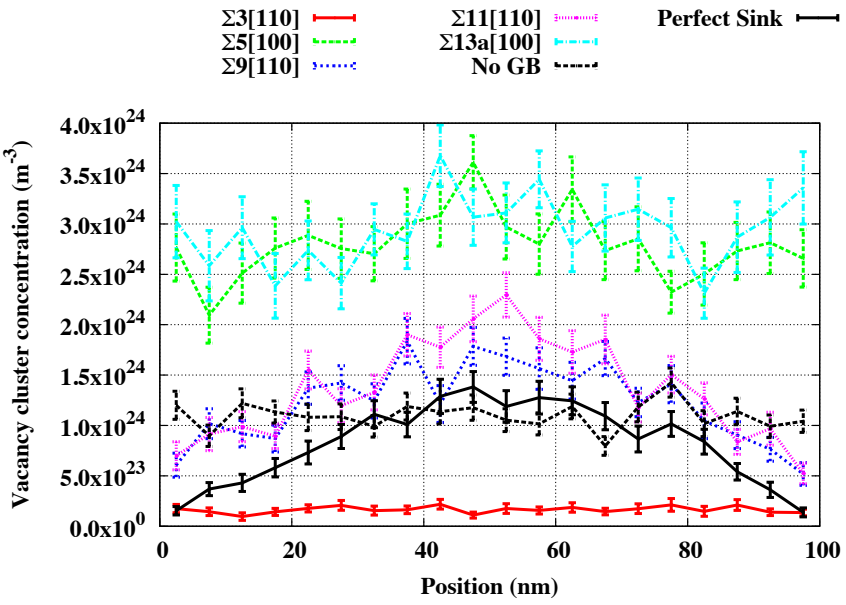

(a)

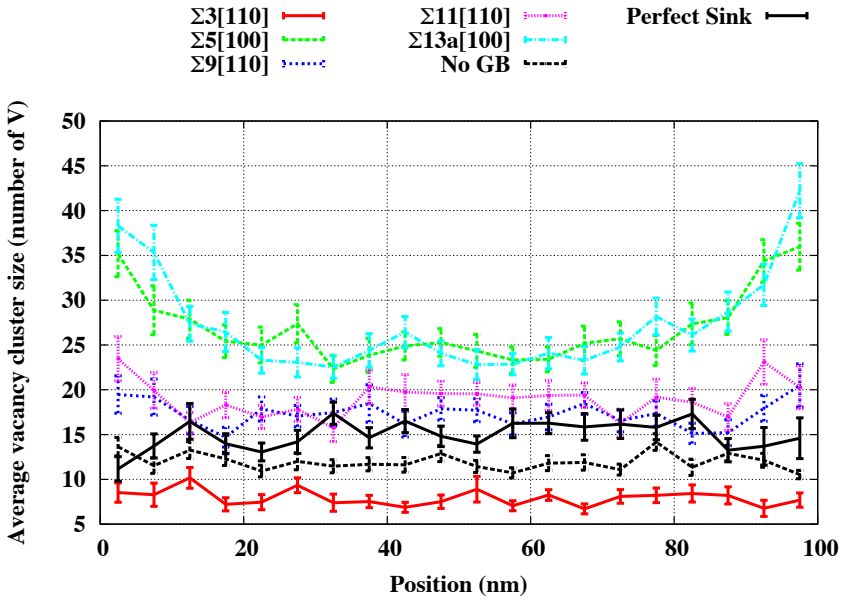

(b)

Figure 60: Profiles showing vacancy cluster concentration and average size inside the bulk for several chosen values of E_b(V) and E_b(SIA), corresponding to values for specific grain boundaries found by Tschopp et al. [225].

grain boundaries. All binding and migration energies not varied in these studies are set to constant values, typically their values in bulk α-Fe. Therefore, the results presented in Section 4.5.3 do not describe the full range of possible defect accumulation behaviors due to the high number of parameters that can be varied inside the grain boundary. A complete description of defect accumulation made by varying all identified parameters simultaneously would be daunting, but a statistical description of the correlation between input and output variables can be made. Therefore, in this section a more complete statistical analysis of the correlations between defect migration and binding energies and the resulting defect accumulation is performed while varying many defect properties simultaneously.

4.5.4.1 Correlation of input and output variables

The same eight variables governing defect behavior inside the grain boundary that are investigated in Sections 4.5.3.1 and 4.5.3.5 are chosen as free variables here: single defect migration energies E_m(V) and E_m(SIA), small defect cluster migration energies E_m(V Cluster) and E_m(SIA Cluster), binding energies of single defects to the grain boundary E_b(V) and E_b(SIA), and parameters A(V) and A(SIA) in the functional form for defect cluster binding energies. Bounds for each variable can be found in Table 14. A total of 3000 sets of these input values are chosen randomly, assuming a uniform probability distribution and domains for each variable given by the same domains tested in in Section 4.5.3. Irradiation is simulated to a total dose of 10^{-3} dpa at room temperature, as described in Section 4.5.2.2. The following metrics are used to probe potential statistical correlations using the eight input variables described above: vacancy concentration in the grain boundary C(V), average vacancy cluster size in the grain boundary, and sink efficiencies η_{V} and η_{I}. Five simulations are run for each set of input variables and average values of output variables are computed. Note that the goal of this analysis is to investigate correlations between input and output variables, rather than between input variables which are uncorrelated due to their random choice. Clearly, correlations do exist between binding and migration energies of defects inside grain boundaries, such as the inverse correlation between E_m(V) and E_m(SIA) in grain boundaries observed by Uberuaga et al. [227], but these relationships

are not investigated here.

Using the eight variables governing defect behavior and four metrics used to measure defect accumulation provided by these simulations, a $n \times m$ matrix X of data points is constructed ($n = 3000$ and $m = 8 + 4 = 12$ here), with x_{ij} representing the value of input or output variable j obtained in dataset i. This matrix is then converted into a deviation matrix D, in which d_{ij} is given by:

$$d_{ij} = \frac{x_{ij} - \overline{x_j}}{\sigma_{x_j}} \tag{95}$$

where $\overline{x_j}$ is the average value of variable j over all datasets and σ_{x_j} is the standard deviation of variable j over all datasets. Next, the $m \times m$ correlation matrix R is computed which provides the correlation between all input and output variables tested here. R is given by:

$$R = \frac{1}{n} D^T \cdot D \tag{96}$$

Thus, the value for correlation r_{ij} between any two variables i and j is:

$$r_{ij} = \frac{d_{ki} d_{kj}}{n} \tag{97}$$

using the Einstein convention to imply a sum over k. This is the standard definition of correlation. A description of the methodology used to find R can be found in ref. [1]. As the correlations between input variables are zero due to their random choice, the subset of R showing correlations between either one input and one output variable or two output variables is shown in Table 15. Correlation values range between -1 and 1, indicating perfect inversely and perfect directly correlated variables, respectively.

Defect behaviors that are strongly correlated with changes in damage accumulation are necessary for accurate simulation of defect evolution in nanocrystalline systems. The strongest correlations found between input and output variables are between the binding energies of single defects to the grain boundary E_b(V) and E_b(SIA) and the corresponding sink efficiencies η_{V} and η_{I}, at 0.724 and 0.763 for vacancies and SIAs, respectively. A strong correlation is also seen between the migration energy of single vacancies E_m(V) and the concentration and average size of vacancies in the grain boundary, at 0.501 and -0.216, respectively. Input parameters with low correlations to output variables are E_m(SIA

Table 15: Correlations between defect binding and migration energies in grain boundaries and metrics for damage accumulation in simulations of Frenkel pair irradiation of nanocrystalline α-Fe, using simulation parameters given in Section 4.5.2.2. All correlation results are reported in the range $[-1, 1]$

Correlation matrix

	C(V)	Size(V)	η_{V}	η_{I}
E_m(V)	0.501026775	-0.216087858	-0.158020377	1.29×10^{-2}
E_m(SIA)	0.147239909	0.145007676	-2.73×10^{-3}	-5.93×10^{-2}
E_m(V Clusters)	0.142412381	-0.138616306	2.10×10^{-2}	7.29×10^{-4}
E_m(SIA Clusters)	3.42×10^{-2}	4.74×10^{-2}	2.21×10^{-2}	-1.97×10^{-2}
E_b(V)	0.207899832	-0.140550804	0.723818559	-1.05×10^{-2}
E_b(SIA)	5.27×10^{-2}	-0.23088202	5.42×10^{-2}	0.762664155
A(V)	-3.28×10^{-2}	2.27×10^{-2}	-7.96×10^{-3}	-7.15×10^{-2}
A(SIA)	2.59×10^{-3}	-7.07×10^{-3}	-1.41×10^{-2}	1.20×10^{-3}
C(V)	1	-0.193738479	0.212013526	6.61×10^{-2}
Size(V)	-0.193738479	1	-0.210381828	-0.312326674
η_{V}	0.212013526	-0.210381828	1	9.21×10^{-2}
η_{I}	6.61×10^{-2}	-0.312326674	9.21×10^{-2}	1

clusters) and cluster binding energy parameters A(V) and A(SIA). The metrics used to measure defect accumulation are also shown to be correlated in this analysis. A positive correlation exists between grain boundary vacancy concentration C(V) and sink efficiency η_{V}, and both of these variables are inversely correlated to average vacancy cluster size. In addition, self-interstitial sink efficiency η_{I} is inversely correlated to average vacancy cluster size on the grain boundary, although η_{I} is not strongly correlated to the other output variables.

To test the convergence of the analysis performed in this section, the eigenvalues λ_k of the correlation matrix R are shown in Figure 61 as a function of the number of sets of input parameters used to generate them. These results show that the values for λ_k and by extension the correlation between the various input and output parameters has converged once 3000 sets of inputs have been generated.

Overall, the results of this section are in agreement with the results presented in Section 4.5.3, indicating that the most important parameters necessary for simulating radiation defect accumulation in nano-grained α-Fe are E_m(V), E_m(SIA), E_b(V), and E_b(SIA). Note that these results are dependent on the irradiation conditions chosen. For the irradiation

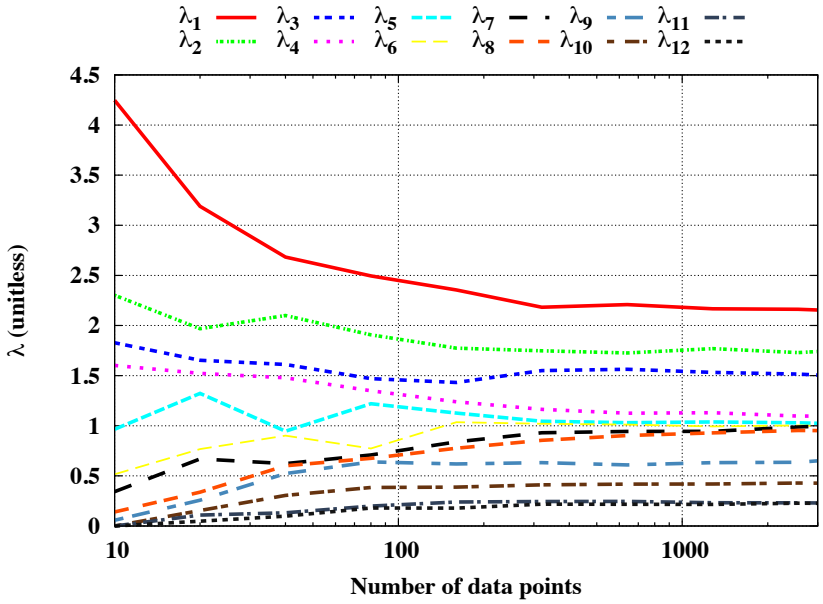

Figure 61: Progression of eigenvalues λ of the correlation matrix as a function of the number of data points used. The data set shows convergence once 3000 sets of inputs have been generated.

conditions chosen in this study, the majority of defects arriving at the grain boundary are single vacancies and SIAs. During cascade damage or at higher dose rates, the impact of cluster behavior at the grain boundary could be more significant.

The correlations described in this section give relationships between individual defect behaviors and damage accumulation in nanocrystalline α-Fe. However, it is also useful to investigate groups of variables that frequently vary together, in order to develop a physical understanding of the processes that drive defect accumulation inside grain boundaries. This analysis is given in 4.5.4.2 using principal component analysis.

4.5.4.2 Principal component analysis

In this section, principal component analysis [104, 1] is performed in order to identify the sets of variables that most strongly influence damage accumulation. The eigenvectors v_k of the correlation matrix R shown in Table 15 are the principal components of the system. The first principal component v_1 represents the direction in m dimensional space along which the value of $v_{1j}d_{ij}$ has maximum variance, for $i \in [1, n]$. The second principal component v_2 is then defined as the direction orthogonal to v_1 with maximum variance of $v_{2j}d_{ij}$, and so on.

The variance of principal component v_k is given by λ_k, the eigenvalue of that eigenvector. Frequently, the majority of the variance in the system can be accounted for by only a few principal components, allowing analysis of the most important relationships between variables. Table 16 shows the principal components of R most responsible for variation in the output variables. Communality between the principal components and the output variables is also given in Table 16b. The communality between variable j and component v_k is the percentage of the variation in d_{ij} accounted for by principal component v_k. This analysis shows that between $77 - 87\%$ of the variation in each of the four output variables is explained by the first four principal components. All of the principal components v_k, variances λ_k, and values of communality for output variables are given in Appendix E.

Table 16: (16a) The four eigenvectors of the correlation matrix R most responsible for the variance in the output variables, referred to a principal components. Variance in $v_{kj}d_{ij}$, for $i \in [1, 3000]$, is given by λ_k. (16b) Communality values between output variables and principal components. Communality indicates the percentage of variation in each output variable that is explained by a given principal component.

(a) Principal components

Input variables	PC_1	PC_2	PC_3	PC_4
E_m(V)	0.189648805	-9.10×10^{-3}	0.663954208	−0.10918847
E_m(SIA)	-3.38×10^{-2}	-8.24×10^{-2}	0.172736756	0.427359208
E_m(V Clusters)	0.113690271	-4.69×10^{-2}	0.162400282	−0.162878248
E_m(SIA Clusters)	-1.34×10^{-2}	-5.53×10^{-2}	2.30×10^{-3}	0.13985207
E_b(V)	0.347789213	−0.522657117	−0.239754004	−0.134593369
E_b(SIA)	0.411961479	0.478592409	−0.155900304	−0.205989958
A(V)	-7.24×10^{-2}	-6.00×10^{-2}	-2.03×10^{-2}	-5.11×10^{-2}
A(SIA)	3.92×10^{-3}	2.13×10^{-2}	7.84×10^{-2}	-3.41×10^{-2}
Output variables				
C(V)	0.344511533	−0.215825353	0.511062898	−0.26503984
Size(V)	−0.42956806	-7.02×10^{-2}	-9.23×10^{-2}	−0.78054255
η_{V}	0.390880624	−0.460214683	−0.341264526	-1.33×10^{-2}
η_{I}	0.444807211	0.46722243	−0.168630532	−0.123915238
Variance (λ_k)	2.154309427	1.740299394	1.505798711	0.650006163

(b) Communality

	PC_1	PC_2	PC_3	PC_4
C(V)	0.255691100	0.081064160	0.393292466	0.045660409
Size(V)	0.397531957	0.008567315	0.012835851	0.396014092
η_{V}	0.329151901	0.368591156	0.175367541	0.000115532
η_{I}	0.426237563	0.379901788	0.042819278	0.009980836

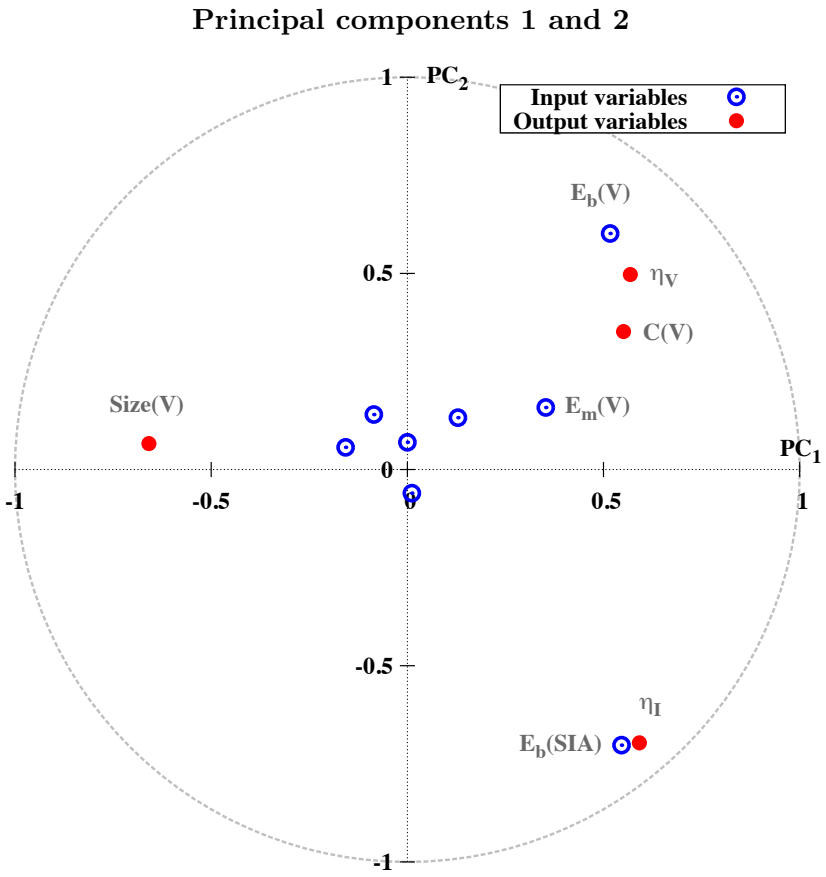

Figure 62: Circle of correlations between input (blue) and output (red) variables for the first two principal components. Input variables with low correlation to principal components are not labeled.

To better understand the relationships between defect behaviors and damage accumulation, the principal components are converted to $\widetilde{v}_k = \lambda^{\frac{1}{2}} v_k$. In this form, the value of $\widetilde{v}_{kj}$ represents the correlation between variable j and principal component k [104]. These values are then plotted for each variable j using two principal components at a time on circles of correlation [1], as shown in Figures 62 and 63. The closer a variable is to the edge of a circle of correlations, the greater percentage of variation in that variable can be explained by those two principal components. By contrast, variables near the center of the circle are less important for those two components. These circles of correlation are used as a visual tool to describe the variables in each principle component as well as their relative significance due to the variance λ of the principal component. By visually inspecting Figures 62 and 63, the following observations can be made:

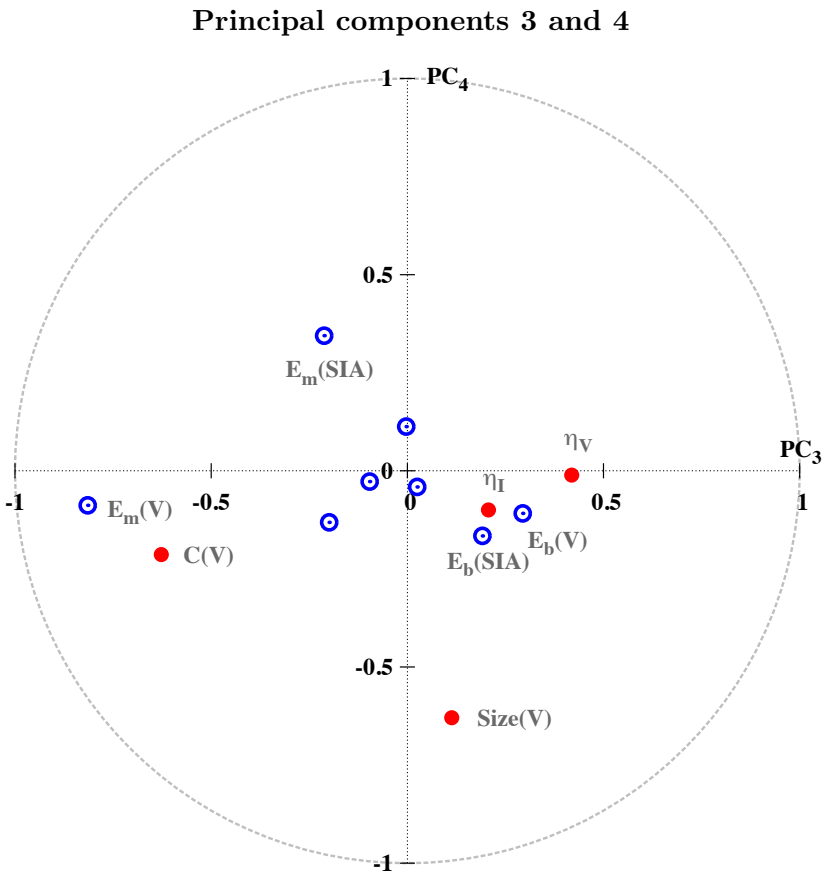

Figure 63: Circle of correlations between input (blue) and output (red) variables and the third and fourth principal components. Input variables with low correlation to principal components are not labeled.

1. In Figure 62, the first principal component indicates an inverse correlation between the size of vacancy clusters and E_m(V), E_b(V), E_b(SIA), C(V), η_{V}, and η_{I}. This is expected, as an increase in vacancy concentration, decrease in vacancy cluster size, and increase in sink efficiency for both vacancies and SIAs occurs when vacancies and self-interstitials are more strongly bound to and less mobile inside the grain boundary.

2. In Figure 62, the second principal component indicates that when E_b(SIA) is inversely correlated with E_b(V), η_{I} is inversely correlated with η_{V} and C(V) as well. This result is also expected, as an increase in binding energy for one defect type accompanied by a decrease in binding energy of another defect type leads to biased trapping of the defect type with the higher binding energy by the grain boundary.

3. In Figure 63, the third principal component indicates that E_m(V) and C(V) are inversely correlated with η_{V} and to a lesser extent η_{I}, E_b(V), and E_b(SIA). This corresponds to the situation in which vacancy clusters are more mobile and simultaneously more tightly bound to the grain boundary, leading to greater sink efficiency but a lower concentration of vacancy clusters due to interactions with other defects (annihilation with interstitials and formation of larger clusters).

4. In Figure 63, the fourth principal component indicates an inverse correlation between E_m(SIA) and the size and concentration of vacancy clusters on the grain boundary. This result is surprising, as it indicates that as self-interstitial diffusion slows (increasing migration energy), the concentration and average size of vacancy clusters in the grain boundary simultaneously decrease. By contrast, in Figure 50 we see that the regions of greatest vacancy concentration and average vacancy cluster size are found when E_m(SIA) is high. Therefore, principal component analysis has enabled identification of a physical result that could not be identified in the two-variable studies of Section 4.5.3. This principal component can be interpreted physically as a decrease in SIA mobility causing an increased number of SIAs to act as recombination sites for mobile vacancy clusters inside the grain boundary, thereby decreasing average vacancy cluster sizes. However, it should be noted that the variance of this principal

component is $\lambda_4 = 0.650$, indicating that this effect is not as strong as the other effects listed here.

4.5.5 Discussion: void denuded zones in irradiated metals

Although the results presented in the previous sections do not represent predictions for specific grain boundaries, some qualitative comparisons with experimental studies of radiation damage near grain boundaries can be made. Experiments of grain boundary-dependent damage accumulation have focused on defect denuded zones near grain boundaries, usually in FCC metals [90, 47, 188]. These studies have demonstrated that the width of void denuded zones, and thus the sink efficiency of grain boundaries for defects, depends on the grain boundary character.

The results of this study cannot be directly compared to experimental measures of denuded zone width in irradiated α-Fe due to the different material and much lower irradiation dose simulated here ($10^{-3} - 10^{-2}$ dpa) than in typical irradiation experiments (> 1 dpa). However, the shape of the vacancy profile in Figures 57a and 60a can give some insight into whether or not denuded zones are expected near various grain boundaries. Grain boundaries that mimic perfect sinks, such as the cases with binding energies corresponding to $\Sigma 9[110]$ and $\Sigma 11[110]$ boundaries shown in Figure 57a, should result in void denuded zones due to the decrease in vacancy cluster concentration near grain boundaries observed in Figure 57a and 60a. By contrast, grain boundaries that are imperfect sinks for vacancies such as the cases with binding energies corresponding to $\Sigma 5[100]$ and $\Sigma 13a[100]$ boundaries shown in Figure 57a have greater vacancy cluster concentration and size than even the case of a material with no grain boundaries, indicating that denuded zone formation is unlikely for these boundaries. Therefore, the experimentally observed sensitivity of void denuded zone formation to grain boundary character is reproduced in this study, although specific predictions cannot be made without further parameters from atomic-scale simulations. A notable exception is the case of $\Sigma 3$ grain boundaries, as discussed in detail in Section 4.5.3.6.

4.5.6 Summary

In this study, a novel scheme for investigating the impact of grain boundary-dependent parameters on defect accumulation in α-Fe with 100 nm grains is implemented using spatially resolved stochastic cluster dynamics (SRSCD). Defect diffusion within grains is treated using three dimensional reaction rates in SRSCD, while defect diffusion and clustering within grain boundaries is treated using two dimensional reaction rates in SRSCD. Grain boundaries are treated as imperfect sinks by applying boundary conditions between the grain interior and the grain boundary associated with perfect sinks but allowing thermal emission of point defects from grain boundaries into the grain interior with a binding energy that is treated as a parameter. Using this scheme, three types of results are used to investigate the influence of grain boundaries on defect accumulation: (1) vacancy concentration and average size inside the grain boundaries, (2) grain boundary sink efficiency η_{V} and η_{I} for vacancies and SIAs, respectively, and (3) the resulting profile of immobile vacancy clusters inside the grains as a function of distance from the grain boundary.

Sensitivity analyses are used to investigate which defect behaviors inside grain boundaries are the most important in governing defect accumulation in and near grain boundaries. Variables identified as having the greatest influence on defect accumulation results are single vacancy and SIA diffusivity inside grain boundaries and the binding energy of vacancies and SIAs to grain boundaries. Vacancy cluster diffusivity inside grain boundaries is also shown to be significant but has a smaller impact on defect accumulation. Variables such as SIA cluster diffusivity inside grain boundaries and the binding energy of point defects to vacancy and SIA clusters inside grain boundaries are shown to be of lesser importance. In addition, emission of defect clusters rather than single defects is shown to have a significant impact on defect accumulation.

Statistical analysis of the results of 3000 randomly chosen sets of input parameters is also performed in order to identify trends in the variance of defect accumulation results when varying many defect behaviors in the grain boundary at once. The results of this analysis agree with the results of the sensitivity studies in identifying the most important parameters to quantify in order to accurately simulate defect accumulation in and near

grain boundaries. Principal component analysis analysis shows that most of the variation in the concentration of vacancies on the grain boundary, the average size of vacancy clusters on the grain boundary, and sink efficiencies η_{V} and η_{I} can be explained by four principal components. These principal components correspond to physical phenomena such as the increase in number and corresponding decrease in size of vacancy clusters on the grain boundary as the migration energy for vacancies $E_m(\mathrm{V})$ and binding energies for vacancies $E_b(\mathrm{V})$ and self-interstitials $E_b(\mathrm{SIA})$ in the grain boundary increase.

The analyses performed in this work are intended to guide future atomistic studies of defect behaviors in grain boundaries. The results presented here indicate that, in order to create reliable multi-scale models of defect accumulation in irradiated nanocrystalline metals, point defect migration energies inside grain boundaries and point defect binding energies to grain boundaries need to be characterized as a function of grain boundary character and defect content. In addition, these results indicate that cluster emission from grain boundaries is a necessary component of multi-scale models of damage accumulation near low-angle grain boundaries such as $\Sigma 3$ boundaries. Once these parameters have been characterized, the methodology presented in this work can be used to simulate defect evolution near specific grain boundaries and compare results to experimental measures of defect accumulation such as void denuded zones and grain boundary void formation.

4.6 Summary of Chapter 4

In Chapter 4, in-depth investigations of the links between irradiation conditions, presence of gases such as helium, and material microstructure on damage evolution are performed. Iron is used as a model material in all studies performed in this chapter, due to the large body of atomistic simulations that have been performed describing defect properties in iron. Therefore, a list of defect parameters that are used throughout the rest of the chapter is given in Section 4.2. The investigations carried out in this chapter are focused on three main microstructural and irradiation regimes:

1. In Section 4.3, helium migration in iron thin films is studied for a variety of irradiation conditions and film thicknesses. This irradiation regime corresponds to experiments

of helium and self-ion irradiation in thin films, which is a popular experimental approach taken to approximate some of the mechanisms expected in reactor environments [231, 114, 186, 92]. Two main studies of helium migration are carried out in this section: helium desorption during low-temperature implantation and annealing, and effective helium diffusivity as a function of irradiation conditions. These studies allow identification of the mechanisms responsible for helium diffusion under various temperature and irradiation regimes.

2. Neutron irradiation of bulk, coarse-grained materials is studied in Section 4.4. This irradiation regime corresponds to experiments carried out in fast reactors [67, 259]. Three mechanisms governing defect evolution are investigated for their relative influence on damage evolution in these irradiation conditions: the impact of ballistic mixing between displacement cascades and defects present in the material, the impact of the PKA energy of displacement cascades, and the ability of impurities such as carbon to act as traps for SIA loops.

   Using the results of the above studies, the experimental conditions reported by Eldrup et al. [67] for neutron damage in bulk iron are replicated as closely as possible, and damage accumulation is compared to experimental measurements using PAS and TEM techniques. A reasonable match is achieved with experimental measurements, although greater saturation is seen in defect populations using SRSCD at high doses than measured in experiments.

3. In Section 4.5 the impact of grain boundaries on damage accumulation is studied in the context of nanocrystalline metals. These materials, which have been shown to exhibit better radiation tolerance than coarse-grained metals in some cases [210, 118, 144, 50], are difficult to study using damage accumulation tools such as cluster dynamics or OKMC due to the large volume required in such simulations and the impacts of grain boundaries on defect accumulation. After using SRSCD to simulate a polycrystalline domain with grain boundaries that act as perfect sinks, the impact of various binding and migration energies inside grain boundaries on those boundaries' sink efficiency is

investigated with a multivariate statistical analysis.

Overall, in Chapter 4 the unique capabilities of the SRSCD methodology developed in this dissertation have been leveraged to address the scientific questions posed in Section 1.2. Namely, in-depth investigations of the impact of irradiation conditions, the presence of helium, and the material microstructures on damage evolution have been carried out. In doing so, the roles of many mechanisms governing damage evolution have been elucidated, including the moderation of helium mobility by vacancy and helium-vacancy clusters, the effect of impurities on dislocation loop mobility, the effect of cascade-defect interactions on void growth and population saturation at high doses, the role of displacement cascade energy, and the role of various grain boundary defect parameters on sink efficiency and denuded zone formation. Taken together, these studies have advanced both the fundamental knowledge of damage evolution in irradiated metals as well as modeling capabilities that can be used for experimental and material design.

CHAPTER V

USING SRSCD IN THE CONTEXT OF MULTISCALE MODELING AND EXPERIMENTAL DESIGN

In the previous chapter, physical mechanisms of defect evolution in irradiated metals are investigated using the SRSCD computational framework. However, the capability of SRSCD to act as an efficient link between time and length scales with the purpose of informing macroscopic models and experimental studies has not been fully demonstrated. Therefore, the goal of this chapter is to demonstrate the use of SRSCD in a multiscale computational framework to inform higher-order models and as a guiding tool for experimental design. These capabilities are demonstrated in two contexts in this chapter: first, SRSCD is used to generate defect populations which are used in a continuum-scale mechanical hardening model to predict the change in yield strength of neutron-irradiated iron. Second, a methodology is proposed for determining temperature shifts required in experimental studies which use proxy radiation sources (such as ion beams) to best reproduce damage expected due to irradiation under 'intended' damage conditions in which the dose rate is significantly different (such as neutron damage).

This chapter is organized as follows: in Section 5.1, a brief overview of the modeling tools used to study irradiation-induced hardening is presented. Next, in Section 5.2, a multiscale computational framework for predicting radiation hardening is proposed and results are compared to experimental hardening results for the case of neutron irradiation of α-Fe. Finally, the relationship between temperature and dose rate in 'intended' and 'proxy' irradiation conditions is explored in Section 5.3. Summary and conclusions are given in Section 5.4.

5.1 Multiscale modeling of irradiation hardening in metals

As discussed in Section 2.1.5, the presence of radiation damage in metals can lead to macroscopic changes in material behavior such as hardening, swelling, and embrittlement

[67, 38, 156, 153, 130, 43, 36]. Similar to the study of radiation damage evolution in irradiated metals, coupling between radiation damage and mechanical fields is a multi-scale phenomenon, spanning atomic and macroscopic length scales. In this section, the atomic-level mechanisms for the interaction between radiation and mechanical properties are presented, along with past efforts to upscale this information to continuum models of radiation-induced hardening.

In irradiated metals, the main mechanism for increasing initial yield strength is glide dislocations interacting with radiation defects in the bulk, acting as obstacles to their motion. To study these mechanisms at the atomic scale, radiation defects such as voids and dislocation loops can be generated in atomistic simulations along with glide dislocations. Shear strains are then applied to the atomistic simulation via boundary conditions and interaction between the glide dislocation and the radiation defect is induced [11, 14, 164]. This strategy allows direct observations of the various mechanisms involved in defect-dislocation interactions. Atomistic studies have shown that glide dislocations are pinned by defects such as voids and dislocation loops and bow around them as the applied stress is increased [11, 14, 169, 164]. This continues until the Orowan stress is reached, allowing the dislocation to break free and continue through the material. Such studies have also provided insight into other defect-level mechanisms that exist in irradiated materials subjected to deformation. Examples include dislocation core spreading in fcc metals during dislocation-defect interactions [164], thermal effects such as dislocation climb during interactions with radiation defects [65], and channel clearing in which glide dislocations absorb radiation defects as they glide through the plastically deforming material [174, 175].

Overall, the mechanisms described above are responsible for the increase in yield strength and decrease in ductility observed in irradiated metals discussed in Section 2.1.5 as well as other radiation effects such as creep and strain softening of irradiated metals. Atomic-scale studies have aided in the understanding of the nature of the interactions between radiation defects and glide dislocations involved in crystal plasticity, but they operate at a scale that is too small to create link between macroscopic stress-strain behavior and radiation damage. Instead, continuum models developed from atomic scale considerations have been developed

for this purpose. Dating back to the original model by Orowan whereby the critical stress for a single dislocation to pass through arrays of impenetrable obstacles is calculated, significant efforts have been placed on understanding the complex interactions between radiation induced defects and glide dislocations at the continuum scale. Historically, three main models have been proposed and used in the literature: the dispersed barrier hardening (DBH) model, the Friedel-Kroupa-Hirsch (FKH) model, and the Bacon-Kocks-Scattergood (BKS) model. Each model provides a different functional form for radiation-induced change in yield stress due to the presence of defects with concentration N and diameter d.

The continuum models described above have allowed for the development of single crystal constitutive laws embedded in different types of homogenization methods (i.e. full-field and mean-field polycrystal homogenization schemes) [158, 7, 53, 21, 171, 172, 244]. Resulting single crystal and polycrystal simulations of radiation induced material property changes based on the DB hardening model have successfully reproduced observed changes in yield strength, initial strain softening, strain softening under cyclic loading, radiation assisted creep, and decreased ductility [158, 7, 53, 21, 171, 172, 244]. For example, Arsenlis et al. [7] treat effective stress and strain in a finite element framework, and include the effect of dislocations cutting stacking fault tetrahedra (SFTs) to create dislocation-free channels and subsequent strain softening. However, defect populations used in the work of Arsenlis et al. are assumed to be all in the form of SFTs with uniform size, and a connection between the defect population and the irradiation conditions is not made. In work of Onimus and Béchade [158], a self-consistent model is used to reproduce the higher yield point and softening under cyclic loading of polycrystalline zirconium due to the presence of irradiation induced dislocation loops. Here too, only one defect type (dislocation loops) is treated with a single initial concentration and size. By contrast, the work of Deo et al. [53] uses a self-consistent scheme to estimate polycrystalline hardening in steel as a function of radiation dose with defect populations and sizes coarsely informed by the results of OKMC simulations, but actual defect concentrations and sizes are not taken from OKMC and a distinction is not made between voids and dislocation loops. In the hardening and creep studies of Patra et al. [171], a rate theory formulation is used to estimate the populations of

single vacancies and self-interstitials, but the initial irradiated defect state is based on the work of Deo et al. [53] and therefore not taken from simulations of damage accumulation.

Despite the gains made in polycrystalline hardening simulations, a direct connection between material property changes and irradiation conditions (i.e. dose rate, cascade energy, and irradiation temperature) is still lacking. In particular, no macroscopic hardening simulations have been carried out that take defect populations directly from a lower level simulation of radiation damage accumulation such as CD or OKMC to predict the resulting changes in material properties. This is a necessary step for multi-scale models of material performance under extreme irradiation conditions to accurately predict material lifetimes in a range of reactor environments.

5.2 Damage-induced hardening in neutron-irradiated bulk iron

As described in the previous section, radiation induced hardening in bulk metals is caused by the presence of defects acting as obstacles to dislocation motion [13, 169, 11]. Establishing a linkage between irradiation conditions and material strength is a particularly challenging problem as (1) microstructure evolution during irradiation is complex and depends on irradiation conditions [37, 184, 233, 125, 67, 38] and (2) constitutive models such as those described in the previous section must describe the effective strengthening resulting from the interaction of glide dislocations with a distribution of defects varying in size, density and position. A link between points (1) and (2) is necessary in order to create predictive models of radiation hardening in irradiation conditions not yet treated experimentally. The objective of the present study is to introduce, validate and apply a coupled modeling strategy linking radiation-induced defect accumulation to the mechanical response of polycrystalline iron. First, radiation damage accumulation in neutron-irradiated α-Fe is simulated in this work using SRSCD. Defect populations are then upscaled into a crystal plasticity framework including radiation-induced hardening using the BKS model. Defect strength parameters are found via use of a mean-field Taylor type model fitted against experimental data on neutron-irradiated α-Fe [38]. Following this, full field rate-independent crystal plasticity

simulations using the material point method (MPM) are performed to investigate the relationships between dose rate, yield strength and internal stress-strain distribution in an α-Fe polycrystal subjected to uniaxial tension.

5.2.1 Mesoscale irradiation hardening model

In this section, the methodology used to simulate polycrystalline plasticity in the presence of radiation damage is discussed. The constitutive framework of the empirical rate-independent crystal plasticity model employed in this work is first described in Section 5.2.1.1. The defect populations in neutron-irradiated iron and the resulting increase in critical resolved shear stress along the slip planes are described in Sections 5.2.1.3 and 5.2.1.2, respectively. The defect populations and average sizes output from SRSCD simulations serve as the inputs into the hardening model. Finally, the implementation of polycrystalline plasticity in the MPM framework is discussed in Section 5.2.1.4.

5.2.1.1 Crystal plasticity framework

Crystal plasticity is treated with a rate-independent, small-strain formulation [93]. Here, plasticity is driven by slip dislocation motion. Therefore, grain boundary mediated plasticity and twinning mechanisms are disregarded. The total strain in the material ϵ (in tensorial form) is decomposed as the sum of elastic and plastic strains:

$$\epsilon = \epsilon^e + \epsilon^p \ . \tag{98}$$

The elastic domain $\mathcal{E}$ is defined for $\alpha = [1, ..., m]$ slip planes as the values of the Cauchy stress tensor σ for which the resolved shear stress $|\tau^\alpha(\sigma)|$ on slip plane α is less than the critical resolved shear stress g^α on that slip plane:

$$\mathcal{E} = \{(\sigma, g^\alpha) | f(\alpha, g^\alpha) = |\tau^\alpha(\sigma)| - g^\alpha \leq 0, \alpha = [1, ..., m]\} \ , \tag{99}$$

Here, $\tau^\alpha(\sigma)$ is given by the projection of the Cauchy stress tensor on slip system α. Within the small strain formulation, the relationship between the Cauchy stress tensor and the elastic strain tensor is given by Hooke's law:

$$\sigma = \mathbb{C} : \epsilon^e \ , \tag{100}$$

Table 17: Iron properties
(values taken from Koester et al. [113])

Elastic modulus	C_{11}	236.9	GPa
Elastic modulus	C_{12}	134.0	GPa
Elastic modulus	C_{44}	119.4	GPa
CRSS	τ_0	29.8	MPa
Saturation Stress	τ_s	193.3	MPa
Initial hardening	h_0	471.2	MPa

where $\mathbb{C}$ is the elastic stiffness tensor. Plastic strain evolution is found by projecting slip on system α onto the global coordinate system:

$$\dot{\epsilon}^p = \sum_\alpha \dot{\gamma}^\alpha \mathbf{P}^\alpha \ , \tag{101}$$

where $\dot{\gamma}^\alpha$ is the plastic slip rate on slip system α and $\mathbf{P}^\alpha$ is the Schmid tensor of slip system α. Slip activity is determined via the use of consistency conditions [189] ensuring positive and maximum dissipation, given by:

$$\dot{\gamma}^\alpha \geq 0 \ , \qquad f^\alpha \leq 0 \ , \qquad \dot{\gamma}^\alpha f^\alpha = 0 \ . \tag{102}$$

The evolution of the critical resolved shear stress (CRSS) g^α on a given slip system α is given by:

$$g^\alpha|_{t=0} = \tau_0^\alpha \ , \qquad \dot{g}^\alpha = h^\alpha \dot{\gamma}^\alpha \ , \tag{103}$$

where τ_0^α is the initial CRSS on that slip plane and h^α is the hardening coefficient on the slip plane α, given by:

$$h^\alpha = h_0^\alpha \text{sech}^2 \left(\frac{h_0^\alpha \overline{\gamma}}{\tau_s^\alpha - \tau_0^\alpha} \right) \ , \tag{104}$$

where h_0^α is the initial hardening modulus on slip system α, $\overline{\gamma}$ is the cumulative plastic slip, and τ_s^α and τ_0^α are the saturation and initial CRSS on slip system α, respectively. The material parameters governing elastic and plastic behavior for iron used in this work are taken from Koester et al. [113] and are given in Table 17. Although rate-independent plasticity is treated in this work, the reference strain rate used by Koester et al. in determining these parameters is $\dot{\gamma}_0 = 2.44 \times 10^7 \ \text{s}^{-1}$ [113].

5.2.1.2 Radiation-induced hardening

In this study, radiation damage accumulation and microstructure evolution resulting from imposed traction or displacement are treated sequentially. The cases of evolving radiation damage during mechanical deformation or non-zero internal stress during the irradiation are disregarded. Therefore, radiation hardening is introduced by replacing the initial and saturation stresses τ_0^α and τ_s^α in equations (103) and (104) with modified versions $\tau_{0,\text{irr}}^\alpha$ and $\tau_{s,\text{irr}}^\alpha$ given by adding a contribution due to the presence of irradiation-induced defects, $\Delta\tau_{\text{irr}}$:

$$\tau_{0,\text{irr}}^\alpha = \tau_0^\alpha + \Delta\tau_{\text{irr}} \quad , \quad \tau_{s,\text{irr}}^\alpha = \tau_s^\alpha + \Delta\tau_{\text{irr}} \tag{105}$$

The BKS radiation hardening model is used to establish a relationship $\Delta\tau_{\text{irr}}$ and the presence and size of defects. In the BKS model, hardening due to a random spatial distribution of obstacles is given by [13, 24]:

$$\begin{aligned} \Delta\tau_{\text{irr}} &= \alpha_{\text{BKS}} \frac{\mu b}{2\pi l} \left(\ln\left(\frac{l}{b}\right)\right)^{-\frac{1}{2}} \left(\ln\left(\frac{d'}{b}\right) + 0.7\right)^{\frac{3}{2}} \ , \\ l &= \frac{1}{\sqrt{Nd}} \ , \\ d' &= \frac{dl}{d+l} \ , \end{aligned} \tag{106}$$

where μ is the shear modulus, N is the density of defects, d is the diameter of those defects, b is the Burgers vector of the material, and α_{BKS} is an unknown defect strength parameter. The parameters l and d' represent the average spacing between defects and the harmonic mean of the spacing between defects and the defect diameter, respectively.

In this work, the BKS model given in equation (106) is used to simulate hardening due to two types of radiation-induced defects, voids and dislocation loops, with populations provided by the results of SRSCD simulations. These defect populations have a specific size distribution that is dependent on the irradiation dose. However, dislocation dynamics results suggest that for both dislocation loops and voids, the hardening due to a distribution of defect sizes can be properly rendered via use of a single average defect size and a

corresponding mean effective distance between defects [196]. Therefore, all hardening simulations in this work are carried out using the average defect diameter for dislocation loops and voids. Figure 64b shows the average defect sizes found in SRSCD as a function of dose. In addition, dislocation dynamics results [196] have shown that the defect strength parameter α_{BKS} is constant over a range of defect sizes d and densities N for a given defect type (void or dislocation loop). Therefore, separate values of $\Delta\tau_{\mathrm{irr}}$ are calculated for voids and dislocation loops at several radiation doses, using constant strength parameters α_{V} and α_{L}, respectively. To model collective hardening from multiple defect types, $\Delta\tau_{\mathrm{irr}}$ is calculated for each defect type and a non-linear superposition law is used to find the total hardening. This law is in the form:

$$\Delta\tau_{\mathrm{irr}} = (\Delta\tau_{\mathrm{V}}^{n} + \Delta\tau_{\mathrm{L}}^{n})^{\frac{1}{n}} \ . \tag{107}$$

The value of n has been found to be approximately $n = 2.22$ in dislocation dynamics simulations [196].

Voids and dislocation loops both contribute to hardening. However, single vacancies and small vacancy clusters are absorbed by dislocations and as such are not considered to contribute to hardening in this study. As the minimum vacancy cluster size that contributes to hardening is unknown, an arbitrary minimum void size is chosen to be one nm. The effect of modifying this minimum size is investigated in Section 5.2.3. Changing the minimum size of voids included in hardening simulations is shown to change the fit values of defect strength parameters α_{V} and α_{L} without qualitatively changing the hardening results in Section 5.2.2.

5.2.1.3 Defect populations in neutron-irradiated α-Fe

In this study, damage accumulation is simulated using the material and irradiation conditions reported by Eldrup et al. [67] for neutron irradiation of bulk iron. Simulation parameters are shown in Table 11. Vacancy and SIA cluster populations evolutions are simulated in SRSCD up to 10^{-1} displacements per atom (dpa). A complete list of defect binding and migration energies as well as reaction rates used in this simulation can be found in Tables 1 and 7 and in [60]. Results of these simulations are presented in Section 4.4.5, and have

been compared to experimentally measured defect populations [67, 259]. Figure 64 shows the SRSCD results in this study for concentrations and average sizes of voids and SIA loops as a function of dose.

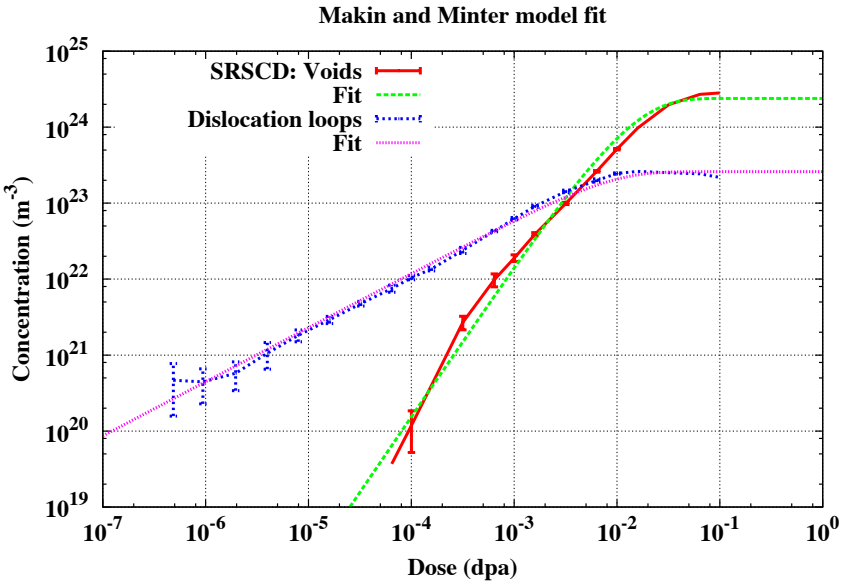

(a)

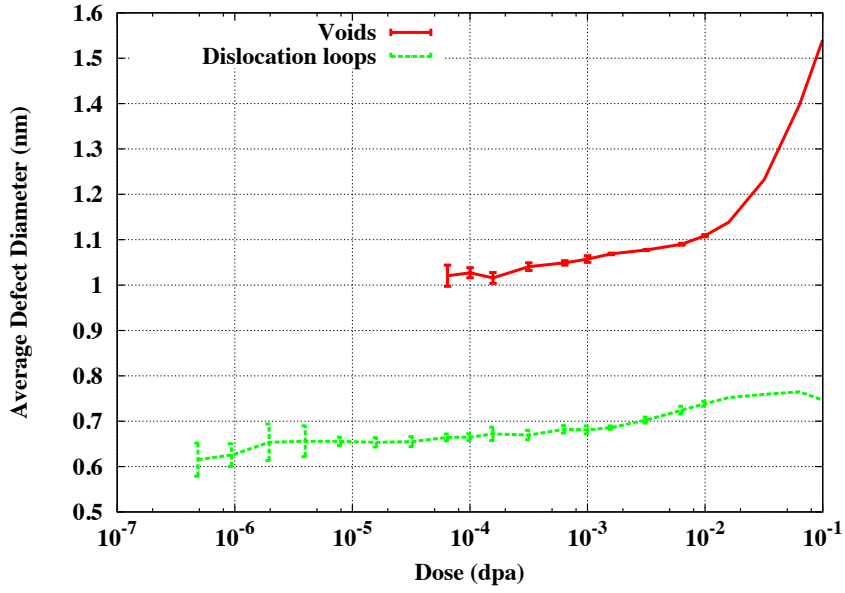

(b)

Figure 64: (64a) Dislocation loop and void (> 1 nm) concentrations as a function of irradiation dose from SRSCD. (64b) Average dislocation loop and void (> 1 nm) sizes as a function of irradiation dose from SRSCD.

The values of defect density and average size at a given dose, N and d, are obtained

Table 18: Defect concentration parameters
(see equation (108))

	Voids	Loops
N_{sat}	2.39×10^{24}	2.59×10^{23}
B	78.39	130.75
p	1.99	0.71
r	1.0	1.0

from SRSCD simulations described in Section 4.4. Simulation results for the densities of dislocation loops and voids greater than one nm in diameter as a function of dose are shown in Figure 64a. These results show a region of fast accumulation of defects at low doses, following by a saturation of defect concentrations after approximately 10^{-2} dpa, due to cascade-defect interactions. SRSCD simulations are carried out to 10^{-1} dpa, while experimental hardening results for neutron-irradiated iron exist at 1 dpa [38]. To estimate defect densities at doses greater than simulated in SRSCD, we propose a modification to the Makin and Minter model for defect concentration evolution [126]:

$$N(\phi) = N_{\text{sat}} \left(1 - e^{-B\phi^r}\right)^p \ , \tag{108}$$

where the values N_{sat}, B, r, and p are calibrated with the output from the damage accumulation model described in Section 4.4 and ϕ is the irradiation dose in dpa. This empirical formula predicts exponential growth in the defect population at low doses, followed by a saturation of defect density at high doses, in agreement with SRSCD results. The use of additional fitting parameters beyond those proposed by Makin and Minter is not meant to indicate a change in physical behavior in the simulated defect accumulation experiment, and is simply adopted in order to provide a better fit to simulated data. All subsequent hardening simulations are carried out using defect densities N provided by equation (108) fit to SRSCD results. A good fit to simulation data shown in Figure 64a is found with $r = 1.0$, and only N_{sat}, B and p are fitted. The values of N_{sat}, B, and p for voids and dislocation loops are given in Table 18.

5.2.1.4 Implementation of crystal plasticity in a polycrystalline setting

Sandia National Laboratories' time-explicit parallelized Material Point Method (MPM) code [251, 20] is applied to model irradiation hardening in iron polycrystals. This MPM framework can be regarded as a spatial discretization method formulated in an arbitrary Lagrangian-Eulerian description of motion. It employs two discretizations to solve for the constitutive equations and equations of motion of solids. All state variables and constitutive equations are tracked at the set of material points while the equations of motion and interactions among the material points are formulated and solved by using a background computational grid. Further details on the formulation of the MPM framework are provided in the technical report by Bartel et al. [20].

5.2.2 Application: Irradiation hardening of Fe

In this section, the methodology outlined in the previous sections is applied to the problem of neutron irradiation and subsequent hardening in bulk iron. Results are compared both to experimental measures of defect content [67, 259] and hardening [38]. Simulation of radiation-induced hardening is first carried out using a reverse-engineering approach in Section 5.2.2.1, in which experimental results are used to fit the hardening parameters α_{V} and α_{L}. Then, in Section 5.2.2.2, the methodology is applied in a predictive fashion to describe the changes in hardening resulting from a change in dose rate of several orders of magnitude.

5.2.2.1 Fitting to experimental hardening

In order to apply the BKS model to defect accumulation data, values for the relative strengths of dislocation loops and voids (α_{L} and α_{V}, respectively) are needed. Therefore the contribution of each defect type to hardening of polycrystalline α-Fe is studied independently. In this way, the defect strength parameters are left as unknowns and later calibrated to fit with experimental results [38].

A mean-field Taylor model with mixed boundary conditions for approximating polycrystalline behavior is adopted to fit values of α_{L} and α_{V} to experimental data in a computationally efficient fashion. In this model, 250 randomly oriented single crystals, each with equal volume fraction, are used to represent a polycrystal subjected to uniaxial tension. The boundary conditions on each single crystal i are the following:

$$\epsilon^i_{xx} = \epsilon_{\mathrm{appl}} \ , \qquad \sigma^i_{yy} = \sigma^i_{zz} = \sigma^i_{xy} = \sigma^i_{yz} = \sigma^i_{xz} = 0 \ , \tag{109}$$

where ϵ_{appl} is the externally applied strain at each step. These boundary conditions correspond to the case of plane stress, with shear deformations allowed inside individual single crystals. Therefore each single crystal is subjected to the same uniaxial strain at each step, and the approximate polycrystalline stress σ_{xx} is found by invoking the macro-homogeneity condition, which gives the macroscopic stress as the average of the local stresses in the individual grains:

$$\sigma_{xx} = \frac{\sum_{i=1}^{N} \sigma^i_{xx}}{N} \ , \tag{110}$$

with $N = 250$ grains. This approximation allows fast computation of approximate polycrystalline stress-strain curves without explicitly representing the microstructure. As such, this method does not account for stress concentrations at grain boundaries and triple junctions or unequal distributions of strains throughout a polycrystalline aggregate. This process is repeated for five different sets of 250 randomly oriented single crystals.

Values for α_{V} and α_{L} are estimated by simulating polycrystalline stress-strain response using the mean-field Taylor model at doses ranging from 10^{-6} dpa to 1 dpa. Change in yield stress due to voids and loops, $\Delta\sigma_{\mathrm{Y,V}}$ and $\Delta\sigma_{\mathrm{Y,L}}$ respectively, is computed separately using the Taylor model and the expected combined hardening $\Delta\sigma_{\mathrm{Y}}$ is then computed using equation (107) with $n = 2.22$. The defect strength parameters α_{V} and α_{L} in equation (106) are adjusted using a least squares algorithm so that the expected combined hardening best fits the change in yield stress given in the work of Byun et al. [38]. Best-fit values for the defect strength parameters for voids and dislocation loops are found to be $\alpha_{\mathrm{V}} = 0.049$ and $\alpha_{\mathrm{L}} = 1.135$, respectively.

Using the fit values for α_{L} and α_{V}, hardening simulations using an explicit representation of the polycrystalline microstructure are performed in the MPM framework for a variety of radiation doses and compared to experimental values [38]. This representative microstructure, illustrated in Figure 66a, is obtained by means of a 3D Potts model of grain evolution [250]. The simulated grain evolution used to generate the representative microstructure employs a Monte Carlo Potts model using a non-physical kinetic Monte Carlo temperature with isotropic grain boundary energy and mobility. Dimensions of the RVE in physical space are 200 μm $\times$ 75 μm $\times$ 75 μm with approximately 100-120 grains in each polycrystal, resulting in a average grain size of 20 μm. The crystallographic orientations assigned to each grain of the representative microstructure are assigned randomly.

Five simulations corresponding to different polycrystalline microstructures are performed at each dose. The polycrystal stress-strain curves and change in yield stress $\Delta\sigma_{\mathrm{Y}}$ are shown as a function of radiation dose in Figure 65. The results from the MPM simulations show good agreement with both the fitted mean-field Taylor model described above and experimental data [38]. As the only sources of variation in MPM simulations of hardening are the polycrystalline microstructures used to represent the material, the standard deviation in the results shown in Figure 65b is several orders of magnitude lower than the change in yield strength $\Delta\sigma_{\mathrm{Y}}$, and as such error bars are not included in Figure 65b. By contrast, experimental studies experience variation in results caused by a number of factors, such as variations in measurement precision, radiation dose, inhomogeneous grain size, and other factors.

To demonstrate the non-uniformity generated in these polycrystalline simulations, Figure 66b shows the internal strain ϵ_{xx} throughout an un-irradiated polycrystal past the yield point and Figure 66c shows the distribution of internal stresses inside the polycrystal at three different average stresses for three different radiation doses. The radiation doses shown here are 10^{-6}, 10^{-3}, and 1 dpa, and the average stresses σ_{xx} shown are 60, 90, and 120 MPa. At 60 MPa, all three polycrystals remain in the elastic regime and the probability density functions for their stress distributions are identical. This results from the fact that the multiscale model used here does not explicitly compute the interaction stress between

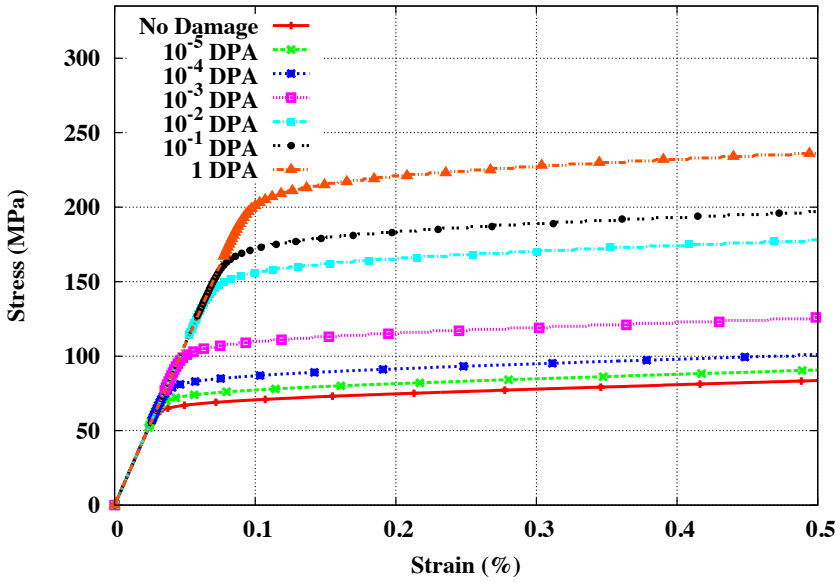

(a) Stress-strain curves

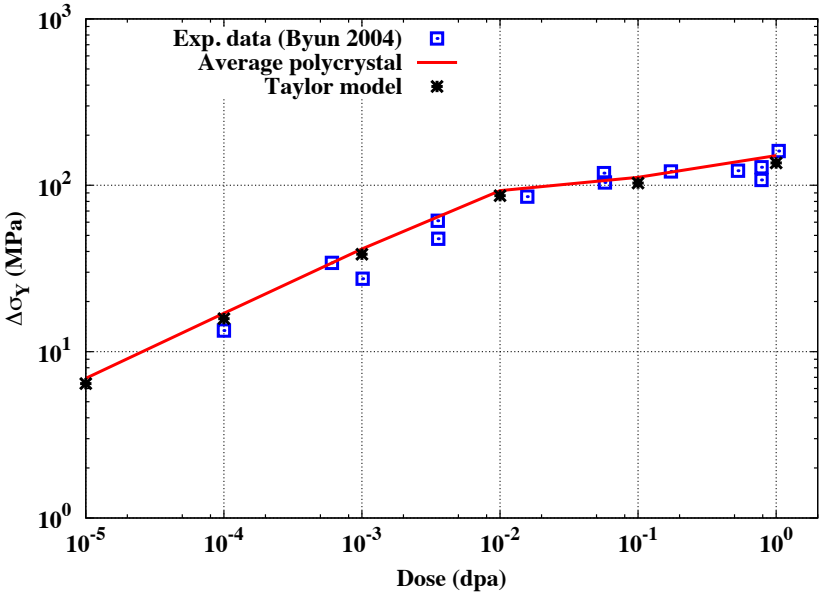

(b) Change in yield stress

Figure 65: Stress-strain curves (65a) and hardening (65b) in simulated neutron-irradiated polycrystalline α-Fe. Defect strength parameters in the BKS hardening model shown in equation (106) are given by $\alpha_{\mathrm{L}} = 1.135$ and $\alpha_{\mathrm{V}} = 0.049$ for dislocation loops and voids, respectively. Polycrystalline hardening results match both the mean-field Taylor model and experimental results.

individual defects. At 90 MPa, the 10^{-6} dpa specimen is in the plastic regime and its stress distribution is therefore both broader and more rounded than the two specimens still in the elastic regime. At 120 MPa, both the 10^{-6} and 10^{-3} dpa specimens have yielded while the 1 dpa specimen remains elastic, and the 10^{-6} dpa specimen shows greater broadening of its stress distribution due to larger plastic strain activity. It is noted here that the spread is significant such that overcoming of thermal activation barriers will necessarily occur at different rates in two materials subjected to the same macroscopic stress state but with different irradiation induced defect densities and distributions.

5.2.2.2 Dose rate dependence of radiation hardening

As previously noted in Section 1.1.2, radiation damage accumulation can occur at a variety of dose rates, ranging from 10^{-12} dpa·s^{-1} in thermal fission reactor pressure vessels [139] to 10^{-2} dpa·s^{-1} in ion beam-irradiated metals [4]. The dose rate used in Section 5.2.2.1, 7×10^{-7} dpa·s^{-1}, corresponds to the dose rate in the HFIR reactor, as reported by Eldrup et al. [67]. Dose rate has been shown to have a significant effect on damage accumulation in irradiated metals [59, 194]. The two-scale model presented here, with fitted defect strength parameters α_{V} and α_{L}, can be used in a predictive fashion to estimate how hardening is impacted by the different populations of defects created by different dose rates.

The impact of dose rate on radiation hardening is studied in this work by choosing two additional dose rates, 7×10^{-12} and 7×10^{-4} dpa·s^{-1}, corresponding to thermal fission and ion beam irradiation, respectively. SRSCD simulations of defect accumulation are then carried out at these additional dose rates, keeping all other parameters the same. As in Section 5.2.1.3, void and loop concentrations and average sizes are computed as a function of total dose using a fit provided by equation (108). The defect concentrations and average sizes computed by SRSCD are shown in Figure 67 and 68 for the two additional dose rates chosen in this study, along with the fitted functional forms for population evolution given by equation (108). Fitted parameters for the modified Makin and Minter formula are given in Table 19 for both dose rates. The main effect of decreasing dose rate is to decrease the population of dislocation loops and increase the population of voids at low doses. By

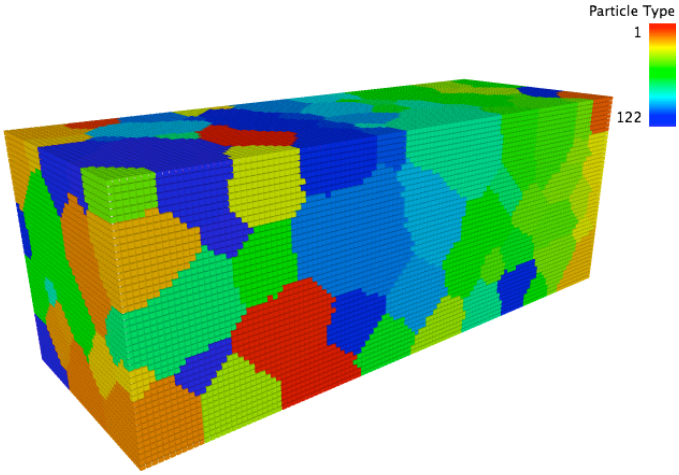

(a) Polycrystalline grain structure

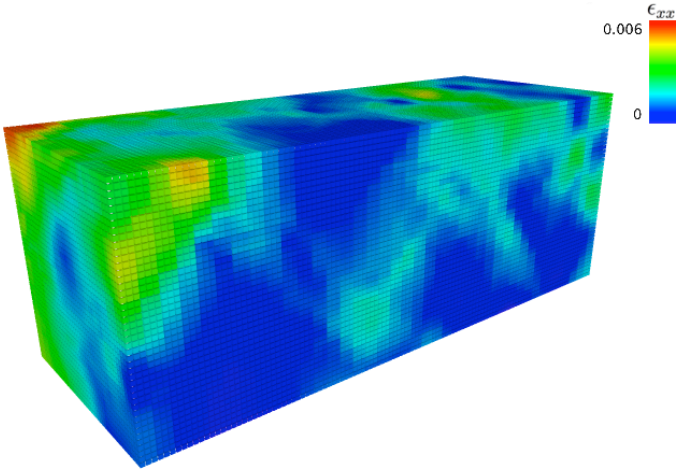

(b) Distribution of internal strains

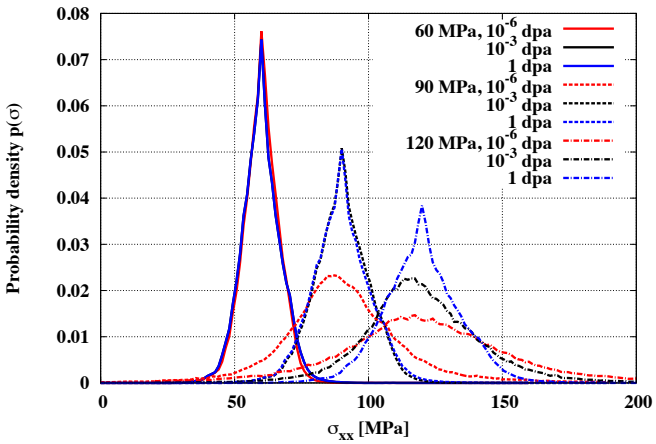

(c) Distribution of internal stresses

Figure 66: Example of explicit polycrystalline microstructure and results using the MPM method. (66a) Grain structure of polycrystal. (66b) ϵ_{xx} component of strain at $\sigma_{xx} = 75$ MPa for the case of no irradiation dose. (66c) Distribution of internal stresses at three different average stresses σ_{xx} for three different radiation doses.

Table 19: Rate-dependent parameters
(see equation (108))

7×10^{-12} dpa·s^{-1}	Voids	Loops
N_{sat}	2.46×10^{24}	3.06×10^{23}
B	62.63	61.46
p	1.32	0.81
r	1.0	1.0
7×10^{-4} dpa·s^{-1}	Voids	Loops
N_{sat}	3.10×10^{24}	2.08×10^{23}
B	14.95	9.18
p	7329.51	7.61
r	0.12	0.20

contrast, at the higher dose rate a larger population of loops and a smaller population of voids is present initially. The differences in defect populations at different dose rates are caused by differences in the ratio of defect diffusion rates to the cascade implantation rate. For example, at 7×10^{-4} dpa·s^{-1}, the diffusion to implantation ratio for single vacancies is 3.5×10^{3} nm^2·dpa^{-1}, while at 7×10^{-12} dpa·s^{-1} that ratio is 3.5×10^{11} nm^2·dpa^{-1}. Therefore, at low dose rates, vacancies have more time to diffuse and cluster or annihilate with SIAs, leading to more voids and fewer loops. By contrast, at high dose rates, vacancy diffusion is slow compared to the implantation rate and vacancies are relatively immobile as a result. Therefore, vacancies remain isolated, decreasing annihilation and allowing SIA loops to form. At higher doses, defect populations are large enough that cascade-defect interactions become significant, causing larger voids to form at all dose rates.

Using the defect accumulation statistics given by SRSCD, polycrystalline tensile tests are simulated using the MPM framework. In order to isolate the effect of dose rate on hardening, all other parameters are the same as in Section 4.4, including the five polycrystalline microstructures used for the hardening simulations and the values of α_{V} and α_{L}. The resulting hardening as a function of dose is shown for all three dose rates simulated in this work in Figure 69. At low doses, the overall effect of increasing dose rate is to increase hardening, while keeping the overall shape of the hardening curve the same. The greatest difference in hardening for dose rates simulated in this work is a factor of 2.5 at 10^{-4} dpa. Once the defect populations begin to saturate due to cascade-defect interactions (past 10^{-2}

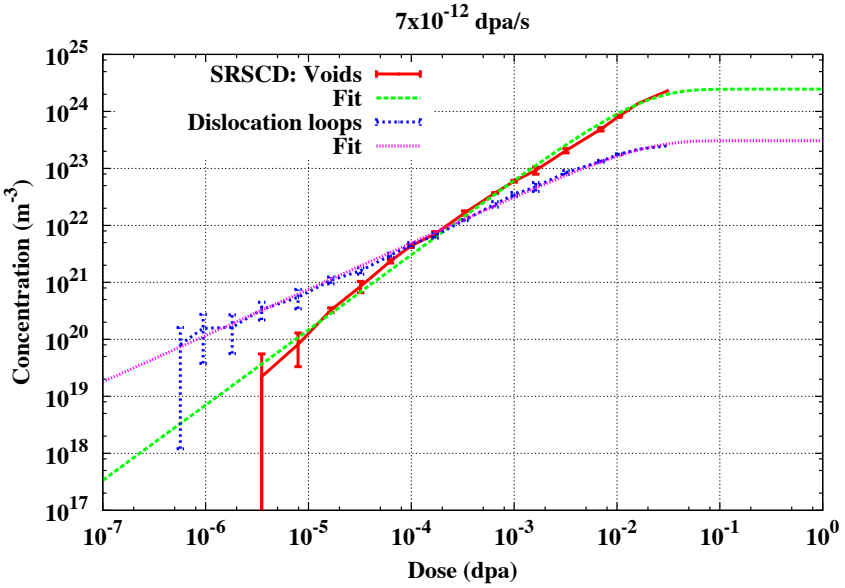

(a)

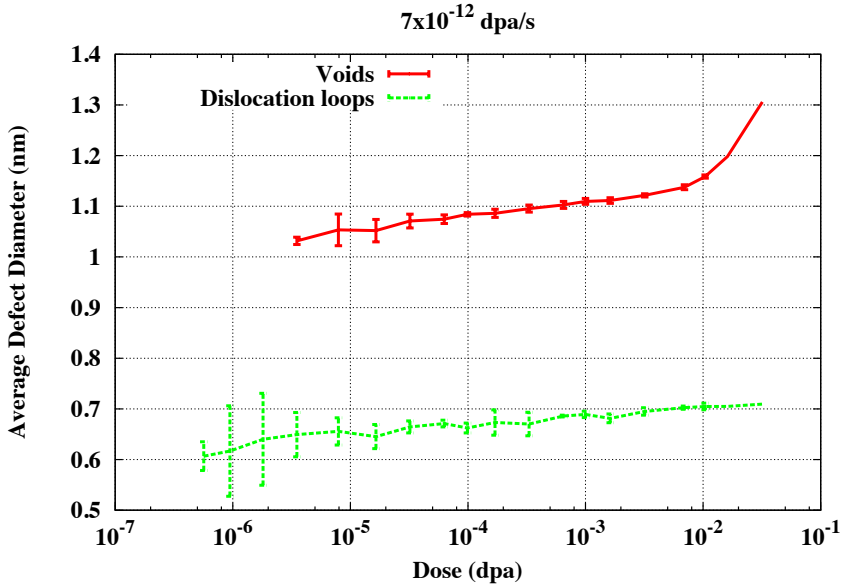

(b)

Figure 67: Dislocation loop and void concentrations and average sizes as a function of total dose at a dose rate of 7×10^{-12} dpa·s^{-1}, corresponding to thermal fission dose rates

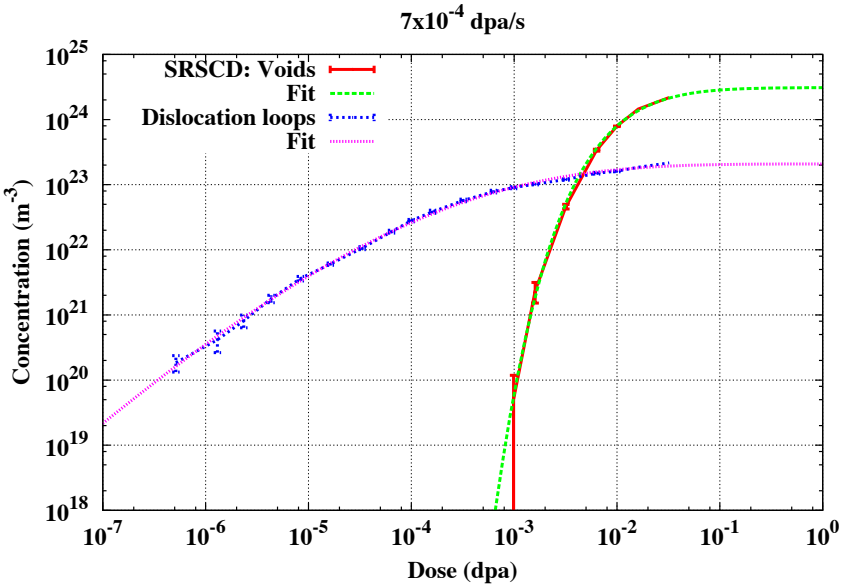

(a)

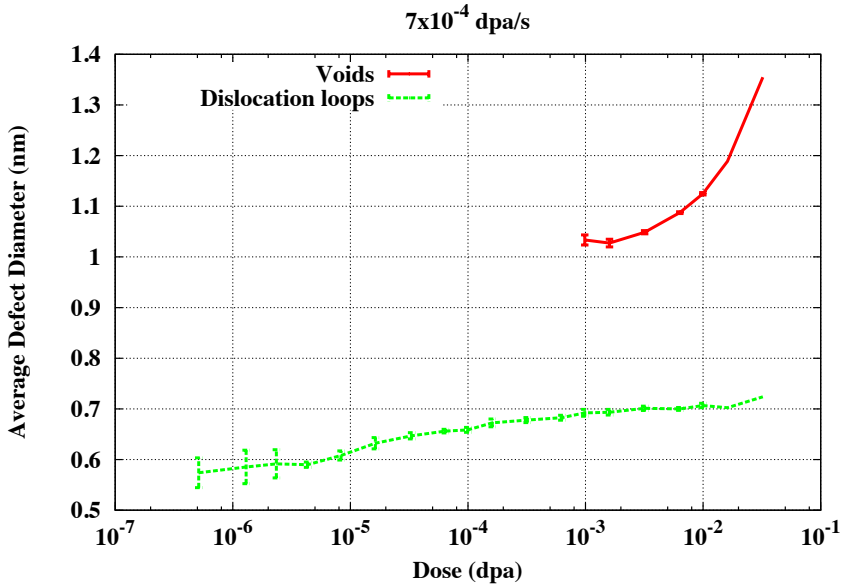

(b)

Figure 68: Dislocation loop and void concentrations and average sizes as a function of total dose at a dose rate of 7×10^{-4} dpa·s^{-1}, corresponding to ion beam irradiation dose rates

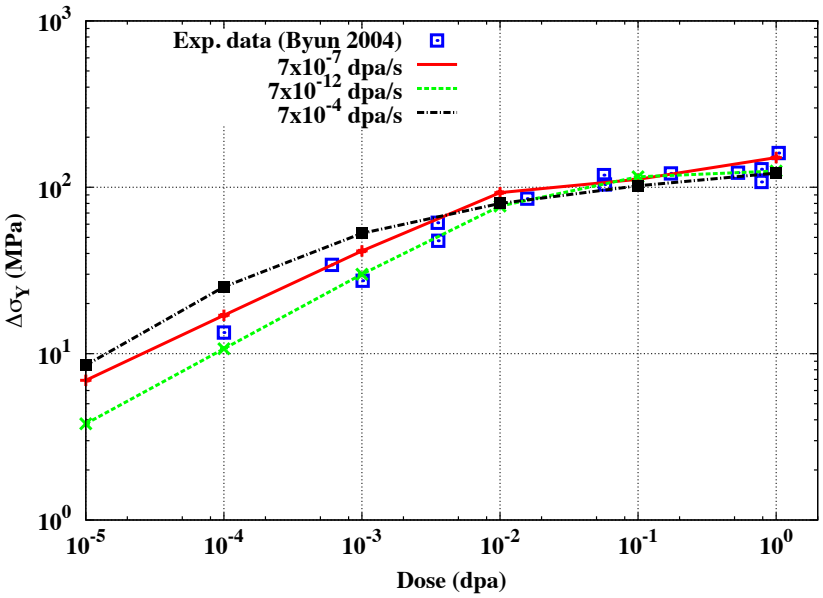

Figure 69: Radiation-induced change in yield strength $\Delta\sigma_{\mathrm{Y}}$ predicted by polycrystalline tensile testing simulations at dose rates corresponding to thermal fission (7×10^{-12} dpa·s^{-1}), fast fission (7×10^{-7} dpa·s^{-1}), and ion beam irradiation (7×10^{-4} dpa·s^{-1}).

dpa), the defect populations populations and resulting hardening become similar between the different dose rates studied.

5.2.3 Choice of hardening model

As previously mentioned in Section 5.1, several theoretical models for radiation-induced hardening exist in addition to the BKS model used in this work. Two of the most common hardening models include the dispersed barrier (DB) model [185, 153, 125] and the Friedel-Kroupa-Hersch (FKH) model [72, 115], which have radiation hardening given by:

$$\begin{aligned}\Delta\tau_{\mathrm{irr}} &= \alpha_{\mathrm{DB}} MGb\sqrt{Nd} \quad \text{(DB)}\ ,\\ \Delta\tau_{\mathrm{irr}} &= \frac{1}{8} MGbN^{\frac{2}{3}}d \quad \text{(FKH)}\ ,\end{aligned} \tag{111}$$

where the constants are the same as in the BKS model given in equation (106). Dislocation dynamics studies [196] have shown that the DB model cannot reproduce hardening due to either voids or SIA loops without using a defect strength parameter α_{DB} that varies wtih the size of the defects d. Because average defect sizes evolve during irradiation, using such a model necessitates the creation of a functional form for α_{DB}. The FKH model, which

was originally formulated for SIA loop hardening in fcc metals, was shown by dislocation dynamics to provide a good fit to bcc SIA loop hardening data when multiplied by a single defect strength parameter α_{FKH} for a range of SIA loop sizes [196]. In the dislocation dynamics study, the quality of the fits of the FKH and BKS models to simulated hardening results are similar. The BKS model is chosen in this work in order to use the same hardening model for both voids and SIA loops. Replacing the BKS model with a FKH-like model for SIA loops would not significantly change the results.

The defect strength parameter α_{L} obtained by fitting hardening results to experimental data, $\alpha_{\mathrm{L}} = 1.135$, is similar to the value estimated by Sobie et al. [196] using discrete dislocation dynamics of $\alpha_{\mathrm{L}} = 1.209$. However, the value of α_{V} estimated using the mean-field Taylor model, $\alpha_{\mathrm{V}} = 0.049$, is much lower than the value of $\alpha_{\mathrm{V}} = 1.003$ reported from discrete dislocation dynamics. This discrepancy may be caused by thermal effects such as depinning and dislocation climb which are not captured in discrete dislocation dynamics, as suggested by others [65, 164]. Due to the low value of α_{V} found using the mean-field Taylor model, dislocation loops are the dominant contributor to radiation hardening in this study. Previous study of dislocation loop accumulation has indicated that the concentration of such loops is strongly dependent on the local concentration of traps for dislocation loops [60]. Such traps have been hypothesized to be caused by the presence of carbon impurities [215, 101]. Therefore, materials with different impurity contents could experience significantly different hardening under the same radiation damage conditions. Such a mechanism is not considered in the present study.

As discussed in Section 5.2.1.2, vacancy clusters with diameter less than 1 nm are not considered voids in this work. Smaller vacancy clusters are not included in the irradiation hardening model presented here. In order to understand the effect of the threshold void size chosen in this study, the analysis carried out in Section 5.2.2 is repeated including all vacancy cluster sizes greater than 5 vacancies (the smallest immobile vacancy cluster simulated in this work). Using the mean-field Taylor model to estimate hardening due to this modified void population, defect strength values of $\alpha_{\mathrm{V}} = 0.103$ and $\alpha_{\mathrm{L}} = 0.914$ are obtained. This does not represent a qualitative change from the defect strength parameters

obtained in Section 5.2.2. More detailed study of the effect of vacancy cluster size on preventing dislocation motion is needed for future iterations of this model to accurately predict hardening in irradiation conditions for which experimental data does not exist.

The use of a single average defect size and concentration for voids and SIA loops instead of a full distribution of defect sizes allows application of the BKS model with only two unknown strength parameters α. Dislocation dynamics studies indicate that the difference in hardening caused by replacing a Gaussian distribution of defect sizes with a single average defect size ranging from $0.3 - 1.5$ nm for voids and $0.5 - 2.5$ nm for SIA loops is not statistically significant, indicating that the effect of this choice is likely to be small [196]. Future treatments of this model could include several bins of void and SIA loop sizes in order to capture the effect of defect size distributions on hardening.

Several approximations are applied in carrying out this two-scale methodology for irradiation hardening. In the SRSCD model, defect segregation at grain boundaries is not accounted for and the effect of cascade-defect interactions at high doses is only accounted for using a preliminary model. In addition, the crystal plasticity model employed does not account for mechanical effects such as dislocation channeling, localization effects, grain boundary effects, or twinning. The advantage of this methodology lies in the fact that all of the irradiation-induced defect statistics come from the defect accumulation simulations, and no fitting of the defect content is necessary. Once values of α_{V} and α_{L} have been found by fitting to experimental results here, these values should be applicable to future simulations in which experimental hardening results do not exist. Therefore, this work allows predictive simulations of irradiation hardening in regimes that are difficult to probe experimentally.

5.2.4 Summary

In this section, a novel computational model is introduced to predict both microstructure evolution during irradiation in polycrystals and the resulting effect on strength. From a general standpoint, the methodology presented in this work enables prediction of irradiation hardening under a wide range of irradiation conditions such as total dose, dose rate, and temperature, as well as for various microstructures such as nano-grained iron without relying

on experimentally measured defect populations or hardening results to calibrate the model.

The strategy delineated is to first simulate defect populations using SRSCD and use these as inputs of a polycrystalline crystal plasticity model in which the single crystal constitutive response explicitly accounts for the effect of radiation-induced hardening. In the specific case treated here, the Bacon, Kocks, and Scattergood (BKS) model [13] is chosen to model the increase in yield strength of an irradiated metal. This choice is informed by recent work based on discrete dislocation dynamics [196] which clearly demonstrates the reliability of the BKS model.

Demonstration of the gain resulting from the level of integration of the damage accumulation and plasticity models is made by considering two problems. First, it is shown that, due to the relative numerical efficiency of the approach, one can quantify the effective contributions of voids and SIA loops on the strength of slip systems. Using a reverse engineering approach, these effects, formally quantified wtih parameters α_{V} and α_{L}, are revealed. It is shown that α_{V} is much smaller than α_{L}. Interestingly we also note that α_{V} is also smaller than reported in [196], thereby suggesting that the effect of very small vacancy clusters on the Orowan bowing process is minimal.

Finally, using the defect strength parameters α_{V} and α_{L} obtained by this approach, we are able to predict hardening in α-Fe under irradiation conditions not tested in experiments. It is found that dose rate does not have a strong effect on radiation-induced hardening of neutron-irradiated bulk iron at room temperature, especially at doses above 10^{-2} dpa.

5.3 Using ions to reproduce neutron damage: investigating the equivalence between dose rate and temperature

The previous section demonstrated the use of SRSCD in a multiscale computational framework to link predictive simulations of damage accumulation to macroscopic radiation hardening. This methodology can also be used as a tool for guiding experimental design, as demonstrated in this section for the case of determining the temperature shift necessary to use ion irradiation as a laboratory approximation for neutron damage. Ion irradiation has long been used as a method for experimentally simulating damage in metals expected from neutron irradiation in reactor environments, due to the lower costs, increased safety, and

faster completion of such experiments [239, 170, 2, 147, 148]. However, the displacement rates in typical ion irradiation experiments range from $10^{-2} - 10^{-5}$ dpa·s^{-1}, while neutron irradiation displacement rates range from $10^{-7} - 10^{-12}$ dpa·s^{-1} [147, 239, 139, 234, 2, 170]. Therefore, in order to produce similar defect concentrations and size distributions, ion irradiation experiments must be performed at higher temperatures than the neutron irradiation conditions they are simulating.

Several experimental and theoretical studies have investigated the temperature shift required to achieve similar results at different displacement rates, using metrics such as swelling and segregation in alloys as metrics for equivalence [239, 170, 129, 2]. In the work of Was [239], a preliminary model is presented that includes only single vacancies and single interstitials. This scheme does not account for effects such as defect clustering, displacement cascades, or spatially resolved microstructures. Abromeit [2] addresses some of these limitations by creating a rate theory model that includes defect cluster populations, but the problem is not applied to a specific material and trends related to mechanisms for defect accumulation as a function of displacement rate are discussed instead.

In this study, the multi-scale damage accumulation tool SRSCD [63] is used to investigate the relationship between dose rate and temperature for a wide range of irradiation conditions. This work improves on previous studies by including a more detailed damage accumulation model, including defect clusters of arbitrary size and the introduction of cascade damage, and investigating a much larger range of displacement rates than previous studies. The methodology described here represents a preliminary step that can be used during experimental design in order to best reproduce radiation damage for irradiation conditions that are difficult to achieve in the laboratory, such as low displacement rate irradiation with neutrons.

Damage accumulation is simulated in this study using both Frenkel pairs (caused by electrons and light ions) and displacement cascade damage (caused by heavy ions and neutrons) as damage sources over a wide range of displacement rates and temperatures. This data is then used to estimate the equivalent temperature required under simulated 'proxy' conditions (for example, using ion irradiation) to reproduce the same damage produced

by simulated 'target' conditions (for example, neutron irradiation) at room temperature. Therefore, damage production is measured during irradiation for two cases:

1. **Target conditions:** room temperature irradiation at $T_T = 20°\text{C}$ or $T_T = 200°\text{C}$ at the 'target' displacement rate ϕ_T

2. **Proxy conditions:** irradiation at the 'proxy' displacement rate ϕ_P and temperature T_P required to produce similar radiation damage accumulation to the 'target' conditions

The temperature shift $\Delta T_P = T_P - T_T$ required when changing from displacement rate ϕ_T to ϕ_P is presented for displacement rates ϕ_T and ϕ_P ranging from $10^{-2} - 10^{-8}$ dpa·s^{-1} for both types of irradiation. Profiles of vacancy cluster sizes at various equivalent displacement rate/temperature pairs $[T, \phi]$ show good agreement for both Frenkel pair and cascade damage.

5.3.1 Methodology

Irradiation of α-Fe is simulated using SRSCD for two types of damage: (1) Frenkel pair irradiation to 10^{-2} dpa inside 100 nm thin films using a $100 \times 50 \times 50$ nm domain with perfect sinks in the x-direction and periodic boundary conditions in the y- and z-directions, as a first order approximation of defect accumulation in a nanocrystalline material with grain boundaries that act as sinks; and (2) cascade damage created by 20 keV primary knock-on atoms (PKAs) to 10^{-2} dpa inside bulk α-Fe using a $100 \times 100 \times 100$ nm domain. Case (1) corresponds to damage conditions in electron and light ion irradiation experiments, while case (2) corresponds to neutron and heavy ion irradiation conditions. All allowed defects and reaction rates are the same as in previous SRSCD simulations of damage accumulation in α-Fe [60]. For case (1), displacement damage (in dpa) is calculated by dividing the number of implanted Frenkel pairs by the number of atoms in the simulated volume. For case (2), displacement cascades created by 20 keV PKAs are taken from atomistic simulations performed by Stoller et al. [204, 203]. The cascades are first annealed for 10 ps in the OKMC code MMonCa [135] in order to allow only reactions triggered automatically by proximity

to occur. By doing so, the defects input into SRSCD include all clusters formed during the cascade itself. Displacement damage (in dpa) is calculated by dividing the number of surviving displaced atoms in the cascade after the thermal spike phase by the number of atoms in the simulated volume. The above simulations are repeated at displacement rates ranging from $10^{-8} - 10^{-2}$ dpa·s^{-1}. The average concentration of vacancies and vacancy clusters over ten simulations for Frenkel pair damage and five simulations for cascade damage at each displacement rate and temperature combination is used as a metric to compare results between different irradiation conditions.

Figure 70 demonstrates the methodology used in this study to compute the 'proxy' temperature T_P at displacement rate ϕ_P required to produce equivalent damage to room temperature irradiation $T_T = 20°\text{C}$ at the 'target' displacement rate ϕ_T. The concentration of vacancies and vacancy clusters at $[T_T, \phi_T]$ is first computed (red arrow), and this result is compared to the concentrations found at other displacement rates ϕ_P as a function of temperature T_P. By taking a linear interpolation of the linear-logarithmic plot of concentrations as a function of temperature, an estimate is made of the temperature T_P at which the displacement rate/temperature pairs $[T_T, \phi_T]$ and $[T_P, \phi_P]$ produce the same concentration of vacancies. This process is repeated using displacement rates $\phi_T, \phi_P \in [10^{-8}, 10^{-2}]$ dpa·s^{-1}. Therefore, the increase or decrease in temperature required to produce equivalent radiation damage to room-temperature irradiation at a different displacement rate is found for a two-dimensional input space of displacement rates ϕ_T and ϕ_P, using vacancy concentration as a metric for equivalent damage.

5.3.2 Results: Temperature Shift ΔT_P

Figure 71 shows maps of the temperature shift ΔT_P found using the above methodology for the cases of Frenkel pair irradiation of nanocrystalline α-Fe (71a) and cascade irradiaiton of bulk α-Fe (71b). Frenkel pair irradiation in bulk α-Fe was also tested, but results are very similar to results for nanocrystalline iron and are not included here. In both cases, increasing the proxy displacement rate ϕ_P requires an increase in proxy irradiation temperature T_P to achieve equivalent radiation damage. Several differences can be seen between the cases

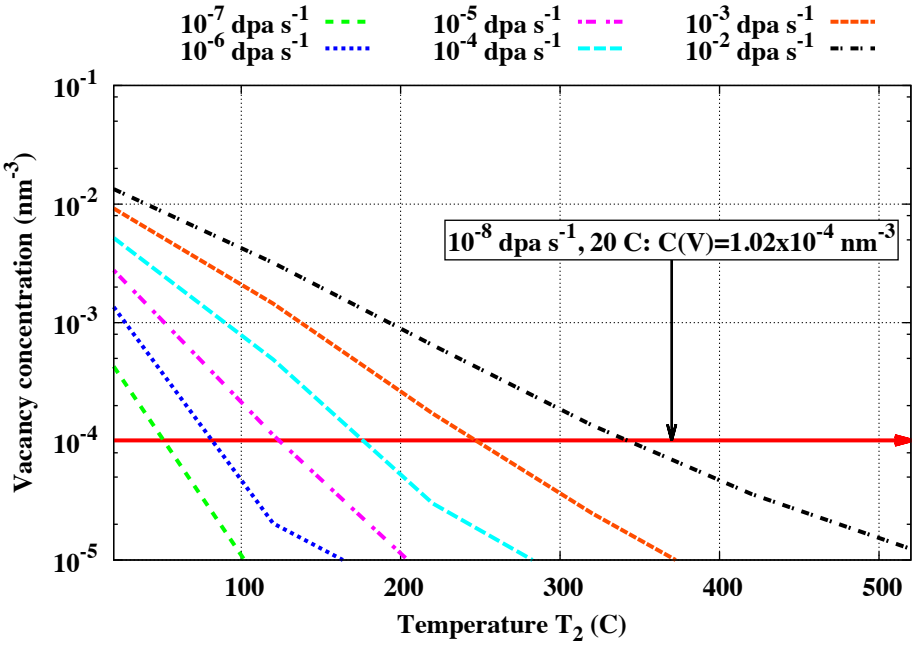

Figure 70: Method used to identify equivalent temperatures for irradiation at various displacement rates in order to simulate room temperature Frenkel pair implantation in 100 nm α-Fe thin films at 10^{-8} dpa·s^{-1}. The intersection of each curve with the red arrow indicates the displacement rate equivalent temperature.

of Frenkel pair and cascade damage in Figures 71a and 71b. A greater temperature shift ΔT_P is required to reproduce radiation damage accumulation at $\phi_T = 10^{-8}$ dpa·s^{-1} when $\phi_P = 10^{-2}$ dpa·s^{-1} for Frenkel pair damage than cascade damage. However, during cascade damage the dependence of temperature T_P on ϕ_T and ϕ_P is much more irregular than for the case of Frenkel pair damage. For example, a temperature shift ΔT_P of approximately 100°C is necessary when $\phi_T = 10^{-6}$ dpa·s^{-1} and $\phi_P = 10^{-5}$ dpa·s^{-1}, whereas for the case of Frenkel pair irradiation the value of ΔT_P is below 50°C for the same values of ϕ_T and ϕ_P. In addition, for the case of cascade implantation, little difference is seen between $\phi_T = 10^{-8}$ and $\phi_T = 10^{-7}$ dpa·s^{-1}, implying that no additional defect mobility is achieved by slowing down the displacement rate below 10^{-7} dpa·s^{-1} at room temperature. The irregularity in the contour line representing $\Delta T_P = 100$°C in Figure 71b is due to statistical fluctuations in the SRSCD output as well as the fact that the region where $\Delta T_P \approx 100$°C is quite broad for the case of cascade damage.

The region of interest corresponding to the use of ion irradiation to reproduce damage

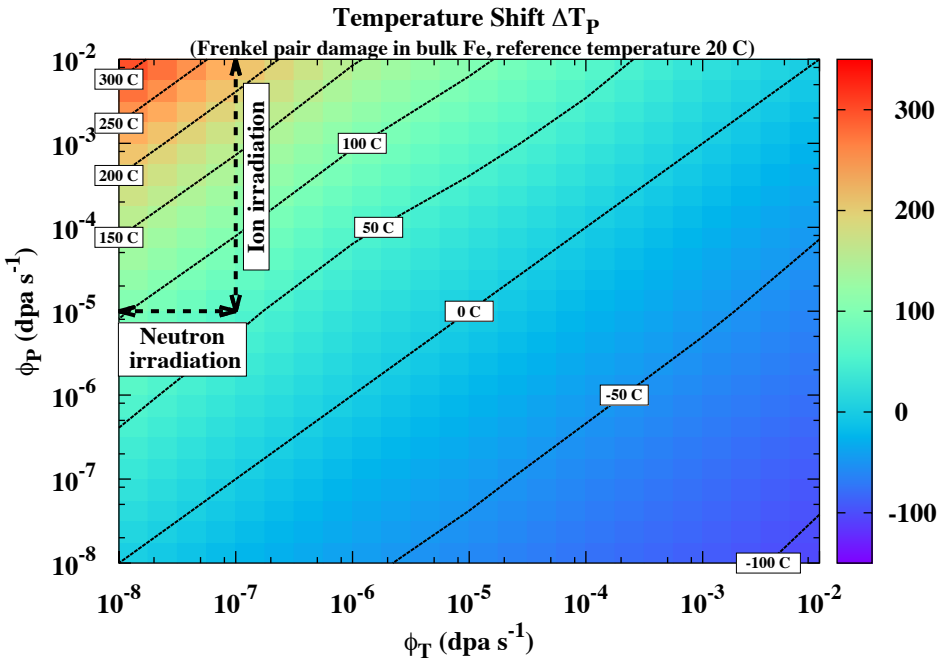

(a) Frenkel pair damage

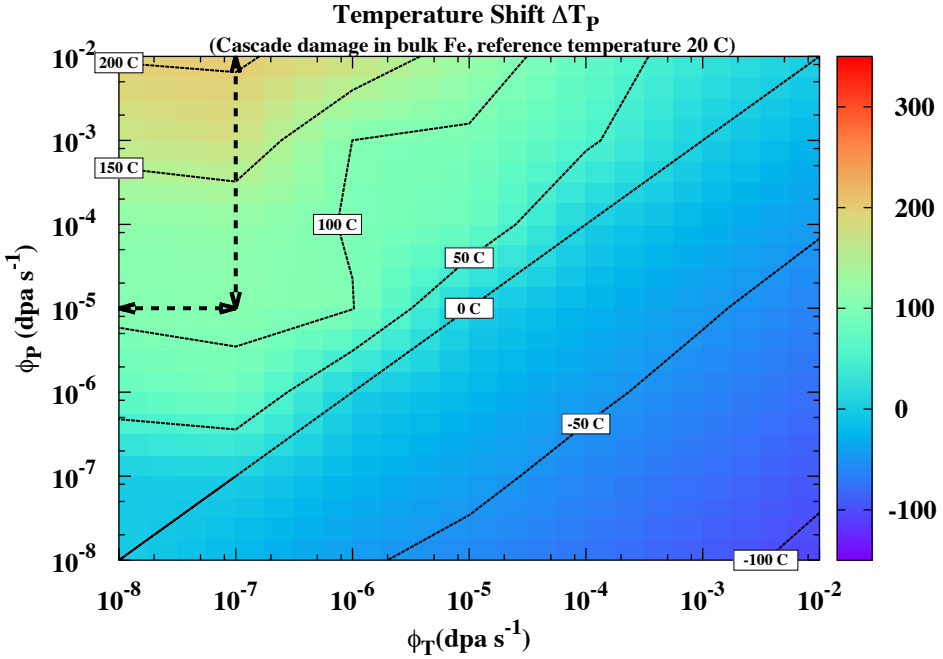

(b) Cascade damage

Figure 71: Temperature shift ΔT_P from room temperature (20°C) required when changing from displacement rate ϕ_T to ϕ_P to produce equivalent vacancy content. Arrows indicate displacement rates that correspond to the use of ion irradiation to reproduce damage caused by neutron irradiation. Results are shown for Frenkel pair implantation in 100 nm thin films (71a) and cascade implantation in bulk α-Fe (71b).

caused by neutron irradiation at room temperature is shown by arrows in Figures 71a and 71b. Although these regions represent a small subset of the entire range of displacement rates ϕ_T and ϕ_P simulated in this study, the temperature required to reproduce damage at displacement rates associated with neutrons using ion irradiation varies by 100-200°C within this region for cascade and Frenkel pair damage, respectively. This result emphasizes the necessity of correctly choosing irradiation temperature based on the proxy and target irradiation conditions.

To test the effect of the density of planar sinks such as grain boundaries and free surfaces on the temperature shift ΔT_P, Figure 72 shows temperature shifts using cascade damage and the same irradiation conditions as presented above for thin films with thickness 50nm and 200 nm. The free surfaces of the thin films are treated as perfect sinks, and therefore these simulations can be seen as a first approximation of the effect of grain size in nanocrystalline materials in which grain boundaries act as perfect sinks. Although some differences in ΔT_P can be seen when film thickness changes from 50 nm to 200 nm in Figures 72a and 72b, the region of interest for using ion irradiation to reproduce damage expected from neutron irradiation (indicated by arrows) is very similar for both thicknesses. This region is also similar to the case of cascade damage in bulk α-Fe shown in Figure 71b. Therefore, grain size is not considered a primary variable when determining temperature shifts ΔT_P required when changing displacement rates.

So far, all results presented in this study assume that the 'target' irradiation conditions are at room temperature. Although some experimental neutron irradiation is carried out at room temperatures [67], it is important to understand how the temperature shifts calculated in this model change when the reference temperature for irradiation T_T is elevated above room temperature. This case is shown in Figure 73 for cascade damage in bulk α-Fe with reference temperature $T_T = 200$°C. Several differences are seen between these results and the case of $T_T = 20$°C in Figure 71b; most notably, the temperature shift required when $\phi_P > \phi_T$ is much more regular due to the increased mobility of defects in this case. Overall, 'target' irradiation temperature T_T is an important parameter in determining the temperature shift required in the proxy environment ΔT_P to reproduce damage when displacement

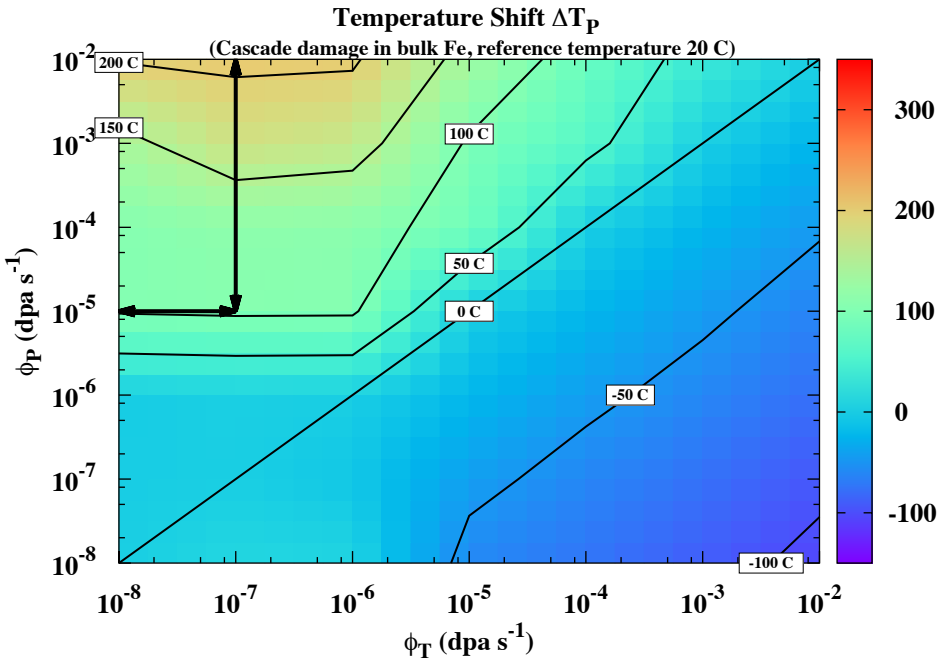

(a) 50 nm thin film

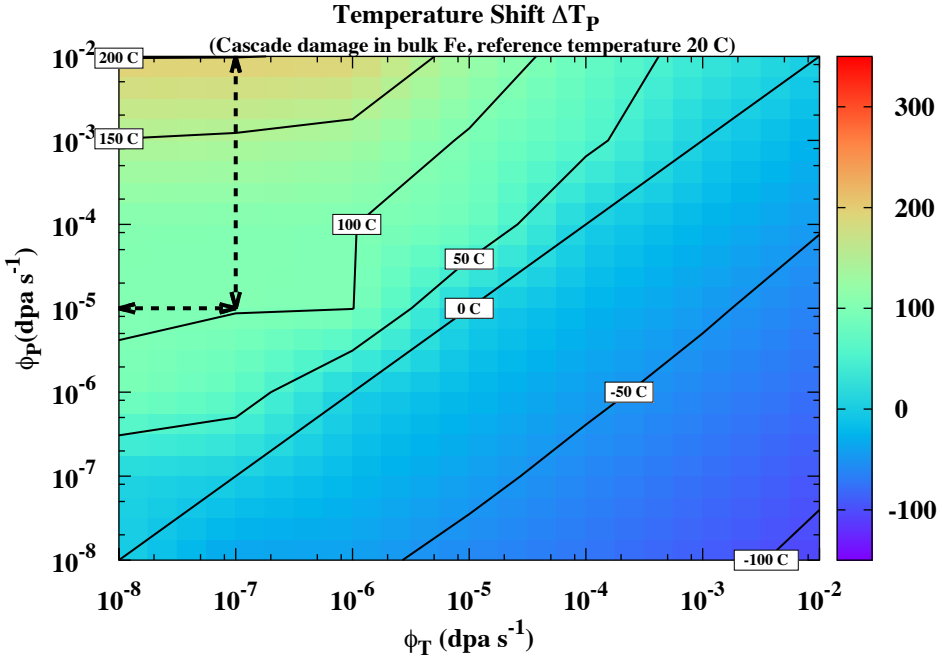

(b) 200 nm thin film

Figure 72: Temperature shift ΔT_P at displacement rates ϕ_P required to reproduce room-temperature irradiation results at target displacement rates ϕ_T for cascade damage in films with thickness ranging from 50-200 nm.

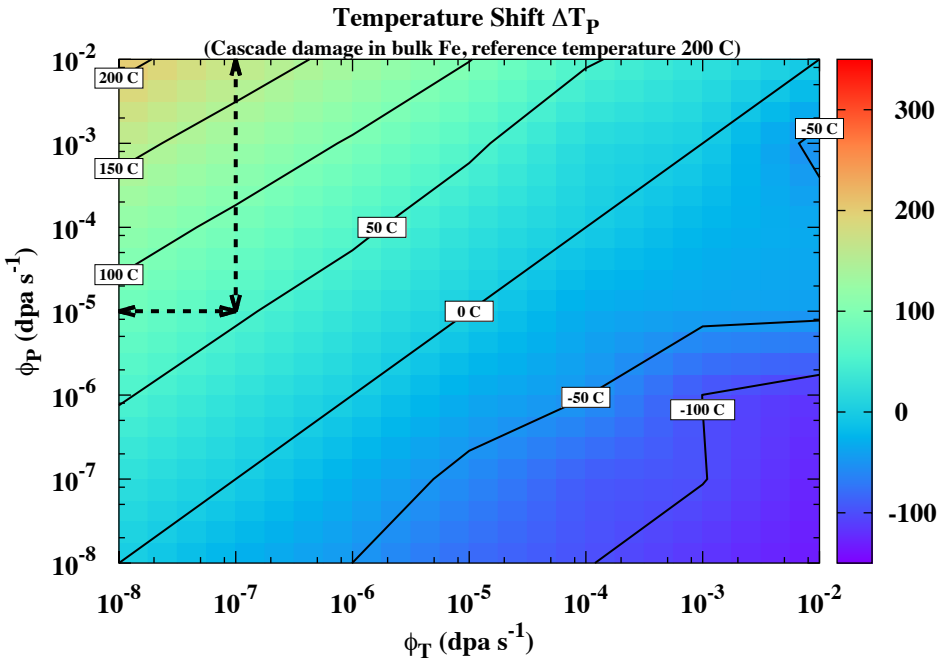

Figure 73: Temperature shift ΔT_P at displacement rates ϕ_P required to reproduce irradiation results at target temperature $T_T = 200°\text{C}$ and target displacement rates ϕ_T for cascade damage in bulk Fe.

rates are varied. Note that a higher value of T_T corresponding to reactor temperatures (approximately 400°C) was not used in this study due to complete annealing of the simulated material at very high temperatures. To capture damage accumulation at these higher temperatures, a more advanced model is needed that can capture effects such as void diffusion and coalescence and the impact of alloying elements and transmutation products such as helium.

5.3.3 Using vacancy concentration as a metric for equivalent damage

The use of the concentration of vacancies and vacancy clusters as a metric for comparing irradiation at different displacement rates and temperatures assumes that other measurable quantities such as the average size of defects will scale with that metric, such that the overall defect state in materials irradiated at different displacement rates but appropriately chosen equivalent temperatures will remain the same. However, reaction rates for defect behaviors such as diffusion and binding are governed by Arrhenius laws in irradiated metals [197], implying that temperature changes do not lead to uniform changes in defect behaviors

as the activation energies for various reactions are not uniform. Therefore, irradiation at different displacement rates using the displacement rate equivalent temperatures shown in Figure 71 may result in differences in damage evolution not measured by the vacancy concentration metric used in this work.

In order to test the quality of vacancy concentration as a metric for displacement rate equivalent temperature, profiles of vacancy cluster concentrations as a function of cluster size are shown in Figure 74 for irradiation temperatures T_T and T_P when the proxy and target displacement rates ϕ_T and ϕ_P are different by several orders of magnitude. Profiles are also shown using high displacement rates ϕ_P while leaving temperature $T_P = 20°\text{C}$ as a reference. Figure 74a shows a comparison between 10^{-6} dpa·s^{-1} and 10^{-2} dpa·s^{-1} irradiation with Frenkel pairs, and Figure 74b shows a comparison between 10^{-8} dpa·s^{-1} and 10^{-2} dpa·s^{-1} irradiation with displacement cascades. In both cases, when using the value of T_P calculated in Figure 71, cluster profiles are very similar for irradiation at displacement rate/temperature pairs $[T_T, \phi_T]$ and $[T_P, \phi_P]$. By contrast, simply irradiating at the higher displacement rate ϕ_P while leaving temperature $T_P = 20°\text{C}$ leads to a significant underestimate of the average cluster size in the simulations. This indicates that vacancy and vacancy cluster concentrations are a good metric for comparing defect accumulation at different displacement rates and temperatures.

5.3.4 Discussion and conclusions

Although this study addresses the effect of compensating for changes in displacement rate by changing temperature in irradiated α-Fe, there are several other differences between ion and neutron irradiation that could have an impact on damage accumulation that are not treated here. In this study, all displacement cascades are created by 20 keV PKAs, while in ion and neutron irradiation conditions displacement cascades have different ranges of PKA energies [138, 234]. Some studies have suggested that when controlling for dpa rate, damage accumulation due to different cascade energies is similar [22, 202, 60], but nonetheless differences between ion and neutron damage could occur due to the different cascade energy spectra in the two types of damage. Also, neutron irradiation of metals

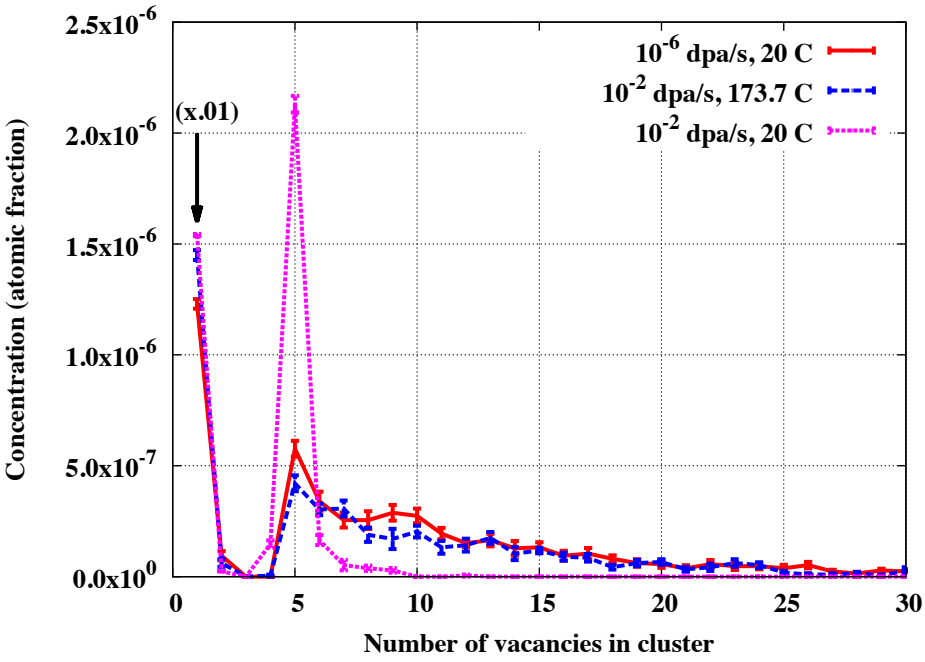

(a) Frenkel pair damage

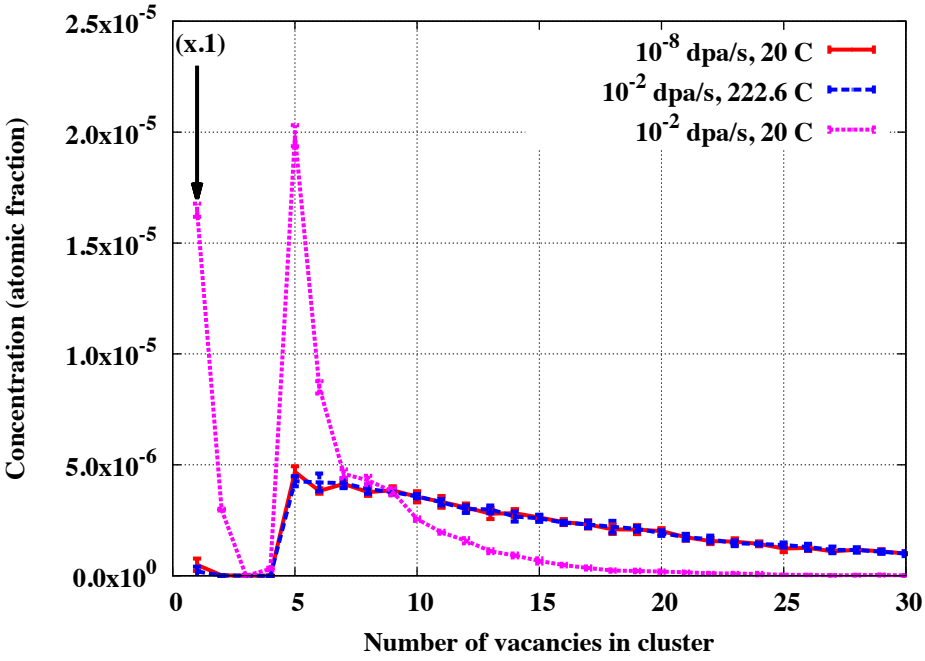

(b) Cascade damage

Figure 74: Comparison of profiles of vacancy cluster size for simulations at equivalent temperatures: (74a) Frenkel pair damage comparing displacement rates of 10^{-2} and 10^{-6} dpa·s^{-1}, and (74b) cascade damage comparing displacement rates of 10^{-2} and 10^{-8} dpa·s^{-1}. The first two values of the results at room temperature and 10^{-2} dpa·s^{-1} are multiplied by 0.01 and 0.1 in 74a and 74b, respectively, for better visualization (indicated by arrows).

creates transmutation products such as hydrogen and helium [234], which can significantly influence damage accumulation by acting as traps for dislocation loops and nucleation sites for bubbles [232, 4, 145, 19]. Although ion irradiation with both self-ions (causing cascade damage) and transmutation products such as hydrogen and helium has been carried out experimentally [212], developing truly equivalent conditions to neutron damage in this case is a very challenging problem. Despite these differences, the results of this study show that the relationship between displacement rate and temperature alone is a primary variable for consideration when designing experiments using ion irradiation to simulate neutron damage.

The methodology proposed here is most appropriate when designing experiments in which the majority of damage accumulation occurs in the grain interior. For irradiation at high temperatures and/or low displacement rates, significant damage accumulation can occur at grain boundaries and triple junctions [90, 191, 256], which are not included in this model. Therefore, in order to extend this method to such cases, greater understanding of damage accumulation on grain boundaries is needed. In addition, neutron irradiation generates gases such as helium through transmutation which can influence damage accumulation [170, 205, 230]. Some experimental techniques include both heavy ion irradiation and light ion implantation [114, 186, 92], making experimental investigation of these phenomena possible. Equivalence between these more complicated scenarios could be investigated by expanding this methodology to include helium generation and implantation in the SRSCD simulations. Finally, the results shown in Figure 71 for Frenkel pairs and cascades at 10^{-2} dpa may change as the total radiation dose increases. Previous studies of the effect of displacement rate on damage accumulation during cascade implantation have shown that damage accumulation at varying displacement rates is similar above 10^{-2} dpa due to the ballistic interactions between damage already present in the material and additional displacement cascades [61], indicating that the temperature shift ΔT_P required at higher doses may decrease.

The results of this analysis show that, for irradiation of iron at 20°C and 200°C over a wide range of displacement rates and damage conditions such as damage type and material microstructure, an equivalent displacement rate and temperature pair can be found which

provides similar defect accumulation results. The temperature shift ΔT_P in a simulated 'proxy' environment with displacement rate ϕ_P required to produce the same radiation damage accumulation results as irradiation at a 'target' displacement rate ϕ_T is shown in this work to depend on both ϕ_T and ϕ_P as well as the radiation damage type (Frenkel pair or cascade damage) and reference temperature T_T. Grain size is not shown to strongly influence ΔT_P in nanocrystalline α-Fe for the irradiation conditions studied.

5.4 Summary and conclusions

SRSCD's computational efficiency and ability to incorporate complex defects and reactions positions it uniquely as an intermediate-scale tool that is capable of linking the results of fundamental studies at the atomic scale such as defect migration and binding energies to experimental design and macroscopic phenomena such as irradiation hardening. In Section 5.2, this capability is demonstrated by constructing a multi-scale computational framework for simulating damage accumulation and subsequent hardening in irradiated α-Fe. Defect populations are first simulated in neutron-irradiated room-temperature iron, and these results are then used as inputs into polycrystalline plasticity simulations including radiation hardening using the BKS hardening model [13]. In Section 5.3, the equivalence between dose rate and temperature is investigated in order to inform experimental studies using ion irradiation at high dose rates that want to reproduce damage content expected in neutron irradiation studies at lower dose rates. The temperature at which irradiation should be carried out in order to reproduce room temperature irradiation results is found for a wide range of dose rates both in thin films irradiated with Frenkel pairs and for cascade damage in coarse-grained iron. The two applications presented in this chapter represent a small subset of the possible uses of SRSCD as a tool for linking multi-scale simulation frameworks and as a companion for experimental design.

CHAPTER VI

CONCLUSIONS

The purpose of this dissertation is two-fold: to link individual defect-level phenomena in irradiated metals to long-term radiation defect evolution, and to link damage content to macroscopic and experimentally verifiable quantities such changes in yield strength. This multi-scale problem is very complex, due to the number of defect types present in irradiated materials, the spatial correlations between defects created in displacement cascades, and the complicated microstructures proposed for future generations of radiation-resistant materials. The complexity of the present problem necessitates development of novel simulation techniques for simulating damage accumulation that can include complex phenomena such as diffusivity of many defect species while maintaining computational efficiency in order to simulate radiation damage over long timescales and in larger simulation volumes than previous methods.

Several challenges associated with the complexity of damage evolution, spatial resolution, and computational scalability must be addressed during the development of such a novel technique. The computational tools developed in this dissertation must include more complex interactions between defects than previous methods. This necessitates developing reaction rates that can be applied to a wider variety of reaction types than exist in the literature, such as interactions between 3D and 1D diffusing defects. The methods developed in this dissertation must also be able to capture the spatial resolution necessary to simulate spatially inhomogeneous microstructures like thin films and nanocrystalline structures as well as displacement cascade damage, which is contains spatially correlated reactions. Finally, the desire to simulate larger volumes, complex microstructures, and radiation doses on the order of one displacement per atom necessitates increased computational efficiency compared to previous methods such as OKMC.

The multi-scale modeling tool developed in this dissertation to address these challenges

is called spatially resolved stochastic cluster dynamics (SRSCD). This tool is developed specifically to address the computational needs of simulations of damage accumulation over long timescales and in complicated microstructural environments such as thin films and polycrystals. SRSCD has been implemented in this dissertation in spatially resolved domains such as polycrystals and thin films, using a synchronous parallel kinetic Monte Carlo algorithm to increase the size of the simulation volumes and total radiation dose accessible by these simulations. Displacement cascade damage has been implemented in SRSCD using three techniques (single volume element implantation, distribution across several volume elements, and adaptive meshing), and these methods have been been shown to correctly reproduce the spatially correlated reactions caused by the proximity of defects inside displacement cascades. Reaction rates for complicated defect interactions such as one-dimensional glide of SIA loops and defect interactions on two-dimensional surfaces have been derived in this dissertation, making simulation of complex defect behaviors and microstructures such as grain boundaries possible. Overall, the development of SRSCD as well as the advancements made to this technique over the course of this dissertation enable simulations of damage evolution in irradiated metals using a larger input space of irradiation conditions as well as in more complicated material microstructures than previous methods. This method has therefore effectively addressed the challenges presented above.

Using this tool, two main scientific questions are investigated in this dissertation: (1) how radiation conditions such as temperature, dose rate, and damage type influence radiation defect accumulation in irradiated metals; and (2) how the presence of microstructural features, namely interfaces, grain boundaries, and free surfaces, influence radiation defect accumulation in irradiated metals. To address these questions, several studies of damage accumulation are performed under a broad range of damage conditions and microstructures. These studies investigate damage evolution in three main material microstructures: thin films, bulk metals, and nanocrystalline metals. In each microstructural environment, the impact of irradiation conditions and microstructural features such as grain boundaries and free surfaces on damage accumulation are quantified.

Thin films are frequently used in ion irradiation experiments, due to their application in

experimental techniques such as in-situ TEM microscopy and the relatively shallow implantation depth of ions in metals. In SRSCD simulations of radiation damage in thin films, displacement damage and helium are implanted into iron thin films in order to study the influence of helium on damage evolution as well as the dependence of helium and radiation damage on implantation conditions such as dose, dose rate, temperature, helium to dpa ratio, film thickness, and damage type (cascade or Frenkel pairs). These studies are first used to validate the SRSCD methodology, by comparing results of helium desorption experiments [231] to experimentally predicted fractions of released helium. Next, a systematic study of effective helium diffusivity is used to link irradiation conditions to helium evolution in iron thin films. In all of these simulations, mechanisms for helium migration in a variety of simulated environments are identified by tracking the mobile species of helium and helium-vacancy clusters responsible for desorption and by using Arrhenius plots of effective diffusivity to identify temperature regions in which various migration and annealing mechanisms are active for a range of irradiation conditions. These studies suggest that helium migration inside iron thin films is highly dependent on the damage content introduced with the helium as well as the irradiation conditions and film thickness.

Bulk metals represent the majority of industrially implemented nuclear materials today as well as common microstructures used in neutron irradiation experiments. Therefore, SRSCD simulations of radiation damage in bulk metals performed in this dissertation focus in damage conditions relevant for neutron irradiation. In these simulations, cascade damage is implanted into coarse-grained iron to experimentally relevant doses and damage accumulation is compared to experimental measurements [67, 259]. The computational efficiency of the adaptive meshing algorithm developed in the SRSCD code allows simulations of doses up to 10^{-1} dpa while accurately including the effects of displacement cascade damage implantation. These simulations investigate the impact of three mechanisms at play in these damage conditions on accumulation: the distribution of displacement cascade PKA energies, interactions between displacement cascades and defects already present in the material during the thermal spike phase, and the influence of traps for SIA loops such as carbon impurities on defect content. Using the knowledge gained by these investigations,

damage accumulation is compared to experimental measures and found to match qualitative trends in defect population growth and saturation as a function of radiation dose. This study represents the first step in the development of a tool which could be used to predict the current state of damage accumulation in aging nuclear reactors.

Nanostructured metals such as nanocrystalline iron have been proposed as potential structural materials in future nuclear reactors due to their high interface to volume ratio, which increases recombination of radiation defects and allows metals to 'self-heal'. The synchronous parallel implementation of SRSCD is shown to enable simulation of damage accumulation in explicitly represented polycrystalline microstructures, and the impact of grain size on damage content is subsequently quantified assuming grain boundaries act as perfect sinks. The ability of SRSCD to resolve polycrystalline domains represents a first-of-its-kind development in this dissertation. Next, the more detailed interaction between radiation defects and grain boundaries is investigated in subsequent simulations. In these studies, the influence of parameters controlling defect behaviors such as diffusivity and binding to grain boundaries on damage accumulation is studied using a multivariate statistical analysis. The correlation between the various migration and binding energies governing defect behavior inside grain boundaries and several metrics for damage evolution is measured, and the most influential defect properties are identified as a guide for future atomic-scale studies. Taken together, these studies represent a significant step towards predictive modeling of radiation damage in complex microstructures such as nanocrystalline metals.

Due to the computational efficiency and complexity of the allowed defects and reactions in the SRSCD model developed in this dissertation, it is an attractive choice for inclusion in multi-scale frameworks linking atomic-scale defect behaviors to macroscopic material property changes. Similarly, SRSCD can be used as a tool to guide experimental design. These capabilities are demonstrated through two studies linking SRSCD results to macroscopic observable quantities. First, the presence of radiation damage is coupled to mechanical response through a crystal plasticity formulation using the Bacon, Kocks, and Scattergood model [13] for the increase in yield strength due to the presence of voids and dislocation loops. This model is applied using the damage accumulation results produced by SRSCD

in simulations of neutron irradiated coarse-grained iron as an input, and defect strength parameters for voids and dislocation loops are varied until hardening best fits experimental results [38]. Using the fitted values for defect strengths, this combined damage accumulation and hardening model is applied in a predictive fashion, and the impact of dose rate on hardening is predicted to be minimal in neutron-irradiated iron at room temperature. The polycrystalline nature of the crystal plasticity simulations are also shown to enable investigation of stress distributions in both the elastic and plastic domain, which could be implemented in future models to predict effects such as crack formation. Next, the application of SRSCD as a tool to guide experimental design is demonstrated. In this study, the equivalence between temperature and dose rate is investigated using SRSCD, using both Frenkel pair and cascade damage as radiation defect sources. The temperature shift required for irradiation experiments to produce equivalent damage content at different dose rates are created for each case, and direct comparisons of damage content between equivalent dose rate-temperature pairs show good agreement. This method can be applied by experimentalists using ion irradiation in order to choose a temperature at which the damage accumulation produced in experiments best matches damage accumulation during neutron irradiation.

The SRSCD methodology and the various mutli-scale frameworks implemented in this dissertation provide a basis upon which several future improvements and applications to new materials systems could be made. For example, application of SRSCD to other metals such as FCC metals and complex alloys will eventually be necessary in order to predict damage evolution in real structural materials rather than proxy materials such as iron. Several atomic-scale questions must be considered when making such changes, such as how and under what irradiation conditions to include the formation of stacking fault tetrahedra and vacancy dislocation loops. In general, a robust description of the various defect types and their migration and binding energies is necessary in order to simulate radiation damage in a given metal, and very few materials systems exist for which such information has been reliably obtained. Such simulations will therefore necessitate statistical model-reduction

techniques in conjunction with experimental data mining in order to provide sufficient input data into SRSCD without relying solely on atomistic scale modeling for inputs. Other potential improvements to the results obtained in this work include simulation of a more complex crystal plasticity and hardening law, in order to include such effects as defect annihilation and radiation softening caused by sweeping out by glide dislocations. Finally, including the effect of stress on defect behaviors, in particular diffusion and binding energies of defects, could allow for simulation of damage evolution near crack tips or other stress concentrations. Overall, advancements in the methods developed in this work will necessitate parallel advancements in our atomistic understanding of defect behaviors in various materials and under various influences such as stresses. Therefore, expanding the use of SRSCD to more material systems and irradiation conditions will also act as a motivating force for investigation of those systems at other time and length scales with other computational tools.

The variety of scientific outcomes of this dissertation demonstrate that efficient multiscale models for damage accumulation such as SRSCD are powerful tools that can be used to investigate fundamental physics associated with radiation damage as well as to link ab-initio and atomistic data on defect behaviors to macroscopic and measurable quantities such as hardness in a predictive fashion. Throughout the course of this dissertation, significant advancements to the state of the art have been made, especially with regards to the ability to predict long-term damage evolution in complicated material microstructures without the use of fitting parameters. The advancements made in this dissertation represent an important step towards predictive models that can be used to design radiation-resistant materials for use in nuclear reactors and to accurately estimate the current levels of radiation damage and corresponding safety factors in current generations of nuclear reactors.

APPENDIX A

DERIVATION OF KINETIC MONTE CARLO ALGORITHM

A derivation of the classic kinetic Monte Carlo algorithm is given here. This derivation is adapted from the work of Gillespie [83]. Given a kinetic system with allowed reactions R_μ and corresponding reaction rates A_μ (in s^{-1}), we define the reaction probability density function $P(\tau, \mu)$, defined such that $P(\tau, \mu)d\tau$ is the probability at time t that the next reaction in volume V will occur in the time interval $(t+\tau, t+\tau+d\tau)$ and the next reaction will be R_μ. This probability function can be expressed as the product of the probability $P_0(\tau)$ that no reaction will occur in V in the time interval $(t, t+\tau)$ and the probability $A_\mu d\tau$ that reaction R_μ will occur in the interval $(t+\tau, t+\tau+d\tau)$:

$$P(\tau, \mu)d\tau = P_0(\tau) \cdot A_\mu d\tau \tag{112}$$

To calculate $P_0(\tau)$, we divide the interval $(t, t+\tau)$ into K sub-intervals of length $\epsilon = \tau/K$. The probability that reaction R_μ with rate A_μ will not occur in the first ϵ subinterval $(t, t+\epsilon)$ is given by

$$1 - A_\mu \epsilon + o(\epsilon) \tag{113}$$

and therefore the probability that no reaction will occur in the first ϵ sub-interval is given by

$$\prod_{\mu=1}^{M} (1 - A_\mu \epsilon + o(\epsilon)) = 1 - \sum_{\mu=1}^{M} A_\mu \epsilon + o(\epsilon) \ . \tag{114}$$

Since this probability is the same for each sub-interval ϵ, then $P_0(\tau)$ can be written as the product of these probabilities over K sub-intervals:

$$P_0(\tau) = \left[1 - \sum_{\mu=1}^{M} A_\mu \epsilon + o(\epsilon) \right]^K \ . \tag{115}$$

Substituting $\epsilon = \tau/K$ and taking the limit of large K, we get:

$$\begin{aligned} P_0(\tau) &= \lim_{K\to\infty} \left[1 - \sum_{\mu=1}^{M} \frac{A_\mu \tau}{K} + o(K^{-1})\right]^K \\ &= \lim_{K\to\infty} \left[1 - \frac{\sum_{\mu=1}^{M} A_\mu \tau}{K} + o(K^{-1})\right]^K \\ &= e^{-A\tau} \end{aligned} \tag{116}$$

where $A = \sum_{\mu=1}^{M} A_\mu$ is the sum of the reaction rates in volume V. Combining equations (112) and (116), we get a formula for the probability density function $P(\tau, \mu)$:

$$P(\tau, \mu) = A_\mu e^{-A\tau} \tag{117}$$

The two-variable probability density function (117) can be written as the product of two single-variable probability density functions [83]:

$$P(\tau, \mu) = P_1(\tau) \cdot P_2(\mu|\tau) \tag{118}$$

where $P_1(\tau)d\tau$ is the probability at time t that the next reaction will occur in the interval $(t+\tau, t+\tau+d\tau)$ and $P_2(\mu|\tau)$ is the probability that the next reaction will be an R_μ reaction given that the reaction occurs at time $t + \tau$. Given the addition theorem for probabilities, we find a formula for $P_1(\tau)$ by summing $P(\tau, \mu)$ over all values μ:

$$P_1(\tau) = \sum_{\mu=1}^{M} P(\tau, \mu) = \sum_{\mu=1}^{M} A_\mu e^{-A\tau} = Ae^{-A\tau} \tag{119}$$

where again we have taken advantage of the fact that $A = \sum_{\mu=1}^{M} A_\mu$. Substituting equation (119) into equation (118), we get a formula for $P_2(\mu|\tau)$:

$$P_2(\mu|\tau) = P_2(\mu) = \frac{A_\mu}{A} \tag{120}$$

Note that in equation (120), we have taken advantage of the fact that $P_2(\mu)$ is independent of τ.

Given the form of $P_1(\tau)$ in equation (119), a random value of τ can be generated according to this distribution by defining a probability distribution function $F(\tau)$ as:

$$F(\tau) = \int_0^\tau P_1(\tau')d\tau' \ . \tag{121}$$

Thus the distribution function $F(\tau_0)$ represents the probability that τ will be less than τ_0. Note that in equation (121) we have discarded all negative values of τ' because $P_1(\tau') = 0$ for $\tau' < 0$. Therefore $F(0) = 0$, $F(\infty) = 1$, and $F(\tau)$ increases monotonically from $\tau = 0$ to ∞.

A discrete timestep can therefore be generated by choosing $r_1 \in (0, 1)$ and taking τ as the value that satisfies $F(\tau) = r_1$. For the case of $P_1(\tau)$ given in equation (119), this gives us $F(\tau) = 1 - e^{-A\tau}$. By setting $F(\tau) = r_1$ and inverting, we get the first part of the kinetic Monte Carlo algorithm given in equation (8):

$$\tau = \frac{1}{A} \ln\left(\frac{1}{r_1}\right) \ . \tag{122}$$

A similar method can be used to choose a reaction R_μ in the system to carry out according to the probability density function $P_2(\mu)$. Here, a discrete probability distribution function $F(\mu)$ is defined as:

$$F(\mu) = \sum_{\nu=1}^{\mu} P_2(\nu) \ , \tag{123}$$

where again $F(\mu_0)$ represents the probability that the reaction chosen R_μ will have μ less than or equal than μ_0. Therefore a reaction can be chosen from the list of allowed reactions by choosing a second random number $r_2 \in (0, 1)$ and taking μ that satisfies:

$$F(\mu - 1) < r_2 \leq F(\mu) \ . \tag{124}$$

Substituting equations (120) and (123) and multiplying by A, equation (124) becomes

$$\sum_{\nu=1}^{\mu-1} A_\nu < r_2 A \leq \sum_{\nu=1}^{\mu} A_\nu \ , \tag{125}$$

which is the second part of the kinetic Monte Carlo algorithm given in equation (8).

APPENDIX B

DEMONSTRATION OF EQUIVALENCE OF STOCHASTIC AND DETERMINISTIC APPROACHES TO RATE THEORY PROBLEMS

In many areas of chemistry and materials science, it is of interest to know the time-evolution of the concentration of several chemical species c_m, $m \in [1, M]$. The concentration of each chemical species is typically mediated by a deterministic rate equation,

$$\frac{dc_m}{dt} = \nabla \cdot (D \nabla c_m) + f_m(t, c_1, ..., c_M) \tag{126}$$

In this analysis we are primarily concerned with the form of f_m, which accounts for all interactions between chemical species. If chemical species m can undergo n reactions of the type $R_1 + R_2 + ... + R_j \rightarrow P_1 + P_2 + ... + P_k$, then we can express f_m as:

$$f_m(t, c_1, ..., c_M) = \sum_{i=1}^{n} \alpha_{im} \tag{127}$$

where α_{im} is a rate constant that depends, in general, on the concentrations of the other defects involved in the reaction.

B.1 Test case: three-species behavior

Here we will assume the presence of three chemical species: A, B, and C. The following reactions will be allowed to occur in our system:

1) 0	$\rightarrow$	$A + B$
2) $A + B$	$\rightarrow$	0
3) $A + A$	$\rightarrow$	C
4) C	$\rightarrow$	$A + A$
5) $B + C$	$\rightarrow$	A

This corresponds to the following physical system in metals subjected to radiation damage: A represents single vacancies in the metallic lattice, B represents self-interstitial atoms (atoms which have been displaced from their lattice site), and C represents clusters of two vacancies. Reaction 1 represents Frenkel pair implantation, in which an atom is knocked

out of its lattice site, creating a vacancy-interstitial pair. Reaction 2 represents vacancy-interstitial recombination, in which a self-interstitial atom falls into an unoccupied lattice site and both defects are annihilated. Reactions 3 and 4 represents vacancy clustering and thermal dissociation of vacancy clusters, respectively. Reaction 5 represents annihilation between a self-interstitial and one of the two vacancies in a di-vacancy pair C.

In this case, the rate equations presented above (neglecting the diffusion term) are:

$$\begin{aligned}
\frac{da}{dt} &= \alpha_1 - \alpha_2 ab - 2\alpha_3 a^2 + 2\alpha_4 c + \alpha_5 bc \\
\frac{db}{dt} &= \alpha_1 - \alpha_2 ab - \alpha_5 bc \\
\frac{dc}{dt} &= \alpha_3 a^2 - \alpha_4 c - \alpha_5 bc
\end{aligned} \tag{128}$$

where rate constant α_i corresponds to reaction i. Here, the use of a instead of A represents a concentration rate equation ($a = \frac{A}{V}$).

B.2 Stochastic Point of View

In this section we will show that when taking a stochastic formulation of the problem, the above rate equations still apply. This approach begins by defining a function $P(A, B, C, t)$ as the probability at time t of finding A, B, and C (integer valued) vacancies, self-interstitials, and 2-vacancy clusters inside a finite volume V. This probability distribution is called the *master equation*, and describes the evolution of the entire system. Assuming an initial state so that $P(A_0, B_0, C_0, 0) = 1$ and $P(A, B, C, 0) = 0$ for all other A, B, and C, a single (stochastic) rate equation can be written which describes the evolution of P.

Another approach for modeling population evolution uses the master equation, which gives the probability that the system is in a given microstate at a given time:

$$P(N_1, ..., N_m, t) \tag{129}$$

where N_i represents the number of species i present in a volume at time t. The evolution of this master equation is similarly given by

$$\frac{\partial P(N_1, ..., N_m, t)}{\partial t} = \sum_{i=1}^{n} \beta_i \tag{130}$$

where β_i is a different rate constant corresponding to reaction i (typically in different units than α_i).

To show the form of the master equation, we again examine the test case presented above. Using the reactions presented for three-species radiation defect evolution, the following rate equation for the evolution of the master equation is obtained:

$$\begin{aligned}\frac{\partial P(A,B,C,t)}{\partial t} = &\beta_1 \left(P(A-1,B-1,C,t) - P(A,B,C,t)\right) + \\ &\beta_2 \left((A+1)(B+1)P(A+1,B+1,C,t) - ABP(A,B,C,t)\right) + \\ &\beta_3 \left(\frac{1}{2}(A+2)(A+1)P(A+2,B,C-1,t) - \frac{1}{2}A(A-1)P(A,B,C,t)\right) + \\ &\beta_4 \left((C+1)P(A-2,B,C+1,t) - CP(A,B,C,t)\right) + \\ &\beta_5 \left((B+1)(C+1)P(A-1,B+1,C+1,t) - BCP(A,B,C,t)\right) \end{aligned} \quad (131)$$

We can see by inspection that reaction i is governed by constant β_i. For simple systems, the master equation is solvable using analytical or numerical methods, but we can see that this problem becomes practically unmanageable very quickly compared to the (relative) ease of numerical simulation of the rate equations presented in the previous section.

B.3 Equivalence between stochastic and deterministic points of view

Next, we will demonstrate the following: the deterministic (rate equation) formulation and the stochastic (master equation) formulations of the problem are equivalent, and the relationship between α_i and β_i are analytically calculable. This has been performed in the literature for both a test case (not the same as this test case) and a general case [159, 119]. The average value of A^l, where A is the number of single vacancy defects present in the material is given by:

$$A(t)^l = \sum_{A_j=0}^{\infty} \sum_{B_j=0}^{\infty} \sum_{C_k=0}^{\infty} A_i^l P(A_i, B_j, C_k, t) \quad (132)$$

and

$$\frac{dA(t)}{dt} = \sum_{A_j=0}^{\infty} \sum_{B_j=0}^{\infty} \sum_{C_k=0}^{\infty} A_i \frac{dP(A_i, B_j, C_k, t)}{dt} \quad (133)$$

In the limit that the number of defects approaches infinity, we can express the probability $P(A,B,C,t)$ as

$$P(A,B,C,t) = P(A,t)P(B,t)P(C,t) \quad (134)$$

Therefore, the average number of defects $A(t)^l$ becomes

$$A(t)^l = \sum_{A_i=0}^{\infty} A_i^l P(A_i,t) \sum_{B_j=0}^{\infty} P(B_j,t) \sum_{C_k=0}^{\infty} P(C_k,t) = \sum_{A_i=0}^{\infty} A_i^l P(A_i,t) \tag{135}$$

Using the above equation, we will substitute the master equation term-by-term to derive the relationship between α_i and β_i. Note that in assuming large defect numbers, we can make the following approximation:

$$\sum_{A_i=0}^{\infty} A_i^l P(A_i,t) = \sum_{A_i=0}^{\infty} (A_i+1)^l P(A_i+1,t) = A(t)^l \tag{136}$$

Substituting the β_1 term of the master equation into equation (133) and using the factorized form of the probability $P(A,B,C,t)$, we get the following:

$$\begin{aligned}
\frac{dA(t)}{dt} &= \sum_{A_i=0}^{\infty} A_i\beta_1(P(A_i-1,t)-P(A_i,t)) \sum_{B_j=0}^{\infty} P(B_j,t) \sum_{C_k=0}^{\infty} P(C_k,t) + (\text{Other terms}) \\
&= \beta_1 \left(\sum_{A_i=0}^{\infty} A_i P(A_i-1,t) - \sum_{A_i=0}^{\infty} A_i P(A_i,t) \right) + ... \\
&= \beta_1 \left(\sum_{A_i=0}^{\infty} (A_i-1) P(A_i-1,t) + \sum_{A_i=0}^{\infty} P(A_i-1,t) - \sum_{A_i=0}^{\infty} A_i P(A_i,t) \right) + ... \\
&= \beta_1(A(t)+1-A(t)) + ... = \beta_1 + (\text{Other terms})
\end{aligned} \tag{137}$$

Similarly, with the β_2 term:

$$\begin{aligned}
&\beta_2 \sum_{A_i=0}^{\infty} \sum_{B_j=0}^{\infty} \sum_{C_k=0}^{\infty} A_i \left((A_i+1)(B_j+1)P(A_i+1,B_j+1,C_k,t) - A_iB_jP(A_i,B_j,C_k,t) \right) \\
&= \beta_2 \left(\sum_{A_i=0}^{\infty} A_i(A_i+1)P(A_i+1,t) \right) \left(\sum_{B_j=0}^{\infty} (B_j+1)P(B_j+1,t) \right) \left(\sum_{C_k=0}^{\infty} P(C_k,t) \right) \\
&\quad -\beta_2 \left(\sum_{A_i=0}^{\infty} A_i^2 P(A_i,t) \right) \left(\sum_{B_j=0}^{\infty} B_j P(B_j,t) \right) \left(\sum_{C_k=0}^{\infty} P(C_k,t) \right) \\
&= \beta_2 \left(B \sum_{A_i=0}^{\infty} (A_i+1)^2 P(A_i+1,t) - B \sum_{A_i=0}^{\infty} (A_i+1)P(A_i+1,t) - B \sum_{A_i=0}^{\infty} A_i^2 P(A_i,t) \right) \\
&= \beta_2(A^2B - AB - A^2B) = -\beta_2 AB
\end{aligned} \tag{138}$$

With the β_3 term:

$$\begin{aligned}
&\frac{\beta_3}{2}\sum_{A_i=0}^{\infty}\sum_{B_j=0}^{\infty}\sum_{C_k=0}^{\infty}A_i((A_i+2)(A_i+1)P(A_i+2,B_j,C_k-1,t)\\
&-A_i(A_i-1)P(A_i,B_j,C_k,t))\\
&=\frac{\beta_3}{2}\sum_{A_i=0}^{\infty}\left(A_i(A_i+1)(A_i+2)P(A_i+2,t)-A_i^2(A_i-1)P(A_i,t)\right)\\
&=\frac{\beta_3}{2}\sum_{A_i=0}^{\infty}\left(\left((A_i+2)^3-3(A_i+2)^2+2(A_i+2)\right)P(A_i+2,t)-(A_i^3-A_i^2)P(A_i,t)\right)\\
&=\frac{\beta_3}{2}(A^3-3A^2+2A-A^3-A^2)=\frac{\beta_3}{2}(-4A^2+2A)\simeq-2\beta_3A^2
\end{aligned}\tag{139}$$

where above we use the fact that, for large A, $A^2 \gg A$. Next, we complete the β_4 term:

$$\begin{aligned}
&\beta_4\sum_{A_i=0}^{\infty}\sum_{B_j=0}^{\infty}\sum_{C_k=0}^{\infty}A_i\left((C_k+1)P(A_i-2,B_j,C_k+1,t)-C_kP(A_i,B_j,C_k,t)\right)\\
&=\beta_4\left(\sum_{A_i=0}^{\infty}A_iP(A_i-2,t)\sum_{C_k=0}^{\infty}(C_k+1)P(C_k+1,t)\right)\\
&-\beta_4\left(\sum_{A_i=0}^{\infty}A_iP(A_i,t)\sum_{C_k=0}^{\infty}C_kP(C_k,t)\right)\\
&=\beta_4\left(\sum_{A_i=0}^{\infty}((A_i-2)P(A_i-2,t)+2P(A_i-2,t))\sum_{C_k=0}^{\infty}(C_k+1)P(C_k+1,t)\right)\\
&-\beta_4\left(\sum_{A_i=0}^{\infty}A_iP(A_i,t)\sum_{C_k=0}^{\infty}C_kP(C_k,t)\right)\\
&=\beta_4((A+2)C-AC)=2\beta_4C
\end{aligned}\tag{140}$$

Finally, the β_5 term:

$$\begin{aligned}
&\beta_5\sum_{A_i=0}^{\infty}\sum_{B_j=0}^{\infty}\sum_{C_k=0}^{\infty}A_i((B_j+1)(C_k+1)P(A_i-1,B_j+1,C_k+1,t)\\
&-B_jC_kP(A_i,B_j,C_k,t))\\
&=\beta_5BC\sum_{A_i=0}^{\infty}(A_iP(A_i-1,t)-A_iP(A_i,t))\\
&=\beta_5BC\sum_{A_i=0}^{\infty}((A_i-1)P(A_i-1,t)+P(A_i-1,t)-A_iP(A_i,t))\\
&=\beta_5BC
\end{aligned}\tag{141}$$

Combining all of the terms in the above equations, we arrive at the following rate equation for the evolution of the average value of $A(t)$, the number of single vacancies in

the volume V at time t:

$$\frac{dA(t)}{dt} = \beta_1 - \beta_2 AB - 2\beta_3 A^2 + 2\beta_4 C + \beta_5 BC \tag{142}$$

Substituting $A = Va$, where a is the concentration of vacancies (m^{-3}), we get:

$$V\frac{da(t)}{dt} = \beta_1 - \beta_2 V^2 ab - 2\beta_3 V^2 a^2 + 2\beta_4 Vc + \beta_5 V^2 bc \tag{143}$$

Dividing by V, we have an equation in the form of equation (128), given by:

$$\frac{da(t)}{dt} = \frac{\beta_1}{V} - \beta_2 Vab - 2\beta_3 Va^2 + 2\beta_4 c + \beta_5 Vbc \tag{144}$$

This gives us the following relationships between the rate constants α_i and β_i: $\beta_1 = \alpha_1 V$, $\beta_2 = \frac{\alpha_2}{V}$, $\beta_3 = \frac{\alpha_3}{V}$, $\beta_4 = \alpha_4$, and $\beta_5 = \frac{\alpha_5}{V}$. We can see that, more generally, when the deterministic and stochastic equations governing such a rate theory problem are written in the form above, the relationship between the constants in each equation is given by $\beta = \alpha V^{1-n}$, where n is the order of the reaction ($n = 2$ reactions require 2 defects to be carried out, for example).

We can repeat this method for the equations governing the time evolution of self-interstitials and vacancy clusters, but we have already solved for the rate constants β in terms of α. We have therefore demonstrated that in the case of the test equation, the stochastic formulation and the deterministic formulation of the time evolution of the system are equivalent (in the limit of a large number of defects). Note that this exercise requires that the concentration of defect types is homogeneous and that the material is in thermal (but not chemical) equilibrium.

APPENDIX C

DEMONSTRATION OF EQUIVALENCE OF SERIAL AND PARALLEL KINETIC MONTE CARLO ALGORITHMS

To prove the equivalence of the parallel and serial solutions, we will first prove that, inside any given volume element, adding a null event with arbitrary rate R_0 does not impact the time evolution of the system. For the test case presented in Appendix B, the probability of being in state (A, B, C) at step t_{n+1} is given by the probabilities of being in various states that can evolve into state (A, B, C) at step t_n:

$$\begin{aligned} P(A,B,C,t_{n+1}) = & \frac{\beta_1}{R} P(A-1,B-1,C,t_n) \\ & + \frac{\beta_2 (A+1)(B+1)}{R} P(A+1,B+1,C,t_n) \\ & + \frac{\beta_3 \frac{1}{2}(A+2)(A+1)}{R} P(A+2,B,C-1,t_n) \\ & + \frac{\beta_4 (C+1)}{R} P(A-2,B,C+1,t_n) \\ & + \frac{\beta_5 (B+1)(C+1)}{R} P(A-1,B+1,C+1,t_n) \end{aligned} \tag{145}$$

This equation is similar to equation (131) except that it assumes a discrete timestep in which a single reaction will occur. Note that R is the sum of all of the rate constants, so that the total sum of all of the coefficients in the above equation is 1. If we now add a null event with arbitrary positive rate R_0, and we re-calculate $R_{\text{new}} = R + R_0$, the above

equation becomes:

$$\begin{aligned}P(A,B,C,t_{n+1}) = &\frac{\beta_1}{R_{\text{new}}}P(A-1,B-1,C,t_n)\\ &+\frac{\beta_2(A+1)(B+1)}{R_{\text{new}}}P(A+1,B+1,C,t_n)\\ &+\frac{\beta_3\frac{1}{2}(A+2)(A+1)}{R_{\text{new}}}P(A+2,B,C-1,t_n)\\ &+\frac{\beta_4(C+1)}{R_{\text{new}}}P(A-2,B,C+1,t_n)\\ &+\frac{\beta_5(B+1)(C+1)}{R_{\text{new}}}P(A-1,B+1,C+1,t_n)\\ &+\frac{R_0}{R_{\text{new}}}P(A,B,C,t_n)\end{aligned} \tag{146}$$

Substituting for R_0 and taking the limit of large A, B, and C:

$$R_0 = R_{\text{new}} - R = R_{\text{new}} - (\beta_1 + \beta_2 AB + \beta_3\frac{1}{2}A^2 + \beta_4 C + \beta_5 BC) \tag{147}$$

we get:

$$\begin{aligned}&R_{\text{new}}(P(A,B,C,t_{n+1}) - P(A,B,C,t_n)) =\\ &\quad\beta_1\left(P(A-1,B-1,C,t_n) - P(A,B,C,t_n)\right) +\\ &\quad\beta_2\left((A+1)(B+1)P(A+1,B+1,C,t_n) - ABP(A,B,C,t_n)\right) +\\ &\quad\beta_3\left(\frac{1}{2}(A+2)(A+1)P(A+2,B,C-1,t_n) - \frac{1}{2}A(A-1)P(A,B,C,t_n)\right) +\\ &\quad\beta_4\left((C+1)P(A-2,B,C+1,t) - CP(A,B,C,t)\right) +\\ &\quad\beta_5\left((B+1)(C+1)P(A-1,B+1,C+1,t_n) - BCP(A,B,C,t_n)\right)\end{aligned} \tag{148}$$

Taking $R_{\text{new}} = \frac{1}{\Delta t}$ and the limit as Δt approaches 0 (R_0 approaches infinity), we get equation (131). Thus, we can see that the evolution of the master equation is independent of the chosen value of R_0.

Therefore, if the volume is subdivided into volume elements Ω_j, each volume element has reactions μ and rates R_μ^j, and a null event rate R_0^j is added to each volume element such that $R_{\max} = \sum_\mu R_\mu^j$ is the same for all volume elements, the master equation will evolve according to equation (131) within each volume element, and the total master equation for the entire volume will evolve according to equation (131) as well.

APPENDIX D

APPLICATION OF SERIAL AND PARALLEL KMC ALGORITHMS TO GENERAL COUPLED INITIAL-VALUE PROBLEMS

In this appendix, the serial and parallel kinetic Monte Carlo algorithms presented in Sections 3.2.5 and 3.4 are presented in a more general form for solving arbitrary coupled initial value problems. These methods are then applied to several classic examples of differential equations and results are presented and compared to other differential equation solvers.

D.1 Application: stiff problems

The first problem treated in this way deals with a stiff differential equation that is in the form of chemical rate equations. The rate equations of the problem are given by:

$$\begin{aligned} \frac{dy_1}{dt} &= -\alpha y_1 + \beta y_2 y_3 \\ \frac{dy_2}{dt} &= \alpha y_1 - \beta y_2 y_3 - \gamma y_2^2 \\ \frac{dy_3}{dt} &= \gamma y_2^2 \end{aligned} \tag{149}$$

Here, the rate constants are given by $\alpha = 0.04$, $\beta = 10^4$, and $\gamma = 3 \times 10^7$, and the initial condition is $y_1 = 1$, $y_2 = y_3 = 0$. This problem can be conceptualized as a set of rate equations governing the time evolution of three chemical species (in units of m^{-3}). There are three reactions in the system, given in Table 20. Note that the reaction governed by γ is written as $2 + 2 \rightarrow 2 + 3$ and not $2 + 2 \rightarrow 3$, which is a more typical reaction in chemical problems. For the latter reaction to occur, the rate constant in the second equation must be 2γ instead of γ, indicating the loss of two particles of type 2 for each particle of type 3 gained.

To convert these concentration rate equations to number rate equations, we change all concentrations to numbers by $y_i = Y_i/V$, where V is some finite volume, and multiply by

V. Our system of equations becomes

$$\begin{aligned}
\frac{dY_1}{dt} &= -\alpha Y_1 + \frac{\beta Y_2 Y_3}{V} \\
\frac{dY_2}{dt} &= \alpha Y_1 - \frac{\beta Y_2 Y_3}{V} - \frac{\gamma Y_2^2}{V} \\
\frac{dY_3}{dt} &= \frac{\gamma Y_2^2}{V}
\end{aligned} \tag{150}$$

We also change our initial condition, so that $Y_1(t = 0) = V \times 1$. The units of each term in the above equation are now s^{-1} and each term represents the rate of each reaction to occur. To change to a kinetic Monte Carlo algorithm, we shift from a rate equation perspective to a reaction rate perspective, with the reaction rates of each of the equations given by:

$$\begin{aligned}
r_\alpha &= \alpha Y_1 \\
r_\beta &= \frac{\beta Y_2 Y_3}{V} \\
r_\gamma &= \frac{\gamma Y_2^2}{V}
\end{aligned} \tag{151}$$

Thus the kinetic Monte Carlo algorithm for advancing the system in time is given by

1. Calculate reaction rates and find total reaction rate $R = r_\alpha + r_\beta + r_\gamma$

2. Choose two random numbers r and s between 0 and 1.

3. Iterate time by timestep $\tau = \frac{1}{R} \ln\left(\frac{1}{r}\right)$ and choose reaction μ such that

$$\sum_{\nu=1}^{\mu-1} r_\nu < Rs \leq \sum_{\nu=1}^{\mu} r_\nu \tag{152}$$

4. Carry out reaction μ by changing the numbers of chemicals in the system accordingly

Table 20: Allowed reactions in problem 5.9

Reaction	rate constant
$1 \to 2$	α
$2 + 3 \to 1 + 3$	β
$2 + 2 \to 2 + 3$	γ

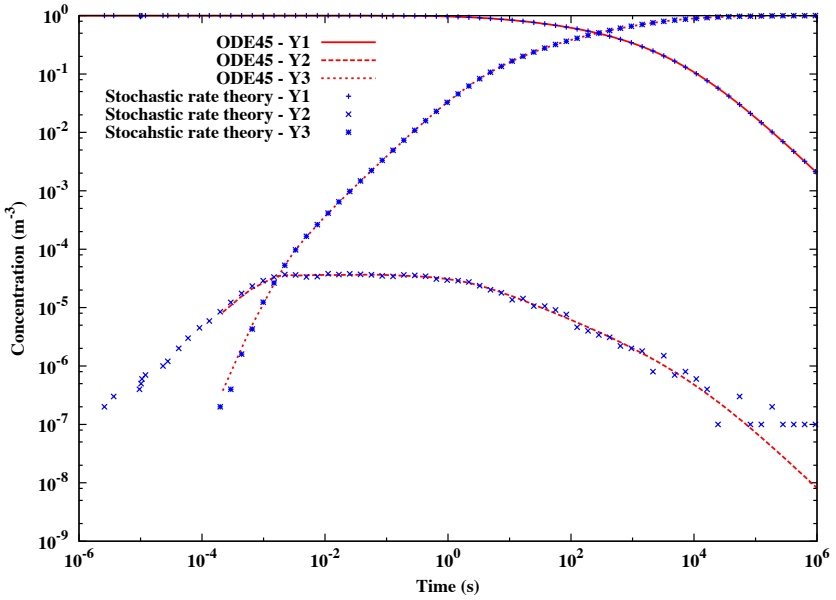

Figure 75: Comparison of stochastic rate theory solution to ODE15 stiff differential equation solver from Matlab for a standard coupled set of stiff rate equations.

Using this algorithm, the numbers of particles of each type in the system as a function of time is evolved, and these numbers can be converted back into concentrations in order to compare the solution of this algorithm to standard differential equation solvers. This was carried out using a short program written in Fortran with a volume of $V = 10^7$ and total time of $t = 10^6$. The results of the stochastic rate theory method are compared to the differential equation solver ODE15 from Matlab in Figure 75. Note that the two methods have good agreement over the entire simulation.

This method has several advantages and disadvantages when compared to traditional stiff differential equation solvers. The fact that the timestep is a product of the Monte Carlo algorithm means that the algorithm naturally treats stiff problems. However, this also means that for large volumes (which are necessary in this problem to resolve the concentration of species 2) the timestep can be very small and therefore the problem can become computationally intensive. In addition, because particle numbers are treated as integers, this method cannot diverge due to a concentration becoming negative (which is a problem with the ODE15 solution to the differential equation). Thus, for problems such as this with conserved particle numbers, the method is always stable.

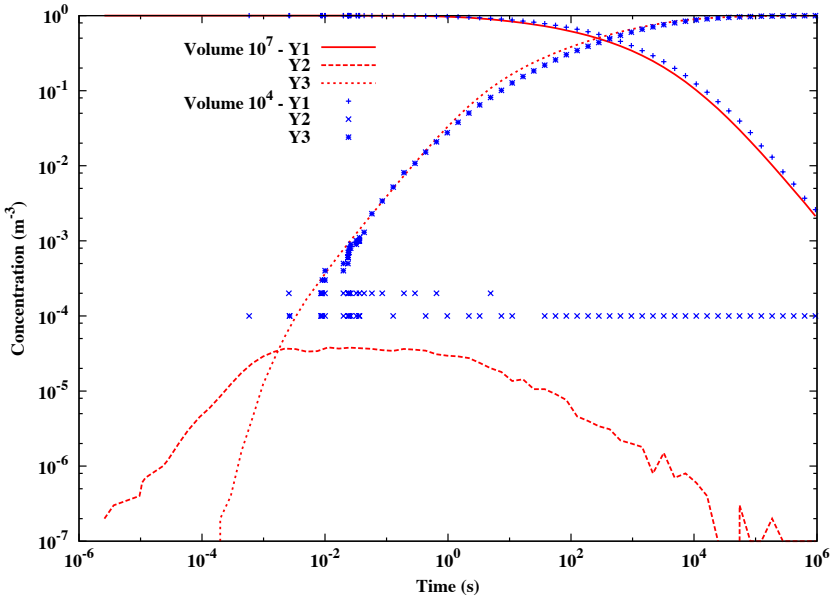

Figure 76: Comparison of results using volumes of 10^4 and 10^7. Note that at 10^4, the concentration of particles of type 2 cannot be resolved, but the concentrations of particles type 1 and 3 remain correct throughout the simulation.

When a small volume is chosen in order to increase the speed of computation, the concentration of particles of type 2 cannot be resolved in this problem. However, the time-evolution of particles type 1 and 3 is only marginally impacted over the course of the simulation, as is shown in Figure 76 using volumes of $V = 10^4$ and $V = 10^7$ for comparison. Again, this ability is due to the inherent ability to solve stiff problems as well as the stability of the method. For example, although particles of species 2 are only present one or two at a time in the smaller volume, the relevant rates change dramatically when they are present due to the high rate of reactions 2 and 3 compared to reaction 1, and the timestep chosen is therefore very different for steps with particles of type 2 present compared to steps with no particles of type 2 present. Therefore, on average, the conversion of particles of type 1 to type 3 happens at the same rate and the macroscopic behavior of the system is the same.

The main benefits of the stochastic rate theory method presented here arise when more complicated problems, which are difficult to treat using traditional coupled equation solvers, are posed. For example, when the number of chemical species changes from 3 to an arbitrarily large number, traditional rate theory methods must approximate the solution by truncating the number of rate equations to a manageable amount. In addition, if there are

n species of particle that can interact with all other species, in general there are n^n allowable reactions. This method naturally accounts for both of these problems by calculating reaction rates only for defects present inside a given volume.

D.2 Application to non-rate theory problems

This method can be extended to problems that are not expressed as rate equations of chemical species as well. As an example, take the case of the classical chaotic system:

$$\begin{aligned}\frac{dy_1}{dt} &= \sigma(y_2 - y_1)\\ \frac{dy_2}{dt} &= ry_1 - y_2 - y_1y_3\\ \frac{dy_3}{dt} &= y_1y_2 - by_3\end{aligned} \tag{153}$$

where σ, b, and r are positive constants and initial condition $y_1(0) = 0$, $y_2(0) = 1$, $y_3(0) = 0$. Assuming y_1, y_2, and y_3 are positive, we can perform the same conversion from concentration to number rate equations by letting $y_i = {}^{Y_i}/_{V}$ and multiplying by V:

$$\begin{aligned}\frac{dY_1}{dt} &= \sigma(Y_2 - Y_1)\\ \frac{dY_2}{dt} &= rY_1 - Y_2 - \frac{Y_1Y_3}{V}\\ \frac{dY_3}{dt} &= \frac{Y_1Y_2}{V} - bY_3\end{aligned} \tag{154}$$

Here, the particle numbers are not conserved. The reactions listed here, while in units of s^{-1}, do not represent physical reactions in the same way as chemical rate equations do. However, we can still create a list of reactions with associated reaction rates, as shown in Table 21.

Table 21: Reactions and rates in the converted chaotic system

Reaction	rate
$0 \to 1$	σY_2
$1 \to 0$	σY_1
$0 \to 2$	rY_1
$2 \to 0$	Y_2
$2 \to 0$	$\frac{Y_1Y_3}{V}$
$0 \to 3$	$\frac{Y_1Y_2}{V}$
$3 \to 0$	bY_3

Thus, we have simply taken each term of the number rate equations and treated it as either a creation or destruction term for one defect, depending on if the term is positive or negative. Note, however, that this step assumes that all rates listed in Table 21 are positive. Due to the fact that particle numbers are no longer conserved, negative particle numbers (and therefore negative rates) can occur. Therefore, to adjust the system for such an occurrence, we use the absolute value of all rates in Table 21 and reverse the direction of the reaction if the rate is negative (thus, reaction $0 \rightarrow 1$ becomes $1 \rightarrow 0$).

Using this slightly modified algorithm, we carry out the kinetic Monte Carlo algorithm in the same way as the previous section, with seven possible reactions here. Figure 77 shows y_1 vs y_3 for $t \in [0, 100]$ using this method and an two different initial volumes V (initial condition is $Y_1 = 0$, $Y_2 = V$, $Y_3 = 0$). Again, the smoothness and computational efficiency of the solution depends on the volume chosen and due to the integer values of Y_i, concentrations cannot be resolved below a lower limit of $1/V$. However, this solution matches qualitatively the ODE45 solution from Matlab of the problem regardless of the volume chosen. In addition, the chaotic nature of this problem means that any two simulations will have quantitatively very different results although the qualitative results will remain the same.

Therefore, the stochastic rate theory method can be applied very broadly to a wide range of problems using a kinetic Monte Carlo algorithm, regardless of whether or not the problems represent actual kinetic systems. The main advantage of this method is that it produces extremely stable results for even very stiff problems and can support an arbitrary number of rate equations and reactions. In addition, the required code for such solutions is extremely simple and is controlled by the number of different reactions to model. The speed of this method for simple problems such as the ones presented above is generally slower than established methods such as ODE45 and ODE15 from MATLAB, but in certain cases (due to the adaptive timestep of the kinetic Monte Carlo algorithm) it can be very fast.

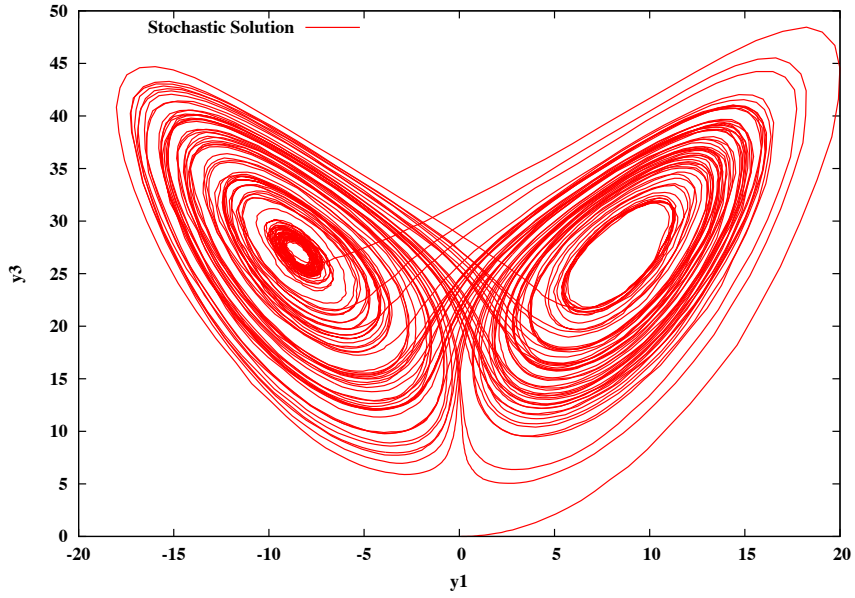

(a) V=1000

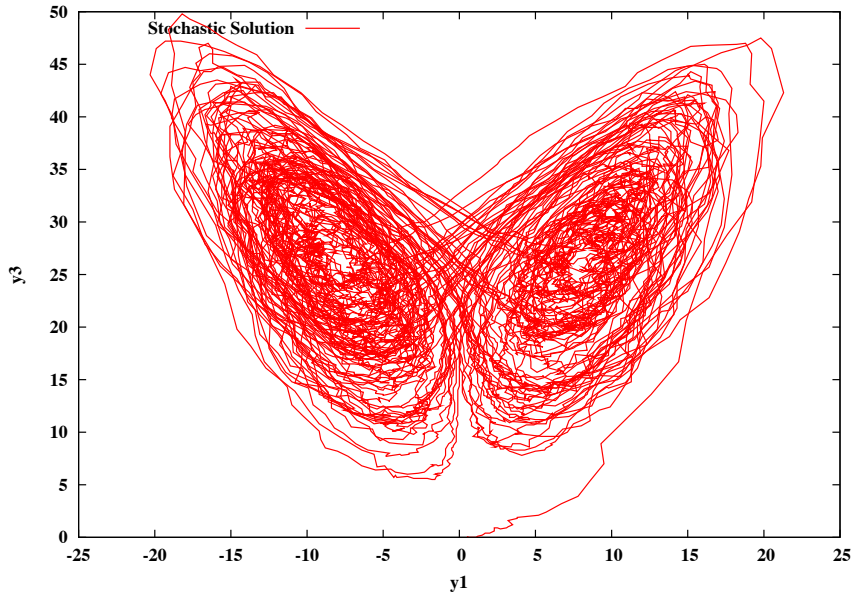

(b) V=100

Figure 77: Solution of the chaotic system of equations presented in equation (153) for $t \in [0, 100]$ using the stochastic rate theory method presented here with two different volumes V. Here, y_1 vs y_3 is shown.

APPENDIX E

PRINCIPAL COMPONENTS OF THE CORRELATION MATRIX

Table 22 shows the 12 principal components v_k of the correlation matrix R, their variances λ_k, and the communality associated with each principal component for the output variables obtained in simulations of damage accumulation inside grain boundaries as a function of defect parameters carried out in Section 4.5.4. Communality represents the percentage of variation in that output variable that is explained by variation along principal component v_k. The analysis in Section 4.5.4 is carried out only using principal components 1, 2, 3, and 9 as these four principal components are responsible for between $77 - 87\%$ of the variance in all four output variables.

Table 22: Principal components v_k and variances λ_k of the correlation matrix R (top), and communality of the output variables for each principal component.

Principal Components	PC_1	PC_2	PC_3	PC_4	PC_5	PC_6
E_m(V)	0.189648805	-9.10E-03	0.663954208	-3.41E-02	0.168638697	-4.53E-02
E_m(SIA)	-3.38E-02	-8.24E-02	0.172736756	0.7413347	-0.392133851	3.18E-02
E_m(V Clusters)	0.113690271	-4.69E-02	0.162400282	-0.409267345	-0.441728281	0.141454574
E_m(SIA Clusters)	-1.34E-02	-5.53E-02	2.30E-03	8.73E-02	0.716297015	0.33818973
E_b(V)	0.347789213	-0.522657117	-0.239754004	5.60E-02	2.55E-02	-2.19E-02
E_b(SIA)	0.411961479	0.478592409	-0.155900304	0.201646381	-4.23E-02	7.04E-02
A(V)	-7.24E-02	-6.00E-02	-2.03E-02	-0.112598606	-0.290611111	0.786914047
A(SIA)	3.92E-03	2.13E-02	7.84E-02	0.181863707	0.150134338	0.484484712
C(V)	0.344511533	-0.215825353	0.511062898	0.137317775	1.01E-02	-1.54E-02
Size(V)	-0.42956806	-7.02E-02	-9.23E-02	0.380569332	-1.81E-03	-3.41E-02
η_V	0.390880624	-0.460214683	-0.341264526	7.28E-02	-6.86E-03	1.16E-02
η_I	0.444807211	0.46722243	-0.168630532	0.124904792	-1.46E-04	4.04E-02
Variance (λ_k)	2.154309427	1.740299394	1.505798711	1.096009155	1.02484058	0.998599854
Communality						
C(V)	0.2556911	0.08106416	0.393292466	0.020666536	0.00010483	0.000237184
Size(V)	0.397531957	0.008567315	0.012835851	0.158738312	3.36288E-06	0.001161783
η_V	0.329151901	0.368591156	0.175367541	0.005809047	4.82023E-05	0.000133301
η_I	0.426237563	0.379901788	0.042819278	0.017099066	2.18566E-08	0.001627554

Principal Components	PC_7	PC_8	PC_9	PC_{10}	PC_{11}	PC_{12}
E_m(V)	-3.48E-02	0.254257005	-0.10918847	-0.554913059	-0.215166361	-0.243852239
E_m(SIA)	0.152732957	-0.175875995	0.427359208	-0.136472162	-4.43E-02	1.96E-02
E_m(V Clusters)	0.123488651	-0.711384795	-0.162878248	-0.156824657	-5.28E-02	-2.52E-02
E_m(SIA Clusters)	0.450618867	-0.369861724	0.13985207	-4.67E-02	4.23E-03	8.24E-03
E_b(V)	-5.29E-02	5.98E-02	-0.134593369	-0.429189218	0.292299164	0.499998237
E_b(SIA)	8.46E-02	-1.84E-02	-0.205989958	-0.12140714	0.576558196	-0.36391917
A(V)	0.267077729	0.447196009	-5.11E-02	4.53E-03	-1.55E-02	1.38E-02
A(SIA)	-0.805970874	-0.225321525	-3.41E-02	3.68E-02	3.52E-03	1.25E-02
C(V)	0.108677298	1.68E-02	-0.26503984	0.647981691	0.156849431	0.165918086
Size(V)	0.102248462	-8.11E-02	-0.78054255	-9.17E-02	-0.136877924	-5.11E-02
η_V	-2.48E-02	-2.73E-03	-1.33E-02	0.134325227	-0.368112893	-0.599269546
η_I	5.83E-02	5.05E-03	-0.123915238	4.87E-03	-0.593272498	0.409150069
Variance (λ_k)	0.995266691	0.951180852	0.650006163	0.427183943	0.230232414	0.226272816
Communality						
C(V)	0.011754851	0.000268479	0.045660409	0.17936611	0.005664119	0.006229022
Size(V)	0.010405262	0.006249348	0.396014092	0.003591109	0.004313535	0.000590763
η_V	0.000610148	7.0911E-06	0.000115532	0.007707794	0.031198127	0.081259996
η_I	0.003386127	2.4254E-05	0.009980836	1.0113E-05	0.081035422	0.037878925

REFERENCES

[1] Abdi, H. and Williams, L. J., "Principal component analysis," *Wiley Interdisciplinary Reviews: Computational Statistics*, vol. 2, no. 4, pp. 433–459, 2010.

[2] Abromeit, C., "Aspects of simulation of neutron damage by ion irradiation," *Journal of nuclear materials*, vol. 216, pp. 78–96, 1994.

[3] Adamantiades, A. and Kessides, I., "Nuclear power for sustainable development: current status and future prospects," *Energy Policy*, vol. 37, no. 12, pp. 5149–5166, 2009.

[4] Arakawa, K., Imamura, R., Ohota, K., and Ono, K., "Evolution of point defect clusters in pure iron under low-energy he+ irradiation," *Journal of Applied Physics*, vol. 89, no. 9, pp. 4752–4757, 2001.

[5] Armstrong, D. E. and Britton, T., "Effect of dislocation density on improved radiation hardening resistance of nano-structured tungsten–rhenium," *Materials Science and Engineering: A*, vol. 611, pp. 388–393, 2014.

[6] Arrhenius, S., "Über die reaktionsgeschwindigkeit bei der inversion von rohrzucker durch säuren," *Zeitschrift für physikalische Chemie*, vol. 4, pp. 226–248, 1889.

[7] Arsenlis, A., Wirth, B., and Rhee, M., "Dislocation density-based constitutive model for the mechanical behaviour of irradiated cu," *Philosophical Magazine*, vol. 84, no. 34, pp. 3617–3635, 2004.

[8] Averback, R., "Atomic displacement processes in irradiated metals," *Journal of nuclear materials*, vol. 216, pp. 49–62, 1994.

[9] Azevedo, C., "Selection of fuel cladding material for nuclear fission reactors," *Engineering Failure Analysis*, vol. 18, no. 8, pp. 1943–1962, 2011.

[10] Bacon, D. J., Osetsky, Y. N., Stoller, R., and Voskoboinikov, R. E., "Md description of damage production in displacement cascades in copper and α-iron," *Journal of nuclear materials*, vol. 323, no. 2, pp. 152–162, 2003.

[11] Bacon, D. J., Osetsky, Y. N., and Rong, Z., "Computer simulation of reactions between an edge dislocation and glissile self-interstitial clusters in iron," *Philosophical Magazine*, vol. 86, no. 25-26, pp. 3921–3936, 2006.

[12] Bacon, D., Gao, F., and Osetsky, Y. N., "The primary damage state in fcc, bcc and hcp metals as seen in molecular dynamics simulations," *Journal of Nuclear Materials*, vol. 276, no. 1, pp. 1–12, 2000.

[13] Bacon, D., Kocks, U., and Scattergood, R., "The effect of dislocation self-interaction on the orowan stress," *Philosophical Magazine*, vol. 28, no. 6, pp. 1241–1263, 1973.

[14] Bacon, D., Osetsky, Y., and Rodney, D., "Dislocation–obstacle interactions at the atomic level," *Dislocations in solids*, vol. 15, pp. 1–90, 2009.

[15] Bai, X.-M., Voter, A. F., Hoagland, R. G., Nastasi, M., and Uberuaga, B. P., "Efficient annealing of radiation damage near grain boundaries via interstitial emission," *Science*, vol. 327, no. 5973, pp. 1631–1634, 2010.

[16] Balluffi, R. and Mehl, R., "Grain boundary diffusion mechanisms in metals," *Metallurgical transactions a*, vol. 13, no. 12, pp. 2069–2095, 1982.

[17] Barbu*, A., Becquart, C., Bocquet, J., Dalla Torre, J., and Domain, C., "Comparison between three complementary approaches to simulate largefluence irradiation: application to electron irradiation of thin foils," *Philosophical Magazine*, vol. 85, no. 4-7, pp. 541–547, 2005.

[18] Barbu, A. and Martin, G., "Radiation induced precipitation in nickel silicon solid solutions: Dose rate effects," *Scripta Metallurgica*, vol. 11, no. 9, pp. 771–775, 1977.

[19] Barnes, R. and Mazey, D., "The migration and coalescence of inert gas bubbles in metals," *Proceedings of the Royal Society of London. Series A. Mathematical and Physical Sciences*, vol. 275, no. 1360, pp. 47–57, 1963.

[20] Bartel, T., Dingreville, R., Robbins, J., Lusk, M., Zhang, L., and Brewer, L., "impale - material point arbitrary lagrangian eulerian code: A time implicit/explicit integration 3-d lagrangian material point method code," Tech. Rep. SAND2012-0957, Sandia National Laboratories, 2012.

[21] Barton, N. R., Arsenlis, A., and Marian, J., "A polycrystal plasticity model of strain localization in irradiated iron," *Journal of the Mechanics and Physics of Solids*, vol. 61, no. 2, pp. 341–351, 2013.

[22] Becquart, C. S., Barbu, A., Bocquet, J., Caturla, M., Domain, C., Fu, C.-C., Golubov, S., Hou, M., Malerba, L., Ortiz, C., and others, "Modeling the long-term evolution of the primary damage in ferritic alloys using coarse-grained methods," *Journal of nuclear materials*, vol. 406, no. 1, pp. 39–54, 2010.

[23] Becquart, C. and Domain, C., "An object kinetic monte carlo simulation of the dynamics of helium and point defects in tungsten," *Journal of Nuclear Materials*, vol. 385, no. 2, pp. 223–227, 2009.

[24] Bergner, F., Pareige, C., Hernández-Mayoral, M., Malerba, L., and Heintze, C., "Application of a three-feature dispersed-barrier hardening model to neutron-irradiated fe–cr model alloys," *Journal of Nuclear Materials*, vol. 448, no. 1, pp. 96–102, 2014.

[25] Beyerlein, I., Caro, A., Demkowicz, M., Mara, N., Misra, A., and Uberuaga, B., "Radiation damage tolerant nanomaterials," *Materials today*, vol. 16, no. 11, pp. 443–449, 2013.

[26] Blewitt, T., Coltman, R., Jamison, R., and Redman, J., "Radiation hardening of copper single crystals," *Journal of Nuclear Materials*, vol. 2, no. 4, pp. 277–298, 1960.

[27] Bolt, H., Barabash, V., Krauss, W., Linke, J., Neu, R., Suzuki, S., Yoshida, N., and Team, A. U., "Materials for the plasma-facing components of fusion reactors," *Journal of Nuclear materials*, vol. 329, pp. 66–73, 2004.

[28] Borodin, V. and Vladimirov, P., "Diffusion coefficients and thermal stability of small helium–vacancy clusters in iron," *Journal of nuclear materials*, vol. 362, no. 2, pp. 161–166, 2007.

[29] Brailsford, A. and Bullough, R., "The rate theory of swelling due to void growth in irradiated metals," *Journal of Nuclear Materials*, vol. 44, no. 2, pp. 121–135, 1972.

[30] Brailsford, A. and Bullough, R., "The theory of sink strengths," *Philosophical Transactions of the Royal Society of London. Series A, Mathematical and Physical Sciences*, vol. 302, no. 1465, pp. 87–137, 1981.

[31] Brimbal, D., Décamps, B., Henry, J., Meslin, E., and Barbu, A., "Single-and dual-beam in situ irradiations of high-purity iron in a transmission electron microscope: Effects of heavy ion irradiation and helium injection," *Acta Materialia*, vol. 64, pp. 391–401, 2014.

[32] Brimbal, D., Meslin, E., Henry, J., Décamps, B., and Barbu, A., "He and cr effects on radiation damage formation in ion-irradiated pure iron and fe–5.40 wt.% cr: A transmission electron microscopy study," *Acta Materialia*, vol. 61, no. 13, pp. 4757–4764, 2013.

[33] Bringa, E., Monk, J., Caro, A., Misra, A., Zepeda-Ruiz, L., Duchaineau, M., Abraham, F., Nastasi, M., Picraux, S., Wang, Y., and others, "Are nanoporous materials radiation resistant?," *Nano letters*, vol. 12, no. 7, pp. 3351–3355, 2011.

[34] Brinkman, J. A., "On the nature of radiation damage in metals," *Journal of Applied Physics*, vol. 25, no. 8, pp. 961–970, 1954.

[35] Budylkin, N. I., Mironova, E. G., Chernov, V., Krasnoselov, V., Porollo, S., and Garner, F. A., "Neutron-induced swelling and embrittlement of pure iron and pure nickel irradiated in the bn-350 and bor-60 fast reactors," *Journal of Nuclear Materials*, vol. 375, no. 3, pp. 359–364, 2008.

[36] Bullough, R., Eyre, B., and Krishan, K., "Cascade damage effects on the swelling of irradiated materials," *Proceedings of the Royal Society of London. A. Mathematical and Physical Sciences*, vol. 346, no. 1644, pp. 81–102, 1975.

[37] Buswell, J., Phythian, W., McElroy, R., Dumbill, S., Ray, P., Mace, J., and Sinclair, R., "Irradiation-induced microstructural changes, and hardening mechanisms, in model pwr reactor pressure vessel steels," *Journal of nuclear materials*, vol. 225, pp. 196–214, 1995.

[38] Byun, T. and Farrell, K., "Irradiation hardening behavior of polycrystalline metals after low temperature irradiation," *Journal of nuclear materials*, vol. 326, no. 2, pp. 86–96, 2004.

[39] Caturla, M., Soneda, N., Alonso, E., Wirth, B., de la Rubia, T. D., and Perlado, J., "Comparative study of radiation damage accumulation in cu and fe," *Journal of nuclear materials*, vol. 276, no. 1, pp. 13–21, 2000.

[40] Cawthorne, C. and Fulton, E., "Voids in irradiated stainless steel," *Nature*, vol. 216, pp. 575–576, 1967.

[41] Cooper, H., Koehler, J., and Marx, J., "Irradiation effects in cu, ag, and au near 10 k," *Physical Review*, vol. 97, no. 3, p. 599, 1955.

[42] Corbett, J., Smith, R., and Walker, R., "Recovery of electron-irradiated copper. ii. interstitial migration," *Physical Review*, vol. 114, no. 6, p. 1460, 1959.

[43] Cottrell, G., "Void migration, coalescence and swelling in fusion materials," *Fusion engineering and design*, vol. 66, pp. 253–257, 2003.

[44] Dalla Torre, J., Fu, C.-C., Willaime, F., Barbu, A., and Bocquet, J.-L., "Resistivity recovery simulations of electron-irradiated iron: Kinetic monte carlo versus cluster dynamics," *Journal of nuclear materials*, vol. 352, no. 1, pp. 42–49, 2006.

[45] Daw, M. S., Foiles, S. M., and Baskes, M. I., "The embedded-atom method: a review of theory and applications," *Materials Science Reports*, vol. 9, no. 7, pp. 251–310, 1993.

[46] De La Rubia, T. D. and Guinan, M., "New mechanism of defect production in metals: A molecular-dynamics study of interstitial-dislocation-loop formation in high-energy displacement cascades," *Physical review letters*, vol. 66, no. 21, p. 2766, 1991.

[47] Demkowicz, M. J., Anderoglu, O., Zhang, X., and Misra, A., "The influence of 3 twin boundaries on the formation of radiation-induced defect clusters in nanotwinned cu," *Journal of Materials Research*, vol. 26, no. 14, pp. 1666–1675, 2011.

[48] Demkowicz, M., Bellon, P., and Wirth, B., "Atomic-scale design of radiation-tolerant nanocomposites," *MRS bulletin*, vol. 35, no. 12, pp. 992–998, 2010.

[49] Demkowicz, M., Bhattacharyya, D., Usov, I., Wang, Y., Nastasi, M., and Misra, A., "The effect of excess atomic volume on he bubble formation at fcc–bcc interfaces," *Applied Physics Letters*, vol. 97, no. 16, pp. 161903–161903, 2010.

[50] Demkowicz, M., Hoagland, R., and Hirth, J., "Interface structure and radiation damage resistance in cu-nb multilayer nanocomposites," *Physical review letters*, vol. 100, no. 13, p. 136102, 2008.

[51] Demkowicz, M., Misra, A., and Caro, A., "The role of interface structure in controlling high helium concentrations," *Current opinion in solid state and materials science*, vol. 16, no. 3, pp. 101–108, 2012.

[52] Demkowicz, M., Wang, Y., Hoagland, R., and Anderoglu, O., "Mechanisms of he escape during implantation in cunb multilayer composites," *Nuclear Instruments and Methods in Physics Research Section B: Beam Interactions with Materials and Atoms*, vol. 261, no. 1, pp. 524–528, 2007.

[53] Deo, C., Tomé, C., Lebensohn, R., and Maloy, S., "Modeling and simulation of irradiation hardening in structural ferritic steels for advanced nuclear reactors," *Journal of Nuclear Materials*, vol. 377, no. 1, pp. 136–140, 2008.

[54] Dierckx, R., "The importance of the pka-energy spectrum for radiation damage simulation," *Journal of Nuclear Materials*, vol. 144, no. 3, pp. 214–227, 1987.

[55] Doan, N. and Martin, G., "Elimination of irradiation point defects in crystalline solids: Sink strengths," *Physical Review B*, vol. 67, no. 13, p. 134107, 2003.

[56] Dollar, M. and Gleiter, H., "Point defect annihilation at grain boundaries in gold," *Scripta metallurgica*, vol. 19, no. 4, pp. 481–484, 1985.

[57] Domain, C., Becquart, C., and Malerba, L., "Simulation of radiation damage in fe alloys: an object kinetic monte carlo approach," *Journal of Nuclear Materials*, vol. 335, no. 1, pp. 121–145, 2004.

[58] Dudarev, S., Semenov, A., and Woo, C., "Heterogeneous void swelling near grain boundaries in irradiated materials," *Physical Review B*, vol. 67, no. 9, p. 094103, 2003.

[59] Dunn, A., Agudo-Merida, L., Martin-Bragado, I., McPhie, M., Cherkaoui, M., and Capolungo, L., "A novel method for computing effective diffusivity: Application to helium implanted α-fe thin films," *Journal of Nuclear Materials*, vol. 448, no. 1, pp. 195–205, 2014.

[60] Dunn, A. and Capolungo, L., "Simulating radiation damage accumulation in α-fe: A spatially resolved stochastic cluster dynamics approach," *Computational Materials Science*, vol. 102, pp. 314–326, 2015.

[61] Dunn, A., Dingreville, R., and Capolungo, L., "Multi-scale simulation of radiation damage accumulation and subsequent hardening in neutron-irradiated α-fe," *Modelling and Simulation in Materials Science and Engineering*, p. (in review), 2015.

[62] Dunn, A., Dingreville, R., Martnez, E., and Capolungo, L., "Synchronous parallel spatially resolved stochastic cluster dynamics," *Journal of Computational Physics*, p. (submitted), 2015.

[63] Dunn, A. Y., Capolungo, L., Martinez, E., and Cherkaoui, M., "Spatially resolved stochastic cluster dynamics for radiation damage evolution in nanostructured metals," *Journal of nuclear materials*, vol. 443, no. 1, pp. 128–139, 2013.

[64] Dunn, A., McPhie, M., Capolungo, L., Martinez, E., and Cherkaoui, M., "A rate theory study of helium bubble formation and retention in cu–nb nanocomposites," *Journal of Nuclear Materials*, vol. 435, no. 1, pp. 141–152, 2013.

[65] Dutta, A., Bhattacharya, M., Gayathri, N., Das, G., and Barat, P., "The mechanism of climb in dislocation–nanovoid interaction," *Acta Materialia*, vol. 60, no. 9, pp. 3789–3798, 2012.

[66] Ehrlich, K., Bloom, E., and Kondo, T., "International strategy for fusion materials development," *Journal of Nuclear Materials*, vol. 283, pp. 79–88, 2000.

[67] Eldrup, M., Singh, B., Zinkle, S., Byun, T., and Farrell, K., "Dose dependence of defect accumulation in neutron irradiated copper and iron," *Journal of nuclear materials*, vol. 307, pp. 912–917, 2002.

[68] Eyre, B., "Transmission electron microscope studies of point defect clusters in fcc and bcc metals," *Journal of Physics F: Metal Physics*, vol. 3, no. 2, p. 422, 1973.

[69] Fabritsiev, S. and Pokrovsky, A., "Effect of irradiation temperature and dose on radiation hardening of some pure metals," *Journal of Nuclear Materials*, vol. 417, no. 1, pp. 940–943, 2011.

[70] Faulkner, R., Song, S., Flewitt, P., Victoria, M., and Marmy, P., "Grain boundary segregation under neutron irradiation in dilute alloys," *Journal of nuclear materials*, vol. 255, no. 2, pp. 189–209, 1998.

[71] Foreman, A. and Singh, B. N., "Gas diffusion and temperature dependence of bubble nucleation during irradiation," *Journal of Nuclear Materials*, vol. 141, pp. 672–676, 1986.

[72] Friedel, J., "Cxxx. on the linear work hardening mate of face-centred cubic single crystals," *The London, Edinburgh, and Dublin Philosophical Magazine and Journal of Science*, vol. 46, no. 382, pp. 1169–1186, 1955.

[73] Frost, B., "Radiation damage in fast-breeder and fusion reactors," *Nuclear Science, IEEE Transactions on*, vol. 19, no. 6, pp. 230–236, 1972.

[74] Fu, C.-C., Dalla Torre, J., Willaime, F., Bocquet, J.-L., and Barbu, A., "Multiscale modelling of defect kinetics in irradiated iron," *Nature materials*, vol. 4, no. 1, pp. 68–74, 2005.

[75] Fu, C.-C. and Willaime, F., "Ab initio study of helium in α-fe: dissolution, migration, and clustering with vacancies," *Physical Review B*, vol. 72, no. 6, p. 064117, 2005.

[76] Fu, E., Caro, M., Zepeda-Ruiz, L., Wang, Y., Baldwin, K., Bringa, E., Nastasi, M., and Caro, A., "Surface effects on the radiation response of nanoporous au foams," *Applied Physics Letters*, vol. 101, no. 19, p. 191607, 2012.

[77] Fu, E., Misra, A., Wang, H., Shao, L., and Zhang, X., "Interface enabled defects reduction in helium ion irradiated cu/v nanolayers," *Journal of Nuclear Materials*, vol. 407, no. 3, pp. 178–188, 2010.

[78] Fujita, F. and Damas, A., "Kinetics of carbon precipitation in irradiated ironii electrical resistivity measurements," *Acta metallurgica*, vol. 12, no. 4, pp. 331–339, 1964.

[79] Gao, F., Bacon, D., Flewitt, P., and Lewis, T., "A molecular dynamics study of temperature effects on defect production by displacement cascades in α-iron," *Journal of nuclear materials*, vol. 249, no. 1, pp. 77–86, 1997.

[80] Gao, F., Heinisch, H. L., and Kurtz, R. J., "Migration of vacancies, he interstitials and he-vacancy clusters at grain boundaries in α-fe," *Journal of Nuclear Materials*, vol. 386, pp. 390–394, 2009.

[81] Ghoniem, N., Sharafat, S., Williams, J., and Mansur, L., "Theory of helium transport and clustering in materials under irradiation," *Journal of Nuclear Materials*, vol. 117, pp. 96–105, 1983.

[82] Gilbert, M., Dudarev, S., Derlet, P., and Pettifor, D., "Structure and metastability of mesoscopic vacancy and interstitial loop defects in iron and tungsten," *Journal of Physics: Condensed Matter*, vol. 20, no. 34, p. 345214, 2008.

[83] Gillespie, D. T., "A general method for numerically simulating the stochastic time evolution of coupled chemical reactions," *Journal of computational physics*, vol. 22, no. 4, pp. 403–434, 1976.

[84] Gokhman, A., Caturla, M., and Bergner, F., "Damage accumulation in pure iron and high concentrated fe–12.5 at% cr alloy: comparison between object kinetic monte carlo and cluster dynamics," *Radiation Effects and Defects in Solids*, vol. 169, no. 3, pp. 185–193, 2014.

[85] Golubov, S., Ovcharenko, A., Barashev, A., and Singh, B., "Grouping method for the approximate solution of a kinetic equation describing the evolution of point-defect clusters," *Philosophical Magazine A*, vol. 81, no. 3, pp. 643–658, 2001.

[86] González, C., Fernández-Pello, D., Cerdeira, M., Palacios, S., and Iglesias, R., "Helium bubble clustering in copper from first principles," *Modelling and Simulation in Materials Science and Engineering*, vol. 22, no. 3, p. 035019, 2014.

[87] González, C. and Iglesias, R., "Migration mechanisms of helium in copper and tungsten," *Journal of Materials Science*, vol. 49, no. 23, pp. 8127–8139, 2014.

[88] Guenthner, W. R., Reiners, P. W., Ketcham, R. A., Nasdala, L., and Giester, G., "Helium diffusion in natural zircon: Radiation damage, anisotropy, and the interpretation of zircon (u-th)/he thermochronology," *American Journal of Science*, vol. 313, no. 3, pp. 145–198, 2013.

[89] Haghighat, S. H., Fivel, M., Fikar, J., and Schaeublin, R., "Dislocation–void interaction in fe: A comparison between molecular dynamics and dislocation dynamics," *Journal of Nuclear Materials*, vol. 386, pp. 102–105, 2009.

[90] Han, W., Demkowicz, M., Fu, E., Wang, Y., and Misra, A., "Effect of grain boundary character on sink efficiency," *Acta materialia*, vol. 60, no. 18, pp. 6341–6351, 2012.

[91] Hattar, K., Demkowicz, M., Misra, A., Robertson, I., and Hoagland, R., "Arrest of he bubble growth in cu–nb multilayer nanocomposites," *Scripta Materialia*, vol. 58, no. 7, pp. 541–544, 2008.

[92] Hattar, K., Bufford, D. C., and Buller, D. L., "Concurrent in situ ion irradiation transmission electron microscope," *Nuclear Instruments and Methods in Physics Research Section B: Beam Interactions with Materials and Atoms*, vol. 338, pp. 56–65, 2014.

[93] Havner, K. S., "The theoretical behavior of a polycrystalline solid as related to certain general concepts of continuum plasticity," *International Journal of Solids and Structures*, vol. 5, no. 3, pp. 215–226, 1969.

[94] Heinisch, H., Gao, F., and Kurtz, R., "Atomistic modeling of helium interacting with screw dislocations in α-fe," *Journal of Nuclear Materials*, vol. 367, pp. 311–315, 2007.

[95] Heinisch, H. L., Gao, F., and Kurtz, R. J., "Atomic-scale modeling of interactions of helium, vacancies and helium–vacancy clusters with screw dislocations in alpha-iron," *Philosophical Magazine*, vol. 90, no. 7-8, pp. 885–895, 2010.

[96] Heinisch, H. L., Gao, F., Kurtz, R. J., and Le, E., "Interaction of helium atoms with edge dislocations in α-fe," *Journal of nuclear materials*, vol. 351, no. 1, pp. 141–148, 2006.

[97] Hernández-Mayoral, M. and Gómez-Briceño, D., "Transmission electron microscopy study on neutron irradiated pure iron and rpv model alloys," *Journal of Nuclear Materials*, vol. 399, no. 2, pp. 146–153, 2010.

[98] Höchbauer, T., Misra, A., Hattar, K., and Hoagland, R., "Influence of interfaces on the storage of ion-implanted he in multilayered metallic composites," *Journal of applied physics*, vol. 98, no. 12, p. 123516, 2005.

[99] Hudson, T. S., Dudarev, S. L., and Sutton, A. P., "Confinement of interstitial cluster diffusion by oversized solute atoms," in *Proceedings of the Royal Society of London A: Mathematical, Physical and Engineering Sciences*, vol. 460, pp. 2457–2475, The Royal Society, 2004.

[100] ITER, "The iter tokamak." `http://www.iter.org/album/Media/7%20-%20Technical`, 2015.

[101] Jansson, V. and Malerba, L., "Simulation of the nanostructure evolution under irradiation in fe–c alloys," *Journal of Nuclear Materials*, vol. 443, no. 1, pp. 274–285, 2013.

[102] Jansson, V. and Malerba, L., "Okmc simulations of fe–c systems under irradiation: Sensitivity studies," *Journal of Nuclear Materials*, vol. 452, no. 1, pp. 118–124, 2014.

[103] Johnson, R., "Interstitials and vacancies in α iron," *Physical Review*, vol. 134, no. 5A, p. A1329, 1964.

[104] Jolliffe, I., *Principal component analysis*. Wiley Online Library, 2002.

[105] Jourdan, T. and Crocombette, J.-P., "Rate theory cluster dynamics simulations including spatial correlations within displacement cascades," *Physical Review B*, vol. 86, no. 5, p. 054113, 2012.

[106] Kato, T., Takahashi, H., and Izumiya, M., "Grain boundary segregation under electron irradiation in austenitic stainless steels modified with oversized elements," *Journal of nuclear materials*, vol. 189, no. 2, pp. 167–174, 1992.

[107] Katz, J. L. and Wiedersich, H., "Nucleation of voids in materials supersaturated with vacancies and interstitials," *The Journal of Chemical Physics*, vol. 55, no. 3, pp. 1414–1425, 1971.

[108] Kesternich, W., Schwahn, D., and Ullmaier, H., "Sizes of he bubbles in bulk grain boundaries and region near the surface of nickel," *Scripta metallurgica*, vol. 18, no. 9, pp. 1011–1016, 1984.

[109] Kinchin, G. and Pease, R., "The displacement of atoms in solids by radiation," *Reports on progress in physics*, vol. 18, no. 1, p. 1, 1955.

[110] Kiritani, M., "Story of stacking fault tetrahedra," *Materials chemistry and physics*, vol. 50, no. 2, pp. 133–138, 1997.

[111] Kiritani, M., "Similarity and difference between fcc, bcc and hcp metals from the view point of point defect cluster formation," *Journal of nuclear materials*, vol. 276, no. 1, pp. 41–49, 2000.

[112] Klueh, R., Ehrlich, K., and Abe, F., "Ferritic/martensitic steels: promises and problems," *Journal of nuclear materials*, vol. 191, pp. 116–124, 1992.

[113] Koester, A., Ma, A., and Hartmaier, A., "Atomistically informed crystal plasticity model for body-centered cubic iron," *Acta Materialia*, vol. 60, no. 9, pp. 3894–3901, 2012.

[114] Kohyama, A., Katoh, Y., Ando, M., and Jimbo, K., "A new multiple beams–material interaction research facility for radiation damage studies in fusion materials," *Fusion engineering and design*, vol. 51, pp. 789–795, 2000.

[115] Kroupa, F. and Hirsch, P., "Elastic interaction between prismatic dislocation loops and straight dislocations," *Discussions of the Faraday Society*, vol. 38, pp. 49–55, 1964.

[116] Kulcinski, G., Doran, D., and Abdou, M., "Comparison of displacement and gas production rates in current fission and future fusion reactors," *Properties of Reactor Structural Alloys after Neutron or Particle Irradiation, ASTM STP*, vol. 570, pp. 329–351, 1976.

[117] Kulcinski, G. L., Laidler, J., and Doran, D., "Simulation of high fluence fast neutron damage with heavy ion bombardment," *Radiation Effects*, vol. 7, no. 3-4, pp. 195–202, 1971.

[118] Kurishita, H., Kobayashi, S., Nakai, K., Ogawa, T., Hasegawa, A., Abe, K., Arakawa, H., Matsuo, S., Takida, T., Takebe, K., and others, "Development of ultra-fine grained w–(0.25–0.8) wt% tic and its superior resistance to neutron and 3mev he-ion irradiations," *Journal of Nuclear Materials*, vol. 377, no. 1, pp. 34–40, 2008.

[119] Kurtz, T. G., "The relationship between stochastic and deterministic models for chemical reactions," *The Journal of Chemical Physics*, vol. 57, no. 7, pp. 2976–2978, 1972.

[120] Kwok, T., Ho, P. S., and Yip, S., "Molecular-dynamics studies of grain-boundary diffusion. ii. vacancy migration, diffusion mechanism, and kinetics," *Physical Review B*, vol. 29, no. 10, p. 5363, 1984.

[121] Kwon, J., Kwon, S. C., and Hong, J.-H., "Prediction of radiation hardening in reactor pressure vessel steel based on a theoretical model," *Annals of Nuclear Energy*, vol. 30, no. 15, pp. 1549–1559, 2003.

[122] Lewis, M., Packan, N., Wells, G., and Buhl, R., "Improved techniques for heavy-ion simulation of neutron radiation damage," *Nuclear Instruments and Methods*, vol. 167, no. 2, pp. 233–247, 1979.

[123] Li, M., Kirk, M., Baldo, P., Xu, D., and Wirth, B., "Study of defect evolution by tem with in situ ion irradiation and coordinated modeling," *Philosophical Magazine*, vol. 92, no. 16, pp. 2048–2078, 2012.

[124] Li, Y., Zhou, W., Huang, L., Zeng, Z., and Ju, X., "Cluster dynamics modeling of accumulation and diffusion of helium in neutron irradiated tungsten," *Journal of Nuclear Materials*, vol. 431, no. 1, pp. 26–32, 2012.

[125] Lucas, G., "The evolution of mechanical property change in irradiated austenitic stainless steels," *Journal of Nuclear Materials*, vol. 206, no. 2, pp. 287–305, 1993.

[126] Makin, M. and Minter, F., "Irradiation hardening in copper and nickel," *Acta Metallurgica*, vol. 8, no. 10, pp. 691–699, 1960.

[127] Malerba, L., Becquart, C. S., and Domain, C., "Object kinetic monte carlo study of sink strengths," *Journal of nuclear materials*, vol. 360, no. 2, pp. 159–169, 2007.

[128] Malerba, L., Marinica, M., Anento, N., Björkas, C., Nguyen, H., Domain, C., Djurabekova, F., Olsson, P., Nordlund, K., Serra, A., and others, "Comparison of empirical interatomic potentials for iron applied to radiation damage studies," *Journal of Nuclear Materials*, vol. 406, no. 1, pp. 19–38, 2010.

[129] Mansur, L., "Correlation of neutron and heavy-ion damage: Ii. the predicted temperature shift if swelling with changes in radiation dose rate," *Journal of Nuclear Materials*, vol. 78, no. 1, pp. 156–160, 1978.

[130] Mansur, L., "Theory and experimental background on dimensional changes in irradiated alloys," *Journal of Nuclear Materials*, vol. 216, pp. 97–123, 1994.

[131] Marian, J. and Bulatov, V. V., "Stochastic cluster dynamics method for simulations of multispecies irradiation damage accumulation," *Journal of Nuclear Materials*, vol. 415, no. 1, pp. 84–95, 2011.

[132] Marian, J., Wirth, B. D., Schäublin, R., Odette, G., and Perlado, J. M., "Md modeling of defects in fe and their interactions," *Journal of nuclear materials*, vol. 323, no. 2, pp. 181–191, 2003.

[133] Marques, J., "Evolution of nuclear fission reactors: Third generation and beyond," *Energy conversion and management*, vol. 51, no. 9, pp. 1774–1780, 2010.

[134] Martin-Bragado, I., Abujas, J., Galindo, P., and Pizarro, J., "Synchronous parallel kinetic monte carlo: Implementation and results for object and lattice approaches," *Nuclear Instruments and Methods in Physics Research Section B: Beam Interactions with Materials and Atoms*, vol. 352, pp. 27–30, 2015.

[135] Martin-Bragado, I., Rivera, A., Valles, G., Gomez-Selles, J. L., and Caturla, M. J., "Mmonca: An object kinetic monte carlo simulator for damage irradiation evolution and defect diffusion," *Computer Physics Communications*, vol. 184, no. 12, pp. 2703–2710, 2013.

[136] Martínez, E., Marian, J., Kalos, M. H., and Perlado, J. M., "Synchronous parallel kinetic monte carlo for continuum diffusion-reaction systems," *Journal of Computational Physics*, vol. 227, no. 8, pp. 3804–3823, 2008.

[137] Martínez, E., Monasterio, P. R., and Marian, J., "Billion-atom synchronous parallel kinetic monte carlo simulations of critical 3d ising systems," *Journal of Computational Physics*, vol. 230, no. 4, pp. 1359–1369, 2011.

[138] Marwick, A., "The primary recoil spectrum in the simulation of fast-reactor radiation damage by charged-particle bombardment," *Journal of Nuclear Materials*, vol. 55, no. 3, pp. 259–266, 1975.

[139] Mascitti, J. and Madariaga, M., "Method for the calculation of dpa in the reactor pressure vessel of atucha ii," *Science and Technology of Nuclear Installations*, vol. 2011, 2011.

[140] McPhie, M., Capolungo, L., Dunn, A., and Cherkaoui, M., "Interfacial trapping mechanism of he in cu–nb multilayer materials," *Journal of Nuclear Materials*, vol. 437, no. 1, pp. 222–228, 2013.

[141] McRickard, S. and Chow, J., "The effect of interstitial impurities on radiation hardening and embrittlement in iron," *Acta Metallurgica*, vol. 14, no. 10, pp. 1195–1200, 1966.

[142] Meslin, E., Barbu, A., Boulanger, L., Radiguet, B., Pareige, P., Arakawa, K., and Fu, C., "Cluster-dynamics modelling of defects in α-iron under cascade damage conditions," *Journal of Nuclear Materials*, vol. 382, no. 2, pp. 190–196, 2008.

[143] Meslin, E., Lambrecht, M., Hernández-Mayoral, M., Bergner, F., Malerba, L., Pareige, P., Radiguet, B., Barbu, A., Gómez-Briceño, D., Ulbricht, A., and others, "Characterization of neutron-irradiated ferritic model alloys and a rpv steel from combined apt, sans, tem and pas analyses," *Journal of Nuclear Materials*, vol. 406, no. 1, pp. 73–83, 2010.

[144] Misra, A., Demkowicz, M., Zhang, X., and Hoagland, R., "The radiation damage tolerance of ultra-high strength nanolayered composites," *Jom*, vol. 59, no. 9, pp. 62–65, 2007.

[145] Morishita, K., Sugano, R., Wirth, B. D., and de La Rubia, T. D., "Thermal stability of helium–vacancy clusters in iron," *Nuclear Instruments and Methods in Physics Research Section B: Beam Interactions with Materials and Atoms*, vol. 202, pp. 76–81, 2003.

[146] Mota, F., Vila, R., Ortiz, C., Garcia, A., Casal, N., Ibarra, A., Rapisarda, D., and Queral, V., "Analysis of displacement damage in materials in nuclear fusion facilities (demo, ifmif and technofusion)," *Fusion Engineering and Design*, vol. 86, no. 9, pp. 2425–2428, 2011.

[147] Muroga, T., Watanabe, H., and Yoshida, N., "Correlation of fast neutron, fusion neutron and electron irradiations based on the dislocation loop density," *Journal of nuclear materials*, vol. 174, no. 2, pp. 282–288, 1990.

[148] Nelson, R., Mazey, D., and Hudson, J., "The use of ion accelerators to simulate fast neutron-induced voidage in metals," *Journal of Nuclear Materials*, vol. 37, no. 1, pp. 1–12, 1970.

[149] Nguyen-Manh, D., Horsfield, A., and Dudarev, S., "Self-interstitial atom defects in bcc transition metals: Group-specific trends," *Physical Review B*, vol. 73, no. 2, p. 020101, 2006.

[150] Nogaret, T., Rodney, D., Fivel, M., and Robertson, C., "Clear band formation simulated by dislocation dynamics: Role of helical turns and pile-ups," *Journal of Nuclear Materials*, vol. 380, no. 1, pp. 22–29, 2008.

[151] Nordlund, K., Wallenius, J., and Malerba, L., "Molecular dynamics simulations of threshold displacement energies in fe," *Nuclear Instruments and Methods in Physics Research Section B: Beam Interactions with Materials and Atoms*, vol. 246, no. 2, pp. 322–332, 2006.

[152] Norgett, M., Robinson, M., and Torrens, I., "A proposed method of calculating displacement dose rates," *Nuclear Engineering and Design*, vol. 33, no. 1, pp. 50–54, 1975.

[153] Odette, G., "On the dominant mechanism of irradiation embrittlement of reactor pressure vessel steels," *Scripta metallurgica*, vol. 17, no. 10, pp. 1183–1188, 1983.

[154] Odette, G., Alinger, M., and Wirth, B., "Recent developments in irradiation-resistant steels," *Annu. Rev. Mater. Res.*, vol. 38, pp. 471–503, 2008.

[155] Odette, G. and Frey, D., "Development of mechanical property correlation methodology for fusion environments," *Journal of Nuclear Materials*, vol. 85, pp. 817–822, 1979.

[156] Odette, G. and Lucas, G., "Embrittlement of nuclear reactor pressure vessels," *Jom*, vol. 53, no. 7, pp. 18–22, 2001.

[157] Olander, D. R., "Fundamental aspects of nuclear reactor fuel elements," tech. rep., California Univ., Berkeley (USA). Dept. of Nuclear Engineering, 1976.

[158] Onimus, F. and Béchade, J.-L., "A polycrystalline modeling of the mechanical behavior of neutron irradiated zirconium alloys," *Journal of Nuclear Materials*, vol. 384, no. 2, pp. 163–174, 2009.

[159] Oppenheim, I., Shuler, K., and Weiss, G., "Stochastic and deterministic formulation of chemical rate equations," *The Journal of Chemical Physics*, vol. 50, no. 1, pp. 460–466, 1969.

[160] Opplestrup, T., Bulatov, V. V., Gilmer, G. H., Kalos, M. H., and Sadigh, B., "First-passage monte carlo algorithm: diffusion without all the hops," *Physical review letters*, vol. 97, no. 23, p. 230602, 2006.

[161] Ortiz, C. and Caturla, M., "Simulation of defect evolution in irradiated materials: role of intracascade clustering and correlated recombination," *Physical Review B*, vol. 75, no. 18, p. 184101, 2007.

[162] Ortiz, C., Caturla, M., Fu, C., and Willaime, F., "He diffusion in irradiated α-fe: An ab-initio-based rate theory model," *Physical Review B*, vol. 75, no. 10, p. 100102, 2007.

[163] Ortiz, C., Caturla, M., Fu, C., and Willaime, F., "Influence of carbon on the kinetics of he migration and clustering in α-fe from first principles," *Physical Review B*, vol. 80, no. 13, p. 134109, 2009.

[164] Osetsky, Y. N. and Bacon, D. J., "Atomic-scale mechanisms of void hardening in bcc and fcc metals," *Philosophical magazine*, vol. 90, no. 7-8, pp. 945–961, 2010.

[165] Osetsky, Y. N. and Bacon, D., "Defect cluster formation in displacement cascades in copper," *Nuclear Instruments and Methods in Physics Research Section B: Beam Interactions with Materials and Atoms*, vol. 180, no. 1, pp. 85–90, 2001.

[166] Osetsky, Y. N., Bacon, D., Singh, B. N., and Wirth, B., "Atomistic study of the generation, interaction, accumulation and annihilation of cascade-induced defect clusters," *Journal of nuclear materials*, vol. 307, pp. 852–861, 2002.

[167] Osetsky, Y. N., Serra, A., and Priego, V., "Interactions between mobile dislocation loops in cu and α-fe," *Journal of nuclear materials*, vol. 276, no. 1, pp. 202–212, 2000.

[168] Osetsky, Y. N., Serra, A., Singh, B., and Golubov, S., "Structure and properties of clusters of self-interstitial atoms in fcc copper and bcc iron," *Philosophical Magazine A*, vol. 80, no. 9, pp. 2131–2157, 2000.

[169] Osetsky, Y. N., Bacon, D., and Mohles, V., "Atomic modelling of strengthening mechanisms due to voids and copper precipitates in α-iron," *Philosophical Magazine*, vol. 83, no. 31-34, pp. 3623–3641, 2003.

[170] Packan, N., Farrell, K., and Stiegler, J., "Correlation of neutron and heavy-ion damage: I. the influence of dose rate and injected helium on swelling in pure nickel," *Journal of Nuclear Materials*, vol. 78, no. 1, pp. 143–155, 1978.

[171] Patra, A. and McDowell, D. L., "Crystal plasticity-based constitutive modelling of irradiated bcc structures," *Philosophical Magazine*, vol. 92, no. 7, pp. 861–887, 2012.

[172] Patra, A. and McDowell, D. L., "Continuum modeling of localized deformation in irradiated bcc materials," *Journal of Nuclear Materials*, vol. 432, no. 1, pp. 414–427, 2013.

[173] Philipps, V., Sonnenberg, K., and Williams, J., "Diffusion of helium in nickel," *Journal of Nuclear Materials*, vol. 107, no. 2, pp. 271–279, 1982.

[174] Rodney, D. and Martin, G., "Dislocation pinning by glissile interstitial loops in a nickel crystal: A molecular-dynamics study," *Physical Review B*, vol. 61, no. 13, p. 8714, 2000.

[175] Rodney, D., "Atomic-scale modeling of clear band formation in fcc metals," *Nuclear Instruments and Methods in Physics Research Section B: Beam Interactions with Materials and Atoms*, vol. 228, no. 1, pp. 100–110, 2005.

[176] Runge, E. and Gross, E. K., "Density-functional theory for time-dependent systems," *Physical Review Letters*, vol. 52, no. 12, p. 997, 1984.

[177] Russell, K. C., "Phase stability under irradiation," *Progress in Materials Science*, vol. 28, no. 3, pp. 229–434, 1984.

[178] Ryazanov, A., Braski, D., Schroeder, H., Trinkaus, H., and Ullmaier, H., "Modeling the effect of creep on the growth of helium bubbles in metals during annealing," *Journal of nuclear materials*, vol. 233, pp. 1076–1079, 1996.

[179] Ryazanov, A., Voskoboinikov, R., and Trinkaus, H., "Model for the final stage of creep failure due to high temperature helium embrittlement," *Journal of nuclear materials*, vol. 233, pp. 1085–1088, 1996.

[180] Sabochick, M. and Yip, S., "Migration energy calculations for small vacancy clusters in copper," *Journal of Physics F: Metal Physics*, vol. 18, no. 8, p. 1689, 1988.

[181] Schilling, W., Schroeder, K., and Wollenberger, H., "Three-dimensional versus crowdion migration of interstitials in annealing stage i of irradiated metals," *physica status solidi (b)*, vol. 38, no. 1, pp. 245–257, 1970.

[182] Schneider, M. and Froggatt, A., "2012–2013 world nuclear industry status report," *Bulletin of the Atomic Scientists*, vol. 70, no. 1, pp. 70–84, 2014.

[183] Schober, H. and Zeller, R., "Structure and dynamics of multiple interstitials in fcc metals," *Journal of Nuclear Materials*, vol. 69, pp. 341–349, 1978.

[184] Scott, P., "A review of irradiation assisted stress corrosion cracking," *Journal of nuclear Materials*, vol. 211, no. 2, pp. 101–122, 1994.

[185] Seeger, A. K., "Deformation of neutron-irradiated copper single crystals," *2nd UN International Conference on Peaceful Uses of Atomic Energy*, vol. 6, 1958.

[186] Serruys, Y., Ruault, M.-O., Trocellier, P., Henry, S., Kaïtasov, O., and Trouslard, P., "Multiple ion beam irradiation and implantation: Jannus project," *Nuclear Instruments and Methods in Physics Research Section B: Beam Interactions with Materials and Atoms*, vol. 240, no. 1, pp. 124–127, 2005.

[187] Shuster, D. L., Flowers, R. M., and Farley, K. A., "The influence of natural radiation damage on helium diffusion kinetics in apatite," *Earth and Planetary Science Letters*, vol. 249, no. 3, pp. 148–161, 2006.

[188] Siegel, R., Chang, S., and Balluffi, R., "Vacancy loss at grain boundaries in quenched polycrystalline gold," *Acta Metallurgica*, vol. 28, no. 3, pp. 249–257, 1980.

[189] Simo, J. C. and Hughes, T. J., *Computational inelasticity*, vol. 7. Springer Science & Business Media, 2006.

[190] Singh, B. N., Leffers, T., Green, W., and Green, S., "The effect of high rate of gas generation on the formation and spatial distribution of cavities in aluminium irradiated with 600 mev protons," *Scripta Metallurgica*, vol. 15, no. 12, pp. 1355–1358, 1981.

[191] Singh, B. N., Leffers, T., Green, W., and Victoria, M., "Nucleation of helium bubbles on dislocations, dislocation networks and dislocations in grain boundaries during 600 mev proton irradiation of aluminium," *Journal of Nuclear Materials*, vol. 125, no. 3, pp. 287–297, 1984.

[192] Singh, B., Foreman, A., and Trinkaus, H., "Radiation hardening revisited: role of intracascade clustering," *Journal of nuclear materials*, vol. 249, no. 2, pp. 103–115, 1997.

[193] Singh, B. and Trinkaus, H., "An analysis of the bubble formation behaviour under different experimental conditions," *Journal of nuclear materials*, vol. 186, no. 2, pp. 153–165, 1992.

[194] Singh, B. and Zinkle, S., "Influence of irradiation parameters on damage accumulation in metals and alloys," *Journal of nuclear materials*, vol. 217, no. 1, pp. 161–171, 1994.

[195] So, M. R., Voter, A. F., and others, "Temperature-accelerated dynamics for simulation of infrequent events," *The Journal of Chemical Physics*, vol. 112, no. 21, pp. 9599–9606, 2000.

[196] Sobie, C., Bertin, N., and Capolungo, L., "Analysis of obstacle hardening models using dislocation dynamics: Application to irradiation-induced defects," *Metallurgical and Materials Transactions A*, pp. 1–12, 2015.

[197] Soneda, N. and De La Rubia, T. D., "Defect production, annealing kinetics and damage evolution in α-fe: an atomic-scale computer simulation," *Philosophical Magazine A*, vol. 78, no. 5, pp. 995–1019, 1998.

[198] Soneda, N. and Diaz de La Rubia, T., "Migration kinetics of the self-interstitial atom and its clusters in bcc fe," *Philosophical Magazine A*, vol. 81, no. 2, pp. 331–343, 2001.

[199] Soneda, N., Ishino, S., and De la Rubia, T. D., "Vacancy loop formation by'cascade collapse'in a-fe: A molecular dynamics study of 50kev cascades," *Philosophical magazine letters*, vol. 81, no. 9, pp. 649–659, 2001.

[200] Soneda, N., Ishino, S., Takahashi, A., and Dohi, K., "Modeling the microstructural evolution in bcc-fe during irradiation using kinetic monte carlo computer simulation," *Journal of nuclear materials*, vol. 323, no. 2, pp. 169–180, 2003.

[201] Sørensen, M. R., Mishin, Y., and Voter, A. F., "Diffusion mechanisms in cu grain boundaries," *Physical Review B*, vol. 62, no. 6, p. 3658, 2000.

[202] Souidi, A., Hou, M., Becquart, C. S., Malerba, L., Domain, C., and Stoller, R. E., "On the correlation between primary damage and long-term nanostructural evolution in iron under irradiation," *Journal of nuclear materials*, vol. 419, no. 1, pp. 122–133, 2011.

[203] Stoller, R. and Calder, A., "Statistical analysis of a library of molecular dynamics cascade simulations in iron at 100 k," *Journal of nuclear materials*, vol. 283, pp. 746–752, 2000.

[204] Stoller, R., Odette, G., and Wirth, B., "Primary damage formation in bcc iron," *Journal of Nuclear Materials*, vol. 251, pp. 49–60, 1997.

[205] Stoller, R. E., "The influence of helium on microstructural evolution: Implications for dt fusion reactors," *Journal of nuclear materials*, vol. 174, no. 2, pp. 289–310, 1990.

[206] Stoller, R. E., "The role of cascade energy and temperature in primary defect formation in iron," *Journal of nuclear materials*, vol. 276, no. 1, pp. 22–32, 2000.

[207] Stoller, R. E., Golubov, S. I., Domain, C., and Becquart, C., "Mean field rate theory and object kinetic monte carlo: a comparison of kinetic models," *Journal of Nuclear Materials*, vol. 382, no. 2, pp. 77–90, 2008.

[208] Sugano, R., Morishita, K., Iwakiri, H., and Yoshida, N., "Effects of dislocation on thermal helium desorption from iron and ferritic steel," *Journal of nuclear materials*, vol. 307, pp. 941–945, 2002.

[209] Sugano, R., Morishita, K., Kimura, A., Iwakiri, H., and Yoshida, N., "Microstructural evolution in fe and fe–cr model alloys after he+ ion irradiations," *Journal of nuclear materials*, vol. 329, pp. 942–946, 2004.

[210] Sun, C., Yu, K., Lee, J., Liu, Y., Wang, H., Shao, L., Maloy, S., Hartwig, K., and Zhang, X., "Enhanced radiation tolerance of ultrafine grained fe–cr–ni alloy," *Journal of Nuclear Materials*, vol. 420, no. 1, pp. 235–240, 2012.

[211] Takaki, S., Fuss, J., Kuglers, H., Dedek, U., and Schultz, H., "The resistivity recovery of high purity and carbon doped iron following low temperature electron irradiation," *Radiation effects*, vol. 79, no. 1-4, pp. 87–122, 1983.

[212] Tanaka, T., Oka, K., Ohnuki, S., Yamashita, S., Suda, T., Watanabe, S., and Wakai, E., "Synergistic effect of helium and hydrogen for defect evolution under multi-ion irradiation of fe–cr ferritic alloys," *Journal of nuclear materials*, vol. 329, pp. 294–298, 2004.

[213] Tapasa, K., Barashev, A., Bacon, D., and Osetsky, Y. N., "Computer simulation of carbon diffusion and vacancy–carbon interaction in α-iron," *Acta materialia*, vol. 55, no. 1, pp. 1–11, 2007.

[214] Terentyev, D., Monnet, G., and Grigorev, P., "Transfer of molecular dynamics data to dislocation dynamics to assess dislocation–dislocation loop interaction in iron," *Scripta Materialia*, vol. 69, no. 8, pp. 578–581, 2013.

[215] Terentyev, D., Anento, N., Serra, A., Jansson, V., Khater, H., and Bonny, G., "Interaction of carbon with vacancy and self-interstitial atom clusters in α-iron studied using metallic–covalent interatomic potential," *Journal of Nuclear Materials*, vol. 408, no. 3, pp. 272–284, 2011.

[216] Terentyev, D., Juslin, N., Nordlund, K., and Sandberg, N., "Fast three dimensional migration of he clusters in bcc fe and fe–cr alloys," *Journal of Applied Physics*, vol. 105, no. 10, p. 103509, 2009.

[217] Terentyev, D., Malerba, L., Klaver, P., and Olsson, P., "Formation of stable sessile interstitial complexes in reactions between glissile dislocation loops in bcc fe," *Journal of Nuclear Materials*, vol. 382, no. 2, pp. 126–133, 2008.

[218] Thorsen, P., Bilde-Sørensen, J., and Singh, B., "Bubble formation at grain boundaries in helium implanted copper," *Scripta materialia*, vol. 51, no. 6, pp. 557–560, 2004.

[219] Tillack, M., Sharafat, S., Youssef, M., Herring, S., Malang, S., and Sze, D. K., "Fusion nuclear technology and materials: status and r&d needs," *Fusion engineering and design*, vol. 25, no. 1, pp. 21–34, 1994.

[220] Trinkaus, H., Heinisch, H., Barashev, A., Golubov, S., and Singh, B., "1d to 3d diffusion-reaction kinetics of defects in crystals," *Physical Review B*, vol. 66, no. 6, p. 060105, 2002.

[221] Trinkaus, H. and Singh, B., "Helium accumulation in metals during irradiation–where do we stand?," *Journal of Nuclear Materials*, vol. 323, no. 2, pp. 229–242, 2003.

[222] Trinkaus, H., Singh, B., and Foreman, A., "Mechanisms for decoration of dislocations by small dislocation loops under cascade damage conditions," *Journal of nuclear materials*, vol. 249, no. 2, pp. 91–102, 1997.

[223] Trinkaus, H., Singh, B., and Foreman, A., "Segregation of cascade induced interstitial loops at dislocations: possible effect on initiation of plastic deformation," *Journal of nuclear materials*, vol. 251, pp. 172–187, 1997.

[224] Trinkaus, H., Singh, B., and Golubov, S., "Progress in modelling the microstructural evolution in metals under cascade damage conditions," *Journal of nuclear materials*, vol. 283, pp. 89–98, 2000.

[225] Tschopp, M. A., Solanki, K., Gao, F., Sun, X., Khaleel, M. A., and Horstemeyer, M., "Probing grain boundary sink strength at the nanoscale: Energetics and length scales of vacancy and interstitial absorption by grain boundaries in α-fe," *Physical Review B*, vol. 85, no. 6, p. 064108, 2012.

[226] Uberuaga, B. P. and Andersson, D. A., "Uranium vacancy mobility at the $\sigma 5$ symmetric tilt and $\sigma 5$ twist grain boundaries in uo 2," *Computational Materials Science*, vol. 108, pp. 80–87, 2015.

[227] Uberuaga, B. P., Vernon, L. J., Martinez, E., and Voter, A. F., "The relationship between grain boundary structure, defect mobility, and grain boundary sink efficiency," *Scientific reports*, vol. 5, 2015.

[228] UK-EPR, "Fundamental safety overview." `http://www.epr-reactor.co.uk/ssmod/liblocal/docs/V3/Volume%201%20-%20Overview/1.A%20-%20EPR%20Design%20Description/1.A%20-%20EPR%20Design%20Description%20-%20v3.pdf`, 2007.

[229] Ukai, S. and Fujiwara, M., "Perspective of ods alloys application in nuclear environments," *Journal of Nuclear Materials*, vol. 307, pp. 749–757, 2002.

[230] Ullmaier, H., "The influence of helium on the bulk properties of fusion reactor structural materials," *Nuclear Fusion*, vol. 24, no. 8, p. 1039, 1984.

[231] Vassen, R., Trinkaus, H., and Jung, P., "Helium desorption from fe and v by atomic diffusion and bubble migration," *Physical Review B*, vol. 44, no. 9, p. 4206, 1991.

[232] Ventelon, L., Wirth, B., and Domain, C., "Helium–self-interstitial atom interaction in α-iron," *Journal of nuclear materials*, vol. 351, no. 1, pp. 119–132, 2006.

[233] Victoria, M., Baluc, N., Bailat, C., Dai, Y., Luppo, M., Schaublin, R., and Singh, B., "The microstructure and associated tensile properties of irradiated fcc and bcc metals," *Journal of nuclear materials*, vol. 276, no. 1, pp. 114–122, 2000.

[234] Vladimirov, P. and Bouffard, S., "Displacement damage and transmutations in metals under neutron and proton irradiation," *Comptes Rendus Physique*, vol. 9, no. 3, pp. 303–322, 2008.

[235] Voskoboinikov, R. E., Osetsky, Y. N., and Bacon, D. J., "Computer simulation of primary damage creation in displacement cascades in copper. i. defect creation and cluster statistics," *Journal of Nuclear Materials*, vol. 377, no. 2, pp. 385–395, 2008.

[236] Voter, A. F., "Parallel replica method for dynamics of infrequent events," *Physical Review B*, vol. 57, no. 22, p. R13985, 1998.

[237] Wang, L., Dodd, R., and Kulcinski, G., "Gas effects on void formation in 14 mev nickel ion irradiated pure nickel," *Journal of Nuclear Materials*, vol. 141, pp. 713–717, 1986.

[238] Ward, A. and Fisher, S., "Dislocation loop growth in pure iron under electron irradiation," *Journal of Nuclear Materials*, vol. 166, no. 3, pp. 227–234, 1989.

[239] Was, G. S., *Fundamentals of radiation materials science: metals and alloys*. Springer Science & Business Media, 2007.

[240] Wen, M., Ghoniem*, N. M., and Singh, B. N., "Dislocation decoration and raft formation in irradiated materials," *Philosophical Magazine*, vol. 85, no. 22, pp. 2561–2580, 2005.

[241] Westdorp, W., Kimura, H., and Maddin, R., "Nucleation and growth of stacking fault tetrahedra in gold," *Acta metallurgica*, vol. 12, no. 5, pp. 495–500, 1964.

[242] Wirth, B., Odette, G., Marian, J., Ventelon, L., Young-Vandersall, J., and Zepeda-Ruiz, L., "Multiscale modeling of radiation damage in fe-based alloys in the fusion environment," *Journal of nuclear materials*, vol. 329, pp. 103–111, 2004.

[243] Wirth, B., Odette, G., Maroudas, D., and Lucas, G., "Energetics of formation and migration of self-interstitials and self-interstitial clusters in α-iron," *Journal of nuclear materials*, vol. 244, no. 3, pp. 185–194, 1997.

[244] Xiao, X., Song, D., Xue, J., Chu, H., and Duan, H., "A size-dependent tensorial plasticity model for fcc single crystal with irradiation," *International Journal of Plasticity*, vol. 65, pp. 152–167, 2015.

[245] Xu, D. and Wirth, B. D., "Modeling spatially dependent kinetics of helium desorption in bcc iron following he ion implantation," *Journal of Nuclear Materials*, vol. 403, no. 1, pp. 184–190, 2010.

[246] Xu, D., Wirth, B. D., Li, M., and Kirk, M. A., "Defect microstructural evolution in ion irradiated metallic nanofoils: Kinetic monte carlo simulation versus cluster dynamics modeling and in situ transmission electron microscopy experiments," *Applied Physics Letters*, vol. 101, no. 10, p. 101905, 2012.

[247] Xu, Q., Yoshida, N., and Yoshiie, T., "Accumulation of helium in tungsten irradiated by helium and neutrons," *Journal of Nuclear Materials*, vol. 367, pp. 806–811, 2007.

[248] Yang, L., Zu, X. T., Wang, Z., Gao, F., Heinisch, H. L., Kurtz, R. J., Wang, X., and Liu, K., "Multiple-interactions of displacement cascades with he–vacancy clusters in α-iron: Computer simulations," *Journal of Nuclear Materials*, vol. 374, no. 3, pp. 437–444, 2008.

[249] Yu, K., Liu, Y., Sun, C., Wang, H., Shao, L., Fu, E., and Zhang, X., "Radiation damage in helium ion irradiated nanocrystalline fe," *Journal of Nuclear Materials*, vol. 425, no. 1, pp. 140–146, 2012.

[250] Zhang, L., Dingreville, R., Bartel, T., and Lusk, M. T., "Hybrid monte carlo simulation of stress-induced texture evolution with inelastic effects," *Metallurgical and Materials Transactions A*, vol. 42, no. 3, pp. 575–581, 2011.

[251] Zhang, L., Dingreville, R., Bartel, T., and Lusk, M. T., "A stochastic approach to capture crystal plasticity," *International Journal of Plasticity*, vol. 27, no. 9, pp. 1432–1444, 2011.

[252] Zhernenkov, M., Jablin, M. S., Misra, A., Nastasi, M., Wang, Y., Demkowicz, M. J., Baldwin, J. K., and Majewski, J., "Trapping of implanted he at cu/nb interfaces measured by neutron reflectometry," *Applied Physics Letters*, vol. 98, no. 24, p. 1913, 2011.

[253] Zinkle, S., Maziasz, P., and Stoller, R., "Dose dependence of the microstructural evolution in neutron-irradiated austenitic stainless steel," *Journal of Nuclear materials*, vol. 206, no. 2, pp. 266–286, 1993.

[254] Zinkle, S. and Singh, B., "Analysis of displacement damage and defect production under cascade damage conditions," *Journal of nuclear materials*, vol. 199, no. 3, pp. 173–191, 1993.

[255] Zinkle, S. and Singh, B., "Microstructure of cu–ni alloys neutron irradiated at 210 c and 420 c to 14 dpa," *Journal of nuclear materials*, vol. 283, pp. 306–312, 2000.

[256] Zinkle, S. J. and Farrell, K., "Void swelling and defect cluster formation in reactor-irradiated copper," *Journal of Nuclear Materials*, vol. 168, no. 3, pp. 262–267, 1989.

[257] Zinkle, S. J., "Advanced materials for fusion technology," *Fusion Engineering and Design*, vol. 74, no. 1, pp. 31–40, 2005.

[258] Zinkle, S. J., "Radiation-induced effects on microstructure," tech. rep., Oak Ridge National Laboratory (ORNL); High Flux Isotope Reactor; Shared Research Equipment Collaborative Research Center, 2012.

[259] Zinkle, S. J. and Singh, B. N., "Microstructure of neutron-irradiated iron before and after tensile deformation," *Journal of nuclear materials*, vol. 351, no. 1, pp. 269–284, 2006.